AD-A254 757

PAGE

1. AGENCY I		3. REPORT TYPE AND DATES COVERED
		Quarterly 13 Apr - 15 Apr 92

4. TITLE AND SUBTITLE	5. FUNDING NUMBERS
DIFFRACTIVE OPTICS: DESIGN FABRICATION & APPLICATIONS	F49620-92-J-0264

6. AUTHOR(S)	
Dr Quinn	AFOSR-TR· 02 0785

7. PERFORMING ORGANIZATION NAME(S) AND ADDRESS(ES)	8. PERFORMING ORGANIZATION REPORT NUMBER
Optical Society of America 2010 Massachusetts Ave NW Washington DC 20036	

9. SPONSORING / MONITORING AGENCY NAME(S) AND ADDRESS(ES)	10. SPONSORING / MONITORING AGENCY REPORT NUMBER
AFOSR/NE Bldg 410 Bolling AFB DC 20332-6448	2301/As

11. SUPPLEMENTARY NOTES

12a. DISTRIBUTION / AVAILABILITY STATEMENT	12b. DISTRIBUTION CODE
unlimited	

13. ABSTRACT (Maximum 200 words)

CONFERENCE WAS HELD

This document has been approved
for public release and sale; its
distribution is unlimited.

DTIC
ELECTE
AUG 12 1992
S A D

14. SUBJECT TERMS		15. NUMBER OF PAGES
		16. PRICE CODE

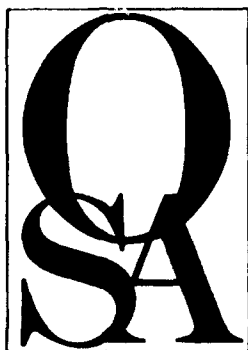| 17. SECURITY CLASSIFICATION OF REPORT	18. SECURITY CLASSIFICATION OF THIS PAGE	19. SECURITY CLASSIFICATION OF ABSTRACT	20. LIMITATION OF ABSTRACT
UNCLASS	UNCLASS	UNCLASS	UL

NSN 7540-01-280-5500

Standard Form 298 (Rev. 2-89)

Diffractive Optics: Design, Fabrication, and Applications

Summaries of papers presented at the Diffractive Optics: Design, Fabrication, and Applications Topical Meeting

April 13–15, 1992
New Orleans, Louisiana

1992 Technical Digest Series
Volume 9

CONFERENCE EDITION

92-22467

Optical Society of America
2010 Massachusetts Avenue, NW
Washington, DC 20036

92 8 7 105

Articles in this publication may be cited in other publications. In order to facilitate access to the original publication source, the following form for the citation is suggested:

Name of Author(s), "Title of Paper," in Diffractive Optics: Design, Fabrication, and Applications Technical Digest, 1992 (Optical Society of America, Washington, D.C., 1992), Vol. 9, pp. xx–xx.

CONTENTS

CABILDO ROOM

8:30 am–10:00 am
MA, DESIGN AND ANALYSIS OF DIFFRACTIVE LENSES
G. Michael Morris, *University of Rochester, Presider*

8:30 am (Invited)
MA1 Raytracing models for diffractive optical elements,
Peter P. Clark, Carmina Londono, *Polaroid Optical Engineering.* We compare several methods for modeling diffractive optical elements for the lens design process on the basis of accuracy, applicability, and ease of use. **(p. 2)**

9:00 am
MA2 Superzone diffractive lenses, John Futhey, Madeleine Fleming, *3M Company.* A novel diffractive lens design with fewer zones than conventional kinoforms is presented. Theoretical performance is discussed, and measured results of diamond-turned examples are given. **(p. 4)**

9:20 am
MA3 Athermalization with diffractive optics, Carmina Londono, William T. Plummer, Peter P. Clark, *Polaroid Optical Engineering.* We athermalize a single-material lens element by using a kinoform on one surface to keep its focal length and aberrations constant with temperature to the first order. **(p. 7)**

9:40 am
MA4 Thermal effects in diffractive lenses, Gregory P. Behrmann, *Harry Diamond Laboratories;* John P. Bowen, *Rochester Photonics Corp.* Expressions, in terms of temperature, describing the change in focal length, diffraction efficiency, and the effects of a thermal gradient for a diffractive lens are presented and discussed. **(p. 8)**

10:00 am–10:30 am Coffee Break

CABILDO ROOM

10:30 am–12:00 m
MB, FABRICATION TECHNOLOGIES: 1
J. Allen Cox, *Honeywell Inc., Presider*

10:30 am (Invited)
MB1 Diffractive optical elements fabricated by electron-beam lithography, Robin Smith, *Imperial College of Science Technology and Medicine, UK.* Unusual and unanticipated defocused images produced by a fabrication exercise combination of binary amplitude (or phase) diffractive cylindrical optical elements are described and analyzed. **(p.12)**

11:00 am
MB2 Pure silica diffraction gratings and microlens arrays made by the sol-gel process, Jean-Luc Nogues, *GELTECH, Inc.* This report details the sol-gel process used by GELTECH, Inc. to replicate diffraction gratings and microlens arrays in silica for ultraviolet, visible, and near-infrared applications. **(p. 15)**

11:20 am
MB3 Fabrication of continuous relief diffractive optical elements by laser writing, M. T. Gale, H. Schutz, *Paul Scherrer Institute, Switzerland;* P. Ehbets, D. Prongue, *Univ. Neuchatel, Switzerland.* An xy raster scan laser writing system has been developed for the fabrication of continuous, surface relief DOE microstructures such as kinoforms. **(p. 18)**

11:40 am
MB4 Dry photopolymer films for computer-generated middle infrared focusing elements fabrication, Yuri B. Boiko, Sergio Calixto, *Centro de Investigaciones en Optica, Mexico.* Dry photopolymer films provide deep relief formation and allow one to reproduce phase function of focusing elements by exposing films mentioned through computer-generated multi-grey-level amplitude mask. **(p. 21)**

12:00 m–2:00 pm LUNCH

CABILDO ROOM

2:00 pm–3:30 pm
MC, OPTICAL INTERCONNECTS FOR COMPUTING: 1
James R. Leger, *University of Minnesota, Presider*

2:00 pm (Invited)
MC1 System design for planar optics, Jurgen Jahns, *AT&T Bell Laboratories.* Various issues related to the fabrication of integrated micro-optic systems are considered such as the fabrication and properties of efficient diffractive optical elements, the design of imaging systems with a large space-bandwidth product, and the hybrid integration of optoelectronic chips with the passive glass optics. **(p. 26)**

2:30 pm
MC2 Diffractive optics in a free-space digital optic system,
R. L. Morrison, S. L. Walker, T. J. Cloonan, F. A. P. Tooley, F. B. McCormick, J. M. Sasian, A. L. Lentine, J. L. Brubaker, R. J. Crisci, S. J. Hinterlong, H. S. Hinton, *AT&T Bell Laboratories.* Diffractive optics have been used to generate an array of beams and to form the interconnection stage in a prototype free-space digital optic system. **(p. 28)**

2:50 pm
MC3 Fabrication and integration of diffractive optical elements into high-density vertical interconnects, Franz Haas, David A. Honey, Harold Bare, *USAF Photonics Center;* David Mikolas, Harold Craighead, Richard Bojko, Graham Pugh, *Cornell Univ.* Diffraction gratings were fabricated and integrated into a vertical optical interconnect architecture. Competing fabrication technologies are compared for grating performance and interconnect packing densities. **(p. 31)**

11:00 am
TuB2   Diffraction efficiency of a grating as a function of the state of polarization of incident light, R. M. A. Azzam, *Univ. New Orleans.* The dependence of the diffraction efficiency of an arbitrary grating in any orientation on the polarization state of incident light is analyzed in the Stokes-Poincare space. **(p. 69)**

11:20 pm
TuB3   Solution to the multiple grooves scattering problem—the fast polarization case, Yon-Lin Kok, *Univ. South Alabama.* A general solution is presented to describe electromagnetic scattering by a finite number of rectangular grooves and of arbitrary feature sizes corrugated in a perfectly conducting ground plane. The scattered field is expressed as a Fourier-type integral in which the angular spectrum is a series of the cylindrical Bessel functions. **(p. 72)**

11:40 am
TuB4   On the convergence of the coupled-wave approach for lamellar diffraction gratings, Lifeng Li, Charles W. Haggans, *Univ. Arizona.* Limitations of the coupled-wave approach when applied to lamellar gratings, especially metallic lamellar gratings, in TM polarization are discussed. **(p. 75)**

12:00 m–2:00 pm   LUNCH

CABILDO ROOM

2:00 pm–3:30 pm
TuC, FABRICATION TECHNOLOGIES: 2
James R. Leger, *University of Minnesota, Presider*

2:00 pm
TuC1   Laser technologies of diffractive element synthesis for mass-application optical systems, V. P. Koronkevich, *Russian Academy of Sciences, Russia.* Masks of elements for interferometers, objectives, readout pickups, scales, and decorations have been generated with a laser photoplotter in amorphous silicon and chromium films. Multiplication into glass (binary or kinoform profile) has been carried out by means of photolithography. **(p. 80)**

2:30 pm   (Invited)
TuC2   Efficient beam splitters and beam deflectors for integrated planar micro-optics, S. J. Walker, J. Jahns, N. K. Ailawadi, W. M. Mansfield, P. P. Mulgrew, J. Z. Pastalon, C. W. Roberts, D. M. Tennant, *AT&T Bell Laboratories.* High-frequency phase gratings with two or multiple phase levels can be used as efficient beam splitters and beam deflectors. We discuss fabrication, physics, and applications of these gratings for integrated micro-optics. **(p. 82)**

2:50 pm
TuC3   Simultaneous and sequential recording of holographic fan-out elements, H. P. Herzig, P. Ehbets, D. Pronque, R. Dandiker, *Univ. Neuchatel, Switzerland.* Coherent and incoherent recording of efficient (>90%) fan-out elements in thick volume holograms have been investigated by using coupled wave theory. **(p. 85)**

3:10 pm
TuC4   Design and fabrication of resonance domain diffractive optical elements, J. Michael Miller, Jari Turunen, Mohammad R. Taghizadeh, *Heriot-Watt Univ. UK;* Eero Noponen, Antti Vasara, *Helsinki Univ., Finland.* High-efficiency fan-out elements, star couplers, and polarization-sensitive devices are generated using the electromagnetic grating theory; some designs are demonstrated at $\lambda = 5.52 \ \mu$m. **(p. 88)**

CABILDO ROOM

3:30 pm–4:00 pm
TuD, POSTER PREVIEW SESSION
(Poster session will immediately follow)
James R. Leger, *University of Minnesota, Presider*

3:30 pm
TuD1   Diffraction grating photopolarimeter, R. M. A. Azzam, K. A. Giardina, *Univ. New Orleans.* The assembly, calibration, and testing of a new photopolarimeter that employs multiple-beam diffraction from a grating, with or without additional linear polarizers, are described. **(p. 92)**

3:32 pm
TuD2   Hybrid diffractive/refractive lens for use in optical data storage, David Kubalak, G. Michael Morris, *Univ. Rochester.* A hybrid diffractive/refractive lens is used to correct longitudinal chromatic aberration and to reduce the size and weight of an objective for an optical data storage system. **(p. 93)**

3:34 pm
TuD3   Beam shaping of high-power laser-diode array by continuous surface-relief elements, P. Ehbets, H. P. Herzig, R. Dandliker, *Univ. of Neuchatel, Switzerland;* I. Kjelberg, *Centre Suisse d'Electronique et de Microtechnique S. A., Switzerland.* The far-field of a 10-element laser-diode array is shaped into a single Gaussian beam using a binary phase plate and a continuous surface-relief element. **(p. 96)**

3:36 pm
TuD4   Grating-enhanced detection of surface acoustic waves using an acousto-optic modulator, D. A. Larson, T. D. Black, *Univ. Texas at Arlington.* Traveling gratings in an acousto-optic modulator are used to detect spatially separated surface acoustic waves. The detection sensitivity falls off slowly with increasing separation distance. **(p. 99)**

3:38 pm
TuD5   Traceable aspheric testing using diamond-machined diffractive null lenses, Clinton Evans, Melvyn Francis, Donald Morrison, *Hughes Leitz Optical Technologies, Canada.* We describe a diffractive null lens arrangement for testing concave aspheric mirrors. The wavefront aberration of the null lens can be verified by simple laboratory measurements.
(p. 102)

3:40 pm
TuD6   Design of dynamic imaging systems using spatial-light-modulator-based kinoform lenses, Eddy C. Tam, *Univ. North Carolina at Charlotte;* Qiwang Song, *Syracuse Univ.* This paper describes a spatial-light-modulator-based, dynamic zooming/focusing optical system that does not require any mechanical movement of the lenses.
(p. 108)

3:42 pm
TuD7   Diffractive properties of gelatin as an aerogel, Richard D. Rallison, Stephen E. Bialkowski, *Ralcon Corp.* Dichromated gelatin changes effective refractive index from 1.54 to 1.27 and expands 20% from processing. This aerogel effect causes aberrations but enables new diffractive optics.
(p. 111)

3:44 pm
TuD8   Binary mask generation for diffractive optical elements using microcomputers, Donald C. O'Shea, James W. Beletic, Menelaos Poutous, *Georgia Institute of Technology.* We present a fast and inexpensive technique for generation of binary masks: we use ordinary desktop publishing software and hardware with a standard photoreduction camera.
(p. 114)

3:46 pm
TuD9   Methods for diffractive elements surface profile fabrication, A. G. Poleshchuk, *Russian Academy of Sciences, Russia.* New lithography technology for high-efficiency diffractive optical element fabrication was proposed and investigated. Comparison with well-known multilevel and continuous-tone ones was made. Experimental results are presented. **(p. 117)**

3:48 pm
TuD10   MacBEEP: a desktop system for binary optics, Philip S. Levin, Lawrence H. Domash, *Foster-Miller, Inc.* MacBEEP is a low-cost system for binary optics based on widely available equipment including industrial laser typesetters (10-μm resolution) and scanning electron microscopes (0.05 μm). **(p. 120)**

3:50 pm
TuD11   Holographic optical elements for incoherent spatial filtering with longitudinal periodicity, S. Gruner Hanson, *Riso National Laboratory, Denmark.* The possibility of using computer generated holographic optical elements for achieving longitudinal periodicity in incoherent systems by wave field replication is addressed and experimentally verified.
(p. 123)

3:52 pm
TuD12   Achromatic Fraunhofer and Fresnel diffraction patterns: theory and experiment, P. Andres, J. Lancis, V. Climent, *Universitat Jaume I, Spain;* W. D. Furlan, *Universitat de Valencia, Spain.* We present some simple optical setups for obtaining achromatic Fraunhofer and Fresnel diffraction patterns, by using solely on-axis zone plates. Experimental results are also included. **(p. 126)**

3:54 pm
TuD13   Robert Aldrich, *Texas Instruments.* Many have suggested the use of diffractive optics as color correctors in the IR, some have even built such devices. Plastic aspheric eyepieces are lighter weight than conventional glass spherical optics due to plastics' smaller specific gravity and the superior correction of aspheres, which allows for fewer elements. Combining the precision of OPT plastics and diffractive optics allows for ultralightweight eyepiece design.
(p. 129)

3:56 pm
TuD14   Holographic-element-array-based laser directional and wavelength discrimination device, Jenkins Chen, Freddie Lin, *Physical Optics Corp.;* William Liu, *Multispace.* A laser warning device, based on a holographic element array in a monolithic–integrated optical substrate, was used to detect both direction and wavelength of laser threat.
(p. 130)

3:58 pm
TuD15   Lamellar gratings as polarizing elements for specularly reflected beams, Charles W. Haggans, Lifeng Li, Raymond K. Kostuk, *Univ. Arizona.* High spatial frequency *lamellar* gratings that function as phase compensators, quarter-wave and half-wave retarders, and polarization rotators for specularly reflected beams are presented. **(p. 133)**

4:00 pm–5:30 pm
TuE, POSTER SESSION
(Presentation of TuD1–TuD15)

PELICAN ROOM

6:00 pm-7:30 pm   CONFERENCE RECEPTION

CABILDO ROOM

8:30 am–10:00 am
WA, FABRICATION TECHNOLOGIES: 3
Peter P. Clark, *Polaroid, Corp., Presider*

8:30 am
WA1 Blazed diffracting optical components, M. C. Hutley, *National Physical Laboratory.* This paper summarizes and compares the merits and limitations of various techniques for manufacturing diffracting components with a blazed surface relief profile for use in the ultraviolet, visible, and infrared. **(p. 138)**

9:00 am
WA2 Implementation of a packed data format for production of computer-generated holograms by e-beam lithography, Daniel M. Newman, Robert W. Hawley, Neal C. Gallagher, *Purdue Univ.* A packed data format for e-beam production of computer-generated holograms has been implemented, which facilitates hologram production that file size would otherwise make impossible. **(p. 140)**

9:20 am
WA3 Process error limitations on performance of diffractive optical elements, J. Allen Cox, *Honeywell Systems & Research Center.* Experimental data are presented to demonstrate the sensitivity of image quality and efficiency to processing errors. Image quality is insensitive to such errors, while efficiency is most sensitive to masked alignment errors. **(p. 143)**

9:40 pm
WA4 Performance of coated diffractive optics, Van Hodgkin, Merle Elson, Lew DeSandre, *U.S. Naval Weapons Center;* Tianji Zhao, Angus Macleod, *Optical Sciences Center.* Theoretical studies and experimental measurements of the performance of coated and uncoated transmissive diffractive elements are reported. Theoretical calculations include (1) Fourier diffraction and (2) coupled-wave diffraction theory. Measurements include the determination of the surface profile and the angle resolved scattering between orders. Comparisons are made between theory and experimental measurements and the influence of an antireflection coating on the performance of the elements is investigated. **(p. 146)**

10:00 am–10:30 am   COFFEE BREAK

CABILDO ROOM

10:30 am–12:00 m
WB, DESIGN TECHNIQUES FOR DIFFRACTIVE OPTICS
Dale A. Buralli, *Sinclair Optics Inc., Presider*

10:30 am   (Invited)
WB1 Signal synthesis and coding in diffractive optics, Frank Wyrowski, *Univ. Essen, Germany.* The synthesis of a desired signal as the diffraction pattern of a diffractive element is the main subject in diffractive optics. The dependence of the diffraction efficiency on the signal is discussed. **(p. 148)**

11:00 am
WB2 Phase optimization of kinoform by simulated annealing, N. Yoshikawa, T. Yatagai, *Univ. Tukuba, Japan.* The phase distribution and quantizing levels in the kinoform are determined by simulated annealing optimizing algorithm. The optimum kinoform calculation is reconstructed with a LCSLM. **(p.151)**

11:20 am
WB3 Annealing binary Fresnel holograms for shaped beam generation, Clark C. Guest, *U.S. Army Missile Command.* Simulated annealing is applied for designing a binary phase-only hologram that produces a specified two-dimensional profile in the Fresnel diffraction regime. **(p. 154)**

11:40 am
WB4 Diffraction efficiency of multilevel binary optics lenses, William H. Southwell, *Rockwell International Science Center.* The diffraction efficiency as a function of beam f/number oscillates. The peak diffraction efficiency does not occur with integer number of Fresnel zones over the beam. **(p. 157)**

12:00 m–2:00 pm   LUNCH

CABILDO ROOM

2:00 pm–3:30 pm
WC, OPTICAL INTERCONNECTS FOR COMPUTING: 2
Jurgen Jahns, *AT&T Bell Laboratories, Presider*

2:00 pm   (Invited)
WC1 Diffractive optical elements in optoelectronics, Norbert Streibl, *Physikalisches Institut, Germany.* Diffractive components such as deflectors, lenses and (multiple) beam splitters can be employed in optoelectronics for optical interconnections, sensors, and laser optics. Volume holograms and computer-generated structures-will be discussed. **(p. 162)**

2:30 pm
WC2   Analysis of weighted fan-out/fan-in volume holographic interconnections, Gregory P. Nordin, Armand R. Tanguay, Jr., B. Keith Jenkins, *Univ. Southern California;* Praveen Asthana, *IBM Corporation.* The weighted interconnection fidelity and throughput efficiencies of both single-source fully coherent and multiple-source incoherent/coherent volume holographic interconnection architectures are compared based on numerical simulation of a ten-to-ten interconnection. (p. 165)

2:50 pm
WC3   Acousto-optic programmable spot array generator, Joseph N. Mait, Dennis W. Prather, *Harry Diamond Laboratories;* Ravindra A. Athale, *George Mason Univ.* An acousto-optic (AO) system is demonstrated that is capable of generating reconfigurable two-dimensional nonseparable spot arrays. The analog nature of the AO devices provides considerable degrees of both magnitude and phase design freedom such that uniform and efficient arrays can be generated. (p. 168)

3:10 pm
WC4   Multiple beam splitter characteristics of holographic surface-relief gratings recorded nonlinearly, P. Langlois, R. Beaulieu, *National Optics Institute;* A. Beauregard, *Lasiris Inc.* Diffraction characteristics of surface-relief gratings that produce several beams of approximately equal intensities and have high diffraction efficiency are presented. Experimental results for the diffraction efficiencies are also presented. (p. 171)

Design and Analysis
of Diffractive Lenses

MA   8:30am–10:00am
Cabildo Room

G. Michael Morris, *Presider*
University of Rochester

Raytracing Models for Diffractive Optical Elements

Peter P. Clark, Carmiña Londoño

Polaroid Optical Engineering

38 Henry Street

Cambridge, MA 02139

(617) 577-4115

Summary:

Optical designers currently have several ways to model surface relief diffractive optical elements (DOE's) on the computer. We are aware of three distinct techniques: the phase model[1,2], the Sweatt model[3] and the Southwell model[4]. We will compare them for accuracy, applicability and ease of use. These models must perform two functions: a) Accurately simulate the performance of the DOE. b) Be translatable into information that will allow the physical part to be produced.

The phase model specifies phase change across the element, which allows ray tracing in one diffracted order at a time. The ray tracing is accurate, but diffraction efficiency is not taken into account. Systems with non-zero field or bandwidth have inevitable efficiency loss that can affect image quality[5].

The Sweatt model simulates a DOE by using a conventional lens representation with a high refractive index. Like the phase model, it traces one diffracted order at a time, ignoring efficiency. Furthermore, the accuracy of the ray trace depends upon the magnitude of the refractive index that was used. To minimize numerical errors, it is desirable to keep the index low. We estimate what it should be to keep ray tracing errors acceptably small. This is a function of system scale, Lagrange invariant, incidence angle and other parameters.

The Southwell phased Fresnel lens model describes the DOE using a multi-faceted configuration of the surface. Rays are traced in the conventional manner. The complex surface description is difficult to represent with current lens design codes, but this model is remarkable because it takes account of efficiency changes automatically.

References:

1- M.J.Hayford, Proc.SPIE, v.554, p.502 (1985).

2- G.J.Swanson, Tech.Report 854, MIT Lincoln Lab. (1989).

3- W.C.Sweatt, JOSA, v.67, p.803 (1977).

4- W.H.Southwell, Proc.SPIE, v.1354, p.38 (1990).

5- C.Londoño, P.Clark, Proc.SPIE, v.1354, p.30 (1990).

Superzone diffractive lenses

John Futhey and Madeleine Fleming

(707) 765-3228   (612) 736-9287

Optics Technology Center 3M Company 1331 Commerce St. Petaluma CA 94952

INTRODUCTION

Diffractive optical elements, particularly kinoforms, can be fabricated by multi-mask photo-lithography or by diamond turning. At the 3M Optics Technology Center in Petaluma California, we are currently investigating methods to diamond turn such optics. As the aperture of the optic increases and the f/number decreases, the number of discrete zones that must be cut increases and the size of the individual zones becomes smaller. This combination of more and smaller zones provides a challenge -- and an eventual limit -- to diamond turning capabilities. We show how a novel design allows us to diamond turn diffractive optics that are larger and faster than was previously possible, but whose theoretical performance is nearly diffraction limited.

KINOFORM GEOMETRY
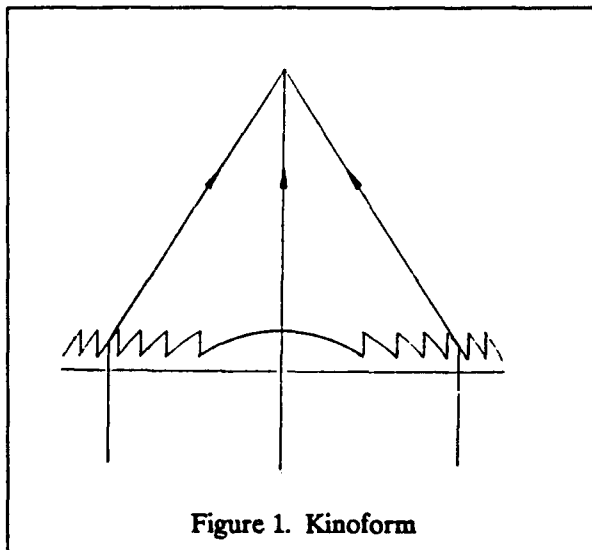
Figure 1. Kinoform

A kinoform[1] is a focusing diffractive lens consisting of a number of circular concentric zones. This is a phase only device and the phase change at each zone discontinuity is equal to 2π. In addition, the region between zone boundaries is a blaze of a curved shape. This combination of blazed zones and 2π discontinuities provides a conservation of

phase at the focal point for all normal rays through the lens, and thus diffraction limited perfomance on axis. Figure 1 is a schematic of the kinoform.

It has been shown[2] that an expression for the radius of the ith zone is given by

$$r_i^2 = 2i\lambda f + i^2\lambda^2 \qquad (1)$$

and the height of the steps at the zone boundaries is

$$step = \lambda/(n-1) \qquad (2)$$

where λ is the design wavelength, f is the focal length, and n is the index of refraction. This represents a phase difference of 2π at the discontinuity.

The number of zones (approximately) of a kinoform of radius R is

$$Number\ of\ zones = R^2/2\lambda f \qquad (3)$$

A rule of thumb is appropriate for finding the width of the smallest zone of the kinoform. For visible light, the width is approximately equal to the f/number of the lens in microns. Using this rule of thumb and equation (3), consider as an example an f/4 lens 25 mm in diameter with $\lambda = .5$ microns. It would have about 1500 zones the smallest of which would be about 4 microns wide. At present such a kinoform would challenge our diamond turning capability.

STREHL RATIO

The Strehl ratio[3] is the on-axis focal intensity of a given lens divided by the on-axis focal intensity of a perfect lens. A diffraction limited lens would therefore have a Strehl ratio of 1. We shall use the Strehl ratio as a merit function in comparing other diffractive designs to the kinoform. The theoretical on-axis intensity of a diffractive element is found by integrating the amplitude and phase at the focal point over the aperture of the lens:

$$I = \int \int A(x,y)e^{-i\phi\,(x,y)}dxdy \qquad (4)$$

where $A(x,y)$ is the amplitude function and $\phi\,(x,y)$ is the phase function. (For our consideration, $A(x,y)$ is assumed to be constant and the intensity is normalized to 1 for a perfect lens.)

VARIATIONS FROM A KINOFORM

2a. Curved Blaze Kinoform

2b. Chord Blaze Kinoform

2c. N2π Diffractive Lens

2d. Superzone Diffractive Lens

Figure 2. Diffractive Lenses
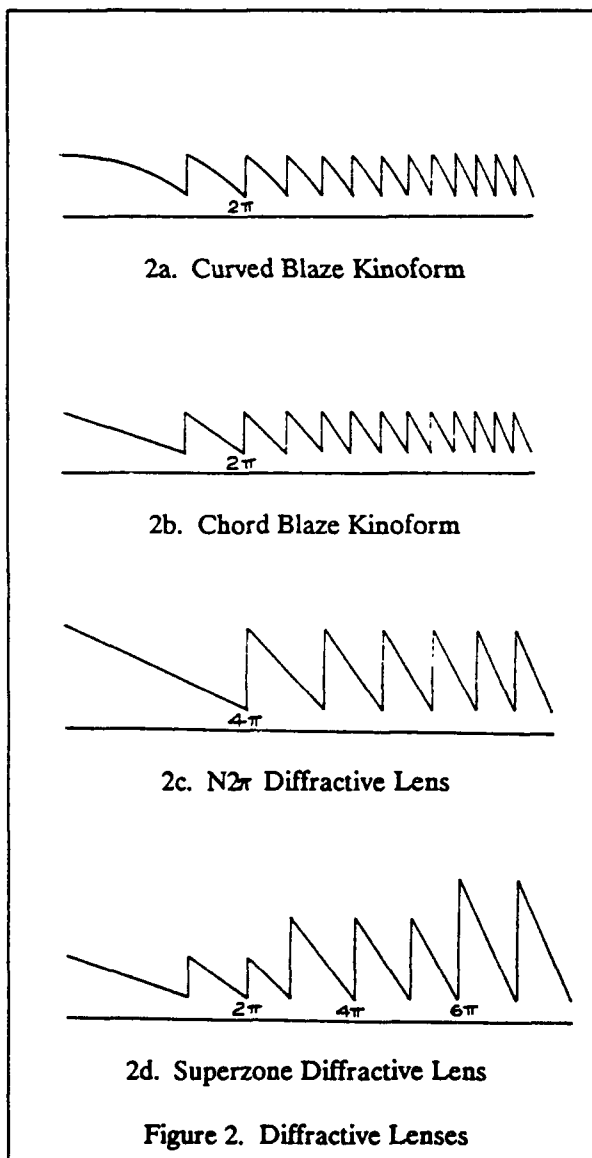
Figure 2 shows "half" cross-sections of several diffractive lenses. The curved blazes of the kinoform of 2a are very difficult to diamond turn, and therefore chord approximations for them are used because of the comparative ease in diamond turning them. This modification is shown in figure 2b.

Figure 2c shows a diffractive lens with only half as many zones, but with each zone boundary representing a phase change of 4π instead of the familiar 2π of the conventional kinoform. (This concept can be generalized to provide 1/N as many zones and N2π boundary steps.)

Figure 2d shows a superzone. In this configuration, the first few zones are conventional kinoform spacing and 2π steps. Then the next several zones each incorporate two of the orginal kinoform zones and have steps of 4π. Then zones of 3 original zones and steps of 6π and so on up to some maximum number N where the steps would be N2π. N is referred to as the superzone number (SZ#).

Although there are any number of possible choices of where to change from i2π steps to (i+1)2π steps, in our work we divided the radius of the lens into N nearly equal sections and made the change from i2π to (i+1)2π at each ith section boundary.

Table 1 shows the Strehl ratios and number of zones for the kinoforms and their variations as described above. These are all f/4 lenses, 25 mm in diameter, with a design wavelength of λ = .5 microns

Lens Description	Strehl Ratio	No. of Zones
Curved blaze Kinoform	1.000	1557
Chord blaze Kinoform	0.999	1557
10x2π Lens	0.958	156
Superzone (SZ# = 10)	0.999	267
25x2π Lens	0.790	63
Superzone (SZ# = 25)	0.997	117

Table 1. Strehl Ratio and number of zones for various diffractive lens designs

The 10x2π and 25x2π lenses refer to the case where all of the zones have their step heights 10 and 25 times the height of a standard kinoform. Similarly the SZ# = 10 and SZ# = 25 refer to the superzone numbers of the two superzone lenses. Again, this means the outer zone step heights are 10 or 25 times that of a kinoform, but inner ones are less, and the central zone step heights are in fact equal to those of a kinoform.

The important thing to note of course is that for the superzones, not only has there been a great reduction in the number of zones, but the Strehl ratio remains very high (nearly diffraction limited). This is not the case with the lenses that have all of their zones equal to multiple kinoform zones.

It follows that the superzone design provides a diffractive optic that is theoretically nearly diffraction limited in its performance but at the same time is much easier to diamond turn than a conventional kinoform.

EXPERIMENTAL RESULTS

Two superzone lenses were diamond turned and tested. A layer of cast acrylic 1.5 mm thick was bonded to a glass flat ($\lambda/10$) that was 75 mm in diameter and 14 mm thick. The superzone lens was diamond turned directly into the acrylic face. The large thick glass substrate upon which the acrylic was mounted provided mechanical and environmental stability that polymers don't have. The lenses were designed to have the finite conjugate on the side of the acrylic/air interface, and the infinite conjugate on the side of the glass/air interface. The aperture of the lens portion was 25 mm. The superzone number of one of the lenses was SZ# = 10 with 211 zones and the other was SZ# = 25 with 91 zones. The design wavelength was chosen to be .6328 microns to facilitate metrology of the lenses.

The wavefronts of the lenses were measured and analyzed with a Zygo Mark IV interferometer. The lens with SZ# = 25 had a peak to valley wavefront error of .557 waves and a Strehl ratio of .675. The lens with SZ# = 10 had a wavefront error of .416 waves and a Strehl ratio of .800.

Previously we[4] reported on the fabrication and testing of two superzone mirrors (SZ# = 10 and SZ# = 25). Their Strehl ratios were .937 and .935 respectively. These mirrors were diamond turned

on large copper blanks and we beleive that the difficulty of diamond turning plastic when compared to the relative ease of cutting copper is the main reason for the disparity in the results between the two efforts.

CONCLUSIONS

The design and theoretical performance of a new diffractive lens, called a superzone, has been presented. This lens is much more easily diamond turned than conventional kinoforms because of its fewer and larger zones. Additionally, the results of two such superzone lenses were presented, and although their performance was not as good as theoretical predictions, this is largely attributed to the plastic material which does not lend itself to accurate diamond turning.

REFERENCES

1. L. Lesem, P. Hirsch, and J. Jordan Jr., "The kinoform: a new wavefront reconstruction device", IBM J.Res.Develop. 13, 150-155, (1969)

2. M. Young, "Zone plates and their aberrations", J.Opt.Soc.Am. 62, 972-976 (1972)

3. K. Strehl, Z.f.Instrumkde., 22, 213, (1902)

4. J. Futhey, M. Fleming, and S. Saxe, "Superzone diffractive opitcs", Technical Digest for the Optical Society Annual Meeting, San Jose, (1991)

Athermalization with Diffractive Optics

Carmiña Londoño

Polaroid Optical Engineering

38 Henry Street

Cambridge, MA 02139

(617) 577-4115

William T. Plummer

Polaroid Optical Engineering

38 Henry Street

Cambridge, MA 02139

(617) 577-4231

Peter P. Clark

Polaroid Optical Engineering

38 Henry Street

Cambridge, MA 02139

(617) 577-3010

We athermalize a single-material lens element by using a
kinoform on one surface to keep its focal length and
aberrations constant with temperature to the first order.

Thermal Effects In Diffractive Lenses

Gregory P. Behrmann
Harry Diamond Laboratories
SLCHD-ST-OP
2800 Powder Mill Road
Adelphi, MD 20783
(301)-394-3800

John P. Bowen
Rochester Photonics Corporation
80 O'Connor Road
Fairport, NY 14450
(716)-377-7990

For military and aerospace applications, temperature is one of the more important environmental influences on optical systems. For example, some systems are required to operate over a temperature range of $-30°C$ to $50°C$. However, little has been reported in the open literature on the effects of temperature on diffractive optical elements[1,2].

The effects of temperature on refractive systems have been investigated[3,4]. By understanding the effect of temperature on diffractive lens performance, the same athermalization techniques that are used for refractive systems can be applied to systems containing diffractive elements. In this work, we develop expressions describing the change in focal length for diffractive lenses. We also discuss the change in diffraction efficiency due to temperature and the effect of radial thermal gradients.

The opto-thermal expansion coefficient for a refractive lens, $x_{f,r}$, as defined by Jamieson,[3] relates the change in focal length to changes in temperature. For a single thin lens, $x_{f,r}$ is given by:

$$x_{f,r} = \frac{1}{f}\frac{df}{dT} = \alpha_g - \frac{1}{n - n_{air}}\left(\frac{dn}{dT} - n\frac{dn_{air}}{dT}\right), \tag{1}$$

where α_g is the coefficient of thermal expansion of the lens material $[°C^{-1}]$, n is its refractive index, and n_{air} is the refractive index of air. Since $x_{f,r}$ is normalized by f it can easily be used to calculate the change in focal length by:

$$\Delta f = f x_{f,r}\Delta T. \tag{2}$$

For multi-lens systems, the opto-thermal coefficient of the system is a function of the thermal properties of the individual lenses. However, techniques for athermalizing refractive optical systems have been developed.[3,4,5]

For a diffractive lens, the focal length is given by:[6]

$$f = \frac{R_m^2}{2m\lambda_o}, m = 1, 2, 3, ..., \tag{3}$$

where R_m is the radius to zone m and λ_o is the design wavelength. If R_m is, to the first order, a function of temperature, it can be expressed as

$$R_m(T) = R_m(1 + \alpha_g\Delta T). \tag{4}$$

The focal length, as a function of temperature, can now be written

$$f(T) = \frac{R_m^2}{2m\lambda_o}[1 + 2\alpha_g\Delta T + \alpha_g^2(\Delta T)^2]. \tag{5}$$

For most materials the second-order term, $\alpha_g^2(\Delta T)^2$, is negligible ($\leq 10^{-11}$) and an opto-thermal expansion coefficient for a diffractive lens can therefore be given as

$$x_{f,d} = 2\alpha_g. \tag{6}$$

The change in focal length for a diffractive lens can be determined by:

$$\Delta f = f 2\alpha_g \Delta T. \tag{7}$$

Unlike a refractive lens, the change in focal length of a diffractive lens is only a function of α_g and is not a function of temperature induced changes in the refractive index. For most optical glasses, $x_{f,d}$ ranges from $10 \times 10^{-6o}C^{-1}$ to $20 \times 10^{-6o}C^{-1}$. In contrast, $x_{f,r}$ varies considerably more, from $-5 \times 10^{-6o}C^{-1}$ to $30 \times 10^{-6o}C^{-1}$. For a few materials, $x_{f,d}$ is significantly less than $x_{f,r}$, e.g., silica, polycarbonate, and acrylic. Since athermalization of optical systems is easier when materials having a wide range of opto-thermal coefficients are available, the limited range offered by diffractive lenses indicates a possible difficulty in athermalizing diffractive optical systems.

Although thermal changes in the index of refraction do not affect the focal length, they do alter the lens blaze height, h, and hence the diffraction efficiency of the lens. If the diffractive lens is in air, h is given by:[6]

$$h = \frac{\lambda_o}{n-1}, \tag{8}$$

where λ_o is the design wavelength and n is the index of refraction of the lens material. A diffraction efficiency of 100% is achieved by having a continuous-phase profile with this blaze. However, due to a change in temperature, the blaze height will change thus reducing the diffraction efficiency. For a relative error, ϵ, in the blaze height, Swanson[7] has shown from scalar diffraction theory, that the first order diffraction efficiency, η_1, is

$$\eta_1 = [\frac{\sin(\pi\epsilon)}{\pi\epsilon}]^2. \tag{9}$$

During a temperature change, a blaze height error is created by both the change in the height of the diffractive surface and the change in index of refraction. Since ϵ is a relative error in blaze height, it can be determined from δ, the true error in height, divided by h.

$$\epsilon = \frac{\delta}{h} \tag{10}$$

δ is defined here as

$$\delta = h_a - h_d, \tag{11}$$

where h_d is the blaze height required to maintain maximum diffraction efficiency by a lens having a temperature modified index of refraction:

$$h_d = \frac{\lambda_o}{[n + (\frac{dn}{dT})\Delta T] - 1}, \tag{12}$$

and h_a is the actual blaze height of the lens due to its coefficient of thermal expansion:

$$h_a = h(1 + \alpha_g \Delta T). \tag{13}$$

By substituting Eq. (12) and Eq. (13) into Eq. (11). δ. for small changes in temperature. can be given by:

$$\delta \approx \frac{\lambda_o \Delta T}{n - 1}[\alpha_g + \frac{1}{n-1}\frac{dn}{dT}]. \tag{14}$$

We have determined that for most materials, including plastic, the change in diffraction efficiency due to temperature effects is negligible.

In some systems, a temperature gradient may exist in the radial direction. Such a gradient affects the optical path and introduces aberrations. Since such a temperature distribution is time varying, an exact

solution to the temperature distribution is difficult. If we assume that the gradient is not time varying and is linear with respect to the radial coordinate, it is possible to determine the change in optical path. In the following it is assumed that the temperature on axis is T and the temperature at the edge of the lens is $T + \Delta T$. The radius of the lens is denoted by R_{max}. If the change in radial distance r is Δr, the new radial distance is

$$r' = r + \Delta r = r[1 + \frac{\alpha_g \Delta T}{2}(\frac{r}{R_{max}})].$$ (15)

As a function of radial distance, the phase $\phi(r)$ of the diffractive surface is commonly represented as

$$\phi(r) = \frac{2\pi}{\lambda_o}[s_1 r^2 + s_2 r^4 + s_3 r^6 + ...],$$ (16)

where $s_1, s_2, ...$ are the phase coefficients and λ_o is the design wavelength. By substituting Eq.(15) into Eq.(16), we obtain the phase function for the diffractive surface as a function of temperature change:

$$\phi(r') = \frac{2\pi}{\lambda_o}[s_1(r^2 + \alpha_g \Delta T r^3) + s_2(r^4 + 4\alpha_g \Delta T r^5)].$$ (17)

In Eq. (17), higher order terms in ΔT have been dropped. Note that the temperature shift produces a term in the wavefront that varies as the third power of the radius over the entire pupil. If a glass substrate is used for the diffractive lens, the coefficient of thermal expansion of the diffractive surface is considered to be the same as the substrate and a typical value of α_g for glass is $7 \times 10^{-6}°C^{-1}$. For an $f/5$ lens having a focal length of 100mm at 632nm, a thermal gradient of $1°C$ introduces an optical path difference at the edge of the aperture of 0.05 waves. For a polycarbonate lens, the path difference is approximately 10 times this, or 0.5 waves.

An analysis of the effects of temperature on a diffractive lens has been performed. We have derived an expression for the opto-thermal expansion coefficient that depends only on the coefficient of thermal expansion of the substrate. This opto-thermal coefficient can be used for the design of hybrid refractive/diffractive systems in order to analyze the effects of thermal changes on image quality. Of course, in the actual design one must consider the mounting materials that are used. For some systems, diffractive surfaces may be useful to help athermalize the system. The technique is analagous to that in which a diffractive surface is added to a refractive lens for aberration correction.

Areas of future investigation include the interaction of epoxy and glass and the effect of thermally induced stresses on transmitted wavefronts. We also plan to conduct experiments in an environmental chamber to measure the performance of diffractive optics during temperature changes.

1. M. Tanigami, S. Ogata, S. Aoyama, T. Yamashita, and K. Imanaka, "Low-Wavefront Aberration and High Temperature Stability Molded Micro Fresnel Lens," IEEE Photonics Tech. Lett. 1 (1989) pp. 384-385.

2. A. McKay and J. White, "Effects of Simulated Space Environments on Dichromated Gelatin Holograms," SPIE Proc. 1044 (1989) pp. 269-275.

3. T. H. Jamieson, "Thermal Effects In Optical Systems," Optical Engr. 20 (1981) pp. 156-160.

4. D. S. Grey, "Athermalization of Optical Systems," JOSA 38, 542, 1948.

5. M. Roberts, "Athermalisation of Infrared Optics: a review," SPIE Proc. 1049 (1989) pp.72-81.

6. D. Buralli and M. Morris, "Design of a Wide Field Diffractive Landscape Lens," Appl. Opt. 28, (1989) pp. 3950-3959.

7. G. J. Swanson, "Binary optics technology: The theory and design of mulit-level diffractive optical elements," MIT Lincoln Laboratory Tech. Rep. 854,(1989).

Fabrication Technologies 1

MB 10:30am–12:00m
Cabildo Room

J. Allen Cox, *Presider*
Honeywell Inc.

Diffractive Optical Elements Fabricated by Electron Beam Lithography

Robin Smith

Applied Optics Group, Blackett Laboratory, Imperial College of Science Technology and Medicine, Prince Consort Road, London SW7 2BZ, UK.   Tel: 071 225 8846

In recent years we have studied binary amplitude diffractive optical elements fabricated by means of electron beam lithography in the form of opaque chrome rulings on glass substrates and binary phase elements produced from these by contact copying into photoresist. We have investigated a range of imaging structures including zone plates, diffractive axicons, Dammann gratings and elements designed for optical testing. We are currently developing elements to generate particular aberrated wavefronts for the direct recording of volume diffractive elements in DCG and elements to generate curved line patterns for single shot CO_2 laser machining.

As a fabrication exercise we have investigated the images produced by a pair of crossed cylindrical diffractive optical elements and have observed, in addition to the expected focal properties, some unanticipated images at different focal distances. In this paper these images and their origin are discussed. These diffractive elements were designed and tested by Andrew West and produced at the SERC e-beam facility at the Rutherford Laboratory.

A convenient way of describing the effect of a conventional spherical glass lens, in the paraxial approximation, is to say that it introduces a quadratic phase term of the form $\exp ikW(x,y) = \exp ik(x^2 + y^2)/2f$ and this has the effect of converting an incoming plane wave to a spherical wave converging to a focus at distance f. Here W represents the modification to the incoming wavefront introduced by the lens.

A simple cylindrical lens acts in a similar way but only in one dimension introducing a wavefront change of the form $x^2/2f$ and a pair of such lenses set orthogonally introduces a change $x^2/2f + y^2/2f$ which is the same as that introduced by the spherical lens. Here of course we are ignoring the higher order terms which represent the different aberrations in the two cases. The diffractive equivalent of the spherical lens is the well known Fresnel zone plate. The one dimensional zone plate structure shown in figure 1 behaves as a cylindrical lens.
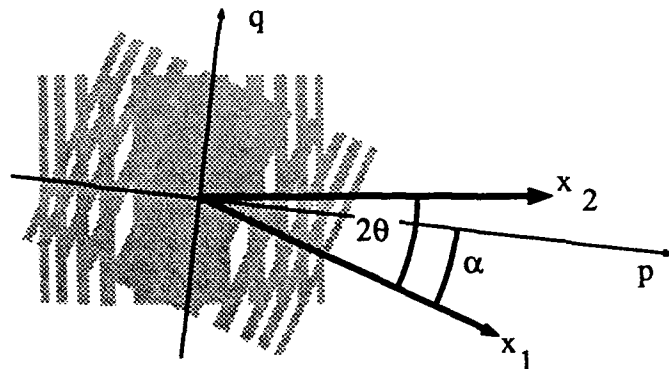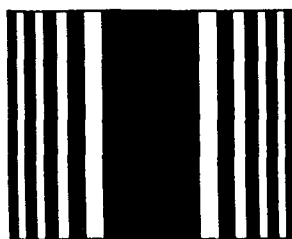
Figure 1. Cylindrical diffractive lens element.   Figure 2. Two superposed elements.

The rulings are at distances $\sqrt{2n\lambda f}$ from the centre where λ is the wavelength and n is the integer ruling number. It will be recalled that a zone plate produces, in addition to its principal focus, foci corresponding to other orders of diffraction m at distances f/m where

the integer m lies in the range $-\infty < m < \infty$. The strengths of these other orders depend on the detailed form of the diffracting structure.

Suppose we have two cylindrical diffractive elements of focal lengths f_1 and f_2 crossed at angle 2θ as in figure 2. We identify *non-orthogonal* axes x_1 and x_2 as shown, these being perpendicular to the rulings of the elements. Note these superposed elements may be two separate elements or a combination element recorded on a single substrate. The incoming wavefront is modified by this structure to produce a multitude of diffracted waves. A simple convenient model is that each diffracted order m_1 from the first element is subsequently diffracted into many orders m_2 by the second element. The complicated output wavefront can be considered to contain output wavefronts of the form

$$W_{m_1,m_2}(x_1,x_2) = \frac{m_1 x_1^2}{2f_1} + \frac{m_2 x_2^2}{2f_2}. \tag{1}$$

In general these wavefronts are astigmatic and in order to find the orientations and locations of the astigmatic line foci we introduce *orthogonal* coordinates p and q set at angles α and $\alpha + \pi/2$ shown in figure 2. The values of x_1 and x_2 corresponding to any point p,q are $x_1 = p\cos\alpha - q\sin\alpha$ and $x_2 = p\cos(2\theta - \alpha) + q\sin(2\theta - \alpha)$ and substitution of these into equation 1 gives a quadratic form containing cross terms in pq.

$$
\begin{aligned}
W_{m_1,m_2}(p,q) = & \left(+\frac{m_1}{f_1}\cos^2\alpha + \frac{m_2}{f_2}\cos^2(2\theta - \alpha)\right)\frac{p^2}{2} + \\
& \left(-\frac{m_1}{f_1}\sin 2\alpha + \frac{m_2}{f_2}\sin 2(2\theta - \alpha)\right)\frac{pq}{2} + \\
& \left(+\frac{m_1}{f_1}\sin^2\alpha + \frac{m_2}{f_2}\sin^2(2\theta - \alpha)\right)\frac{q^2}{2}
\end{aligned}
\tag{2}
$$

By choosing the angle α to make the coefficient of the cross term zero we can find the orientation of the foci of this astigmatic wavefront. The required value for α is given by the solution of

$$\tan\alpha = \frac{\dfrac{m_2}{f_2}\sin 4\theta}{\dfrac{m_1}{f_1} - \dfrac{m_2}{f_2}\cos 4\theta}. \tag{3}$$

Using this value of α we can cast equation 2 in the form

$$W(p,q) = \frac{p^2}{2f_p} + \frac{q^2}{2f_q} \tag{4}$$

and hence find the two astigmatic focal lengths f_p and f_q.
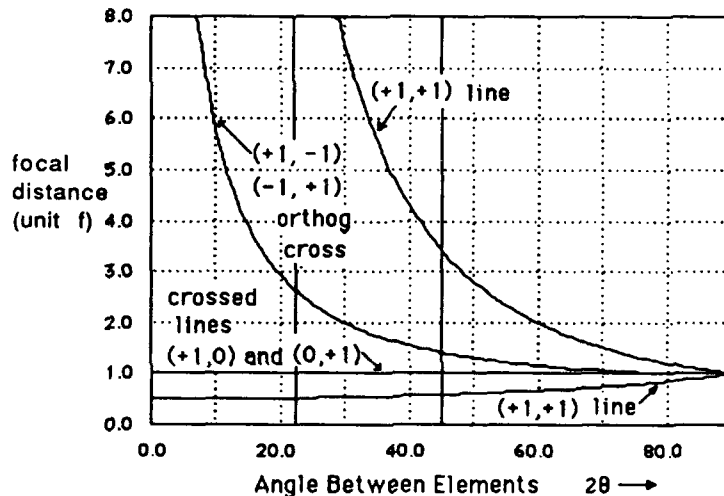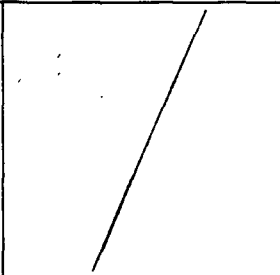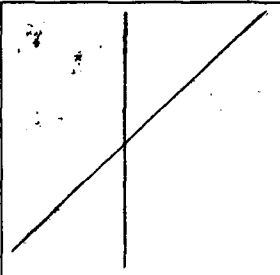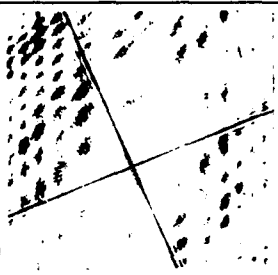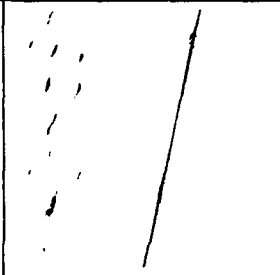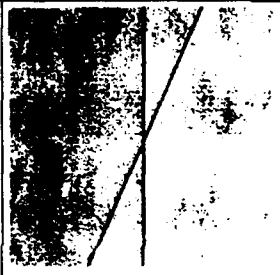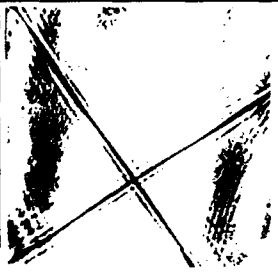
Figure 3. Foci locations for equal elements.

In the table we show some experimental and theoretical results for the combination of two identical elements of focal length $f_1 = f_2 = f = 150$mm set at $2\theta = 45°$ and $2\theta = 22.5°$ for different values of m_1 and m_2.

14 / MB1-3

2θ = 45°					
expt	89	150	216		525
theory	88	150	212		512
m_1	+1	0	+1	+1	−1	+1
m_2	+1	+1	0	−1	+1	+1
focus	$\dfrac{\pm f}{2\cos^2\theta}$	$\pm f$	$\pm f$	$\dfrac{\pm f}{\sin 2\theta}$	$\dfrac{\mp f}{\sin 2\theta}$	$\dfrac{\pm f}{2\sin^2\theta}$
2θ = 22.5°					
expt	78	150	390		
theory	78	150	392		1971

The elements were designed to produce crossed line foci at 150mm. When the effects of defocus were examined the two orthogonally orientated single line images were found at the shortest and longest focal positions. These correspond to the interaction of the two +1 diffractive orders from each cylindrical element. These lines bisect the angle 2θ between the two elements. The surprising foci were the pair of orthogonally crossed foci aligned along the *bisectors of the bisectors* of the angle between the two elements for all angles θ. One line of the pair is generated by the interaction of the +1 order of one grating with the -1 order of the other, and vice-versa. The distances from the lenses to these different extra foci are determined by the angle 2θ between the lenses. The locations of these foci as a function of the angle between the elements is shown in figure 3, the two vertical lines corresponding to the angles shown in the table. It can been seen that as $2\theta \rightarrow 90°$ all the real images of order 1 appear at the same distance f. When elements were combined to produce a square line focus by superposing four such cylindrical elements set at 90° to each other, it was found that four very strong sharp point images were generated in the corners. This corresponds to the result seen in figure 3 for $2\theta \rightarrow 90°$. Similar unexpected point images were also obtained when an octagonal line focus element was fabricated in which next but one elements, were at 90°. Their overlap regions generated sharp point images at locations outside the octagon where the sides projected would meet.

The combination of elements of different focal lengths i.e. $f_1 \neq f_2$ results in similar foci at different distances and orientations.

Pure Silica Diffraction Gratings and Mocrolens Arrays Made by the Sol-Gel Process

Jean-Luc Nogues, GELTECH, Inc., Two Inovation Drive, Alachua, FL 32615

Surface feature optics, including binary optics, sinusoidal gratings, and high-fill factor microlens arrays, are being intensively developed for use in beam splitting and optical computing. Most are fabricated in plastics, and are therefore subject to such general disadvantages as limited optical transmission and high CTE. Some can be scribed in silica but dimensions are limited and fabrication costs are extremely high. Using the sol-gel process, it is possible to fabricate surface feature optics in pure silica by a room-temperature molding technique. This technique provides the advantage of the highly favorable optical qualities of silica, such as broadband transmission, low CTE and exceptional resistance to laser damage.

The pure silica sol-gel process described in this paper includes several steps: mixing, casting, gelation, aging, drying, densification. Total control of each process step is required for success. Figure 1 gives a synoptic view of the entire gel-silica process.
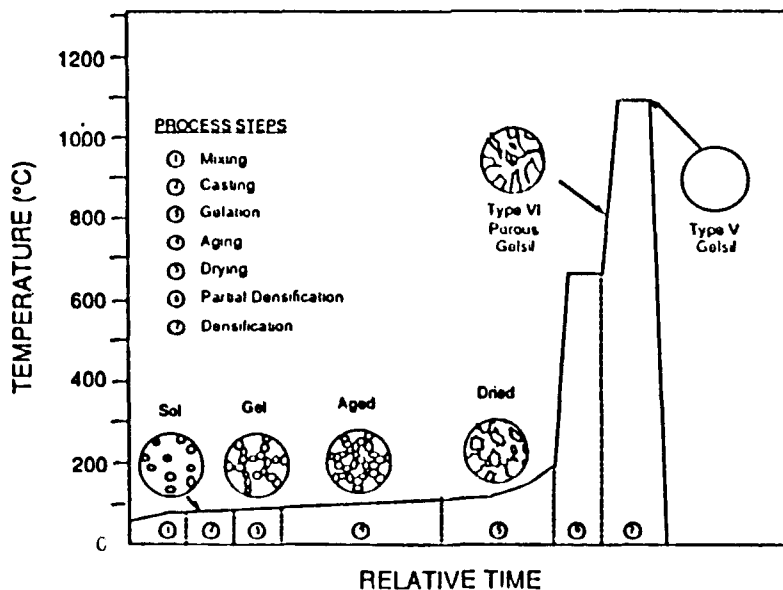
Figure 1: Gel-silica Process Sequence

Alkoxide silicon precursors are chosen over colloidal suspension raw materials because of their higher level of purity and the superior gel structure they give. Typical silica precursors are tetraethylorthosilicate (TEOS) and tetramethylorthosilicate (TMOS), which are produced in the USA in various levels of purity. The silica sol is prepared by adding the silica precursor to deionized water. Hydrolysis of the silica precursor and condensation reactions occur during this mixing step:

Hydrolysis: $\quad\quad\quad Si(OR)_4 + 4H_2O \rightarrow Si(OH)_4 + 4ROH \quad\quad (1)$

Condensation: $\quad\quad\quad Si(OH)_4 \rightarrow SiO_2 \text{ (gel)} + 2H_2O \quad\quad (2)$
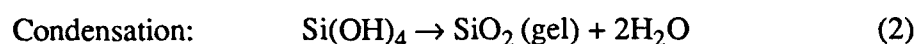
After complete homogeneity of the sol is reached, the solution is cast into molds of specific shapes. The polycondensation reaction continues and the silica particles randomly link together and form a three-dimensional network. This mechanism increases the viscosity, the sol loses its freedom of movement and becomes a rigid, wet gel having the shape and surface quality of the mold. This phenomena is called gelation.

During the aging step, the polycondensation reaction continues to build the glass network, at the same time giving enough strength to the sol to resist the stresses developed during the drying step without cracking. During this drying step, the by-products of the hydrolysis and condensation reactions are eliminated and the final product is an ultraporous monolithic body with the shape and surface details of the original mold.

The last step of this process corresponds to the densification of the dried gel via elimination of the porosity by heat treatment. During the first part of this densification treatment the organic impurities present in the pores of the gel are eliminated in order to leave a pure silica material which can be heated for full densification after an additional dehydration period.

Because it is a room-temperature molding technique the sol-gel process can be used to replicate virtually any surface optic. GELTECH has produced Fresnel lenses, gratings, and 2-dimensional arrays. A photomicrograph of a replicated Fresnel surface is shown in Figure 2. The fidelity of

the silica copy is excellent.
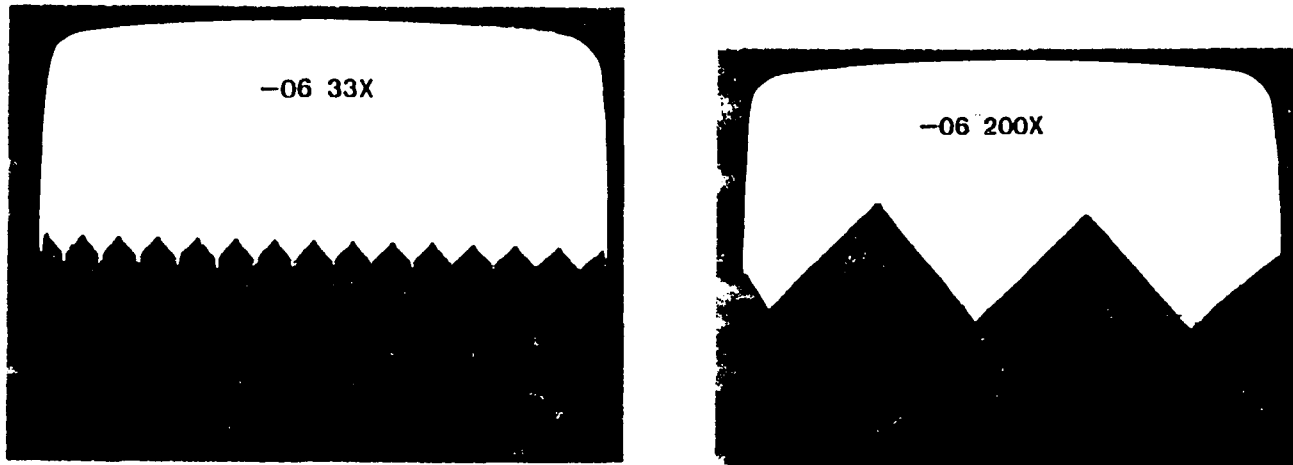
Figure 2: Replication of a Fresnel Surface by Sol-Gel Processing

Figure 3 shows the transmission characteristics of the sol-gel derived silica glass as compared to fused silica (Type III). The sol-gel glass is equal to or better than other commercial silicas in optical transmission.
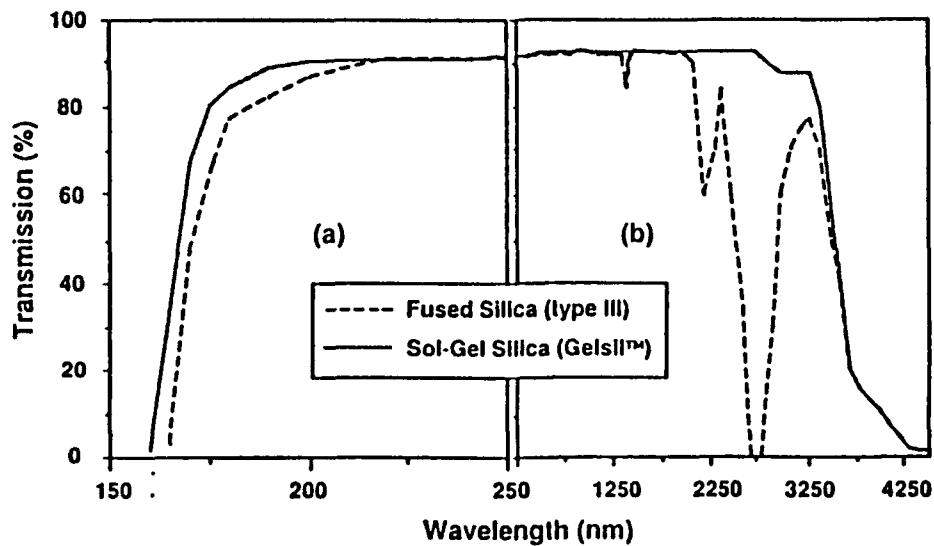
Surface feature optics are becoming increasingly significant in the optics field, and the sol-gel process enables the direct replication of micro-optics in pure silica of high optical quality.

Fabrication of continuous relief diffractive optical elements by laser writing

M.T. Gale and H. Schütz

Paul Scherrer Institute, Badenerstrasse 569, 8048 Zurich, Switzerland
Tel. +41-1-492 63 50

P. Ehbets and D. Prongué

Institute of Microtechnology, University of Neuchâtel,
Rue A.-L. Breguet 2, 2000 Neuchâtel, Switzerland
Tel. +41-38-24 60 00

1. INTRODUCTION

The fabrication of Diffractive Optical Elements (DOEs) in the form of continuous microrelief structures with programmable, complex phase profiles is still a challenging application of modern microlithographic technology. This paper describes the status and recent results of a laser writing system which has been built-up at the Paul Scherrer Institute in Zurich (PSIZ) and constantly refined over recent years.

In the PSIZ laser writing system, a photoresist-coated substrate is raster scanned under a focused laser beam by programmed movement of a precision xy table, synchronously controlling the spot intensity to write a fully programmable, 2-dimensional exposure pattern. Development of the resist then results in a microrelief of the desired structure, provided that the resist development characteristic (depth removed as a function of local exposure) has been accurately taken into account.

The ability to program complex xyz microrelief profiles enables a wide range of structures to be fabricated, ranging from 1- and 2-dimensional (continuous relief) Kinoform elements and arrays of micro-Fresnel lenslets to highly complex phase structures for new types of DOEs such as diffractive diffusers. Typical periods of 10-100 μm and maximum relief amplitudes of about 5 μm can conveniently be realized. The microreliefs can be used directly as phase structures (resist on glass) or for fabricating replication shims.

2. FABRICATION BY LASER WRITING

Laser writing system

The basic laser writing system and data processing is shown in Figure 1 and is described in more detail elsewhere [1]. In contrast to systems based upon rotation stages and suitable mainly for the fabrication of circularly symmetric elements [2], this system uses an xy scanning approach and is well suited to the fabrication of periodic DOE structures such as Kinoforms. The resist-coated substrate is mounted on a precision air-bearing xy translation table and scanned under a focused laser spot of diameter about 1.5 μm (1/e intensity points) with a raster line spacing of 1 μm and a dynamic positioning accuracy of about 150 nm rms. Exposure data are computed from the desired final microrelief and the (measured) resist development characteristic. Shipley AZ 1400 resist is used for film thicknesses up to 5 μm, developed in AZ 303 developer to obtain a relatively linear dependence of the developed microrelief as a function of the local exposure [1].
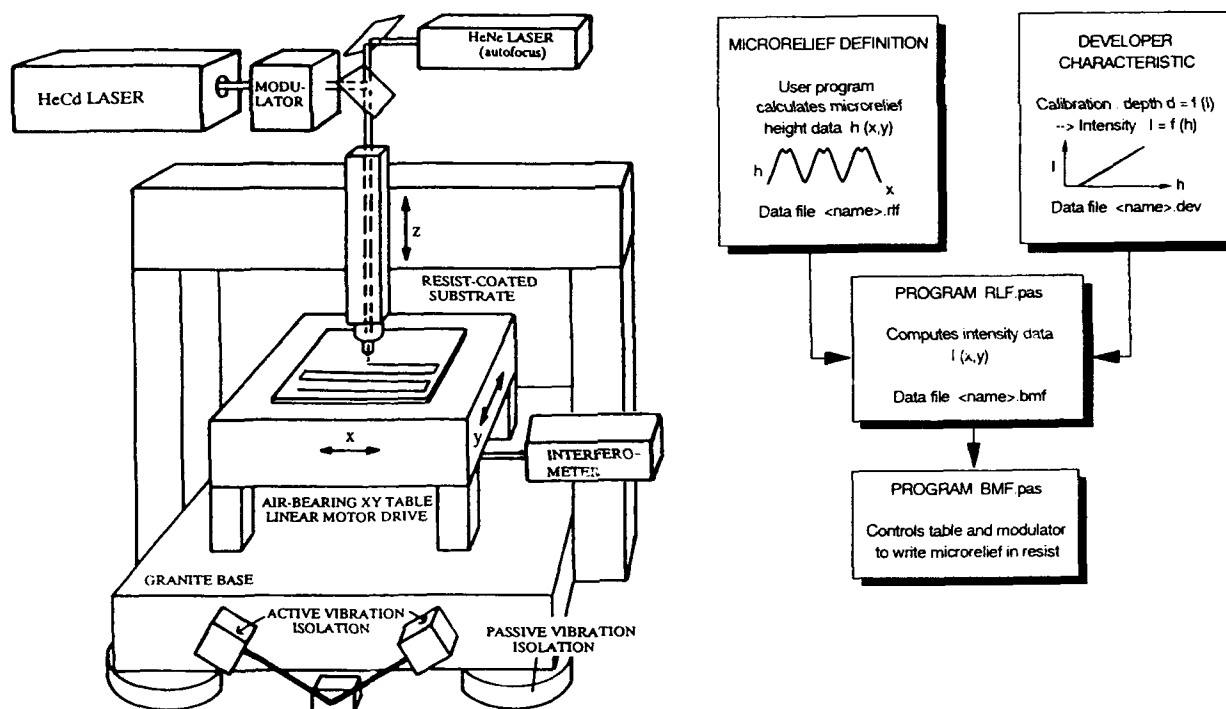
Figure 1. Laser writing system and control software schematic.

Element characterization

The performance of fabricated DOEs depends upon the design and the degree to which the design microrelief is realised in practice. Elements are assessed by measuring 3 characteristic parameters:

- Performance of the DOE for the intended application (e.g. efficiency and relative beam intensities for a fan-out DOE kinoform).
- Scattered light - this results primarily from roughness in the surface profile (typically about 20 nm rms at the present) due to positioning errors in the writing procedure.
- Diffracted light intensity from the residual grating component corresponding to the raster line spacing - this component of the unwanted scattered light is minimized by optimum choice of the raster line spacing to spot diameter ratio [3].

Replication

An important feature of DOE structures recorded as surface microreliefs is the ability to reproduce the structures by replication techniques such as embossing and casting. Writing using the laboratory system described here is relatively slow - a microstructure of 10×10 mm^2 requires about 12 hours writing time - so that faithful replication is essential if more than 1 copy of the DOE is required.

The first step is the generation of a metal copy of the required microrelief - the replication shim (Figure 2). The recording in photoresist must first be made conductive, either by evaporating a thin gold film onto the surface or by electroless Ni plating. A Ni shim is fabricated by electroplating Ni to a thickness of about 60 μm. High quality replicas can then be fabricated by techniques such as..

- Hot embossing into polycarbonate sheet
- Casting in a thin layer of epoxy (e.g. EPO-TEK 301-2 or UV-curable Norland 61) on a glass substrate.

Laser written microrelief

Pressure

Au

Ni

Epoxy

Glass

Heat

Plastic

Cast replica

Embossed replica
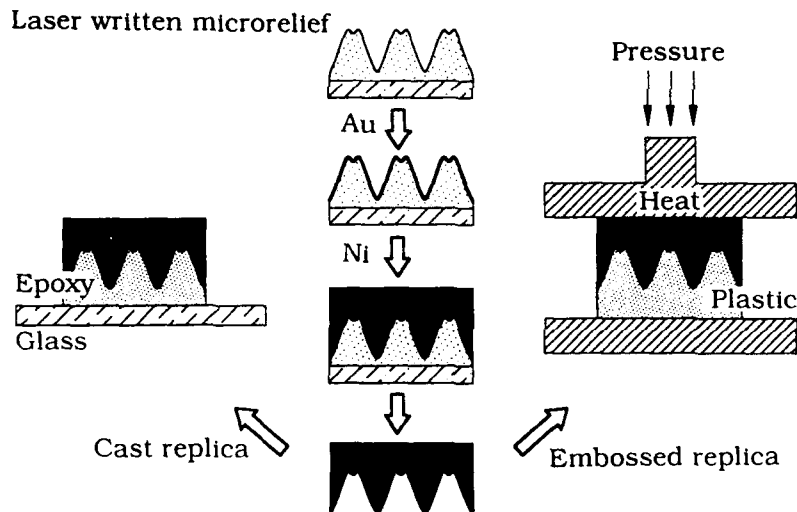
Figure 2. Typical steps involved in the replication of DOE microrelief structures.

3. RESULTS

A variety of continuous relief DOEs have been fabricated with the laser writing system described here. Examples of elements produced recently include..

- **Kinoforms** for fan-out and fan-in applications in optical computing (Figure 3). Both 1-dimensional and 2-dimensional kinoform structures have been fabricated. Efficiencies of greater than 92% with uniformity of better than ± 7% have been realized for 1:9 fan-out DOE structures [4].

- **Micro-Fresnel lenses and lens arrays** for applications in wavefront testing and novel optical systems.

- **Complex phase structures** resulting from DOE designs for a variety of applications in optical systems.
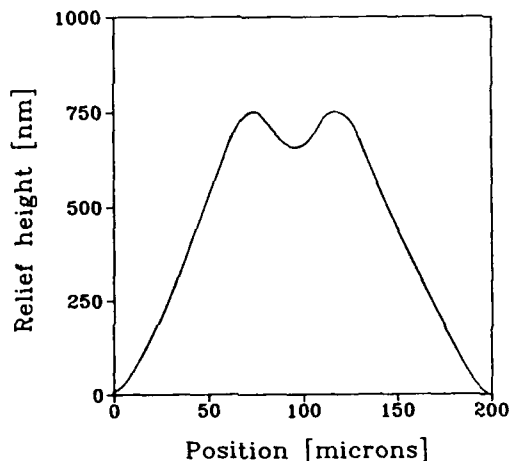
Figure 3. Example of measured profile (1 period) of kinoform fabricated for beam fan-out application.

Latest results, in particular for 2-dimensional kinoform structures, will be presented.

REFERENCES

1. M.T. Gale et al., "Fabrication of microoptical components by laser beam writing in photoresist", ECO4, Proc. SPIE **1506**, 65-70 (1991).
2. For example see : M. Haruna, M. Takahashi, K. Wakahayasi and H. Nishihara, "Laser beam lithographed micro-Fresnel lenses", Appl. Optics **29**, 5120 (1990).
3. M.T. Gale and K. Knop, "The Fabrication of Fine Lens Arrays by Laser Beam Writing", Proc. SPIE **398**, pp. 347-353, (1983).
4. H.P. Herzig, D. Prongué and R. Dändliker, "Design and fabrication of highly efficient fan-out elements", Jap. J. Appl. Phys., **27**, 1307-1309 (1990).

DRY PHOTOPOLYMER FILMS FOR COMPUTER GENERATED MIDDLE INFRARED FOCUSING ELEMENTS FABRICATION

Yuri B. Boiko, Sergio Calixto

Centro de Investigaciones en Optica, Apartado Postal 948, 37000 Leon, Mexico; phone (47) 17-58-23, fax (47) 175-000

Fabrication of the relief focusing elements are known to include the illumination of light sensitive materials through computer generated /1/ multy-grey-level amplitude mask with corresponding amplitude function of the focusing element /2,3/. In this report the use of dry photopolymer films (see /4/) is discussed. The photopolymer films based on the acrylamide (monomer), polyvinylalcohol (binder), methylene blue (sensitizer) and triethanolamine (initiator) were prepared according to the procedure previously described /4/. The exposure set up used is shown on the fig.1. The photosensitive layer provided sensitivity in the 600-700 nm
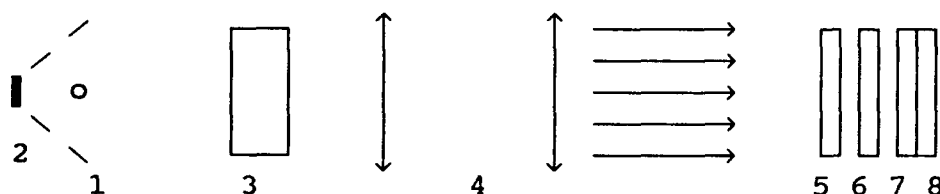
Fig.1. Exposure set up for relief elements fabrication:

1- light source: 2- mirrow; 3- heat absorbing filter; 4- objective lenses; 5,8- glass substrates; 6- -amplitude mask; 7- photosensitive layer; 8- substrate.

spectral region, so as a light source 1 the 300 Watt halogen lamp with the reflector 2 was used. The filter 3 absorbed the heat radiation to prevent the amplitude mask damaging. The parallel beam at the output was formed by lenses 4. Polymer layer 7 was placed on the glass substrate 8. The direct contact of polymer layer and amplitude mask 6 was provided by glass substrate 5. Polymer layer thickness was 100 μm.

To measure the relief recorded parameters the standart U.S. test chart with different spatial frequencies was used as an amplitude mask. Efficiency of the relief formation was found to be dependent on the initiated light intensity: encreasing of the output light density from 1 to 2 mW/sm^2 (for λ=633 nm) gave the final increase of the relief depth of about 2 times (from 3.5 μm to 7 μm). The relief formation starts immediately after exposure and lasts a few hours due to postpolymerization

The initial relief depth was measured (with the help of interferometric microscope) to be as high as 0.5 μm for the exposure time of 20 min at light density 1.2 mW/sm^2 (λ=633 nm) and 1.0 μm for the exposure time of 1 min at light density 28.0 μW/sm^2 (λ=633 nm). After 10 hours in the darkness the relief depth encreased 7 times in both cases. Relief growing up could be stoped at any desirable moment by overall exposure to the initiated light of photopolymer layer involved. The relief maxima are found to coinside with the highlight areas that correlates well with previously reported /5/ results for the liquid photopolymerizable layers. As in /5/ it allows one to suppose the mass transport mechanizm of monomer from dark to highlight areas according to the thermodynamical model of interactions inside photopolymer system under spatially periodical illumination /6/. The resolution power of the relief formation prosess considered was found to be not worse than 20 lines/mm. It is enough for fabrication of the middle infrared radiation (CO_2 laser with λ=10.6 μm including) focusing elements (see /1,2,7/).

References.

1.K.E.Bambulevich, M.A.Golub, N.L.Kazanskij, Packet of Application Programs for the Processing of Images and for Digital Holography. General Characteristics. Programs for Synthesis of Computer Optics Components (ed. by V.A.Sojfer) [in Russian], Kuibyshev Aviation Institute (1984).

2.M.A.Golub, S.V.Karpeev, I.N.Sisakyan, V.A.Sojfer, "Experimental investigation of the wavefronts formed by computer optics components",- Sov. J.Quantum Electron., v.19, No.12, pp.1664-5 (1989).

3.M.A.Golub, E.S.Zhivopitsev, S.V.Karpeev, A.M.Prokhorov, I.N.Sisakyan, V.A.Sojfer,- Sov.Phys.Doklady, v.25, p.627 (1980).

4. S.Calixto, Dry polymer for holographic recording,- Appl.Opt., v.26, No.18, pp.3904-3910 (1987).

5. Yu.B.Boiko, V.S.Solovjev, V.M.Granchak, I.N.Sisakian, I.I.Dilung, V.A.Sojfer. "Relief hologram recording on photopolymerizable layers".- Proc. SPIE, v.1238, pp.253-257 (1990).

6. Yu.B.Boiko, V.Yu.Mironchenko, V.M.Granchak, I.I.Dilung. "Volume holograms in liquid photopolymerizable layers".- Proc. SPIE, v.1238, pp.258-265 (1990).

7. V.S.Solovjev, Yu.B.Boiko. "Recording relief representation on liquid photopolymerizable compositions".- Comp'uternaya Optika (Computer Optics), No.8, pp.74-76, 1990 (in Russ. and Engl.)

Optical Interconnects
for Computing 1

MC 2:00pm–3:30pm
Cabildo Room

James R. Leger, *Presider*
University of Minnesota

System Design for Planar Optics

Jürgen Jahns

AT&T Bell Laboratories, Rm. 4G-524
Crawfords Corner Road
Holmdel, New Jersey 07733
Tel. 908-949-4093

SUMMARY

Planar optics was proposed as a way to build miniaturized free-space optical systems by using planar fabrication techniques that are used the production of integrated circuits and with minimal need for mechanical assembly and alignment [1-3]. Furthermore, the use of computer aided design tools and foundry-based manufacturing is supposed to further adapt the procedures of the electronics industry to optics [4-6].

The principle of planar optics is shown in Figure 1. In the following, we will discuss the three main features of this concept.

GaAs chip   microoptic elements   detector chip

substrate
with reflective coating
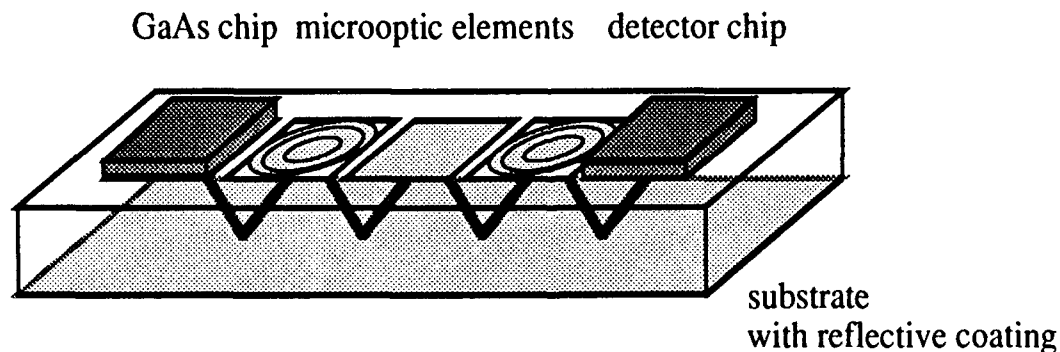
Fig. 1: Schematic of an integrated free-space optical system using a folded optical system.

1. The optical elements are fabricated simultaneously onto one or both surfaces of an optical flat by using lithographic and etching techniques. This provides precise positioning of the optical elements relative to each other as well as mechanical and thermal stability. Both, diffractive and refractive microoptic elements can be used. The fabrication of efficient elements is one of the requirements for using diffractive optics. Optical lithography can be used for the fabrication using the concept of "binary optics" [7] as well as direct electron-beam write techniques [8].

2. In a planar optics system, the light propagates inside the optical substrate (usually quartz) along a zigzag path thereby hitting one component after the other. The absence of air-glass interfaces, except for input and output windows, eliminates the need for antireflection coatings and also

provides environmental stability where dust and humidity are not a problem. However, the non-normal propagation of the light signal relative to the optical elements requires a special design of the optics. Diffractive lenses used for collimating and focusing beams that travel under large angles have been designed and demonstrated [8]. Using hybrid imaging systems which comprise lenslet arrays close to the input devices and to the detector, one is able to build integrated imaging systems with a large space-bandwidth product.

3. Opto-electronic chips, for example made of gallium arsenide, are integrated with the optical substrate by using flip-chip bonding. Flip-chip bonding is a process that is being used in electronics and that is also being investigated for optoelectronics [9-10].The solder bumps used for this process provide at the same time mechanical and electrical contact between the two substrates. A high positioning accuracy between substrate and chip might be achieved by using a reflow operation during which the solder bumps are melted. This process, however, requires a precise prealignment and a careful consideration of the difference in thermal expansion between the two substrates.

Proper design of the optical components, the optical system and the procedures used for hybrid integration will eventually allow to build integrated systems with a high complexity at a cost much lower than current free-space optical systems.

References

1. J. Jahns and A. Huang, "Planar integration of free-space optical components," Appl. Opt. 28 (1989) 1602-1605.
2. J. Jahns, "Integrated optical imaging system," Appl. Opt. 29 (1990) 1998.
3. S. J. Walker and J. Jahns, "Integrated-optical clock distribution using a binary beam splitter tree," OSA Ann. Meeting (1990) TuX6.
4. K. S. Urquhart, S. H. Lee, C. C. Guest, M. R. Feldman and H. Farhoosh, "Computer aided design of computer generated holograms for electron beam fabrication," Appl. Opt. 28 (1989) 3387-3396.
5. M. M. Downs and J. Jahns, "A computer-aided design tool for planar free space optics," OSA Ann. Meeting (1990) Tu-W5.
6. J. Jahns, "A platform for integrated microoptics," 3rd Microoptics Conf., Yokohama, Japan (1991) 110.
7. G. J. Swanson, "Binary optics technology: the theory and design of multi-level diffractive optical elements," MIT Lincoln Laboratory, NTIS Publ. No. AD-A213-404 (1989).
8. T. Shiono and H. Ogawa, "Diffraction-limited blazed reflection diffractive microlens for oblique incidence fabricated by electron-beam lithography," Appl. Opt. 30 (1991) 3643-3649.
9. A. von Lehmen, "Electronically and optically controllable vertical cavity surface emitting laser arrays for optical interconnects and signal processing applications," OE/Fibers '91, Boston, MA (1991).
10. J. Jahns, R. A. Morgan, H. Nguyen, S. J. Walker and Y. M. Wong, "Hybrid packaging of surface-emitting microlaser arrays on planar optical systems," OE/Fibers '91, Boston, MA (1991).

Diffractive optics in a free-space digital optic system

R.L. Morrison, S.L. Walker, T.J. Cloonan, F.A.P. Tooley, F.B. McCormick, J.M. Sasian,
A.L. Lentine, J.L. Brubaker, R.J. Crisci, S.J. Hinterlong, and H.S. Hinton

AT&T Bell Laboratories
200 Park Plaza
Naperville, IL 60566

Introduction

The high throughput of optical interconnections was first utilized in the long distance telecommunication network. With advances in technology, optical communication continues to penetrate to ever shorter interconnection distances. Free-space optical interconnections at the chip and gate level can enhance the performance of electrical connections since light can exploit the dimension perpendicular to the planar electronic surface and can overcome the impedance losses typically experienced by high speed electronic signals.

A series of free-space digital optic protoype switching systems have been built to demonstrate the feasibility of optical connections between simple processing elements[1]. A prototype composed of a six stage free-space digital optic system has been developed that fully interconnects 16 input channels (each 32 bits wide) with 32 output channels. The optical devices are arrays of application specific symmetric self electro-optic devices (AS-SEED)[2] that function as simple two input switching cells. The interconnection network that routes information via modulated light beams is based on a Banyan configuration.

One of the critical technologies that has enabled the advance of digital optics systems is the development of diffractive optical elements. Binary phase gratings (BPG) provide the functionality of Fourier holograms that can not be achieved using conventional optics. Two areas that are well served by diffractive optics are the generation of spot arrays to illuminate the array of opto-electronic devices and the linking stage in the interconnection network. Figure 1 shows a schematic of one module of the six-stage prototype. The BPG nearest the laser power supply, also referred to as a Dammann grating[3], diffracts the beam into 2048 beams that are imaged via the objective lens. The modulated beams then pass through an interconnection BPG as it passes to the next module. This unique use of the BPG at the interconnection stage provides an exceptionally compact and straight-forward means of implementing the optical link.

Spot Array Generation

In the described system, light is provided by an external source to illuminate the AS-SEED modulators. Such external illumination is more suitable than integrated light sources due to the limitations of the current processing technology and problems of heat dissipation. A BPG was inserted into the collimated beam from a laser diode to diffract the light into a rectangular array of uniform intensity beams. The BPG consist of a periodically replicated pattern etched into a fused silica substrate. These beams were then imaged onto the S-SEED array using an objective lens with a focal length of 15.6 mm. An even numbered design was chosen to both match the array configuration and improve intensity uniformity[4]. The first module of the prototype system requires a 64x16 spot array with spots on 20 and 80μm centers. A pitch of 1327μm and 331.7μm

respectively was used to replicate the basic patterns. The remaining stages use a 64x32 array (as shown in figure 2) with 1327μm and 663.5μm pitches to produce spots on 20 and 40μm centers.

The BPG's were designed using an optimization program based on simulated annealing and gradient descent. Each two dimensional pattern was produced by combining the design from separable one dimensional even number designs. The theoretical efficiencies of the 1x16, 1x32, and 1x64 patterns are 80%, 83% and 80% respectively. The intensity uniformity of each spot array was measured using a high spatial resolution CCD camera with fine intensity sensitivity. Measurements showed that all spot intensities were confined to a distribution within +/-10% of the mean intensity value.

Interconnection

In order to serve as a Banyan type interconnection (an example is shown in figure 3a) the basic 1x3 BPG design and the S-SEED photosensitive windows must be modified. Normally, extraneous beams from the space-invariant 1x3 design spoil the symmetry of the Banyan interconnection. In the figure, dark lines represent the standard Banyan connections, while lighter lines delineate the unnecessary beams. The solution is to spatially separate the three spots formed in each detector and mask the photosensitive areas where the extra beam is incident via metallization. Although this implementation wastes part of the available power, the simplicity of alignment and the compactness with which it provides its functionality is highly desirable.

An additional modification is also necessary. A typical 1x3 BPG contains only 86% of its total intensity in the central three spots. The remaining energy is distributed into the other odd numbered orders. Light directed into these "noise order" beams would cause interference wherever they aligned with photosensitive windows. The most severe case occurs in the first link stage where the first order beam links the nearest neighbor switch cell. This is illustrated for the first few orders in figure 4. Given a 21μm photosensitive window spaced on 40μm centers with a spot spacing of 33μm, orders 5, 7, 13, 17, 19, 21, 23, 27, 29, 33, and 35 must be designed to have negligible intensity. During the optimization process these orders are designed to have an intensity less than 0.2% of that of any of the central three spots. The fabricated gratings had features as small as 1μm. The overall performance of these gratings meets system tolerances for proper operation.

References

[1]   F.B. McCormick et. al., "Optomechanics of a free-space photonic switching fabric: the system," Proc. of the SPIE symposium on optical applied science and engineering, vol. 1533 (1991).

[2]   A.L. Lentine et. al., "Symmetric self electro-optic effect device: optical set-reset latch, differential logic gate and differential modulator/detector," J. of Quant. Elect. QE-25, p. 1928. (1989).

[3]   H. Dammann and K. Gortler, "High efficiency in-line multiple imaging by means of multiple phase holograms," Opt. Comm. v3, 312-315 (1971).

[4]   R.L. Morrison and S.L. Walker, "Progress in diffractive phase gratings used for spot array generators," in Optical Computing 1991 Technical Digest Vol. 6, 144-147 (1991).
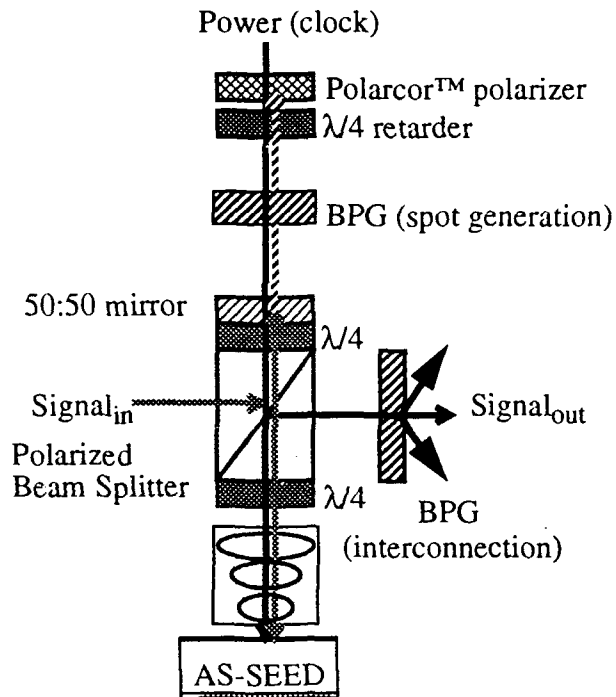
Figure 1 - Basic elements of one module of the six stage demonstration system.
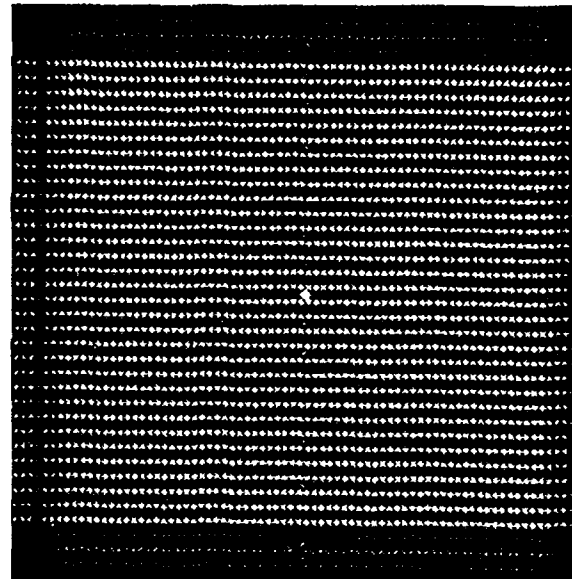
Figure 2 - 64x32 spot array generated by BPG.
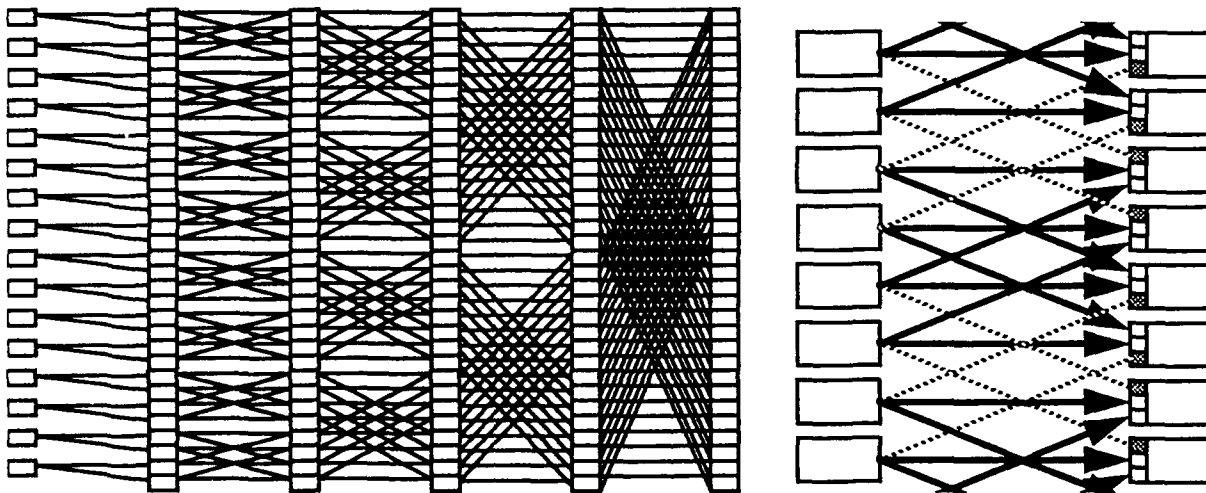
Figure 3 a) Banyan network used in multi-stage demonstration system. b) Magnification of second link stage showing beams (dashed lines) that must be eliminated to form the interconnection from a 1x3 split at each output.

0 1 2 3 4 5 6 7 8 9 10 11 12 13 14 15 16 17 18
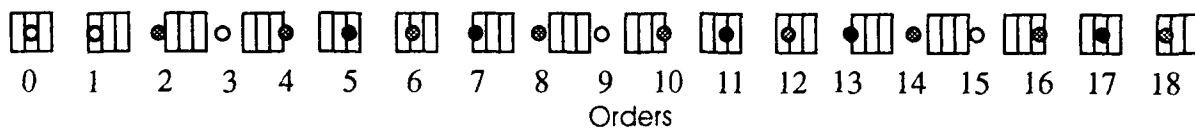
Orders

Figure 4 - Several positive order spots shown aligned with S-SEED detector windows for first link stage. Even numbered orders (shaded gray) are naturally suppressed by the even numbered design. Black circles represent orders that must be suppressed by the optimization program. Spots between the windows can be neglected.

Fabrication and Integration of DOEs into High Density Vertical Interconnects

Franz Haas, David A Honey, Harold Bare
USAF Photonics Center, Rome Laboratory, Griffiss AFB, NY 13441
(315) 330-7670

David Mikolas, Harold Craighead, Richard Bojko, Graham Pugh
National Nanofabrication Facility and School of Applied and Engineering Physics,
Cornell University, Ithaca NY 14853
(607) 255-2329

SUMMARY

Diffractive optical element (DOE) designs and fabrication techniques were investigated for a vertical optical interconnect architecture illustrated in Fig 1. This design provides high interconnect densities for stacked Multi Chip Module (MCM) computer architectures required in future high speed, low power, and small size computer systems. A 16 channel interconnect was demonstrated and an evaluation of greater interconnect densities is presented. Key design parameters for this effort were: ease of fabrication, compatibility of fabrication techniques with industry standards, density of interconnects, misalignment tolerance, data rates, and power consumption.

Each reflective off-axis DOE focuses light from an array of light sources to an array of photodetectors on a different MCM. Four level gratings were etched in Si using both photo and electron beam lithography. Diffractive elements were defined on silicon substrates using standard microlithographic techniques (at the National Nanofabrication Facility) and implemented with Reactive Ion Etching. One grating could potentially service tens to hundreds of interconnect paths between processing layers. The number of source/detector pairs is limited by the angular aperture of the grating. Grating quality depends on the number of etched steps and the alignment accuracy of multiple mask/etch steps. The angular aperture is limited by the smallest achievable feature size.

Arrays of GaAsP LEDs and Metal Semiconductor Metal (MSM) photodetectors were fabricated as source/detector pairs for the first generation of this architecture. The combination of LEDs and MSM detector arrays offer a low power, high density interconnect which can be readily fabricated. A data rate of 100-300 Mhz is possible with LED's which is sufficient considering the parallel nature of the interconnect architecture. Electronic signals from each output of a processor die situated near the optical interconnect module map to individual source/detector pairs. There is no parallel to serial conversion

typical of high speed, single channel optical interconnects. We present the results of a 16 channel interconnect and extrapolate these results to determine the maximum interconnect density possible for this architecture given the capabilities of current fabrication technologies.

The viability of this, and other, free space optical interconnects depends on its tolerance to misalignments due to system integration technology, thermal expansion, and in-use vibrations. For a fixed plane-to-plane geometry, this requirement defines the detector size and lateral source to source spacing. The optical interconnect that was constructed has a 1 mil misalignment tolerance in the X, Y, and Z axes. A high misalignment tolerance requirement will be a limiting factor in the density of interconnects.

The quality of a DOE is a function of the minimum structure size and alignment accuracy of multiple etch steps. Photo and electron-beam lithography were compared for grating fabrication. Photolithography is a common industry standard which offers a fast and relatively inexpensive method of producing large numbers of gratings. Photolithography is limited, however, in minimum feature size, which in turn limits the angular acceptance of the grating. Electron beam lithography offers smaller structure sizes and better alignment to previous etched structures, but is limited by cost and access to machinery. Electron beam lithography writes the pattern directly onto the resist covered substrate allowing for precision alignments of 0.05 micron and 0.1 micron structure sizes.
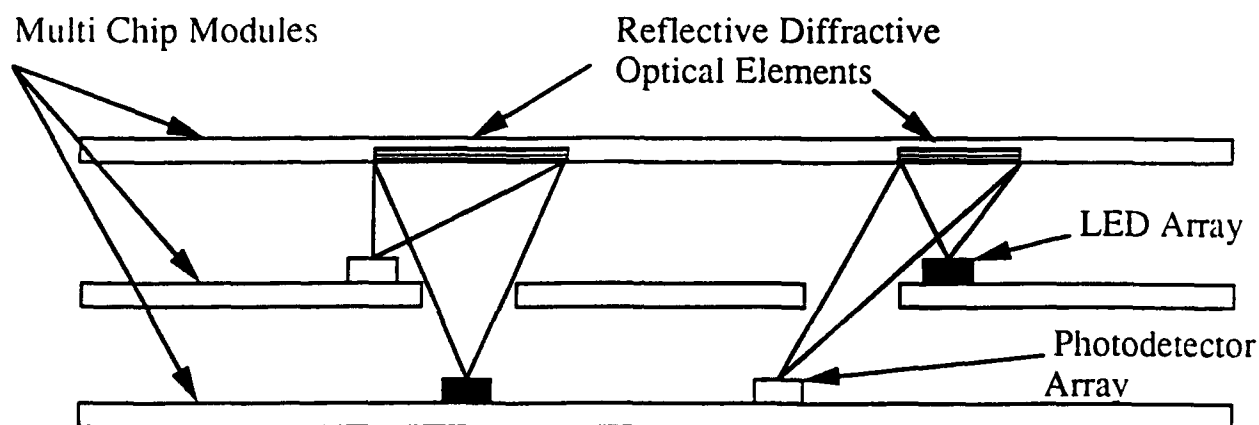
Fig. 1 Optical Interconnect for a Stacked Multi Chip Module (MCM) Computer Architecture

Diffractive-refractive microlens arrays for beam permutation

Frank Sauer and Jürgen Jahns
AT&T Bell Labs, 101 Crawfords Corner Road, Holmdel, NJ 07733
Tel 908-949-2259/4093

A. Y. Feldblum, C. Nijander, and W. Townsend
Engineering Research Center (AT&T Bell Labs), Carter Road, Princeton, NJ 08540

Summary

The combination of refractive with diffractive elements has already been demonstrated in 1966 [1] and has further been discussed by various authors (see for example [2]). In most cases, diffractive optics has been used to reduce chromatic aberrations of lens systems by making use of the opposite dispersion of diffractive and refractive optical elements. Recent developments in the fabrication of microoptical elements allow one to implement both refractive as well as diffractive microlenses by using lithographic techniques. For optical interconnection applications, the flexibility of lithographically fabricated diffractive optics is of interest for the implementation of beam permutation operations (see for example [3]).

Here, we consider the use of monolithically integrated diffractive-refractive microlens arrays for the implementation of fixed, but space-variant interconnections of two-dimensional arrays of optical data channels (Fig. 1).

input component   output component
collimates and deflects deflects and focuses
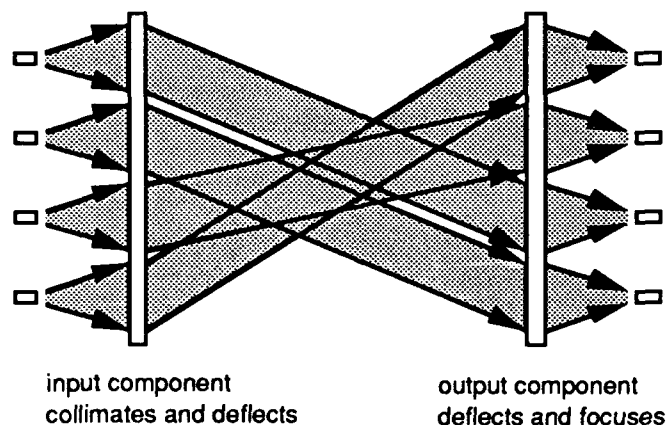
Figure 1. Free-space permutation interconnect providing a fixed but arbitrary interconnection between two fiber arrays or between an array of microlasers and an array of detectors.

We do not add gratings to a given lens in order to improve its basic function but rather have lenses and gratings perform different specific tasks they are especially well suited for. These are the tasks of collimation and focussing for the refractive lenses and the task of deflecting for the diffractive gratings (Fig.2).
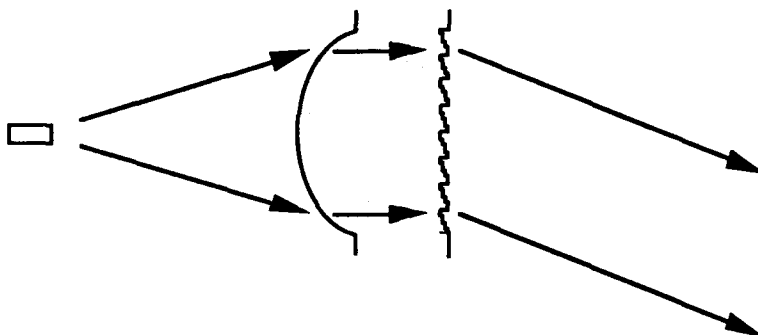
Figure 2. Monolithic refractive-diffractive doublet.

We fabricate both the lenses and the gratings using lithographic techniques. The refractive lenses are produced by photoresist patterning, photoresist melting and subsequent reactive ion etching [4,5]. The gratings, too, are produced by photoresist patterning and reactive ion etching. Lenses and gratings are placed onto adjacent sides of the same substrate to achieve a monolithic integration.

What are the advantages of introducing the refractive-diffractive doublets?

First, one has to note that, in principle, it is possible to perform the tasks of the input and output components (see Fig. 1) by single elements. Pure lenses, used in an off-center/off-axis configuration will both collimate and deflect (respectively deflect and focus) the light beams at the same time. The numerical aperture of the lenses would here be used partially for the collimation of the beams and partially for their deflection. Such a solution is not practical because one is not able to produce refractive or diffractive microlenses which have high enough numerical apertures. (One might consider off-axis holographic lenses. But also here, there are technical difficulties to produce single-plane arrays which simultaneously both collimate and deflect in a space-variant pattern. So far, holographic permutation interconnects have only been demonstrated for parallel beam to parallel beam interconnection, e.g. [6])

Second, if one accepts that one has to split tasks and use different elements to perform them, one can now independently choose the elements which are best suited for each specific task. (1) Collimation and focussing: refractive lenses have less chromatic aberrations then diffractive lenses, and with them it is easier to achieve the high numerical apertures needed for the collimation of strongly divergent light sources. (2) Deflection: Diffractive gratings are the only feasible approach because there is no fabrication method for space-variant arrays of refractive microprisms.

We fabricated the optical system for an 8x8 interconnect and demonstrated the single channels using a He-Ne laser and HeNe single mode fiber. The channel (lens) diameters were 200μ, and the lens spacing was 250μ. The distance between the input and the output component was 20mm.

To include a higher number of channels one has to increase the channel diameter for less diffraction spreading, or one has to increase the resolution of the lithographic process (now 1.25μ) for larger deflection angles.

References

[1] J. Upatnieks, A. Vander Lugt, and E. Leith, "Correction of lens aberrations by means of holograms", Appl. Opt. **5** (1966) 589.

[2] Th. Stone and N. George, "Hybrid diffractive-reflective lenses and achromats", Appl. Opt. **27** (1988) 2961.

[3] J. Jahns and W. Däschner, "Optical cyclic shifter using diffractive lenslet arrays", Opt. Comm. **79** (1990) 407.

[4] L.G. Cohen and M.V. Schneider, Appl. Opt. **13** (1974) 90.

[5] O. Wada, S. Yamakoshi, M. Abe, Y. Nishitani, and T. Sakurai, IEEE J. Quantum Electronics, **QE-17** (1981) 174.

[6] H. Kobolla, F. Sauer, and R. Völkel, "Holographic tandem arrays", Proc. SPIE **1136** (1989).

Modeling of
Diffractive Devices

MD   4:00pm–5:30pm
Cabildo Room

Neal C. Gallagher, *Presider*
Purdue University

Review and Applications of Rigorous Coupled-Wave Analysis of Grating Diffraction

Elias N. Glytsis and Thomas K. Gaylord
School of Electrical Engineering and Microelectronics Research Center
Georgia Institute of Technology, Atlanta, Georgia 30332

The diffraction of electromagnetic waves by periodic structures continues to be of great interest and practical importance owing to numerous applications in a variety of fields such as acousto-optics, electro-optics, integrated optics, spectroscopy, optical computing, optical interconnects, and quantum electronics. Optical gratings may be planar (slab, volume gratings) or surface-relief (corrugated gratings). The periodic modulation may be in the permittivity (resulting in index of refraction gratings), or in conductivity (absorption) or in a combination of these. Diffraction gratings can be fabricated in dielectrics, semiconductors, metals, or even plasmas. They can be characterized as isotropic, uniaxial-, biaxial-anisotropic or gyrotropic depending on the properties of their materials. They can be of constant or of varying modulation and can be cascaded or multiplexed. The grating diffraction methods of analysis can be divided into two major categories, the integral methods,[1] and the differential methods.[1-7] The most common and accurate differential methods are the coupled-wave approaches[2-5] and the modal approaches.[6,7]

In this paper a brief review of the rigorous coupled-wave analysis is presented along with two specific applications: (a) antireflection surface-relief gratings for the generation of soft-x-ray pulses, and (b) holographic laser scanners. The general geometry of a grating structure along with an incident plane wave is shown in Fig. 1. This figure corresponds to a surface-relief type grating but it applies to volume gratings too. The grating and the surrounding regions can be general anisotropic. The configuration in Fig. 1 corresponds to any general three-dimensional incidence and any allowable linear polarization. The electric and magnetic fields in the grating region(s) are expanded in terms of spatial harmonics $\vec{E} = \sum_i \vec{S}_i(z) \exp(-j\vec{\sigma}_i \cdot \vec{r})$ and $\vec{H} = (\epsilon_0/\mu_0)^{1/2} \sum_i \vec{U}_i(z) \exp(-j\vec{\sigma}_i \cdot \vec{r})$, where $\vec{\sigma}_i = \vec{k}_{inc} - i\vec{K}$ ($i = 0, \pm 1, \pm 2, \cdots$), $\vec{S}_i$, $\vec{U}_i$ are the space harmonic amplitudes, $\vec{k}_{inc}$ is the incident wavevector (in the grating region), $\vec{K}$ is the grating vector, and ϵ_0, μ_0 are the permittivity and permeability of freespace, and ω is the angular frequency of the incident wave. The field expansions must satisfy Maxwell's curl equations in the grating region(s):

$$\vec{\nabla} \times \vec{E} = -j\omega\vec{B} = j\omega\mu_0\tilde{\mu}(x,z)\vec{H},$$
$$\vec{\nabla} \times \vec{H} = \vec{J} + j\omega\vec{D} = [j\omega\epsilon_0\tilde{\epsilon}(x,z) + \tilde{\sigma}(x,z)]\vec{E}, \tag{1}$$

where $\tilde{\epsilon}$, $\tilde{\mu}$, and $\tilde{\sigma}$ are the relative permittivity, relative permeability, and conductivity tensors of the grating regions and are periodic in the direction of the grating vector. More general equations can be written if constitutive relations of the form $\vec{D} = \tilde{\epsilon}\vec{E} + \tilde{g}\vec{H}$ and $\vec{B} = \tilde{h}\vec{E} + \tilde{\mu}\vec{H}$ (for bianisotropic media) are used where $\tilde{g}$ and $\tilde{h}$ are the coupling tensors between $\vec{D}$ and $\vec{H}$, and $\vec{B}$ and $\vec{E}$. However, the most common and practical case in optics is when only the permittivity tensor is modulated. Using the spatial expansions of the fields into Eq. (1) an infinite set of linear coupled-wave differential equations is derived. If the infinite number of possible diffracted orders is truncated to a finite number m then the total number of coupled-wave equations becomes $6m$. Eliminating the components along the propagation direction (z in Fig. 1), the tangential components of the electric and magnetic fields can be expressed in the following compact matrix form[3-5]

$$d\vec{V}/dz = j\tilde{A}\vec{V}, \tag{2}$$

where $\vec{V}$ is a $4m \times 1$ vector containing the tangential space harmonic components of the electric and magnetic fields and $\tilde{A}$ is a $4m \times 4m$ coupling matrix.[3-5] All special cases can be derived from the above general expression. For example if angle $\alpha = 0°$ (Fig. 1) and $\psi = 90°$, only the y-components of the electric field and the x-components of the magnetic field exist (TE polarization) and Eq. (2) reduces to a system of $2m$ equations. Similarly, Eq. (2) reduces to $2m$ equations in the case of $\alpha = 0°$ and $\psi = 0°$ (TM polarization). The above conclusions in these limiting cases are valid if isotropic or special orientation (with respect to the principal axes) anisotropic grating region(s) are considered. In general, for three-dimensional incidence (conical diffraction) the two orthogonal polarizations are coupled even in the isotropic case. Independently

of the grating characteristics Eq. (2) can be solved in the form $\tilde{V} = \tilde{W}\exp(\tilde{\Lambda}z)\tilde{C}$, where $\tilde{W}$ and $\tilde{\Lambda}$ contain the eigenvectors and eigenvalues of the coupling matrix $\tilde{A}$ and $\tilde{C}$ contains $4m$ unknown constants.[2-4] Combining the previous field solutions with the known plane wave solutions in the regions external to the grating, a set of boundary conditions is formed. Solution of this set of conditions (a linear system of the form $Ax = b$) specifies all the unknown field coefficients.[3-5] Knowledge of the electric and magnetic fields in any region of the problem determines all quantities of interest, such as the diffraction efficiencies. The same approach is valid for any type of volume or surface-relief grating of constant or varying modulation since they can represented as cascaded gratings.[5] The same formulation can be applied to multiplexed gratings.[5]

Antireflection Gratings for Enhanced Absorption and X-Ray Emission in Femtosecond Laser Produced Plasmas[8]: Laser produced plasmas created by intense femtosecond laser pulses have been demonstrated to produce subpicosecond soft-x-rays. The use of terawatt femtosecond lasers permits the generation of more intense x-ray sources. However, increase target reflectivity at high fluence results in less efficient coupling. Grating targets can dramatically increase this coupling.[8] The rigorous coupled-wave analysis was applied to analyze photolithographically produced SiO, Si, and SiN diffraction surface-relief gratings with varying groove depths and filling factors and with periods of 240 or 300 nm. Good agreement between the experimental data and the calculated rigorous coupled-wave results was obtained (Figs. 2a and 2b). The plasma gratings are inhomogeneous due to the varying plasma temperature. However, the rigorous coupled-wave analysis can be applied since the plasma grating can be decomposed into a series of cascade homogeneous gratings. Especially designed antireflection gratings could potentially increase absorption resulting in an enhanced energy deposition, a hotter plasma, and consequently more intense x-ray emission.

Holographic Scanner Diffraction Analysis[9]: Holographic scanners are used in laser output writers to provide rapid accurate scanning of the focused laser beam. Useful resolutions of 1800-2400 dots per inch are achievable. However, it is found that the intensity along the scan line may vary and this produces undesirable "banding" effects. This variation is due to a corresponding variation in the diffraction efficiency as the beam scans across a grating facet. The rigorous coupled-wave analysis can be applied to this problem in order to optimize the diffraction efficiency as a function of the scan angle. This problem is complicated by the fact that is a vector (conical) diffraction problem. The input polarization changes along the scan line. Furthermore, during the scan the grating vector does not lie in the plane of incidence. This produces coupling between TE and TM polarizations inside the grating resulting in an elliptical rather than linear polarization in the output of the grating. This problem corresponds to a varying angle β (scan angle) in Fig. 1. An example calculation of the diffraction efficiency of the first forward-diffracted order as a function of the scan angle is given in Fig. 3.

[1] R. Petit, Ed., *Electromagnetic Theory of Gratings*, Springer-Verlag, 62 (1980).
[2] H. Kogelnik, *Bell Syst. Tech. J.* **48**, 2909 (1969).
[3] M. G. Moharam and T. K. Gaylord, *J. Opt. Soc. Am.* **71**, 811 (1981).
[4] T. K. Gaylord and M. G. Moharam, *Proc. IEEE* **73**, 894 (1985).
[5] E. N. Glytsis and T. K. Gaylord, *J. Opt. Soc. Am. A* **7**, 1399 (1990).
[6] T. Tamir, H. C. Wang, and A. A. Oliner, *IEEE Trans. Microwave Theory Tech.* **MTT-12**, 323 (1964).
[7] R. S. Chu and J. A. Kong, *IEEE Trans. Microwave Theory Tech.* **MTT-25**, 18 (1977).
[8] M. Murnane, H. Kapteyn, J. Bokor, W. Mansfield, R. Gnall, E. N. Glytsis, T. K. Gaylord, and R. Falcone, *OSA Topical Meeting on Short Wavelength Coherent Radiation*, Monterey, CA, April 1991.
[9] C. J. Kramer, *Proc. SPIE* on Metrology of Optoelectronic Systems **776**, 81 (1987).
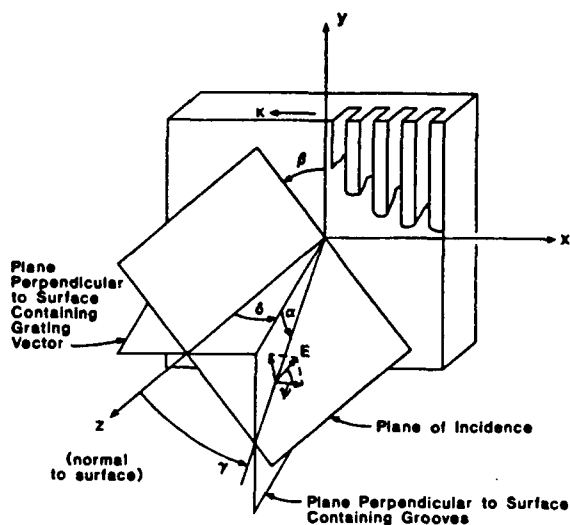
Figure 1: The three-dimensional geometry of the grating structure and the incident plane wave. The angle of incidence is γ (in the plane of incidence). The angle ψ specifies the angular orientation of the incident polarization. An angle $\alpha = 0°$ and $\psi = 90°$ correspond to TE polarization while an angle $\alpha = 0°$ and $\psi = 0°$ corresponds to TM polarization.
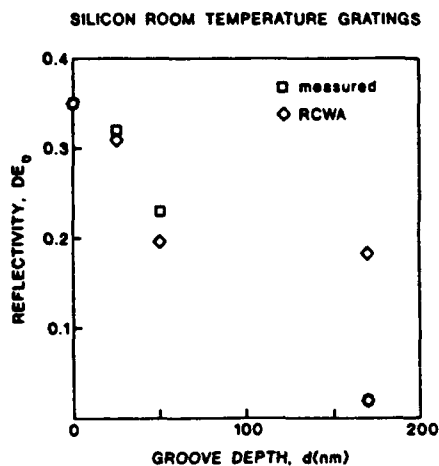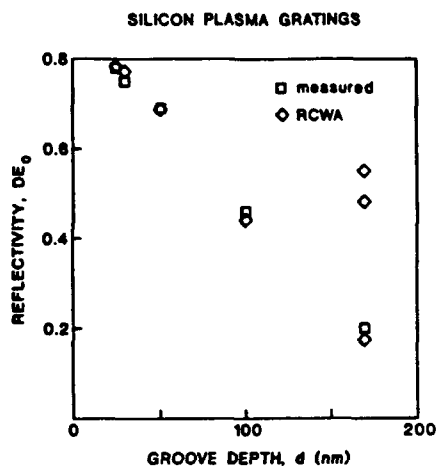
Figure 2: Comparison of experimental and theoretical data (computed using the rigorous coupled-wave analysis, RCWA) for different Si gratings using single or double cascaded gratings approximations. (a) Silicon room temperature gratings, and (b) silicon plasma gratings.
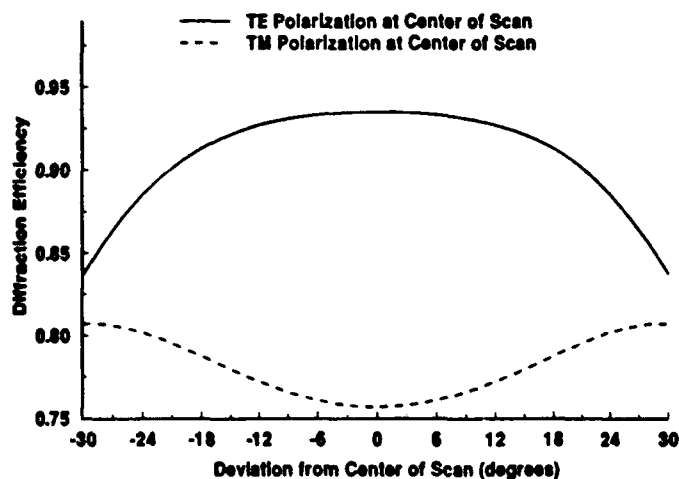
Figure 3: Diffraction efficiency of the first forward-diffracted order of a holographic grating in air as a function of the scan angle for both TE and TM polarizations (at the center of the scan). The grating parameters are: grating period 0.8717 μm, angle $\gamma = 35°$, angle $\alpha = 0°$ at the center of the scan, filling factor is 0.50, grating refractive index is 1.5 and freespace wavelength is 1.0 μm. The number of diffracted orders used in the RCWA was 11.

Artificial distributed index structures realized by zero order gratings

H. Haidner, P. Kipfer, J.T. Sheridan, W. Stork, N. Streibl
Physikalisches Institut, Staudtstraße 7
D-8520 Erlangen, Germany

The effective refractive index of a high frequency grating can be altered by changing its duty cycle. First experiments for infrared optical distributed index components are presented.

1. Introduction

The zero diffraction order for normal incidence is transmitted by a grating without change in the direction of propagation. Thus it is analogous to a slab of homogeneous material. Higher diffraction order, in general, emerge from a grating at an angle. However if the grating period is very small, they become evanescent. Hence, we consider it as an "artificial" material that has unconventional optical properties (refractive index, dispersion, polarization). In this paper a microstructure is considered, that is composed of two materials with refractive index n_1 and n_2. The (zero-order) transmitted light will experience within this "artificial material" a certain phase shift and attenuation, that will be described by an overall "effective" refractive index n_{EFF}. In case of a one-dimensional grating the artificial material will be anisotropic and therefore birefringent. For two-dimensional gratings the effective index can be made independent of polarization. Our main idea is, that the effective refractive index depends on the duty cycle of the structure, i. e. the ratio of composition between the two materials. By varying the duty cycle the effective refractive index can be varied. We propose to realize distributed index components based on this principle. An analogous physical principle was proposed with III-V semiconductor heterostructures for realizing a graded bandgap structure by means of a sequence of narrow quantum wells /1/.

If the zero order grating is fabricated as a surface relief structure, lithographic techniques such as electron beam writing and dry etching can be used for manufacturing a master. Embossing and galvanotechniques can then be used for industrial replication. For gratings with (approximately) rectangular surface profile, only one lithographic mask fabrication step is necessary for fabrication. For visible wavelengths zero order gratings can be manufactured by using holographic techniques. These require submicron structures. In the infrared fabrication using lithographic techniques is also possible. Zero order gratings for CO_2-lasers at 10.6 μm wavelength /2/ are very attractive because of the many industrial applications and as conventional optics relies on expensive materials. They can be made of cheap low loss materials, so that they can withstand the high powers used in material processing, and the replication technology is available for mass production. In this paper, we sketch how to calculate the effective refractive index of a microstructure and we propose applications for distributed index structures based on zero order gratings with variable duty cycle /3/. The physical principle of artificial distributed index media realized as compositional microstructure is demonstrated with water waves. First experiments and results with infrared lasers are presented.

2. The effective refactive index

Fig. 1 shows schematically the profile of a rectangular surface relief grating with period p, grating depth h and duty cycle γ. It is composed of two materials with refractive index n_1 and n_2. Light with a wavelength λ will not be diffracted into diffraction orders outside the grating, if the following condition holds:

$$p \leq \lambda/(2n_1) \quad \text{and} \quad p \leq \lambda/(2n_2) \tag{1}$$

In a crude approximation the electric field within the grating grooves is considered homogeneous (period $\ll$ wavelength). Then, the grating behaves like a negative uniaxial crystal: the effective refractive index for the ordinary and the extraordinary beam are from

crystal: the effective refractive index for the ordinary and the extraordinary beam are from the theory of form birefringence:

$$n_{EXO}^2 = \frac{n_1^2 n_2^2}{\gamma n_1^2 + (1-\gamma) n_2^2} \qquad\qquad n_{ORD}^2 = \gamma n_2^2 - (1-\gamma) n_1^2 \qquad (2)$$

For crossed gratings the birefringence vanishes and both polarizations experience the same effective refractive index. It can be seen, that the efffective index depends on the duty cycle γ. Thus, we may consider a grating with variable duty cycle as as artificial distributed index medium (see fig. 2). For better results Bloch wave theories or rigorous theories are required.

3. Applications

Artificial dielectrics are attractive, because for blazed grating or a blazed Fresnel zone plate a binary surface profile structure is sufficient. Therefore only one single step (for example dry etching) is required for fabricating one master. Normally, for a blazed component, a continuous surface profile has to be fabricated (for example by ion milling under an oblique angle or by several lithographic mask steps, that require highly precise pattern alignment). In order to demonstrate the physical principle an experiment with water surface waves was performed. Here the retardation of the wavefronts can be directly observed and the zero order gratings can easily be fabricated by milling. For our experiment a zero order grating was fabricated, in which the composition of the microscopic grating varies periodically, as is required for a macroscopic blazed grating. The calculated deflection angle was $16°$. Fig. 4 shows a photo, where a deflection angle of $17°$ is measured (with about $2°$ accuracy).

References:

/1/ T. Ishikawa, K. Tada: *Jap. J. Appl. Phys.* **28**, 1982 (1989).
/2/ F. Keilmann: *German Patent*, Offenlegungsschrift DE 370 984 A1, 22.09.1988.
/3/ W. Stork, N. Streibl, H. Haidner, P. Kipfer: to be published Optics Letters 15.12.1991.
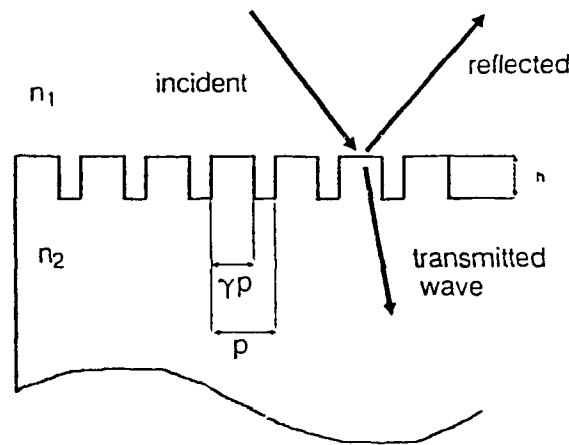
Fig. 1: Schematic of a binary surface relief grating with period p and duty cycle γ at the interface of two materials with refractive index n_1 and n_2.
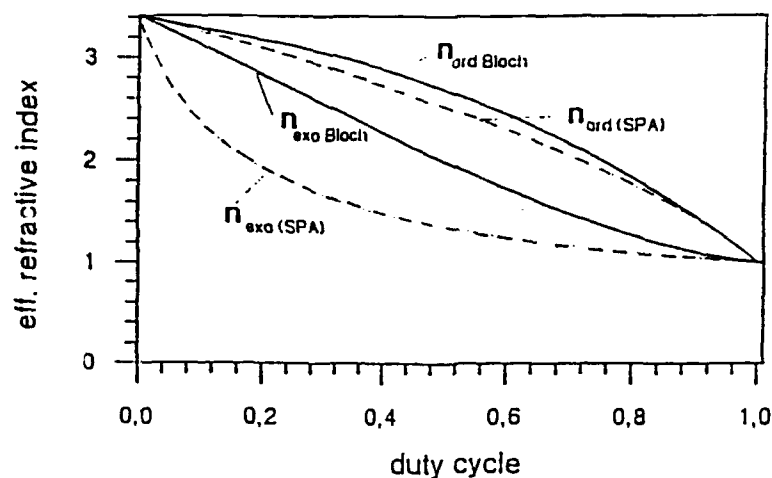
Fig. 2: Dependence of the effective refractive index for ordinary (TL) and extraordinary (TM) waves within a binary grating on the duty cycle. Dashed lines: small period approximation (SPA) of eq. (2). Continuous lines: calculation from Bloch waves The grating was assumed to have a period $p = 1.5$ μm, wavelength is $l = 10.6$ μm, the materials are air $(n_1 = 1)$ and silicon $(n_2 = 3.4)$. Normal incidence on the grating $\varphi = 0^o$ is assumed.
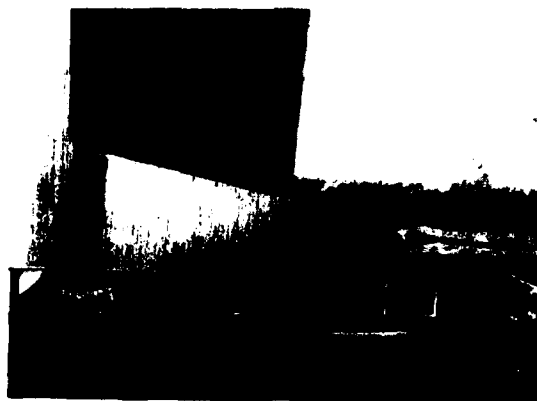
Fig. 3: Side view of the zero order grating for water waves: The duty cycle increases in such a way that a linear increase in phase is expected along the component. Thus an index gradient or a microprism is emulated.

Fig. 4: Experimental result showing the deflection of water waves by the component shown in fig. 3.

Design of 1-D Anti-Reflection Structured Surfaces Using Second-Order Effective Medium Theory

Daniel H. Raguin and G. Michael Morris
The Institute of Optics, University of Rochester, Rochester, NY 14627, (716) 275-8008

I. Introduction

Recently, the use of anti-reflection structured (ARS) surfaces has been proposed to reduce unwanted reflections off optical surfaces, see for example, Refs. 1-3. As shown in Fig. 1, ARS surfaces are surface-relief gratings that are designed such that only the zeroth-order transmitted and reflected waves propogate. In order for no diffracted waves to propogate for all incident angles, θ_i, up to a maximum angle of incidence, θ_{max}, the wavelength to surface period ratio, λ/Λ, must be larger than unity and satisfy

$$\lambda/\Lambda > \mathbf{Max}[n_i, n_s] + n_i \sin\theta_{max}, \tag{1}$$

where **Max** is equal to the maximum value of its arguments. Since light does not diffract when interacting with these subwavelength surface features, the optical characteristics of the system can be completely described if the structured region is represented by a film having an effective permittivity.

Previous authors have designed ARS surfaces with 1-D profiles using wavelength independent zeroth-order effective medium theory[1-3] (EMT). These zeroth-order EMTs become less and less accurate as the surface period-to-wavelength ratio, Λ/λ, becomes large, or if the difference between the incident medium's and substrate's permittivity becomes large. In this paper we present a second-order EMT formulated by Rytov[4] and use it to design selected 1-D ARS surfaces. Second-order EMT designs are compared to zeroth-order EMT designs as well as to designs obtained using a rigorous coupled-wave approach (RCWA) developed by Moharam and Gaylord[5]. Computer implementation of this RCWA was achieved using a program written at MIT Lincoln Laboratory[6].
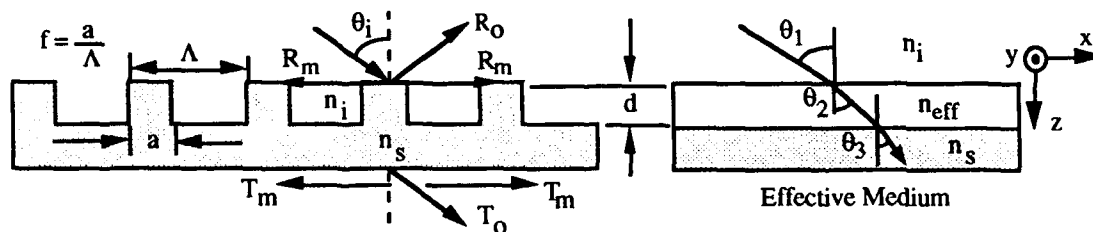
Fig.1. ARS surface. For a given angle of incidence, θ_i, all orders are evanescent except the zeroth orders, R_0 and T_0. For a binary profile, the effective medium is a single dielectric film.

II. Second-order EMT applied to 1-D ARS Surfaces

For both x and y polarized light, the effective dielectric constants ε_x and ε_y, derived using second-order EMT[5], are of the form

$$\varepsilon_j = \varepsilon_j^{(o)}\left[1+\left(\frac{\Lambda}{\lambda}\right)^2 \delta\varepsilon_j(f)\right] = \varepsilon_j^{(o)}\left[1+\Delta\varepsilon_j(f)\right] , \qquad (2)$$

where $\varepsilon_j^{(o)}$ and $\Delta\varepsilon_j$ represent the zeroth-order effective dielectric constant and the second-order correction factor for the effective dielectric constant respectively. The parameter f in Eq. (2) is called the filling factor of the profile and as defined in Fig. 1, it denotes the percentage of substrate material present at a given depth into the ARS surface profile. Due to manufacturing constraints, it is desirable to design ARS surfaces so that they have the largest surface period-to-wavelength ratio, Λ/λ. If diffracted orders must not propogate for all angles of incidence then Eq. (1) requires that

$$\Lambda = \frac{\lambda}{n_i+n_s} . \qquad (3)$$

By requiring the surface period to be as large as possible, deviations of zeroth-order EMT from second-order EMT can become quite large. Table 1 illustrates how large these errors can become and the filling factor, f_o, they occur at for a given set of incident and substrate materials and for both x and y-polarized light.

Material	ns	x-polarization			y-polarization		
		$f_{o,x}$	$\Delta\varepsilon_x(f_{o,x})$	$\Delta n_x(f_{o,x})$	$f_{o,y}$	$\Delta\varepsilon_y(f_{o,y})$	$\Delta n_y(f_{o,y})$
Ge	4.0	0.8354	0.6295	0.2765	0.3659	0.2457	0.1161
Si	3.5	0.8164	0.5007	0.2250	0.3735	0.2164	0.1029
ZnSe	2.4	0.7520	0.2160	0.1027	0.4018	0.1279	0.0620
AgCl	2.0	0.7137	0.1249	0.0606	0.4191	0.0864	0.0423
Glass	1.5	0.6394	0.0374	0.0185	0.4505	0.0322	0.0160

Table 1. Maximum values of the second-order correction factors, $\Delta\varepsilon$ and Δn for selected substrate mediums for both x and y polarizations. Incident medium was taken to be air, and the period, Λ, of the profiles was taken to satisfy Eq. (3).

One notes from Table 1 that the maximum value of the 2nd-order correction terms increases with substrate refractive index. For germanium, zeroth-order EMT values of n_x and n_y can be off by as much as 28% and 12% respectively. Consequently, in the design of ARS surfaces on IR transmissible materials, second-order EMT is essential.

III. Selected ARS Surfaces

Both binary and multi-level 1-D profiles have been designed and analyzed using second-order effective medium theory. Figure 2 illustrates the dependence of the power reflection coefficient, R, on profile depth for a 4-level 1-D triangle ARS surface. RCWA results are compared to those obtained from EMT for normally-incident y-polarized light, $n_i=1$, and the period of the profiles satisfying Eq. (3). Although the substrate for Fig. 2(a), glass with $n_S=1.581$, is relatively rare, one still notes substantial deviations of zeroth-order EMT from second-order EMT and RCWA results. These differences become even more pronounced when the substrate medium is taken to be silicon ($n_S=3.5$).
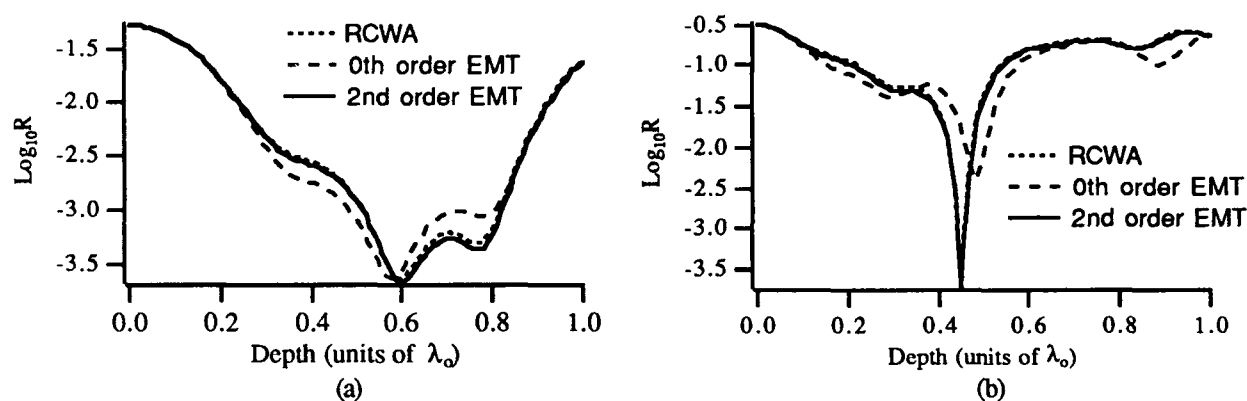
Fig. 2 Power reflection coefficient, R, dependence on profile depth for a 4-level 1-D triangle ARS surface. RCWA results are compared to zeroth- and second-order EMT results for (a) glass substrate ($n_S=1.581$) and (b) silicon substrate ($n_S=3.5$). Radiation is normally incident and y-polarized, $n_i=1$, and for both substrates, Λ satisfies Eq. (3). Note that 2nd-order EMT results match the RCWA data very well.

Second-order EMT analysis of other multi-level 1-D profiles, in addition to binary 1-D profiles will be presented. Laboratory experiments are in progress and their results will be presented as well.

References

1.   T.K. Gaylord, W.E. Baird, and M.G. Moharam, "Zero-reflectivity high spatial-frequency rectangular dielectric surface-relief gratings," *Appl. Opt.*, **25**, 4562-4567 (1986).

2.   Y. Oni, Y. Kimura, Y. Ohta, and N. Nishada, "Antireflection effect in ultrahigh spatial-frequency holographic relief gratings," *Appl. Opt.*, **26**, 1142-1146 (1987).

3.   D.H. Raguin and G.M. Morris, "Analysis of 1-D antireflection structured surfaces," *OSA Tech. Digest*, **17**, 153 (1991).

4.   S.M. Rytov, "The electromagnetic properties of finely layered medium," *Soviet Phys. JETP* **2**, 466-475 (1956).

5.   T.K. Gaylord and M.G. Moharam, "Analysis and applications of optical diffraction by gratings," *Proc. IEEE*, **73**, 894-937 (1985).

6.   W.B. Veldkamp, G.J. Swanson, S.A. Gaither, C-L. Chen, and T.R. Osborne, "Binary Optics: A Diffraction Analysis," Project Report ODT-20 (1989).

Filter Properties of Dielectric Waveguide Gratings

R. Magnusson and S. S. Wang
Department of Electrical Engineering
The University of Texas at Arlington
Arlington, Texas 76019
(817) 273-3474

By using an exact electromagnetic model (rigorous coupled-wave theory) to analyze periodic dielectric waveguides, sharp resonance phenomena where 100% switching of light energy between waves occurs over small parameter ranges have been discovered.[1] Physically, this is due to coupling of external diffracted fields with the modes of the waveguide. Several interesting applications and devices based on this resonance effect can be envisioned. For example, efficient, low-power switching elements appear to be feasible using this concept. Lossless spectral filters (static and tunable) with arbitrarily narrow, controllable linewidth may also be feasible. Using a high spatial frequency dielectric waveguide grating may lead to 100% reflective narrow-band spectrally selective mirrors. These elements can then be used to line-narrow lasers in bulk systems and possibly in integrated optics. Improved thin-film structures and high-precision sensor applications may also be feasible.

In 1965, Hessel and Oliner[2] constructed the first model to describe these resonance effects. They modeled a reflection grating as a periodic reactance surface and presented calculated results. Zhang and Tamir[3] treated the effects of Wood's anomalies on Gaussian beams diffracted by a reflection grating using the Hessel-Oliner model.[2] DeSandre and Elson[4] studied guided-mode resonances in overcoated reflection gratings, pointing out that these effects can induce catastrophic failures of components in high power applications. The authors treated dielectric transmissive waveguide grating structures using explicit connections of waveguide theory and diffraction theory to find approximate locations and ranges of the resonances.[1]

The elemental single-grating resonance structure of interest here is shown in Fig. 1. The permittivity of region 2 is spatially modulated as $\varepsilon_2(x) = \varepsilon_g + \Delta\varepsilon \cos Kx$, where ε_g is the average permittivity, $\Delta\varepsilon$ is the modulation amplitude and $K = 2\pi/\Lambda$ where Λ is the grating

period. Region 2 is a waveguide grating and thus $\varepsilon_g > \varepsilon_1, \varepsilon_3$. We call this structure a "guided-mode resonance filter". The principal analytical tool, the rigorous coupled-wave theory, has been described in the literature[5].

Figures 2 and 3 show the resonance behavior of the zeroth-order propagating waves. No higher order diffracted waves propagate since the structure, in this example, is of high spatial frequency, i. e. the wavelength, λ, is larger than the grating period, Λ. The diffraction efficiency represents the power in the various diffracted waves. The waveguide is asymmetric with $\varepsilon_1 = 1$, $\varepsilon_g = 3$, $\varepsilon_3 = 2.161$ and modulation index $\Delta\varepsilon/\varepsilon_g = 0.01$. In Fig. 2 the first Bragg condition is satisfied with the incident wave at an angle $\theta' = 31°$. Close to 100% energy exchange with smooth lines is obtained at the resonance location d_0/Λ by varying d/Λ. Figure 3 shows the spectral variation of the resonance at the fundamental waveguide mode with the grating thickness set to $d/\Lambda = 1$ at normal incidence. Again, complete energy exchange between the forward and backward propagating waves is found. Figure 4 shows the calculated relation between linewidth in normalized thickness, $\Delta d/\Lambda$, as a function of the modulation index $\Delta\varepsilon/\varepsilon_g$. Similarly, in Fig. 5 the normalized spectral linewidth in $\Delta\lambda/\Lambda$ is given. Near straight-line relationships are found in each case. The width of the resonance lines is thus controlled by the modulation amplitude, $\Delta\varepsilon$. Associated free spectral ranges of the filters can also be predicted. This paper is based in part on research supported by the Texas Advanced Technology Program under grant #003656023.

1. S. S. Wang, R. Magnusson, J. S. Bagby, and M. G. Moharam, "Guided-mode resonances in planar dielectric-layer diffraction gratings," J.Opt. Soc. Am. A, vol. 7, pp. 1470-1474, 1990.

2. A. Hessel and A. A. Oliner, "A new theory of Wood's anomalies on optical gratings," Appl. Opt., vol. 10, pp. 1275-1297, 1965.

3. S. Zhang and T. Tamir, "Spatial modifications of Gaussian beams diffracted by reflection gratings," J. Opt. Soc. Am., vol. 6, pp. 1368-1381, 1989.

4. L.F. DeSandre and J.M. Elson, "Extinction-theorem analysis of diffraction anomalies in overcoated gratings," J. Opt. Soc. Am., A, vol. 8, pp.763-777, 1991.

5. T. K. Gaylord and M. G. Moharam, "Analysis and applications of optical diffraction by gratings," Proc. IEEE, vol. 73, pp. 894-937, 1985.
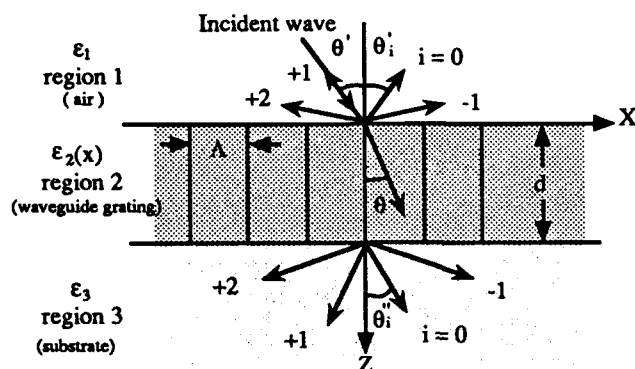
Figure 1. The basic planar waveguide grating diffraction model used. The angles $\theta i'$ represent the angles of the wave vector of the i-th backward-diffracted wave with respect to the z-axis; $\theta i''$ are the corresponding angles for the forward-diffracted waves. The angle of incidence (θ') is arbitrary.
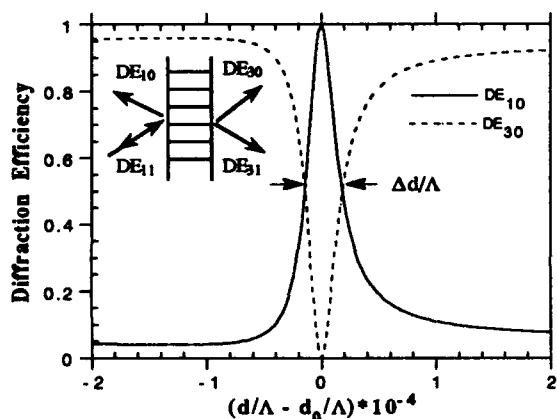
Figure 2. Resonance behavior of propagating waves at first Bragg incidence with respect to d/Λ, with $d_0/\Lambda = 0.32058$ and $\theta' = 31^0$
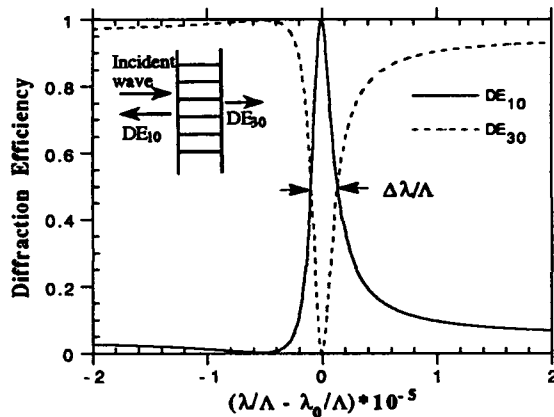
Figure 3. Resonance behavior of propagating waves at normal incidence with respect to λ/Λ, $\lambda_0/\Lambda = 1.642683$.
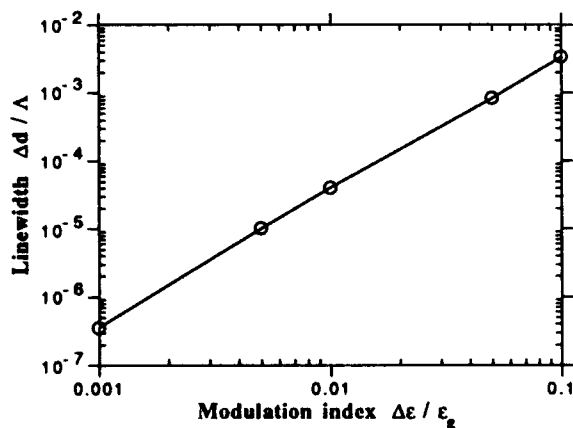
Figure 4. Calculated relation between linewidth $\Delta d/\Lambda$ as a function of the modulation index $\Delta\varepsilon/\varepsilon_g$.
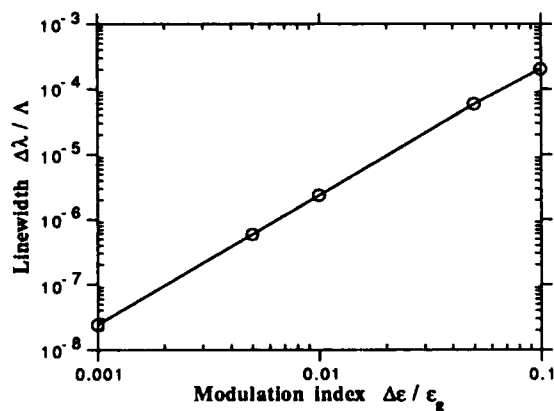
Figure 5. Calculated relation between linewidth $\Delta\lambda/\Lambda$ as a function of the modulation index $\Delta\varepsilon/\varepsilon_g$.

Diffractive Optics
for Laser Systems

TuA   8:30am–10:00am
Cabildo Room

Norbert Streibl, *Presider*
University of Erlangen-Nurnberg, Germany

RECENT PROGRESS IN HOE OPTICAL PICKUP

Wai-Hon Lee
HOETRON INC.
776 Palomar Avenue
Sunnyvale, CA 94086

The popularity of the compact disc players today indicates that the era for optical recording is here to stay. For this reason many improvements made on the optical pickups are being incorporated by manufacturer of compact disc players, especially those in JAPAN. In this short article I will review some of the progress in the HOE pickups(Ref. 1) as developed at HOETRON INC.

Figure 1 shows two optical pickups for compact disc players. The one on the right is based on conventional optical components such as beamsplitter, packaged laser and detector. The metal housing below the sliding base contains all of the optical components excluding the objective lens. The optical pickup on the left uses a HOETRON's hybrid optical device which contains a HOE, a laser chip and a detector chip, all in a small mechanical package. The hybrid device performs the same function as the conventional optical system. Figure 2 shows an enlarged view of the optical hybrid device. The bottom of the hybrid device has eight soldering pads for making electrical connections to the devices inside the package.

Figure 3 shows The optical layout of the optical pickup using the hybrid device. A laser chip is mounted on a ceramic board with two photodetectors nearby. One photodetector is used to monitor the laser power emitted by the laser chip and the second one is to detect the light reflected by the compact disc. A parallel line grating is placed above the laser chip to divide the laser beam into three beams as required by most of the compact player system. Finally, a HOE is inserted on the top of the hybrid housing to diffract the returned beam to the detector. The HOE is designed to perform four functions. First of all, it serves as a beam splitter. As the light propagates from the laser source to the disc, the 0 order diffraction from the HOE allows a part of the laser light to be focused on the disc. As the light reflects from the disc and incidents on the HOE again, the HOE focuses one of the 1st diffracted order beam on the detector surface(Ref. 1). Secondly, the HOE produces an astigmatic beam at the detector for the purpose of sensing any focusing error caused by the disc motion. Thirdly, since the laser emitting surface is not on the same plane as the detector, the HOE also provides the function as a spherical lens. It is well known that when a converging beam incidents on a grating, the diffracted beam from the grating will have coma and astigmatism. The HOE used in this design contains correction for coma and astigmatism. The amount of aberration correction needed are obtained from a ray tracing computer program. Figure 4 shows the spot diagrams of the laser beam at equal distances from the detector plane. As can be seen, the beam quality is significantly improved by using aberration correction. Figure 5 shows the RF signal obtained from a compact disc player using the HOE optical pickup technique. Typical jitter from the pickup is about 16 ns.

SUMMARY REMARKS

Whenever a HOE is used in an optical system, the often asked question is what is the diffraction efficiency? In this particular application the advantage of using HOE to obtain a small optical package far surpasses its low light efficiency. It is difficult to design and manufacture small three beam optical pickups without using hybrid concept and HOEs as described in this paper.

REFERENCE:

1. W-H. Lee, Opt. Eng., vol. 28, no. 26, p.650-653(1988).
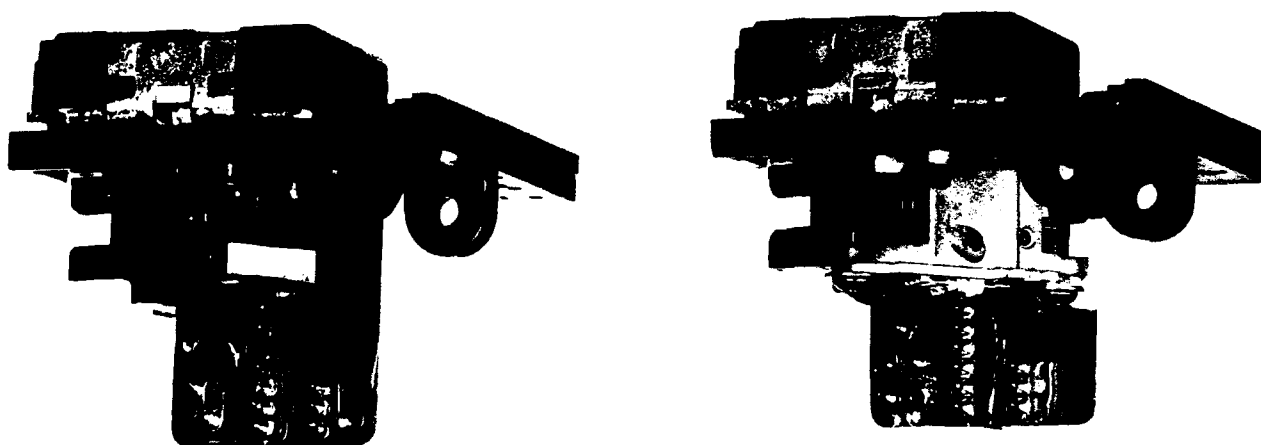
Fig. 1: Comparison between HOE pickup and conventional pickup
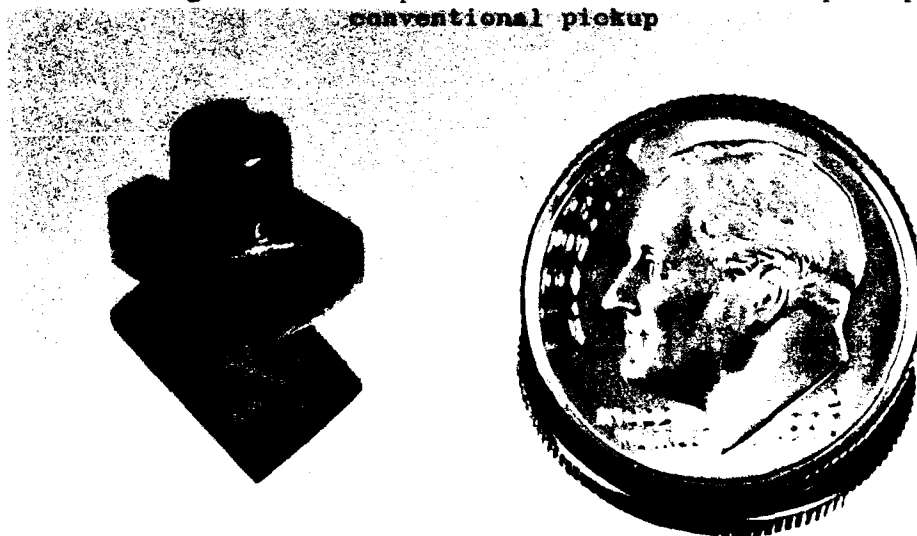
Fig. 2 : Optical hybrid device
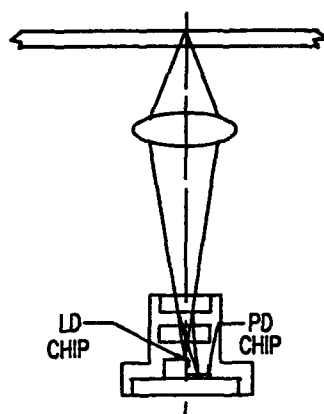
Fig. 3 : Optical systems for compact disc
player using HOE

(a)

(b)
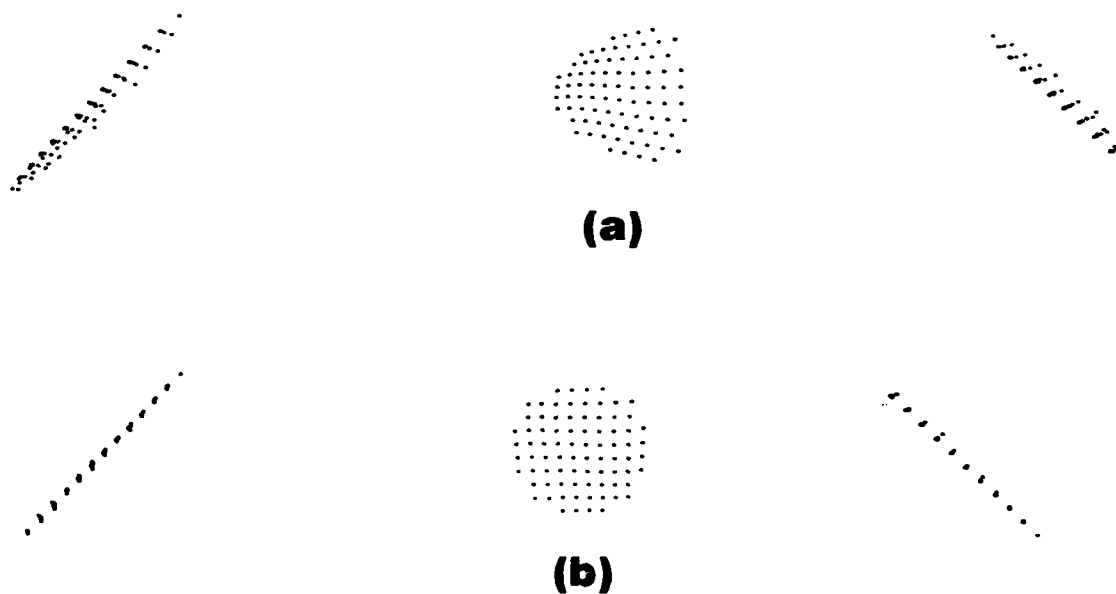
Fig. 4: Spot diagrams of the beam at the detector plane
(a) without aberration correction
(b) with aberration correction.
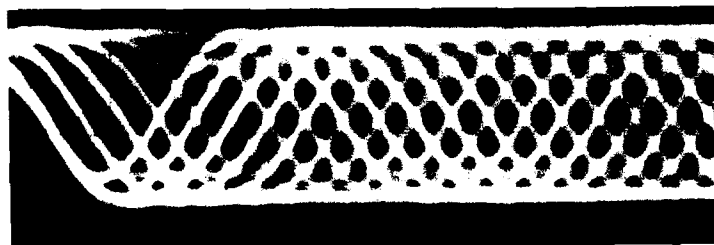
Fig. 5: Eye patterns of the HF signal from
compact disc player

Design of Diffractive Optics for Concentration of Light From Diode Laser Arrays

J. R. Leger
University of Minnesota
Minneapolis, Minnesota 55455

W. C. Goltsos, W.F. Delaney, M.P. Griswold
MIT Lincoln Laboratory
Lexington, Massachusetts 02173

Diode-laser arrays are becoming increasingly popular as illumination sources because of their high efficiency, reliability, and ability to produce large amounts of optical power from a small package. In addition, their relatively narrow spectral bandwidth makes them ideal pump sources for solid-state lasers. This paper describes an optical technique to concentrate light from a linear diode-laser array into a small spot with a minimum divergence. Such optics are ideally suited to coupling into multimode optical fibers and longitudinal pumping of solid-state lasers.

The emitting aperture of a linear diode-laser array is very narrow (≈ 1 μm), but can exceed 1 cm in width. Often the array is designed to emit nonuniformly over this width so that heat can dissipate into the nonradiating regions. The coupling optics must convert this nonuniform one-dimensional source into a quasi-uniform two-dimensional distribution whose shape matches the receiving optical device. In addition, many optical devices have constraints on the numerical aperture of the illumination. For example, the light illuminating a multimode fiber must both be focused into the fiber core and have a divergence that is less than the numerical aperture of the fiber. Unfortunately, diode laser arrays usually have nonsymmetric divergences and do not optimally utilize the angular acceptance of the optical device. Good coupling optics must therefore symmetrize the divergence of the illumination as well.

The diode-laser array used in this experiment (SDL 3480) was a 1-cm wide bar consisting of 200 quasi-incoherent gain-guided lasers. The array contained 20 subarrays of 10 lasers each. The spacing between lasers was 10 μm, resulting in a total subarray width of approximately 100 μm. The spacing between subarrays was 500 μm. The illumination thus contained alternating regions of light and dark areas, with a fill factor of approximately 20%. The divergence was approximately 40° (FWHM) transverse to the junction, and 10° parallel to the junction.

A conceptual diagram of the optical system is shown in fig. 1. A pair of cylindrical lenses is used in an afocal configuration parallel to the laser junction to image each subarray with a magnification of 50$\times$. The magnified subarrays contain images of the laser apertures spaced by 500 μm, with the image of each laser aperture slightly less than 500 μm. Each afocal imaging system also contains a pair of prisms. The first plane of prisms tilts the images of the various subarrays to the same location along the x-axis, and the second plane of prisms removes the tilts.

The optics transverse to the laser junction (fig. 1b) consist of cylindrical lenses to collimate the beams, and prisms to redirect them in the y-direction. The focal length of the collimating lenses was chosen to correct the astigmatism from the gain-guided lasers and produce a collimated beam
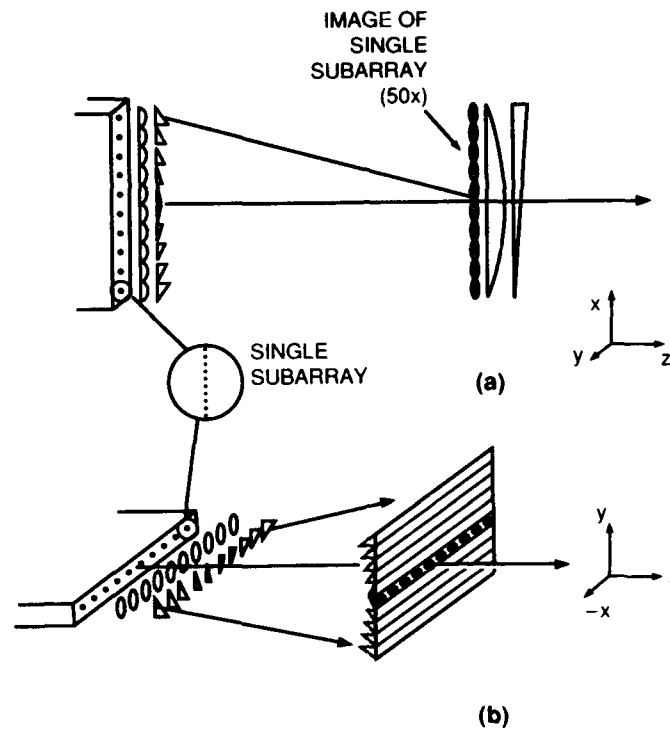
Figure 1: Conceptual design of optical system (a) parallel to the laser junction and (b) transverse to the junction.

in the y-direction that matches the beam size in the x-direction. The resulting symmetric shape of the individual laser beams produces an illumination with symmetric divergence. The first plane of prisms is used to tilt the beams out of the plane of propagation, producing a two-dimensional array of light. The second set of prisms removes the tilts and redirects the light down the optical axis. The degree of tilt is chosen to produce a square array of 10 × 10 laser apertures.

The optics shown in fig. 1 were applied to half (ten subarrays) of the SDL 3480. An identical set of optics was applied to the other half of the array, producing a second square array. The two square arrays were then polarization-multiplexed by a polarizing beamsplitter into a single symmetric array with symmetric divergence.

The optical functions described in fig. 1 were performed by two planes of diffractive optics. The optics were fabricated on two separate pieces of fused silica by reactive-ion etching, and were separated by 2.6 cm. Fig. 2 shows the optical system pumping a solid-state laser rod, where the two planes are integrated into a single substrate. Only seven of the ten subarrays are shown for clarity, and the polarization multiplexing with the second set of ten subarrays is not shown. This single element replaces the collimating lenses and anamorphic prism pairs of a conventional pumping system, and concentrates the light in a near-optimal manner. In addition, the focusing power of the mode matching lens can be incorporated into the second plane of diffractive optics if desired.

The optical system was applied to the SDL 3480 diode laser array. The light distribution from the laser array is shown in fig. 3a, where each spot corresponds to a subarray of ten lasers. After transformation by the diffractive optics, light from the linear laser array forms two square arrays of 10 × 10 spots (fig. 3b). Each row of 10 spots is an image of a single subarray. The size of each square array is 5 mm × 5 mm, and the divergence is approximately 1.5 mrad in both the x and y
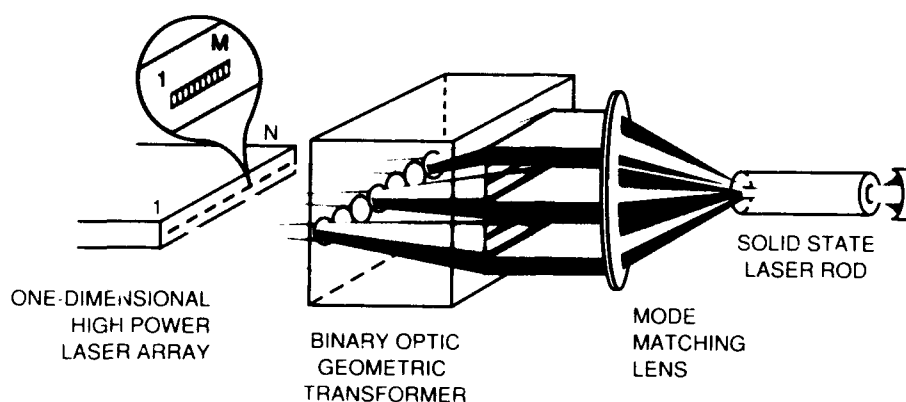
Figure 2: Diffractive optics implementation of beam concentrator used to longitudinally pump a solid-state laser.
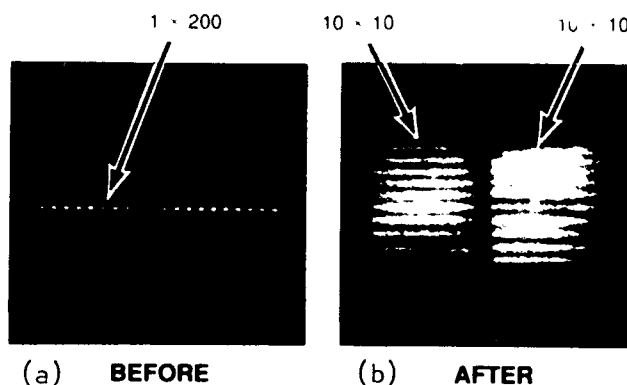
Figure 3: Photograph of the light patterns before and after geometric transformation optics.

directions. The étendue (product of the area and solid angle divergence) is within a factor of three of the theoretical value given by the radiance theorem.

The diffraction efficiency of each diffractive element was approximately 50%. The reason for this relatively low efficiency was primarily because the lenses were required to have large numerical apertures, and the substrate material (fused silica) had a low refractive index. Significantly higher efficiency should be achievable by using a refractive cylindrical lens to reduce the laser array divergence, and by using higher index materials as substrates for the diffractive optics. After geometrical transformation by the diffractive optics and polarization multiplexing, the radiance of the focused spot from the 5 watt array was 0.62 $MW/cm^2 Sr$.

The optical system was used to longitudinally pump a Nd:YAG laser. Due to the optimized pumping geometry, a small solid-state laser mode could be used (mode radius of 210 μm) without danger of exciting higher-order transverse modes. This small mode radius resulted in a relatively low threshold (140 mW), and the good overlap between the pump and solid-state laser modes produced a TEM_{00}-mode slope efficiency of 56%.

In conclusion, a pair of diffractive optical elements has been designed and fabricated to transform a 200-element linear diode-laser array into a two-dimensional, symmetric source with symmetric divergence. This optical configuration is expected to find applications in multimode fiber illumination and solid state laser pumping.

Holographic beam samplers for high power laser

J.M. Trudeau, J. Fréchette, M. Côté, P. Langlois, M.P. Bélanger and P. Galarneau

Institut National d'Optique, 369 Franquet, Ste-Foy, Qc, Canada, G1P 4N8

Tel: (418) 657-7006, Fax: (418) 657-7009

R.E. Vander Haeghe and S. Barsetti

Gentec Inc., 2625 Dalton, Ste-Foy, Qc, Canada, G1P 3S9

Tel: (418) 651-8000, Fax: (418) 651-6695

INTRODUCTION.

Smart laser-based material processing systems require complete monitoring of the laser beam characteristics. The development of such monitoring units depends strongly on the beam sampling device employed. Beam samplers compatible with a randomly polarized 1 kW average power Nd:YAG laser has been realized by etching an holographic grating directly onto the surface of a high quality fused silica substrate [1].

HOLOGRAPHIC BEAM SAMPLERS (HBS).

Due to the large average power involved, low sampling factors were required. Holographic beam samplers (HBS) were produced with sampling factors of 0.1% and 0.05% in the first diffraction order. HBS were found to sustain easily the 1 kW of average power at 1.064 μm and were inherently insensitive to vibrations making such optical device especially suited for industrial environment. The very low sampling factors associated with high order terms were advantageously used to measure spatial and temporal properties of the laser beam since these measurements usually require a much lower power level than the ones for absolute power or energy measurements.

POLARIZATION SENSITIVITY.

Polarization sensitivity was one of the major concerns related to the development of the HBS, since the laser beam was randomly polarized. In figure 1, the setup used to evaluate the sampling factor sensitivity on light polarization is illustrated. Figure 2 presents a typical

variation of the sampling factor with the waveplate angle. The polarization sensitivity was found to be of ~1.2% for a grating period of 5 µm and less than 0.3% for a grating period of 10 µm.
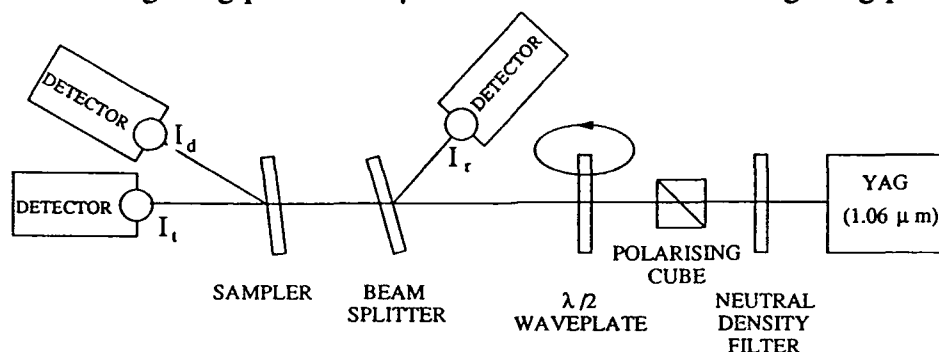
Figure 1 Polarization sensitivity evaluation setup.
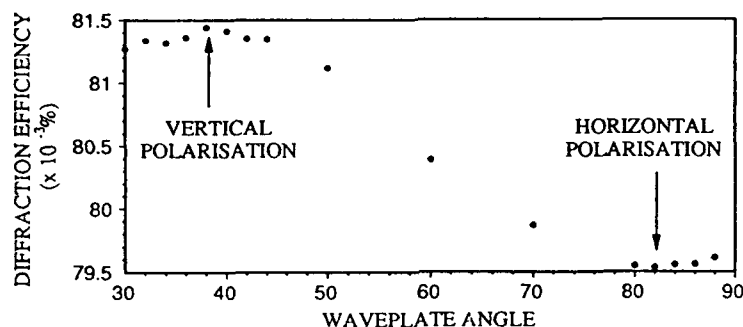
Figure 2 Polarization sensitivity evaluation typical results.

TEMPERATURE SENSITIVITY.

The other concern related to the use of HBS with high power laser is associated with the temperature variation due to residual absorption at the Nd:YAG wavelength. Such temperature variation is expected to induce modification of the sampling factor through both, variation of the refractive index with temperature and thermal expansion which will alter the modulation depth of the grating. Using dn/dT of $1.18 \times 10^{-5}/°C$ [2] and a thermal expansion coefficient of $5.5 \times 10^{-7}/°C$ [3], the relative sampling factor sensitivity on temperature ($1/\eta \ d\eta/dT$, where η is the sampling factor) can be computed to $5.4 \times 10^{-5}/°C$.

Considering that the absorption coefficient of fused silica is smaller than 5 ppm/mm at 1.064 µm [4], the laser power absorbed in the 3.2 mm thick HBS is less than 16 mW for a 1 kW laser beam. To evaluate the temperature increase induced by absorption of the Nd:YAG laser, a CO_2 laser was employed to emulate the power deposition (since its emitted wavelength is completely absorbed by the fused silica substrate). This method increases the accuracy of the absorption measurements. The CO_2 laser beam spotsize was 5 mm which was similar to the

targetted specification of the Nd:YAG laser-based system. In figure 3, the temperature of the substrate at the center of the illuminated region is shown as a function of the incident laser beam power. The right vertical scale shows the relative variation of the sampling factor as evaluated from published data. As it can be seen the variation of the sampling factor due to temperature variation will be negligible even at average power of 1 kW (16 mW of absorbed power).
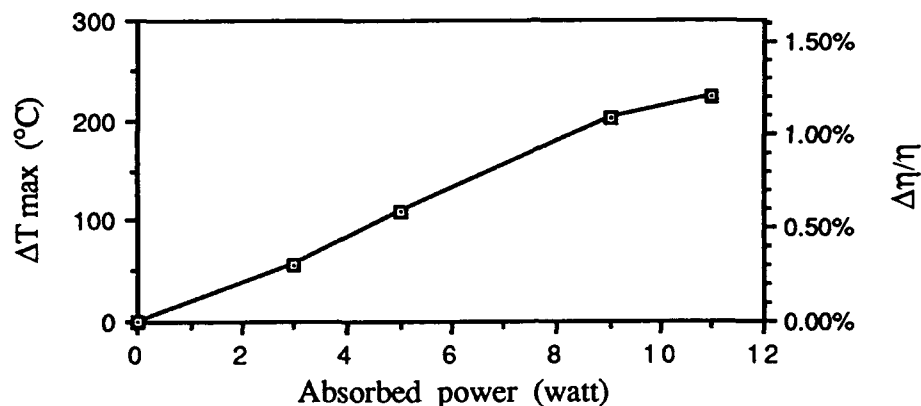
Figure 3 HBS temperature vs CO_2 laser power absorbed.

CONCLUSION.

Holographic sampling is an attractive and versatile component in a high power laser control chain or system. HBS offer several advantages. Among them are the ease in obtaining a low sampling factor, a high damage threshold, the production of calibrated replicas of the transmitted beam and a low sensitivity with respect to light polarization at low diffraction angle, temperature variation and vibration.

REFERENCES.

1-   P. Galarneau, P. Langlois, M. Bélanger, "Monitoring high-power lasers", Photonics Spectra, 25, Jan. 1991, p. 112-113.

2-   Handbook of infrared optical materials, P. Klocek ed., Marcel Dekker, 1991, p. 448.

3-   Optical materials and components handbook, Esco products Inc., p. 6.

4-   F.P. Milanovich, J.T. Hut, J.N. Roe, "Measurements of optical loss in transparent solids using a novel spectrometer based on optical cavity decay", Proc. SPIE, 1047, 1989, p. 244-249.

Diffractive Optics for Industrial Lasers

Russell Gruhlke, Larry Giamona, William Sullivan

Coherent Optics Division, 2301 Lindbergh St., Auburn, CA 95603

916-823 9550

Theory predicts that monochromatic radiation can be focussed by a diffractive optical element to a diffraction limited focal spot with nearly 100 % efficiency. Thus, large energy densities are predicted at the focal point making diffractive optical elements well suited for application to industrial laser cutting and welding technology. To utilize this potential, Coherent, in collaboration with HoloOr, has fabricated ZnSe and GaAs diffractive optical elements designed to be used in carbon dioxide industrial laser systems. These elements exhibit high diffraction efficiency and diffraction limited focal spot sizes.

Industrial carbon dioxide lasers produce a collimated laser beam ($\lambda=10.6\,\mu m$) which is typically 10 to 40 mm in diameter. To effectively focus such radiation, a diffractive optical element must be of comparable size and exhibit high diffraction efficiency over large areas of its surface. This causes fabrication difficulties since feature size decreases significantly with increasing radial distance. To overcome this difficulty Coherent and HoloOr have developed a unique masking algorithm to be used in conjunction with well established photolithography techniques and dry chemical etching. The surface relief thus fabricated consists of concentric rings or phase zones having stepped cross-sectional profiles. These rings are grouped into two or more annular regions as illustrated in Figure 1 for the case of an 2.5 inch focal length element. Here the inner annular region is comprised of 14 step/zone microstructure while the outer region contains 7 step/zone cross sectional profiles. The reduced number of steps in a phase zone allows accurate fabrication of the microstructure in the outer region. When the laser beam is centered on the diffractive optical element, the most intense portion of the laser beam is intercepted by the high efficiency inner region of the diffractive element while the lower energy "tail" of the laser beam intensity distribution is collected by the outer portion of the element. This strategy enables high diffraction efficiency over large areas while reducing fabrication errors near the periphery of the diffractive element.

The optical performance of the diffractive optical elements fabricated was evaluated by measuring spot size and efficiency relative that of a conventional refractive lens. The spot size of light focussed by diffractive as well as refractive elements was determined by monitoring the $1/e^2$ points of the intensity distribution of the light not blocked by a razor blade partially obstructing the laser beam near the focal point. The resulting spot size is plotted in Figure 2 as a function of the razor blade position for an aspherical lens, meniscus lens, plano convex lens, and a diffractive optical element. All elements have a 2.5 inch focal length. These results indicate that
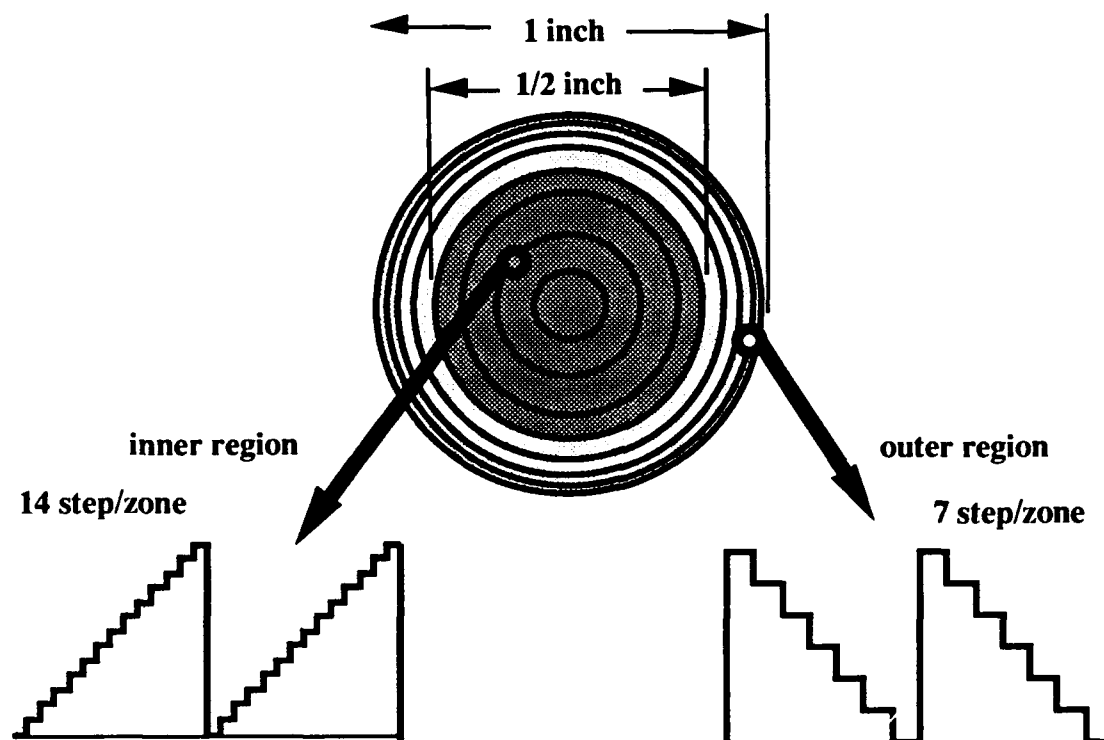
Figure 1   Multiple efficiency regions of a 2.5" focal length diffractive optical element.

the focal spot size of the diffractive element is significantly smaller than that of both the conventional meniscus and plano-convex lens.

Relative efficiency measurements were also made by measuring the intensity of light focussed by both refractive and diffractive elements. All experimental parameters were kept fixed as elements were interchanged in a lens holder. The ratio of the diffracted intensity divided by the refracted intensity as measured near the focal point is defined as replacement efficiency and is a measure of the proportion of light directed to the focal spot when a conventional refractive lens is
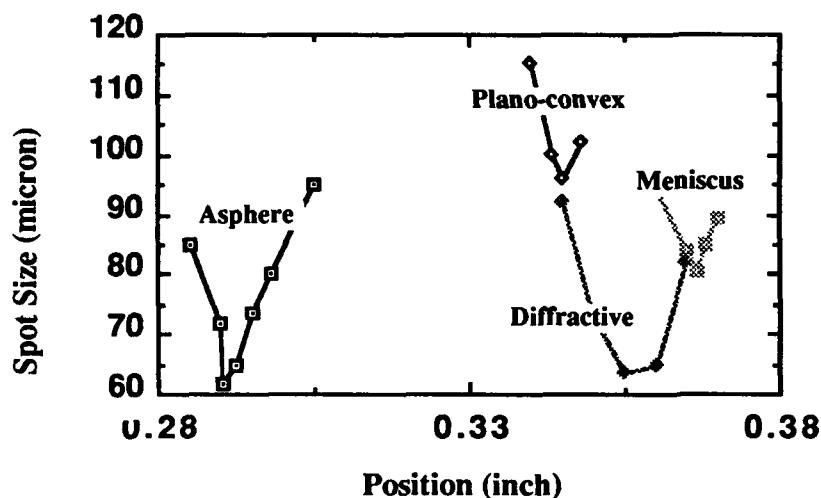
Figure 2   Spot size.
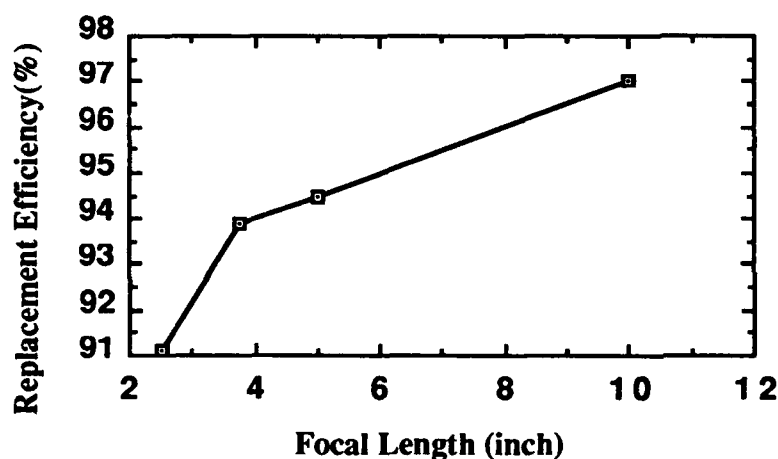
Figure 3   Replacement
Efficiency (%).

replaced by a diffractive element. Measured values of replacement efficiency are plotted in Figure 3 as a function of focal length. Light not focussed by a diffractive element is scattered into higher orders diffraction modes or is internally reflected within the element and absorbed.

In summary, diffractive optical elements incorporating multiple efficiency regions can focus large diameter industrial laser beams efficiently. Moreover, the diffractive element is capable of smaller focal spot sizes and, hence, higher energy densities than the conventional refractive lens. These properties are very advantageous in many laser cutting applications. A second generation of diffractive optical elements incorporating a new design as well as better fabrication techniques is currently being developed to increase efficiency performance.

Theory of Grating Diffraction

TuB 10:30am–12:00m
Cabildo Room

M. G. Moharam, *Presider*
University of Central Florida

On the Limits of Scalar Diffraction Theory for Conducting Gratings

Douglas A. Gremaux and Neal C. Gallagher, School of Electrical Engineering,
Purdue University, West Layfayette, IN 47907

Many diffractive elements such as computer generated holograms and periodic gratings are designed by using scalar diffraction theory. The Lohmann hologram is an example of this [1]. The Lohmann method utilizes a two dimensional planar array of square cells each containing a rectangular aperture. Ideally by choosing the proper size and position of each aperture, any arbitrary wavefront can be created. The number of cells in the hologram determine how accurately it can produce the desired wavefront. So in order to reduce error, one would want as many cells in as small a space as necessary to achieve the desired accuracy. In the past, these holograms, as well as other diffractive elements, were limited by the manufacturing process which prevented very small cell sizes, or in more general terms, limited the space bandwidth product of the element. Many of the early computer generated holograms were plotted on paper or even laid out by hand, and then photo-reduced to the proper size. But today, thanks to advances in computer technology and microlithography devices such as electron beam machines, these diffractive elements can be made with micron or sub-micron feature sizes. Some devices made with very small features do not perform as expected. This is not due to fabrication constraints, but rather due to the design process itself. Scalar diffraction theories are used to describe the interaction of light with these diffractive elements [2]. But scalar diffraction theory begins to break down as feature sizes shrink to the order of a few wavelengths or less.

We decided to make the comparison by analyzing a conducting, rectangular grooved grating. We choose this structure since much research has been done to characterize plane wave diffraction from these structures using electromagnetic vector methods for arbitrary angles of incidence [3, 4, 5]. Although there may be some loss of generality by choosing a specific structure, the conclusions reached should apply to more general structures as well. Also, most computer generated holograms can be viewed as modulated gratings, and linear gratings may be viewed as very simple holograms.

The results of this study are illustrated by Fig. 1. This figure compares the relative zero order diffraction efficiencies for the scalar theory, slow polarization (E perpendicular to the grooves) and fast polarization (H perpendicular to the grooves).

REFERENCES

1. A. W. Lohmann and D. P. Paris, "Binary Fraunhofer Holograms, Generated by Computer," *Appl. Opt.*, 6, 1739 (1967).

2. J. W. Goodman, *Introduction to Fourier Optics*, (McGraw-Hill, New York, 1968).

3. Y. L. Kok and N. C. Gallagher, "Relative phases of electromagnetic waves diffracted by a perfectly conducting rectangular-grooved grating," J. Opt. Soc. Am., Vol. 5, 65-73 (1988).

4. R. Petit, *Electromagnetic Theory of Gratings*, Vol. 22 of Topics in Current Physics, R. Petit, ed. (Springer-Verlag, Berlin, 1980).

5. Y. L. Kok, N. C. Gallagher, and R. W. Ziolkowski, "Dual Series Solution to the Scattering of Plane Waves from a Binary Conducting Grating," IEEE Trans. on Antennas and Propagation, Vol. 37, 901-917, July 1989.
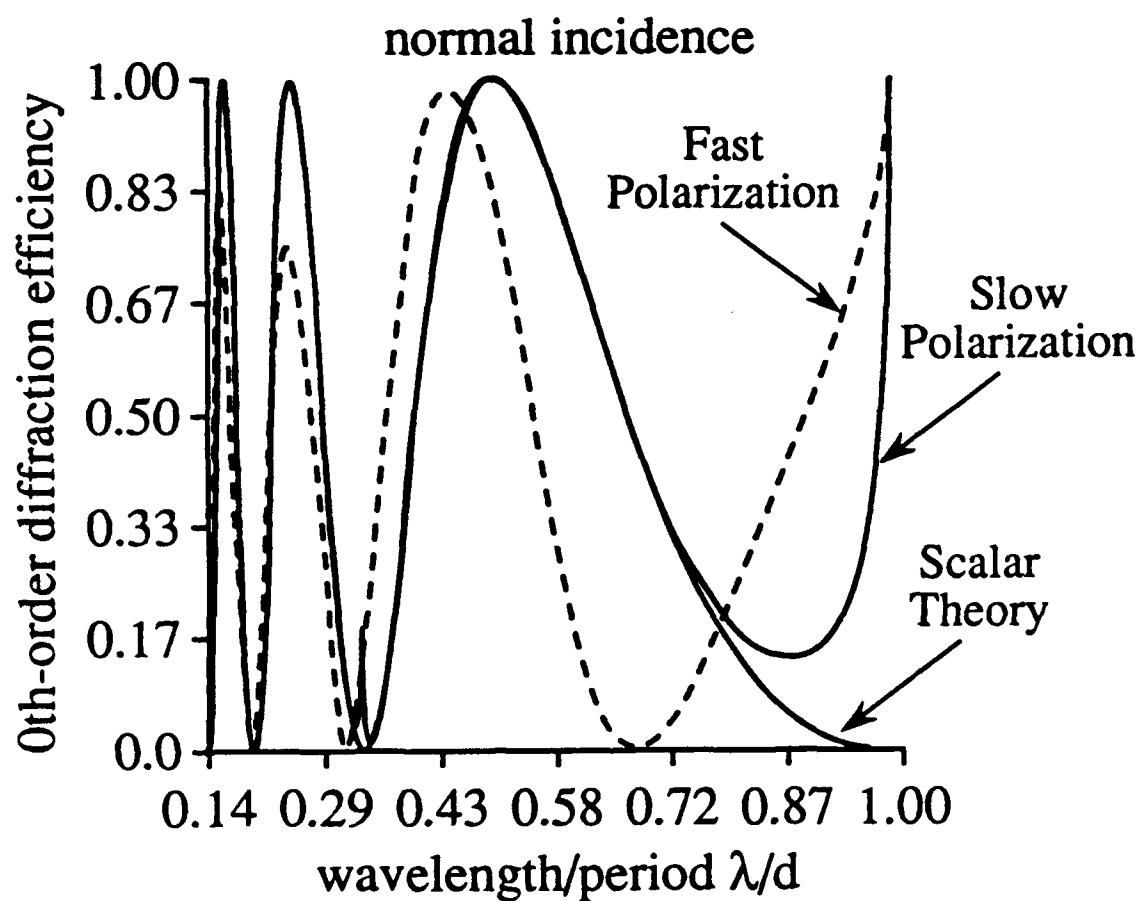
Fig. 1. Zero order diffraction efficiency calculations. The dashed line is the fast polarization 0 order diffraction efficiency, the solid line that approaches one for $\lambda/d=1$ is the slow polarization case, and the other solid line is the scalar solution.

Diffraction Efficiency of a Grating as a Function of the State of Polarization of Incident Light

R. M. A. Azzam

Department of Electrical Engineering
University of New Orleans
Lakefront, New Orleans, Louisiana 70148
[Tel. (504) 286-6181]

For light of a given wavelength incident on a grating in an arbitrary orientation the distribution of light among the various (reflected and/or transmitted) diffracted orders depends on the incident wave polarization. Such polarization effects of gratings, first discovered by Fraunhofer[1], require a full electromagnetic approach[2] for their explanation.

In this paper the diffraction efficiency is considered as a function of the state of polarization (SOP) of the incident light. The diffraction efficiency for a given order is defined as the fraction of power of the incident wave that appears in that order. For that purpose, one can imagine the diffraction grating enclosed in a black box with the incident wave at its input and a diffracted order at its output. The type of grating, its orientation, the wavelength of incident light, and the particular diffracted order need not be specified. The only important assumption is that nonlinear optical effects are absent, so that the grating can be treated as a linear optical system of the general type conceptualized by Jones[3]. To allow for an arbitrary state of (partial elliptical) polarization of the incident light, the SOP is represented by the Stokes vector[4]

$$\underline{S} = [S_0 \ S_1 \ S_2 \ S_3]^t, \tag{1}$$

where t means the transpose. The diffraction of a specific order is represented by a 4x4 scattering Mueller matrix[4] $\underline{M}$, so that the Stokes vector of the diffracted light is

$$\underline{S}' = \underline{M} \ \underline{S}. \tag{2}$$

The intensity (or power) of the diffracted order is the first element of $\underline{S}'$, which from Eq. (2) is given by

$$S'_0 = m_{00} S_0 + m_{01} S_1 + m_{02} S_2 + m_{03} S_3, \tag{3}$$

and m_{00}, m_{01}, m_{02}, and m_{03} are the elements of the first row of $\underline{M}$. From Eq. (3) the polarization-dependent diffraction efficiency is given by

$$f = S'_0 / S_0 \tag{4}$$

$$= m_{00} + m_{01} s_1 + m_{02} s_2 + m_{03} s_3. \tag{5}$$

In a more elegant and revealing form, f can be written as

$$f = f_0(1 + \underline{m} \cdot \underline{s}), \tag{6}$$

$$f_0 = m_{00}, \tag{7}$$

$$\underline{m} = (m_{01}/m_{00}, \ m_{02}/m_{00}, \ m_{03}/m_{00}), \tag{8}$$

$$\underline{s} = (S_1/S_0, \ S_2/S_0, \ S_3/S_0). \tag{9}$$

Equation (6) is a concise expression for the diffraction efficiency as a function of the input polarization-state vector $\underline{s}$ of Eq. (9) in the three-dimensional Stokes-Poincaré space. In that space, $|\underline{s}| = 1$ is the Poincaré sphere, which is the locus of all possible states of total polarization, and $|\underline{s}| < 1$ represents partially polarized light. For incident unpolarized light, $\underline{s} = 0$, and Eq. (6) gives $f = f_0$ as the corresponding diffraction efficiency. f_0 also represents the average value of f integrated over the entire polarization space. An alternate form of Eq. (6) is

$$f = f_0 (1 + m \ s \ \cos\theta) \tag{10}$$

in which $m = |\underline{m}|$, $s = |\underline{s}|$ is the degree of polarization, and θ is the angle between the variable polarization vector $\underline{s}$ and the fixed characteristic grating vector (CGV) $\underline{m}$. The maximum and minimum diffraction efficiencies are given by

$$f_{max} = f_0(1 + m), \qquad f_{min} = f_0(1 - m), \tag{11}$$

and occur when $\underline{s}$ is the unit vector parallel $(\theta = 0)$ and antiparallel $(\theta = 180°)$ to $\underline{m}$, respectively. The two polarizations that produce maximum and minimum diffraction efficiency are in general orthogonal elliptical states that are represented by the opposite points of the diameter of the Poincaré sphere along the straightline extension of the vector $\underline{m}$. For any incident SOP, f is in the range

$$f_0(1 - m) \leq f \leq f_0(1 + m). \tag{12}$$

Because f is always non-negative, $m = |\underline{m}| \leq \ ^\cdot$, which places a constraint on the elements of the first row of the scattering Mueller matrix of any diffracted order.

The loci of polarization states that produce the same diffraction efficiency are determined by setting $\underline{m} \cdot \underline{s} = $ constant in Eq. (6). This represents a family of parallel circular discs orthogonal to the CGV $\underline{m}$ that lie within the Poincaré sphere (PS), Fig. 1.
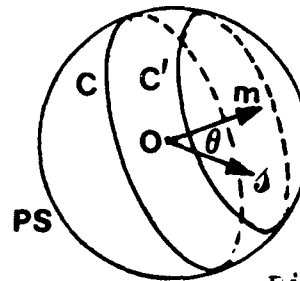
Fig. 1

For any grating in any orientation (relative to the incident light) at any wavelength, the CGV $\underline{m}$ is different for the different diffracted orders. Figure 2 illustrates a case in which four orders appear and their respective CGV's $\underline{m}_i$ (i = 0, 1, 2, 3). The point P_i on the PS represents the total polarization state that maximizes the diffraction efficiency of the ith order. For each P_i, there is a diametrically opposite point Q_i, not shown, that represents the state of minimum diffraction efficiency for the ith order.
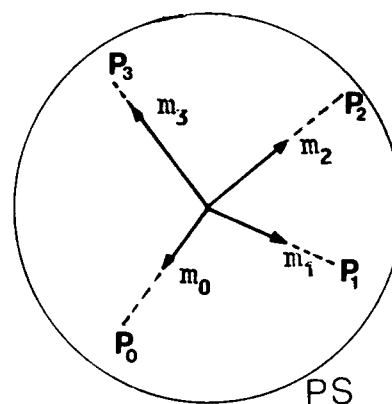
Fig. 2

As an example, consider the zeroth-order diffraction efficiency of an Al-coated 1200 g/mm holographic grating which is set at 65° angle of incidence with the grating lines inclined at 45° with respect to the plane of ˙ ˙dence. The Mueller matrix, normalized with respect to m_{00}, was measured recently[5] at 633-nm wavelength. The associated CGV is $\underline{m}$ (- 0.427, 0.310, - 0.115), from which m = 0.540 (< 1, as expected). The ratio of maximum to minimum diffraction efficiency, (1 + m)/(1 - m) = 3.348, is significant. Finally, the orthogonal elliptical states that produce the maximum and minimum diffraction efficiency are specified by +$\underline{s}$ and -$\underline{s}$, respectively, where $\underline{s}$ = (- 0.791, 0.574, - 0.213).

In summary, the polarization dependence of the diffraction efficiency of an arbitrary grating in a general orientation has been analyzed. It is shown that for any diffracted order the diffraction efficiency has a range of values between a minimum and a maximum. The extrema of the diffraction efficiency, and the orthogonal elliptical states that produce them, are determined.

References

1. C. F. Meyer, The Diffraction of Light, X-Rays, and Material Particles (J. E. Edwards, Ann Arbor, Michigan, 1949), pp. 136-137.

2. M. G. Moharam and T. K. Gaylord, JOSA 73, 1105 (1983).

3. R. C. Jones, JOSA 37, 107 (1947).

4. See, e.g., R. M. A. Azzam and N. M. Bashara, Ellipsometry and Polarized Light (North Holland, Amsterdam, 1987).

5. R. M. A. Azzam, K. A. Giardina, and A. G. Lopez, Opt. Eng. 30, 1583 (1991).

Solution to the Multiple Grooves Scattering Problem--
The Fast Polarization Case

Yon-Lin Kok, University of South Alabama, Department of Electrical Engineering, Mobile, AL 36688

The problem of electromagnetic scattering by a perfectly conducting grating has been extensively studied in the field of antennas and optics. Most of the solution forms of the Fourier series type are derived with the assumption that grating structures extend in space with an infinite periodicity. In this paper a much more practical model of the grating structure is introduced for the first time to the field of diffractive optics. The model is given as follows: A finite number of rectangular grooves of arbitrary width and depths are arbitrarily spaced and corrugated into a perfectly conducting plane forming a grooves array with an aperiodic geometry.

The vector-field diffraction theories are exploited to develop an exact formulation of the scattered fields both above the grating plane and inside the groove corrugations. For the simplicity of presenting the solution techniques, only the fast polarization scattering geometry is discussed in this paper. The field inside the groove is expressed as the sum of all the rectangular waveguide modes. For example, the z-component of electric field in the n-th groove can be written as the following:

$$E_z(x,y) = \sum_{m=1}^{\infty} a_{n,m}\sin[A_{n,m}(y+h_n)]\sin[\frac{m\pi}{c_n}(x+\frac{c_n}{2})], \quad for \ 0 \le |x-d_n| \le c_n/2, \tag{1}$$

The fields in the half-space region above the groove is expressed in terms of a Fourier integral with an unknown angular spectrum $r_f(u)$.

$$u(x,y) = \exp[i(\alpha_0 x - \beta_0 y)] + \int_{-\infty}^{\infty} r_f(u)\exp[i\sqrt{k^2-(2\pi u)^2}y]\exp(2i\pi ux)du , \tag{2}$$

With a novel use of the mathematical properties of the cylindrical Bessel functions, I have been able to expand this angular spectrum function in a series form :

$$r_f(u) = \sum_{n=1}^{N} \sum_{m=1}^{\infty} c_{n,m} \frac{J_m(\pi c_n u)}{u} - \delta(u - \frac{\alpha_0}{2\pi}) \quad, \tag{3}$$

This formulation provides a *modal* expression of the fields in its spatial-frequency domain and leads to an analytic representation as the Fourier integral can be evaluated in terms of the method of steepest descent. Although not rigorously proved to be convergent yet, the computation of the Fourier integral shows good numerical stablility for solutions from the far to the near fields and from the low to the high frequency regions. To obtain the modal coefficients, $\{c_{n,m}\}$, the continuity of the tangential electric and magnetic fields must be enforced in each of the groove apertures, which then results in a system of linear equations of the order of N^2 where N is the truncation number for the index m in equation (3). This algebraic problem can be solved using some existing computer library subroutines.

On the other hand, It is interesting to find that this N^2 by N^2 characteristic matrix $\overline{M}$ consists of N^2 Jordan blocks, each describing the coupling effect between the corresponding pair of grooves. If we define

$$\overline{M} = \overline{M}_d + \overline{F} \tag{4}$$

where $\overline{M}_d$ contains only the diagonal Jordan blocks and $\overline{F}$ has null blocks along the diagonal, and

$$C = [c_{1,1}, \ c_{1,2}, \dots, \ c_{1,N},$$
$$c_{2,1}, \ c_{2,2}, \dots \ c_{2,N}, \tag{5}$$
$$\dots$$
$$c_{N,N}, \ c_{N,2}, \dots \ c_{N,N}]^t \quad,$$

then

$$\underline{C} = \lim_{i \to \infty} \frac{\left\{ I - [\overline{M_d}^{-1}(-\overline{F})]^{i+1} \right\}}{\left[I - \overline{M_d}(-\overline{F}) \right]} \underline{C}^0 \tag{6}$$

where $\underline{C}^0$ is the superposition of N solutions resulted from N respective single groove scattering problems. This is important because the problem complexity may be reduced to the order of N when the multiplication factor to $\underline{C}^0$ in equation (6) approaches to the identity matrix in the limit that index i goes to infinity. Computer simulation shows that this effect is significant when the groove width is in the neighborhood of half wavelength and it is not sensitive to the groove-to-groove spacing.

To predict the diffracted-field patterns in the radiation-zone with respect to the origin on the ground plane, contour integration and Watson transform are utilized to convert the original eigenvalue series into a radially fast converging, asymptotic series (for large values of kr, where k is the effective wave number and r is the radial distance in polar coordinates) so that only N leading terms (e.i. $c_{n,1}$, n=1,2,...,N) in the two-dimensional series are dominant and adequate to provide the approximation. The far-zone field patterns can therefore be obtained. Computer simulation shows that the continuous spectrum of the scattered field becomes more and more discretized as the number of grooves increases. This is consistent with results obtained using the conventional model of infinite periodicity in gratings where an infinite number of discrete diffraction orders exist. In the other limiting case where the groove depth approaches zero, the solution converges to the simple result that can be verified by the theory of physical optics.

On the Convergence of the Coupled-Wave Approach for Lamellar Diffraction Gratings

Lifeng Li and Charles W. Haggans

Optical Sciences Center, University of Arizona, Tucson, AZ 85721. Phone: (602) 621-1789

I.   INTRODUCTION

Among the many existing rigorous methods for analyzing diffraction of electromagnetic waves by diffraction gratings, the coupled-wave approach[1] stands out because of its versatility and simplicity. It can be applied to volume gratings and surface relief gratings, and its numerical implementation is much simpler than others. In addition, its predictions have been experimentally validated in several cases[2-4]. These facts explain the popularity of the coupled-wave approach among many optical engineers in the field of diffractive optics. However, a comprehensive analysis of the convergence of the model predictions has never been presented, although several authors[5,6] have recently reported convergence difficulties with the model when it is used for metallic gratings in TM polarization.

In this short paper, we will make three points: *(1) In the TM case, the coupled-wave approach converges much slower than the modal approach of Botten et al.[7,8]. (2) The slow convergence is caused by the use of Fourier expansions for the permittivity and the fields in the grating region, and (3) is manifested by the slow convergence of the eigenvalues and the associated modal fields.* The reader is assumed to be familiar with the mathematical formulations of the coupled-wave approach and the modal approach.

II.   ANALYSIS

a.   Two Types of Modal Approaches

There are two types of modal approaches: Modal Approach using a Scalar (characteristic) Equation[7,8] (MASE) and Modal Approach using a Matrix (characteristic) Equation[9] (MAME). *The coupled-wave approach (CWA) is equivalent to a MAME.* In the MASE, the eigenvalues and modal fields in the grating region are solved one at a time from a scalar characteristic equation. Each modal field thus found satisfies Maxwell's equations and the boundary conditions exactly. In the MAME, however, N eigenvalues and modal fields are solved simultaneously from a matrix characteristic equation. Unless $N = \infty$, none of these modes satisfies Maxwell's equation exactly.

b.   Two Kinds of Infinities

When solving grating problems by any method, one always has to deal with two kinds of infinities: the infinity of the discrete set Z (the set of all integers), and the infinity of the continuum $[0,d)$, where d is the grating period. The first infinity is due to the periodicity of the grating, which generates an infinite number of diffraction orders. The second infinity is related to the continuous nature of Maxwell's equations. In any method, one has to solve Maxwell's equations on $[0,d)$, with the pseudo-periodic boundary condition. In the MASE, the infinity of $[0,d)$ is handled analytically. The infinity of Z is not truncated until the matching of boundary conditions at the interfaces between uniform regions and corrugated region is completed. In the MAME, the infinity of Z is handled similarly. However, the infinity of $[0,d)$ is transformed into that of the coefficients of the Fourier expansions, which happens to be degenerate with the infinity of the diffraction orders. *It is this tempering of the infinity of* $[0,d)$ *that leads to the slow convergence of the CWA.*

c.   Two Convergence Processes

In the CWA, the permittivity of the periodic medium in the grating region is represented by its Fourier expansion. When this infinite expansion is truncated, *the physical problem is changed (*the original discontinuous permittivity is changed to a smooth-varying one). Hence, both the electromagnetic field and the grating profile are approximated as a result of the truncation. This means that the convergence of the diffraction efficiency and phase values relies on the convergence

of both the modal fields and the permittivity representation.

d. *The Convergence Rates of Related Fourier Series*

The analysis above indicates that the CWA, or the MAME in general, should be expected to converge slower than the MASE. This point is reinforced by the following asymptotic analysis of the Fourier coefficients for the permittivity and the fields. Let the permittivity be $\epsilon(x+d) = \epsilon(x)$, $\epsilon(x) = \epsilon_1$, $|x| < a$, and $\epsilon(x) = \epsilon_2$, $a < |x| < d/2$. It is easy to check that $c_n = O(n^{-1})$ as $n \to \infty$, where c_n is a Fourier coefficient of $\epsilon(x)$. Evidently, the convergence of the permittivity expansion is very slow.

We now consider the Fourier expansion coefficient, f_n, of the fields. For TE polarization, the boundary conditions demand that both the electric field and its derivative be continuous at the permittivity discontinuity. Consequently, $f_n = O(n^{-3})$, as $n \to \infty$. For TM polarization, the magnetic field is continuous, but its derivative is not. Instead, we have $\epsilon_1^{-1}(dH/dx)|_{x-\pm a \pm 0} = \epsilon_2^{-1}(dH/dx)|_{x-\pm a \pm 0}$; therefore, $f_n = O(n^{-2})$, as $n \to \infty$. Hence the Fourier expansion for a TM field converges slower than that for a TE field. Next, suppose $\epsilon_1 = 1$, and the polarization is TM. For a lossless dielectric grating, ϵ_1 and ϵ_2 are both positive; while for a metallic grating, ϵ_1 and ϵ_2 have different signs, if the small imaginary part of ϵ_2 is neglected. Accordingly, the H-field at the permittivity discontinuity in a dielectric grating is "smoother" than it is in a metallic grating. In other words, the H-field has weaker high frequency components in a dielectric grating than it has in a metallic grating. The analysis above rationalizes why the CWA converges slower for TM polarization than for TE polarization, and why it converges slower for metallic gratings than for dielectric gratings.

e. *Eigenvalues and Modal fields*

The difficulty in the analysis of gratings lies in the accurate characterization of the fields in the grating region. For modal approaches of both types (including the CWA), this means that *it is imperative to determine the eigenvalues accurately* because it is trivial to determine the modal fields once the eigenvalues are known. In the CWA approach, the eigenvalues are solved from the characteristic matrix equation, which is obtained from the truncated and slowly converging Fourier expansions of the permittivity and the fields. Thus, the convergence of the eigenvalues is slow, as numerically demonstrated in the next section.

III. NUMERICAL EXAMPLES

Let us arbitrarily choose a fixed groove depth to wavelength ratio, say $d/\lambda = 1$, from Fig. 3 of Ref. 5 (a gold lamellar grating). We examine how the diffraction efficiencies and the eigenvalues converge with the CWA and with the MASE. Our numerical implementation of the CWA is based on the third paper in Ref. 1. The truncated matrix ϵ_{mn}^{-1} is obtained by numerically taking the inverse of ϵ_{mn}, as recommended by Moharam and Gaylord[10]. Our numerical implementation of the MASE is based on Refs. 7 and 8. Both computer programs have been thoroughly checked against the available results in the literature and against each other. In the following, N denotes the total number of space-harmonics retained in the computations. For the results of the MASE, the number of modal fields is set to equal N.

Figs. 1a and 1b show the convergence of diffraction efficiencies as N increases for TE and TM polarizations. For both polarizations, the MASE converges extremely fast. For TE polarization, the CWA converges reasonably fast toward the MASE. For TM polarization, however, the CWA converges very slowly toward the MASE; in fact, it does not begin converging until $N > 40$.

Figs. 2a and 2b show the convergence of the real and imaginary parts of the square of the tenth TE eigenvalue and the ninth TM eigenvalue, respectively. Similar to the convergence of diffraction efficiencies, the TE eigenvalue computed with CWA converges reasonably fast toward that computed with the MASE (dashed-lines), but the TM eigenvalue converges very slowly. We should mention that all the TE eigenvalues computed with CWA converge at a rate similar to that in Fig. 2a, and some of the TM eigenvalues do converge faster than the one shown in Fig. 2b.
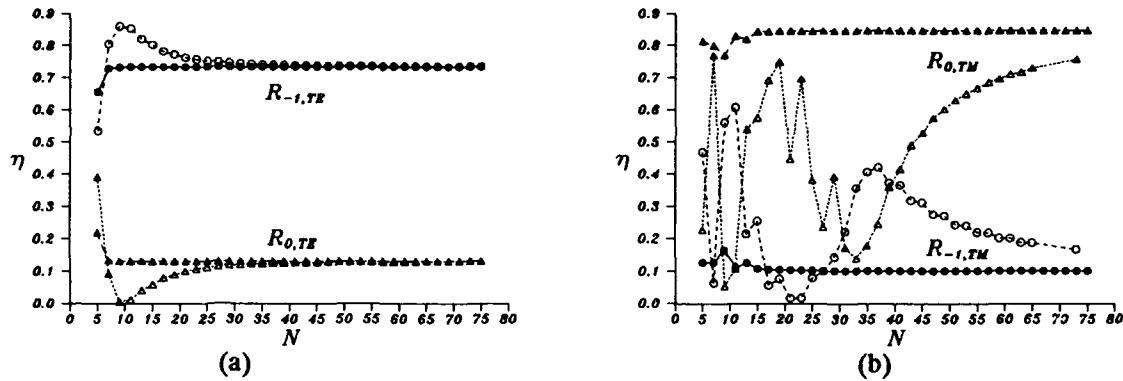
Fig. 1. Convergence of diffraction efficiencies. Solid symbols, MASE. Open symbols, CWA.
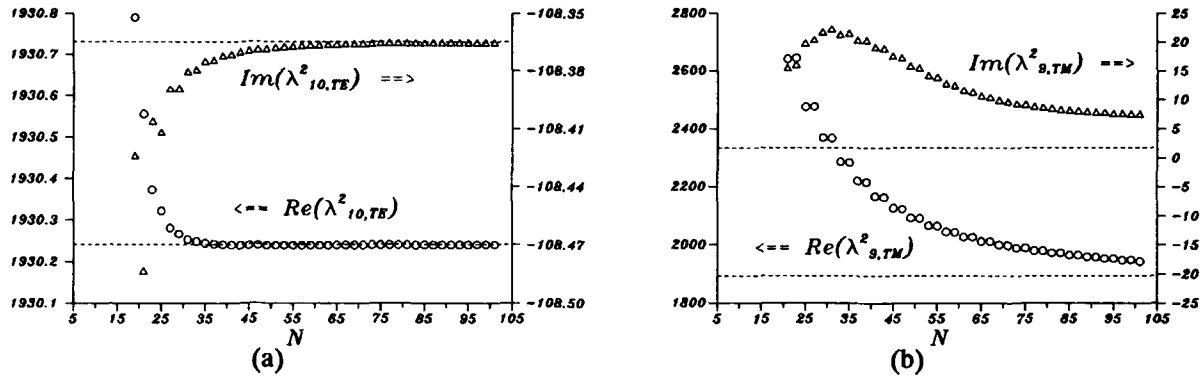
Fig. 2. Convergence of eigenvalues computed with coupled-wave approach.

IV. CONCLUSIONS

We have demonstrated with numerical examples that the predictions of the CWA converge slowly toward those of the MASE of Botten *et al.* for metallic gratings in TM polarization. We have shown that the slow convergence is caused by the use of slowly convergent Fourier expansions for the permittivity and the fields in the grating region. *Despite its popularity, versatility, and simplicity, the coupled-wave approach should be used with caution for metallic surface relief gratings in TM polarization.* Although we have only compared the CWA with the MASE, much of the analysis applies to the MAME and differential methods utilizing Fourier expansions in general.

Li's work is supported by the Optical Data Storage Center at the University of Arizona. Haggans' work is supported by IBM SUR-0499 and a graduate fellowship from Itek Optical Systems.

V. REFERENCES

1. M. G. Moharam and T. K. Gaylord, JOSA, 72, 1385(1982), 73, 451(1983), and 73, 1105(1983).
2. M. G. Moharam *et al.*, Appl. Opt., 23, 3214(1984).
3. T. Schimert and R. Magnusson, JOSA, A9, 1719(1990).
4. C. W. Haggans and R. K. Kostuk, SPIE 1499, 293(1991)
5. M. G. Moharam and T. K. Gaylord, JOSA, A3, 1780(1986).
6. C. W. Haggans *et al.*, paper submitted to JOSA.
7. L. C. Botten, *et al.*, Optica Acta, 28, 413(1981), 28, 1087(1981), and 28, 1103(1981).
8. J. Y. Suratteau, *et al.*, J. Optics (Paris), 14, 273(1983).
9. C. B. Burckhardt, JOSA, 56, 1502(1966).
10. Personal communication on November 8, 1991.

Fabrication Technologies 2

TuC 2:00pm–3:30pm
Cabildo Room

James R. Leger, *Presider*
University of Minnesota

LASER TECHNOLOGIES OF DIFFRACTIVE ELEMENT SYNTHESIS FOR MASS-APPLICATION OPTICAL SYSTEMS

V.P.Koronkevich

Institute of Automation and Electrometry, Russian Academy of Sciences, Siberian Branch

630090 Novosibirsk, Russia

Raster scanning with a laser image generator operating in a polar coordinate system is applied for recording of an arbitrary-topology diffraction structure [1]. The synthesis technology of element masks is based on the effects of thermo-chemical modifications in thin metal films (chromium, 100-200 nm thick). Nanosecond-pulse radiation causes the growth of an oxide layer, its etching rate being many times lower than the etching rate of chromium. It allows one to carry out negative recording of a mask structure [2]. The pattern transfer into glass and formation of a binary, multilevel and continuous profile is performed by means of photolithography methods [3].

Half-tone or binary microimages can be formed in thin films (100 nm) of amorphous silica. Optical recording is based on solid-phase transition of silica from amorphous state into polychrystal one. Radiation-induced transparency of the film takes place. The transmission spectrum is shifted to the short-wavelength range. The pattern is formed during the recording process with no consequent chemical processing. The spatial resolution of the pattern is over 2000 lines/mm.

The technology developed provided the fabrication of a series of diffraction elements for projective and caustic transformations, and optical schemes of new devices and system were worked and on this basis.

In the diffraction interferometer a spot at the input is transformed in the image area into a light line being the focus of non-localized Fresnel pattern. The fringes can be observed at distances over 100 m (Fig.1). Under illumination by a parallel monochromatic beam "shadow" fringes appear (Fig.2). The interferometer consists of a single diffraction element and is substituted for three refractive components: a positive lens a negative one, and a

Fig. 1.
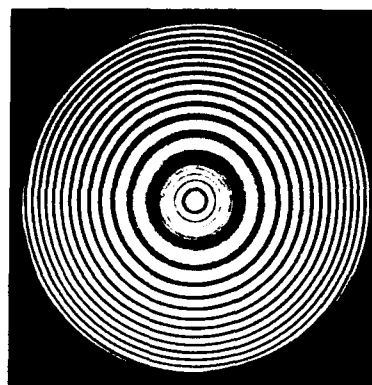
Fig. 2.

conc. It was applied for rectlinearity checking of side plates, levelling, centering,and shape checking of objects with the method of "light section".

In the high-aperture microlens ($u = 0,55, \lambda = 0,78$ mm) for information readout from magnet-optical disks a scheme was performed consisting of diffraction corrector and a flat - convex refraction lens made of hard glass. Experimental tests of the microlens confirmed the calculation correctness. A spot of 1,6 mm was produced in the image plane.

Application of diffraction optics for the design of a laser player pickup required to reconsider the concept of the optical scheme. The pickup we proposed [4] consists of two main elements: laser diode and a glass plate with a diffraction lens and a ring-shaped photo receiver on one of its sides. The high light energy efficiency is achieved

by means of spatial separation of the channels for disk illumination and for information readout. Such pickup is not inferior in size and mass to an integrated one.

Diffraction circular scales were developed for angle-code sensors. The limb strobes were carried out as binary or kinoform gratings. The gratings deflect light in the plane normal to the movement direction of the scale. It provides an auxiliary degree of freedom and increases the readout reliability of measurement information.

The optical system of the sensor is based on Littrov autocollimation scheme, and for increase in light efficiency the range is chosen of abnormal wood diffraction. In reflected-light operation the scale diffraction efficiency approaches 100%. The dynamic method for scale fabrication provided the accuracy of stroke positioning equal to $\pm 2''$ [6].

For domestic lamps glasses were developed with hexagonal binary and harmonic gratings. The artistic effect originates from multiplication and spectral decomposition of the image of a glow-lamp filament. Commercial samples of the lamps were manufactured.

REFERENCE

1. V.P.Koronkevich, A.G.Poleshchuk et al "Fabrication of kinoform optical elements." Optik,67,N 3,259-266 (1984).

2.V.P.Koronkevich,A.G.Poleshchuk,E.G.Churin and Yu.I.Yurlov "The laser thermochemical technology for synthesis of diffraction optical elements on chromium films". Kvantovaya Elektronika ,12, N 4,755-761 (1985).

3. V.P.Koronkevich, "Computer synthesis of diffraction optical elements". Optical Processing and Computing, Academic Press(1989).

4. V.P.Koronkevich, I.G.Palchikova, A.G.Poleshchuk, "Data readout from compact disks with the use of a diffraction-optic laser pickup". Kvantovaya Elektronika, 15, N 10, 2128-2134 (1988).

5. A.G.Sedukhin, " Diffraction reticules : the capabilities of novel optical components for displacements or distance measurement ", Optik, 85, N 2, 47-52 (1990).

6. A.G.Sedukhin, "On improving the spectral properties of diffraction gratings provided by scanning method of ruling", Optik, 86, N 4, 135-140 (1991).

Efficient Beamsplitters and Beam Deflectors
for Integrated Planar Micro-optics

S. J. Walker[1], J. Jahns[1], N. K. Ailawadi[2], W. M. Mansfield[3],
P. P. Mulgrew[1], J. Z. Pastalon[1], C. W. Roberts[1], and D. M. Tennant[1]

AT&T Bell Laboratories
[1] Crawfords Corner Road, Holmdel, NJ 07733
[2] Laurel Avenue, Middletown, NJ 07748
[3] Mountain Avenue, Murray Hill NJ 07974
(908)-949-2125

SUMMARY

Diffraction gratings are of wide interest in integrated planar micro-optics to provide beamsplitting, multi-beam generation, beam deflection, beam focussing, and anti-reflection properties. Applications for integrated planar microoptics include; imaging[1], clock distribution[2], computing and switching systems. By using lithographic and etching techniques, multiple micro-optic elements can be integrated on a single substrate with submicron positioning accuracy. By using through wafer alignment, elements can be positioned on the substrates top and bottom surfaces. This allows the signal to travel within the substrate, in a zig-zag fashion, from one element to the next (see fig. 1). This approach is attractive because it provides a stable compact system compared to discrete bulk optics.

The purpose of this paper is to present high frequency gratings with two and multiple phase levels for providing high efficiency beam splitters and beam deflectors. When integrating many optical elements, high efficiency elements are essential for the system's overall performance. For example, figure 2 demonstrates a system that splits a single input beam into four equal intensity beams and distributes them to four equally space destinations. This is of interest in applications such as an optical clock distribution system. The input signal
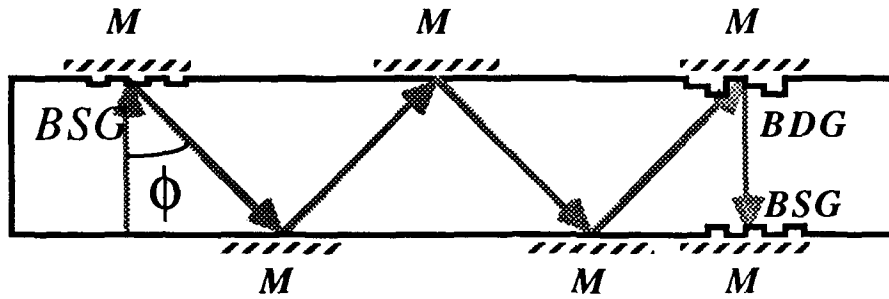
Figure 1: Sideview of an integrated planar microoptic system.

is split by beamsplitter gratings (BSG), reflected by mirrors (M), and deflected by beam deflector gratings (BDG) . In this particular example, it is feasible to achieve better than 1x64 distribution if high efficiency BSG, BDG , and M are used. Theoretically, BSG and BDG with efficiencies > 90 % can be achieved using high frequency and multi-phase gratings and mirrors with reflectivities > 95% can be achieved using the appropriate metallic coating.

The efficiency enhancement provided by high frequency gratings is explained by the fact that higher diffraction orders become evanescent. For a regular binary phase grating with a π phase shift, light is coupled into the ± 1 diffraction orders. For relatively coarse periods, higher orders will carry away light energy and approximately 81% will go to the two first orders. However, if the period of the grating is reduced, the diffraction angle of the higher m-th orders will increase according to the grating equation; $\phi_m = \sin^{-1}[m\lambda/(np)]$, where λ is the wavelength of light, n is the medium's refractive index, and p is the grating period. For periods $p < 2\lambda/n$, all higher orders will exceed 90 degrees, become cut off (evanesce), and transfer their power to the remaining orders. For a grating with a mark to space ratio of 1:1, the even orders are suppressed, particularly the second orders. Therefore, for a grating to produce only the ± 1 orders, it is only necessary that the grating has a period of $\leq 3\lambda/n$.

The efficiency of deflector gratings can be enhanced by using more than two phase levels. For a grating with a regular staircase profile and L phase levels, only every L-th order will exist. By combining this with the evanescence effect of high frequency gratings one can
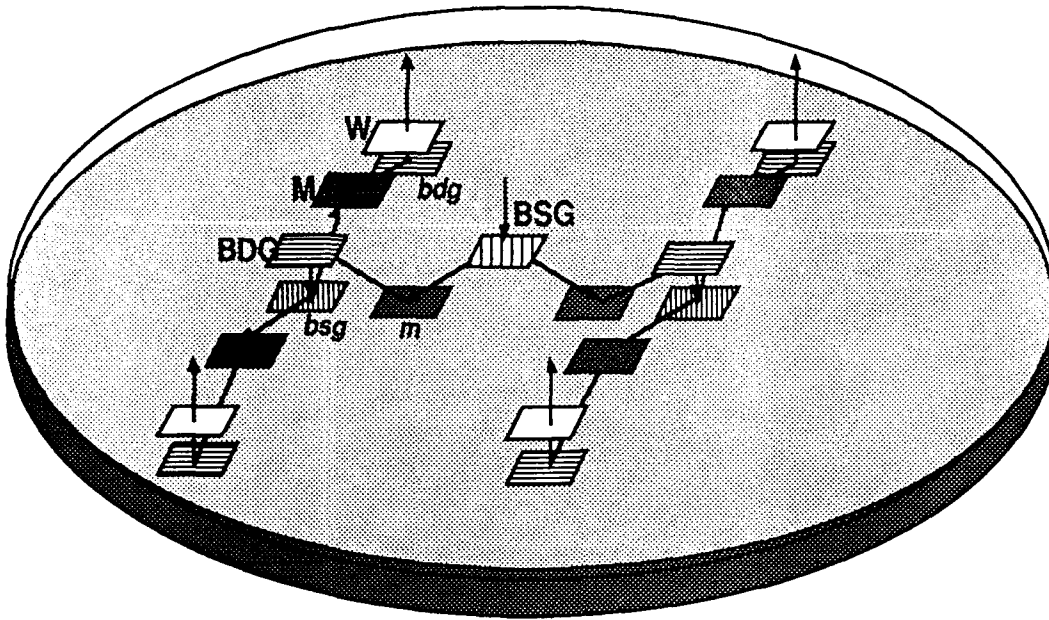
Figure 2:   1x4 distribution system using integrated planar microoptics. The upper case letters represent elements on the top surface and the lower case letters represent elements on the bottom surface of the substrate.

maximize the signal that is diffracted to the first order. The condition necessary to have all the higher orders evanesce is $p < (L-1) \lambda/n$.

The fabrication of the gratings consist of lithographic and etching techniques. The processing parameters are optimized to provide straight side walls, precise step heights, and precise step widths. Reactive ion etching is used to fabricate our gratings in silicon, glass, and GaAs. Both photo resist masks and tri-level masks have been used as our protective layer. The pattern transfer has been done using computer generated electron-beam exposure masks and contact lithography. Experimentally, we have achieved BSG with 98 % efficiency and BDG with 90 % efficiencies. To overcome feature size limitations, reduction stepper techniques and e-beam direct writes techniques are being used as well.

REFERENCES

1   J. Jahns and A. Huang, "Planar integration of free-space components," *Appl. Opt.* **28** (1989) 1602-16052.

2.   S. J. Walker and J. Jahns, "Optical Clock Distribution using Integrated free space optics," *Proceedings of the Opt Soc. Amer.* Optcon meeting (1990).

Simultaneous and Sequential Recording of Holographic Fan-Out Elements

H. P. Herzig, P. Ehbets, D. Prongué, R. Dändliker

Institute of Microtechnology, University of Neuchâtel, Rue A.-L. Breguet 2,
CH-2000 Neuchâtel, Switzerland Phone: +41 38 20 51 21

Introduction

Binary phase gratings, also called Dammann gratings, represent a successful technique to fabricate fan-out elements with good uniformity of the generated array of beams, but moderate efficiency (60 - 70 %). Multilevel phase gratings [1], or smooth surface relief structures [2] have been investigated yielding improved diffraction efficiencies (> 90 %). However, proper modulation at large carrier frequencies (> 1000 lines/mm) is difficult to achieve by mask projection or laser beam writing. Therefore, interferometrically recorded holograms are still of interest for realizing off-axis elements and large fan-out numbers. This paper deals with simultaneous and sequential recording of efficient fan-out elements in thick volume holograms. We have applied coupled wave theory to the special problem of regular fan-out elements.

Simultaneous recording

In the case of simultaneous recording of a fan-out element, N object waves and one reference wave are present at the same time. The waves are characterized by their wavevectors k_i, amplitudes A_i, and phases ϕ_i, where $i = 0$ denotes the reference beam (Fig. 1). Besides the desired N primary gratings $K_{0i} = k_0 - k_i$, $N(N - 1)/2$ unwanted intermodulation gratings $K_{pq} = k_p - k_q$ are recorded. At readout, they generate intermodulation waves, which are coupled with the desired
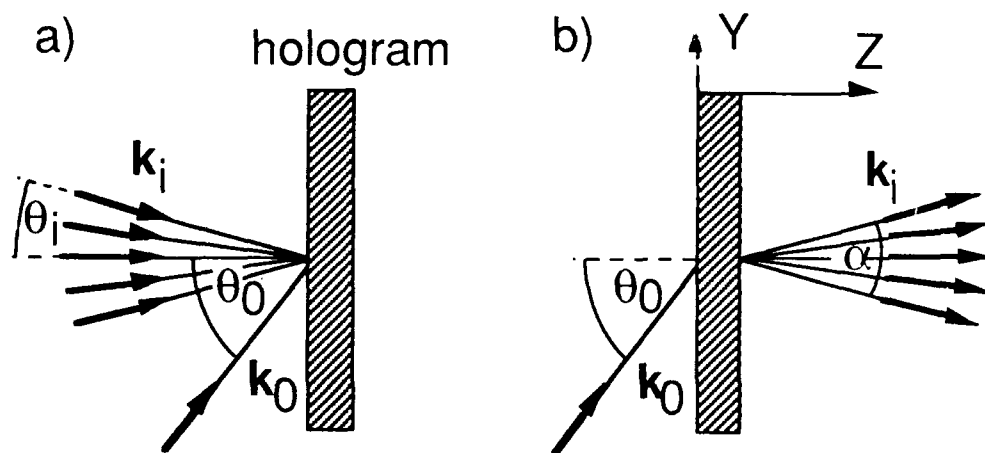

Fig. 1. (a) Recording and (b) readout of holographic fan-out elements. The angles are defined inside the recording medium with refractive index n, α is the full fan-out angle.

reconstructed beams through the primary gratings K_{0i}. For small interbeam angles $\Delta\alpha$, these interactions are only slightly off-Bragg. As a consequence the diffraction efficiency and the uniformity of the fan-out are reduced. In addition, at recording the intermodulations produce a spatially variable irradiance of the object wave field, which requires a large dynamic response of the recording material.

It turns out, that efficiency and uniformity of regular fan-outs depend strongly on the relative phases of the N object waves [3], if the thickness of the holographic emulsion is less than

$$t = \lambda/(n \tan\theta_0 \Delta\alpha), \tag{1}$$

where $\Delta\alpha = \alpha/(N-1)$ is the angle between two neighboring beams. We obtain $t = 32 \ \mu m$ for the following typical parameters: wavelength $\lambda = 488$ nm, refractive index $n = 1.5$, reference beam angle $\beta = 30°$ and interbeam angle $\Delta\alpha = 1°$.

High efficiency (> 90 %) and uniformity (< 5 %) can be achieved by optimized phases of the object beams, so that only a low dynamic range of the holographic material is required.

Sequential recording

In sequential recording of N object beams, N subsequent exposures to each object beam and the reference are required. The advantage of this method is the absence of intermodulation gratings formed by the mutual interference of the object beams. According to theoretical results obtained by coupled wave theory, sequentially recorded fan-out elements should have a slightly higher efficiency than those obtained by simultaneous recording, namely close to 100 %. However, the control of the object phases is also required for a hologram thickness less than $t = \lambda/(n \tan\theta_0 \Delta\alpha)$, see Eq. (1).

A major drawback of sequential recording is that the exposure energy for the same diffraction efficiency is higher than for simultaneous recording. We have found a factor of $\sqrt{N}/2$ in the case of optimized phases. The maximum number of fan-out beams is then limited by the dynamic range of the holographic material.

Beside controlling the object phases, material properties may be responsible for the poor diffraction efficiencies reported in the literature (e.g. [4]). For silver halide materials the linearity assumed at recording is not satisfied for sequentially recorded holograms [5]. These effects have not been observed in dichromated gelatine holograms, thus high efficiency should be possible.

Experimental results and discussion

An array of object beams with optimized phases can be generated with the aid of a computer-generated hologram (CGH). The CGH is in our case a binary amplitude grating with a carrier frequency of 125 lines/mm, which has been fabricated by e-beam lithography. The phase distribution of the CGH has been calculated according to Ref. 2. The CGH is then imaged onto the hologram plane through a standard 4-f lens system. The desired N object beams with optimized phases are contained in the first diffraction order of the CGH. The higher orders have been

filtered. Note, that an incorrect filtering may strongly disturb the fan-out properties of the recorded hologram. A more detailed analysis of the spatial filtering is found in Ref. 6.

N = 9 object beams have been recorded in dichromated gelatine (DCG) at the wavelength $\lambda = 488$ nm. We have chosen a reference beam angle of $\theta_0 = 30°$ and an interbeam angle of $\Delta\alpha = 0.057°$, which yields a spacing of 100 μm at a distance of 100 mm.

Fig. 2. Readout of the holographic fan-out.

Figure 2 shows the readout of the holographic fan-out element in the case of **simultaneous recording**. The measured uniformity error was found to be ±5 % and for the overall diffraction efficiency we have obtained 84 %. Note, that 10 % of the light is already lost due to reflections at the surfaces and absorption in the medium.

In the case of **sequential recording** we have used the same recording set-up, but only two beams at the time, the reference and one of the object beams. The highest overall diffraction efficiency was measured to be 73 % while the uniformity error was ±19 %.

The experimental results for sequential recording are inferior to those obtained by simultaneous recording. We assume, that the phase relationship during the 9 recording steps could not be controlled sufficiently well. Higher efficiency, close to the theoretical results, can be expected from an improved recording system.

References

[1] S. J. Walker, J. Jahns, "Array generation with multilevel phase gratings," J. Opt. Soc. Am. A. **7**, 1509-1513 (1990).

[2] H. P. Herzig, D. Prongué, R. Dändliker, "Design and fabrication of highly efficient fan-out elements," Jpn. J. Appl. Phys. **29**, L 1307-L 1309 (1990).

[3] H. P. Herzig, P. Ehbets, D. Prongué, R. Dändliker, "Fan-out elements by multiple beam recording in volume holograms," Proc. SPIE **1507**, 247-255 (1991).

[4] C.W. Slinger, R. R. A. Syms, L. Solymar,"Multiple holographic transmission gratings in silver halide emulsion," Appl. Phys. B **28**, 121-128 (1987).

[5] K. M. Johnson, L. Hesselink, J. Goodman, "Holographic reciprocity law failure," Appl. Opt. **24**, 4467-4471 (1985).

[6] B. Robertson, J. Turunen, H. Ichikawa, J. M. Miller, M. R. Taghizadeh, A. Vasara, "Hybrid kinoform fan-out holograms in dichromated gelatin," Appl. Opt. **30**, 3711-3720 (1991).

Design and Fabrication of Resonance Domain Diffractive Optical Elements

J. Michael Miller

Department of Physics, Heriot-Watt University, Riccarton, Edinburgh EH14 4AS, UK

Eero Noponen and Antti Vasara

Department of Technical Physics, Helsinki University of Technology, 02150 Espoo, Finland

Jari Turunen and Mohammad R. Taghizadeh

Department of Physics, Heriot-Watt University, Riccarton, Edinburgh EH14 4AS, UK

The design of computer generated diffractive optical elements has traditionally relied upon Fourier optics [1], i.e. the Fresnel or Fraunhofer diffraction theories encompassing the paraxial approximation. Fourier optics, however, is not valid if the surface relief profile contains transverse features that are less than an order of magnitude larger than the incident wavelength. In this regime, non-paraxial theories based on Kirchhoff boundary conditions should be used [2]. Even these theories fail in the resonance domain where, by definition, features of the order of one wavelength are critical [3], and so rigorous electromagnetic theory is required. The fabrication of such resonance domain diffractive optical components is becoming more plausible with the development of microlithographic fabrication technology, which can already achieve sub-micron features with a positional accuracy of about 0.1 μm.

So far, the analysis of resonance domain elements has been largely restricted to gratings with one strong diffraction order, e.g. for use in spectroscopy. We have used the electromagnetic theory to analyze gratings that utilize several orders [4], and taken preliminary steps to enhance, by resonance-domain design, the performance of some Fourier domain diffractive elements [5]. Here, this approach is carried out further. We optimize 1 to $\mathcal{N}$ fanout gratings and $\mathcal{N}$ to $\mathcal{N}$ star couplers, and resonance domain components that cannot be represented in Fourier optics, i.e. polarization dependent optical switches.

In defining the generalized synthesis and design problem we consider the binary lamellar grating structure of Fig. 1, with the index modulated volume $-H \leq z \leq 0$ containing J grooves per period (length d). Treating TE and TM polarizations separately [3] the reflected and transmitted fields generated by Q mutually uncorrellated incident plane waves may be expressed as Rayleigh expansions ($q = 1, \ldots, Q$)

$$U_{R,q}(x, z) = \sum_{m=-\infty}^{\infty} R_{m,q} \exp[i(\gamma_{m,q} x - r_{m,q} z)]$$

$$U_{T,q}(x, z) = \sum_{m=-\infty}^{\infty} T_{m,q} \exp[i(\gamma_{m,q} x + t_{m,q} z)],$$

where $\gamma_{m,q} = k_q n_0 \sin\theta + 2\pi m/d$, $r_{m,q}^2 = (k_q n_0)^2 - \gamma_{m,q}^2$, $t_{m,q}^2 = (k_q n_3)^2 - \gamma_{m,q}^2$, and $k_q = 2\pi/\lambda_q$.

In the resonance domain we are interested in only the propagating diffraction orders, namely the sets $\mathcal{R}_q = \{m | r_{m,q} \text{real}\}$ and $\mathcal{T}_q = \{m | t_{m,q} \text{real}\}$. The evanescent waves, however, affect the propagating order amplitudes, and so cannot be ignored when solving the electromagnetic boundary value problem. The intensities of the reflected and transmitted propagating orders are $I_{m,q} = (r_{m,q}/r_0)|R_{m,q}|^2$ and $I_{m,q} = C(t_{m,q}/r_0)|T_{m,q}|^2$, where $C = 1$ for TE polarization and $C = (n_0/n_3)^2$ for TM polarization. A goal power spectrum $\mathcal{P}_q$ is specified within a spatial frequency image window $\mathcal{W}_q = \mathcal{R}_q$ (reflection elements)

or $W_q = T_q$ (transmission elements), as $\mathcal{P}_q = \{\hat{I}_{m,q} | \hat{I}_{m,q} = \{0,1\}, m \in W_q\}$ having $N_q = \sum_{m \in W_q} \hat{I}_{m,q}$ equal order intensities. The generalized synthesis problem can now be stated as follows:

Obtain a periodic index modulated structure that maximizes the diffraction efficiency $\eta_q = \sum_{m \in W_q} \hat{I}_{m,q} I_{m,q}$ and minimizes the reconstruction error $E_q = \max_{m \in W_q} \hat{I}_{m,q} |1 - N_q I_{m,q}/\eta_q|$ for the Q relevant inputs.

To solve the generalized synthesis problem, we use nonlinear parametric optimization to minimize a quadratic merit function $Mf = \sum_{q=1}^{Q} \sum_{m \in W_q} [I_{m,q} - \hat{I}_{m,q} \hat{\eta}_q / N_q]^2$, where $\hat{\eta}_q$ is the goal efficiency. The design freedoms available in the resonance domain (cf. Ref. [6] for the freedoms in the Fourier domain) are the phases of the signal beams inside W_q, the complex amplitudes of the evanescent waves outside W_q and, for the case of transmission gratings, the complex amplitudes of the reflected orders. For dielectric gratings a space harmonic expansion method was used to evaluate Mf [5], whereas for ideal perfectly conducting gratings a generalized modal method was employed [7]. The search for an acceptable solution was implemented using a gradient algorithm. This method of steepest descent often stagnated in a local minimum (especially for large fanout) and so many random starting configurations were used.

As examples of resonance domain optical elements we synthesized first a simple dielectric ($n_0 = n_1 = 1.5$, $n_2 = n_3 = 1$) two beam fanout grating (Fig. 2). We optimized the period d, the relief height H, and the groove width $c = b_1 - a_1$ to obtain the solution $\{d/\lambda, H/\lambda, c/\lambda\} = \{1.769, 1.396, 0.322\}$, with efficiencies of $I_{\pm 1} = 47.3\%$, $I_0 = 0.2\%$, while 5.2% was reflected. Design of higher fanout gratings involves increasing the number of grooves in one period as to obtain the required degrees of freedom. Examples of dielectric and perfectly conducting gratings are shown in Table 1.

To illustrate the design of elements involving $Q > 1$ independent inputs we consider synthesis of resonance domain star couplers illustrated in Fig. 3. Here the element is to connect each of the $\mathcal{N}$ mutually uncorrelated sources $A, B, C, \ldots$ to all of the $\mathcal{N}$ receivers $A', B', C', \ldots$. The performance of these components is also shown in Table 1. Finally, we consider the design of resonance domain polarization dependent switches. A polarization beamsplitter illustrated in Fig. 4, for which $Q = 2$, was first designed: a dielectric structure with $d = 0.724\lambda$, $H = 1.720\lambda$, $c = 0.140\lambda$ and angle of incidence $\theta = 27.4°$ (inside $n = 1.5$) was found that gave efficiencies of 98.5% and 0.02% into the zeroth and minus one order for TM polarization, and 0.05% and 95.9%, respectively, for TE polarization. Owing to the symmetry of the grating structure, this polarization beamsplitter can also act as a four-port device that either passes through or swaps two beams incident at angles $\pm\theta$, depending on their states of polarization.

$\mathcal{M}$ to $\mathcal{N}$	Dielectric J / $\eta_q(\%)$, $E_q\%$	Perf. Conductor J / $E_q\%$
1 to 8	3 / 90.1, 2.5	3 / 3.5
1 to 9	3 / 93.2, 3.1	3 / 6.3
3 to 3	2 / 96.9, 0.8 / 96.0, 3.0	1 / 0.2 / 0.3
4 to 4	3 / 88.2, 1.0 / 88.9, 1.3	3 / 0.9 / 0.9

Table 1. Performance of resonance domain fan-out elements and star couplers. The efficiency of each perfectly conducting solution is 100%, and for star couplers the figures of merit for incidence at $-\theta$ are the same as the given values for incidence at θ.

We found by numerical simulations that for experimental demonstration of useful resonance domain elements the transition placement must be better than $\lambda/20$. Consequently we investigated the performance of some 1 to $\mathcal{N}$ perfectly conducting fanout gratings for $\lambda = 5.52\mu m$. Although on the limit of the
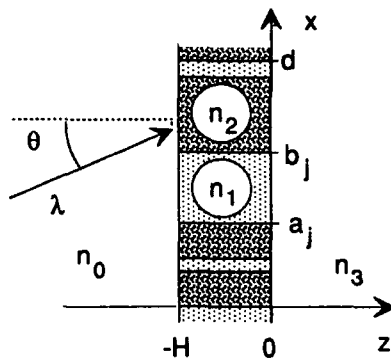
Fig. 1. The geometry.
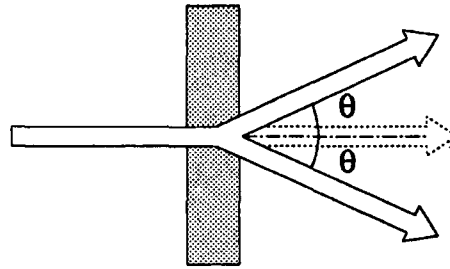
Fig. 2. Fan—out to two.
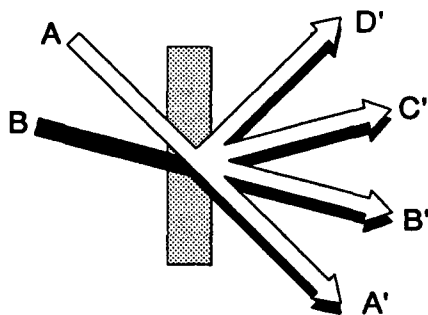
Fig. 3. Principle of a star coupler.
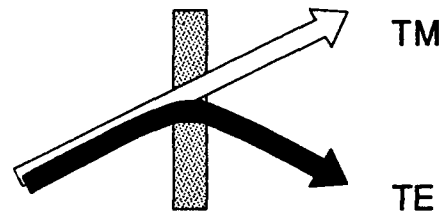
Fig. 4. Polarizing beamsplitter.

maximum allowable placement error the uniformity of the 1 to 9 grating was ±14%, and only ±7% with the zeroth order excluded; numerical simulations indicated that this order is most sensitive to fabrication errors such as incorrect relief depth and slanted sidewalls.

In this summary (more detais will be given elsewhere [8]) we have defined and solved the synthesis problem for resonance domain diffractive optical elements. Utilizing parametric optimization, synthesis examples of these diffractive components have been given and experimentally verified for $\lambda = 5.52$ μm.

[1] J. W. Goodman, *Introduction to Fourier Optics* (McGraw-Hill, San Francisco, 1968).

[2] P. Beckmann, in *Progress in Optics VI*, E. Wolf, ed. (North-Holland, Amsterdam, 1967), pp. 53–69.

[3] D. Maystre, in *Progress in Optics XXI*, E. Wolf, ed. (North-Holland, Amsterdam, 1984), pp. 1–67.

[4] A. Vasara, E. Noponen, J. Turunen, J. M. Miller, and M. R. Taghizadeh, *Opt. Commun.* **81**, 337–342 (1991).

[5] A. Vasara, E. Noponen, J. Turunen, J. M. Miller, M. R. Taghizadeh, and J. Tuovinen, in *Holographic Optics III: Principles and Applications*, G. M. Morris, ed., Proc. SPIE **1507**, 224–238 (1991).

[6] O. Bryngdahl and F. Wyrowski, in *Progress in Optics XXVIII*, E. Wolf, ed. (North-Holland, Amsterdam, 1990), pp. 1–86.

[7] J. M. Miller, J. Turunen, M. R. Taghizadeh, A. Vasara, and E. Noponen, *Holographic Systems, Components, and Applications* **342**, 99–102 (Inst. of Electrical Engineers, 1991).

[8] E. Noponen, A. Vasara, J. Turunen, J. M. Miller, and M. R. Taghizadeh, "Synthetic diffractive optics in the resonance domain", *J. Opt. Soc. Am. A* (in press).

Poster Preview

TuD   3:30pm–4:00pm
Cabildo Room

James R. Leger, *Presider*
University of Minnesota

(Poster Session, **TuE**, follows: 4:00pm–5:30pm.)

A Diffraction Grating Photopolarimeter

R. M. A. Azzam and K. A. Giardina

Department of Electrical Engineering,
University of New Orleans,
Lakefront, New Orleans, Louisiana 70148
[Tel. (504) 286-6181]

Summary

A new division-of-amplitude photopolarimeter[1] with no moving parts or modulators is described that employs the conical diffraction of light from a grating which is set for oblique incidence with the grating lines inclined with respect to the plane of incidence, Fig. 1. The grating G splits the incident light beam, whose state of polarization is to be measured, into four or more beams that are intercepted by linear photodetectors D_m (m = 0, 1, 2, ...). This produces four or more signals i_m that represent multiple projections of the unknown Stokes vector $\underline{S}$. $\underline{S}$ is reconstructed from its projections by matrix inversion. We have built a prototype photopolarimeter of this type using an Al-coated, 600-grooves/mm, holographic grating set at $65°$ angle of incidence with the grooves oriented at $45°$ with respect to the plane of incidence, and a 633-nm He-Ne laser as the light source. This novel photopolarimeter has been calibrated and tested, with and without the linear polarizers P_m in front of the photodetectors, using the same procedures[2,3] recently established for the four-detector photopolarimeter[2,3]. This polarization-analysis scheme has several advantages and degrees of flexibility. In particular, it can be adapted using detector arrays so as to perform time-resolved spectropolarimetry.

References

1. R. M. A. Azzam, Opt. Acta, 29, 685 (1982), ibid, 32, 767 (1985).

2. R. M. A. Azzam, E. Masetti, I. M. Elminyawi, and F. G. Grosz, Rev. Sci. Instrum., 59, 84 (1988).

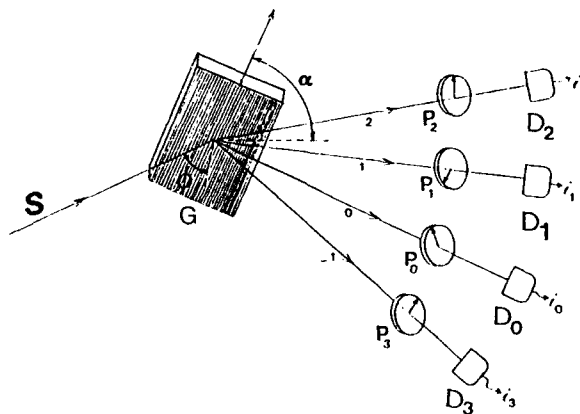3. R. M. A. Azzam and A. G. Lopez, J. Opt. Soc. Am. A, 6, 1513 (1989).

Fig. 1

A Hybrid Diffractive/Refractive Lens for Use in Optical Data Storage

David Kubalak and G Michael Morris

The Institute of Optics, University of Rochester, Rochester, NY 14627

Introduction

Optical data storage (ODS) lenses are mounted with an automatic refocusing mechanism to account for possible variations in the lens-disk distance, e.g., disk wobble. This auto-focus system, however, cannot compensate for laser mode hopping, which occurs on a nanosecond scale. One possible solution is to use frequency stabilized lasers, but these tend to be very expensive. Another option is to correct the longitudinal chromatic aberration of the lens over the spectral bandwidth of the source. Unfortunately, achromatizing the lens using conventional glass requires a positive and negative element, which significantly increases the size and weight of the lens, neither of which is desirable for optical data storage. An alternative option is the use of gradient index glass, and a fourth possible solution is to use a diffractive/refractive hybrid lens, which is the focus of this paper.

Hybrid diffractive/refractive lens

The problem with correcting longitudinal chromatic aberration using conventional glass, as mentioned above, is the significant increase in size and weight of the lens due to the need for a very strong crown element. In a diffractive/refractive hybrid lens, however, a diffractive element is used in place of the flint to compensate for the dispersion in the crown[1-4]. The success of this type of lens lies in the dispersion of the diffractive element. A diffractive lens has an Abbe V numver V_{diff} = -3.45, about six times more dispersive than any glass, and with the opposite sign. This means a weak positive diffractive lens can be used to achromatize a positive glass lens, as shown schematically in Fig.1. Compared to conventional flint glass, the use of a diffractive surface results in thinner lenses, as well as lower curvatures on the surfaces. Therefore, lower f-number achromats are possible, making the diffractive/refractive hybrid very attractive for optical data storage applications, where lenses are designed to work at f-numbers less than f/1.0.

It is desirable for optical data storage lenses to have a short focal length, extremely low f-number, and a finite field of view for tolerancing purposes. We have designed an f/0.9 ODS lens with a focal length of about 3mm, NA = 0.55, and 1° half field of view. The working distance, from the rear surface of the lens to the disk, was designed to be approximately 1.1mm, but allowed to change during

performance evaluations to mimic the automatic refocus mechanism of ODS machines. A singlet was also designed with the same specifications for performance comparisons.
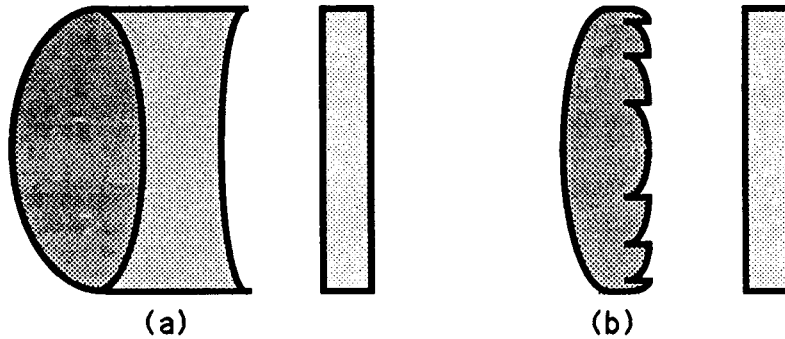
Fig. 1. Possible configurations for optical data storage lenses: (a) conventional glass doublet, (b) hybrid doublet. Both are shown with the polycarbonate disk coating.

The diffractive/refractive hybrid lens was designed using a thin lens model for the diffractive surface[5,6]. The common surface was held flat. Aspheric coefficients were allowed on the front surface of the glass element, and on the back surface of the thin lens model. The singlet was also designed using aspheric coefficients to minimize aberrations. Figure 2 shows the Strehl ratio as a function of field angle for the hybrid and for a singlet made of the same glass.
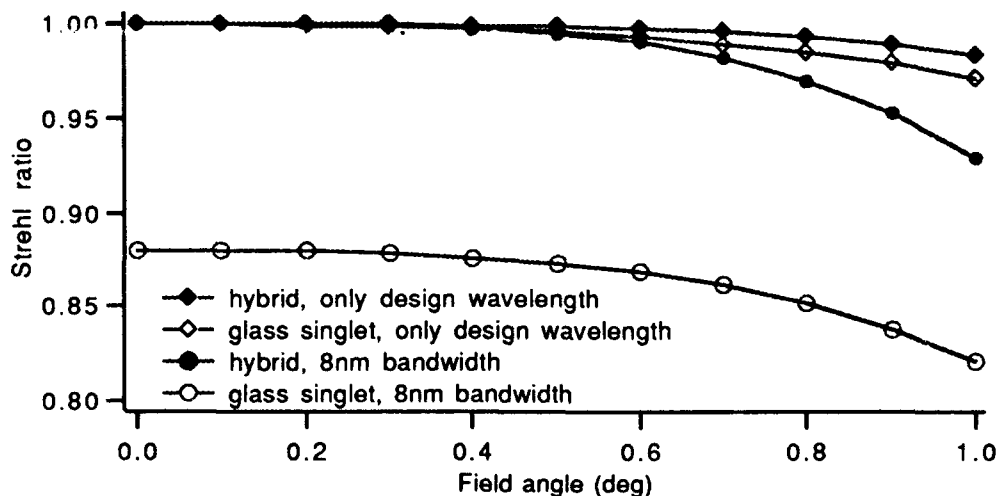
Fig. 2. Strehl ratio vs field angle for the diffractive/refractive hybrid, and a glass singlet. Both the Strehl ration at only the design wavelength and with an 8nm bandwidth is shown. Refocusing for optimal Strehl ratio, at the design wavelength only, is taken into account at each field angle for all plots.

A design goal for the lens is to keep the Strehl ratio greater than 0.96. As seen in Fig. 2, both lenses meet this criteria monochromatically, indeed the two types of lenses perform almost the same at the design wavelength. The hybrid lens, however, can be achromatized without adding to it's size or weight. For ODS lenses, it is desirable to keep the focal length change per wavelength change to under 0.1μm/nm. The hybrid lens does this effectively, with a focal length change of less than 0.03μm/nm. With the glass singlet, color correction is, of course, not possible. The effect of laser mode hopping on the Strehl ratios of both lenses is shown in Fig. 2. Note that the Strehl ratio of the glass singlet is reduced significantly with a polychromatic source.

Diffraction efficiency

An additional factor that must be considered with the diffractive/refractive hybrid lens is the diffraction efficiency. Since the dispersion from the diffractive surface is so extreme, the power in that element is very weak. Grating spacings are much larger than the wavelength of light, and scalar diffraction theory can therefore be used. The efficiency of the diffractive surface will be most sensitive to wavelength change due to mode hopping, however, since the incident wavelength won't change more than about 0.3%, the efficiency in the design order only drops about 0.005%. Another measure of the noise introduced by stray light from other diffracted orders in a diffractive lens is the integrated efficiency, investigated by Buralli and Morris[7]. They show the integrated efficiency to be the limiting value of the OTF at the desired focal point due to light from unwanted orders. The integrated efficiency for our diffractive surface was found to be 0.9998. Diffraction efficiency doesn't appear to be a problem.

References

1. T Stone and N George, "Hybrid diffractive-refractive lenses and Achromats," Appl. Opt. 27 2960-2971 (1988)

2. A. Tudorovskii, "An objective with a phase plate," Opt. and Spect. 2 126 (1959)

3. K. Miyamoto, "The Phase Fresnel Lens," J. Opt. Soc. Am. 51, 17-20 (1961)

4. H. Madjidi-Zolbanine and C. Froely, "Holographic Correction of Both Chromatic and Spherical Aberrations of Single Glass Lenses," Appl Opt. 18, 2385-2393 (1979)

5. W Sweatt, "Describing holographic optical elements as lenses," J. Opt.Soc.Am. 67 803-808 (1977)

6. W. Kleinhans, "Abberrations of Curved Zone Plates and Fresnel Lenses," Appl. Opt. 16, 1701-1704 (1977)

7. D Buralli and GM Morris, "Effects of diffraction efficiency on diffractive lens image quality," submitted to Appl. Opt, March 1991, in review

Beam Shaping of High-Power Laser Diode Array by Continuous Surface-Relief Elements

P. Ehbets, H. P. Herzig, R. Dändliker
Institute of Microtechnology, University of Neuchâtel, Rue A.-L Breguet 2, Switzerland
Phone: +41 38 20 51 21

I. Kjelberg
Centre Suisse d'Electronique et de Microtechnique S.A. (CSEM), Jaquet-Droz 7, Switzerland
Phone: +41 38 20 56 11

Summary

Laser diode arrays (LDAs) can generate coherent light beams of high power. Unfortunately, LDAs generate poor quality output beams, which cannot be properly collimated by conventional diode laser optics. In order to improve the optical quality of the output, Veldkamp et al. [1] have proposed different possibilities using binary optical elements. Our approach is based on the tandem component described in Ref. 2, but it uses a simple phase plate and a continuous surface relief-element for the fan-in of the N beams. Theory for the design and the realization of the diffractive optical elements (DOEs), simulated results for the performance of the system, as well as experimental results for a compact set-up will be presented.

The presented beam shaping requires LDAs which emit in a single transverse mode. The basic arrangement is shown in Fig. 1. A first optical element close to the LDA acts on the phases in the near-field in order to get a smooth Gaussian beam intensity distribution in the far-field, i.e. in the back focal plane of the lens. However, the phase distribution is not yet uniform, and therefore a second DOE has to be added to correct the phase profile without changing the intensity profile. This DOE acts as a coherent N beam fan-in element. The result is a plane wave with a Gaussian intensity profile, which can fill perfectly well the aperture of a collimator.
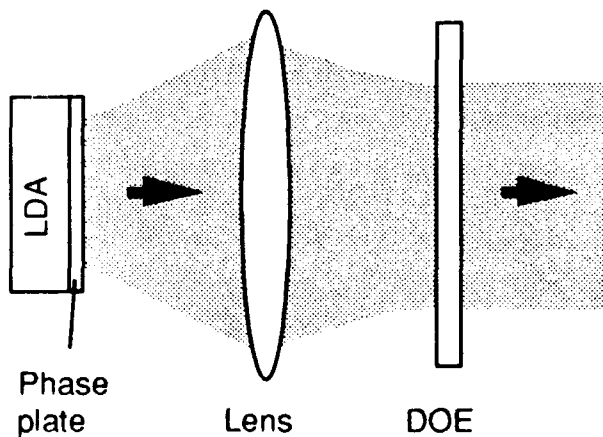

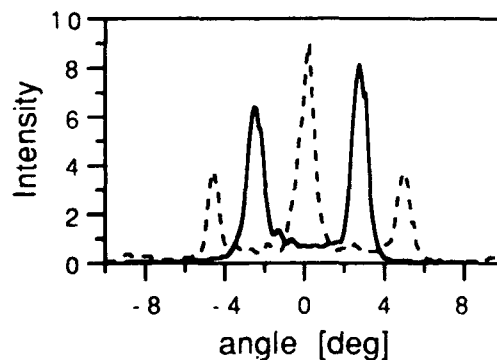Fig. 1: Basic arrangement for far-field shaping.

Fig. 2: Experimental results for the LDA: inital far-field (solid line), converted by the phase-plate (dashed line).

The first optical element is realized by a phase plate (Fig. 3) near the LDA, where the beams of the different array elements are still separated. Experimental results for a phase plate converting the double lobed 180°-mode of the LDA into the single lobed 0°-mode are shown in Fig. 2. The phase plate for the optimum beam shaping is calculated following the concept developed in Ref. 3. The near-field distribution $U(x,y)$ at the LDA output is approximated by an array of N Gaussian beams. The relative phases of these N beams are optimized to get a smooth Gaussian intensity profile in the far-field. The far-field is related to the near-field $U(x,y)$ by a Fourier transform

$$\hat{U}(u,v) = | \hat{U}(u,v) | \exp\{i\Psi(u,v)\} = FT\{U(x,y)\} .$$ (1)

The envelope of the intensity distribution $I(u,v) = |\hat{U}|^2$ is given by the Gaussian far-field distribution I_G of a single stripe. The condition for the optimum phases can therefore by formulated as

$$\int_{-\infty}^{\infty} \int_{-\infty}^{\infty} [I(u,v) - I_G(u,v)]^2 \, dudv \rightarrow min.$$ (2)

The optimum phases for the N beams in the near-field are numerically calculated from Eq. 2 with a downhill simplex algorithm. The phase distribution $\Psi(u,v)$ in the far-field is obtained from the Fourier transform $\hat{U}(u,v)$ by Eq. 1. A second DOE with the complex amplitude transmittance

$$T(u,v) = \exp\{-\Psi(u,v)\}$$ (3)

has to be added in the far-field, in order to generate a plane wavefront.

For the experiments we have used a SDL-240 LDA from Spectra Diode Labs, which offers 10 phase coupled emitters spaced by $s = 10 \, \mu m$ at $\lambda = 801$ nm. The emitters have an alternating 0°/180° phase distribution producing a nice double lobed mode in the far-field (Fig. 2). The phase plate consists of 10 zones with a length of 10 μm. The element is fabricated at CSEM by repeated reactive ion etching (RIE) of fused silica, using a binary set of masks. We have found a good solution by distributing the 10 optimum phases on 16 equally spaced levels between 0 and 2π. Theoretically, 97.3% of the emitted power by the LDA can be collimated into a single Gaussian beam for the optimum set of phases. The quantization reduces the efficiency only slightly to 96.7%. The calculated results are summarized in the Table below. It shows the optimum phases and the quantified phases of the N beams, as well as the output phases of the LDA and the values of the phase plate zones.

Beam	1	2	3	4	5	6	7	8	9	10
Opt. phases [rad]	0.00	6.80	6.52	5.11	5.05	1.41	1.52	4.58	2.02	4.61
Quant. phases [rad]	0.00	0.39	0.39	1.18	5.11	1.57	1.57	-1.57	1.96	-1.57
LDA phases [rad]	0.00	3.14	0.00	3.14	0.00	3.14	0.00	3.14	0.00	3.14
Phase plate [rad]	0.00	3.53	0.39	1.96	5.10	4.71	1.57	1.57	1.96	1.57

For the compact system a lens with high numerical aperture of N.A. = 0.276 and a focal length of f = 14.5 mm has been chosen. In that case the periodicity for the second DOE in the Fourier plane

of the lens becomes $\lambda f/s = 1161.45$ µm. In this set-up only about 2.5 periods of the second DOE are illuminated. The fan-in element has to be fabricated very accurately and the experimental set-up must allow exact adjustment to match the phase profile to the phase pattern in the Fourier plane. We have opted for a continuous surface-relief element as the second DOE. The calculated profile is shown in Fig. 4. The highest shaping efficiency is obtained with an asymmetric phase distribution in the near-field (Fig. 3). Therefore, the phase function within one period of the fan-in element is also asymmetric (Fig. 4). The element is written in photoresist using the laser beam writing system at the Paul Scherrer Institute, Zurich (Ref. 4). On the same system, highly efficient fan-out elements with similar profiles have already been realized.

Experimental results for a compact prototype will be presented.
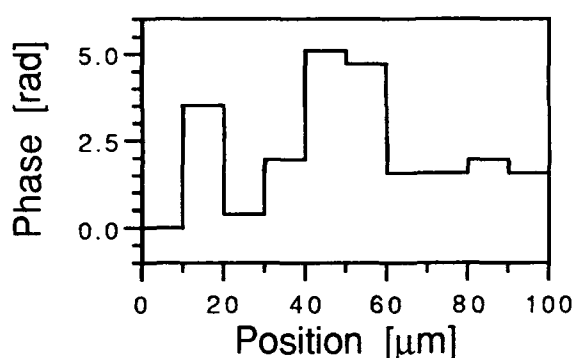
Fig. 3: Profile of the phase plate
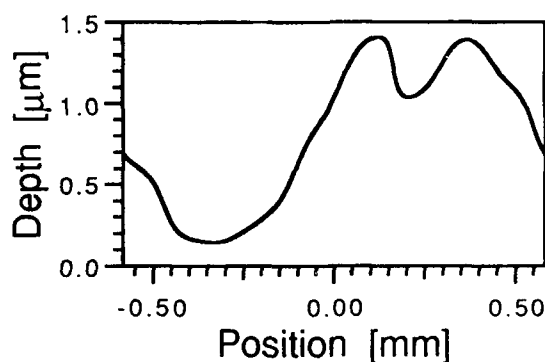
Fig. 4: One period of the calculated surface-relief element

References

1. J.R. Leger, M. Holz, G.J. Swanson, W.B. Veldkamp, "Coherent Laser Beam Addition: An Application of Binary-optics Technology", The Lincoln Lab. Jou., 1, No. 2, 225-246 (1988)

2. H.O. Bartelt, "Applications of the tandem component: an element with optimum light efficiency", Appl. Opt., 24, 3811-3816 (1985)

3. H.P. Herzig, R. Dändliker, J. M. Teijido, "Beam Shaping for High Power Laser Diode Array by Holographic Optical Elements", Holographic Systems, Components and Applications, Bath, UK, Conference Publication No. 311, 133-137 (IEE, 1989)

4. M.T. Gale, G.K Lang, J.M. Raynor, H. Schütz, D. Prongué, "Fabrication of Kinoform Structures for Optical Computing", accepted for publication in Appl. Opt. (1992)

Grating Enhanced Detection of Surface Acoustic Waves
Using an Acousto- optic Modulator

D. A. Larson and T. D. Black

Department of Physics, The University of Texas at Arlington

P.O. Box 19059, Arlington, Texas 76019

(817) 273-2450

SUMMARY

The sensitivity for enhanced detection of surface acoustic waves (SAW) using a traveling Bragg regime grating was found to be similar to that obtained using stationary reference gratings operating in the Raman-Nath diffraction regimes.[1] An acousto-optic modulator (AOM) with a nominal frequency of 40 MHz was used to detect traveling gratings produced by SAW on a $LiNbO_3$ substrate. The center frequency of the SAW was 34.88 MHz corresponding to a wavelength, Λ_S, of 100 μm. With the AOM tuned to 38.5 MHz, the wavelength of the bulk acoustic wave, Λ_B, in the flint glass modulator was also about 100 μm. The AOM was operating in the Bragg diffraction regime ($Q' \approx 11$) and the SAW in these experiments was a weakly modulated traveling grating, either cw or pulsed, operating in the Raman-Nath diffraction regime.[2]

Figure 1 illustrates the basic experimental configuration with the two dynamic gratings separated by a distance L. For these experiments, L was varied from an initial separation of approximately 20 mm to a maximum separation of about 400 mm to demonstrate the gradual
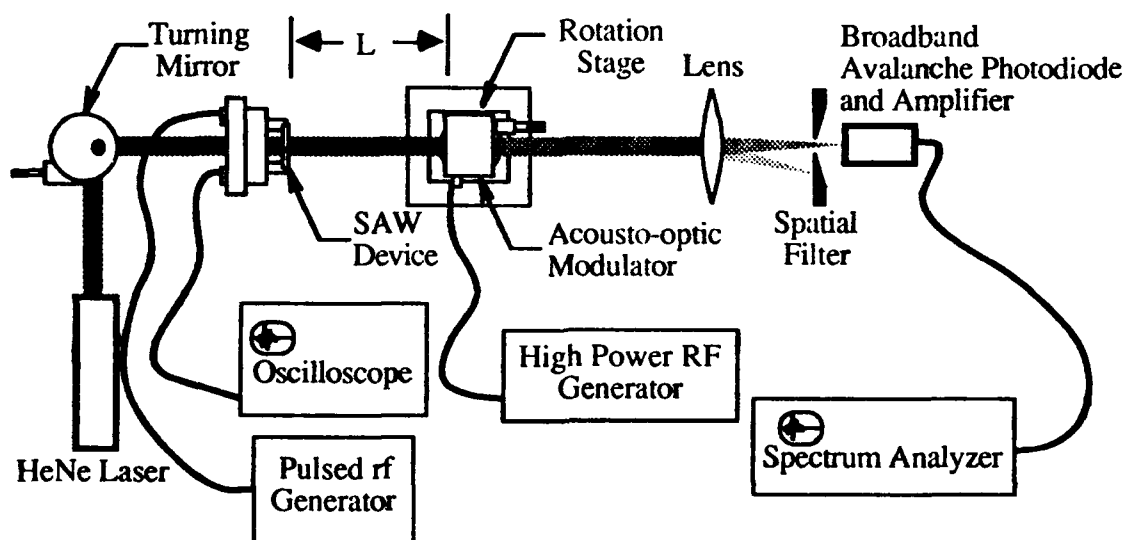
Fig. 1. Experimental schematic for the enhanced detection of SAW using an AOM.

signal fall off with increasing separation distance. With the two traveling gratings properly aligned and tuned to approximately the same wavelength, the spatial frequency components of both gratings were harmonically related. The major temporal modulation terms of the intensity in the resulting diffracted beams were near the sum (73.4 MHz) and difference (3.4 MHz) frequencies. The excellent sensitivity and selectivity was achieved due to the "tuned" coherent intermodulation.

A stationary Bragg regime reference grating used to enhance the detection of a contiguous SAW was analyzed previously.[3] In the case at hand, however, the Bragg reference grating was dynamic (traveling). In addition, the SAW was separated by a distance L. Figure 2 shows schematically the basic diagram used for our analysis. The probing laser beam was considered to be incident on the SAW at the anticipated Bragg angle of the AOM. In this way two orders from the SAW (m = 0 and m = -1 as shown schematically) simultaneously satisfy the Bragg condition of the AOM and therefore were coupled. Coupled mode analysis including the relative velocity between the gratings was used to analyze the AOM, and Raman-Nath theory was used to
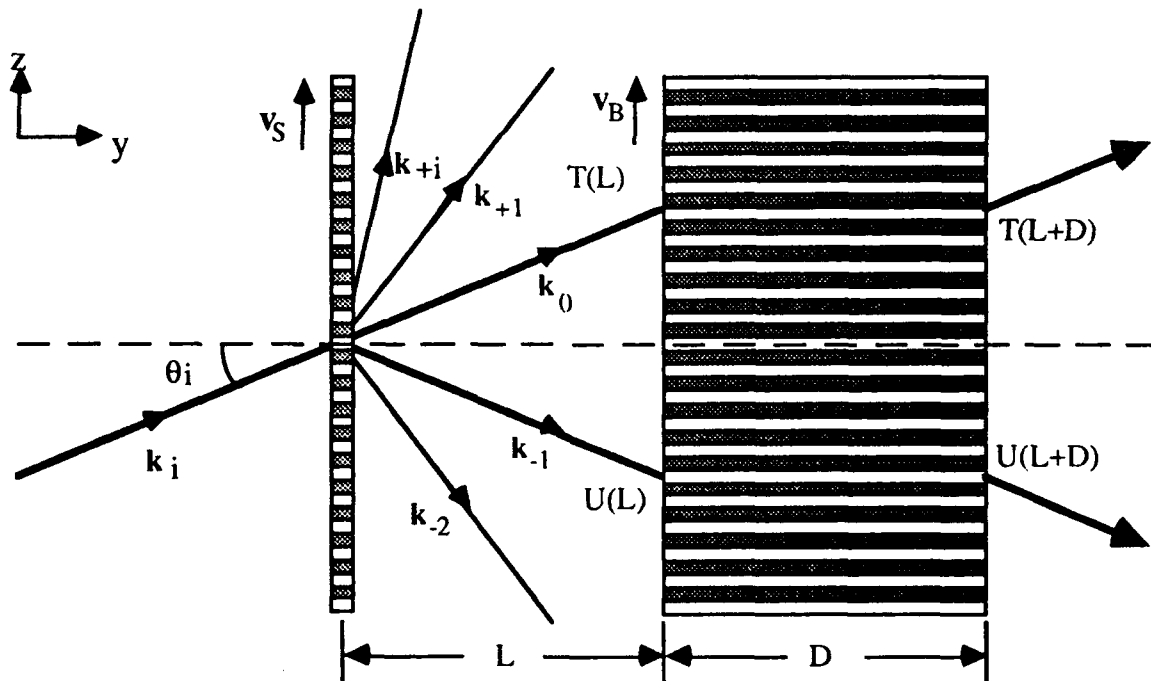
Fig. 2. Schematic diagram for analysis for enhanced detection of SAW using an AOM.

determine the output from the SAW. The results were consistent with the previous contiguous analysis but included the additional effect of the Doppler shift.

Neither Raman-Nath theory or coupled mode analysis can account for the gradual fall off of the detected signal strength. However, a general spatial frequency analysis can be used to

include finite beam size and divergence.[4] Figure 3 compares the fall off of the detected signal using the traveling Bragg regime reference grating with a theoretical curve generated for a thin reference grating. Since the Bragg regime reference grating filters higher order diffraction terms, the intermodulation coherence length was about three times greater than that of a corresponding Raman-Nath reference grating resulting in a far less severe fall off with increasing proximity.
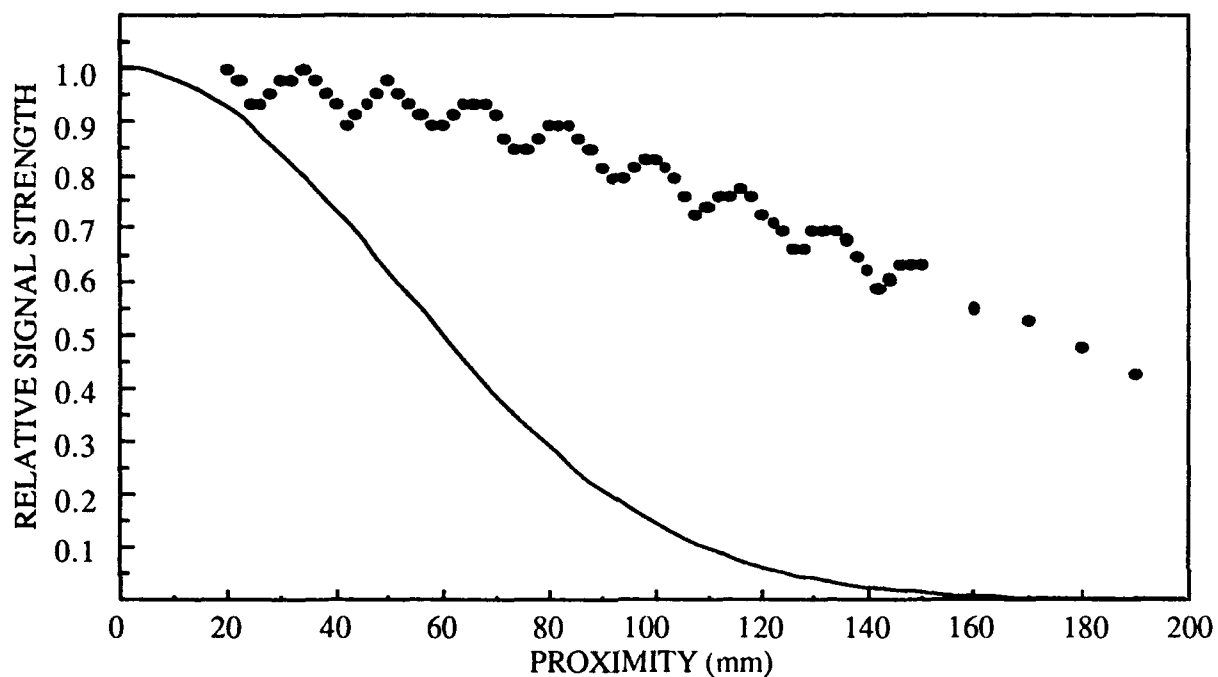
Fig. 3. Comparison of the gradual fall off of the experimentally detected signal at 73.3 MHz using a probing beam with approximately 0.6 mrad half angle divergence to a theoretical model.

1. D. A. Larson,T. D. Black, M. Green, R.G. Torti, Y.J. Wang, and R. Magnusson, "Optical Modulation by a Traveling Surface Acoustic Wave and a Holographic Reference Grating," J. Opt. Soc. of Am.,A 7,1745-1750 (1990).

2. R. Magnusson and T. K. Gaylord, "Diffraction regimes of transmission gratings," J. Opt. Soc. Am. 68(6), 809-814 (1978).

3. R. Magnusson and T. D. Black, "Enhanced detection of acoustic waves using thick and thin reference gratings," J. Opt. Soc. Am. A 4, 498-502 (1987).

4. T. D. Black, T. Haghighatjou, and D. A. Larson, "Determination of laser beam divergence using the acousto-optic interaction with surface waves," Proc. IEEE Ultrason. Symp., 404-408 (1985).

Traceable Aspheric Testing Using Diamond-Machine Diffractive Null Lenses

Clinton Evans, Melvyn Francis and Donald Morrison
Hughes Leitz Optical Technologies

Figure 1 shows a 5.6 inch diameter aspheric mirror which we wish to manufacture and test. Figure 2 shows the mirror's wavefront aberration when used with one infinite conjugate. The most significant feature of this plot is a large spherical zone of about 25 waves.

We wish to use a null-lens testing method in production, to produce an immediate assessment of the whole surface. Unfortunately, a null test lens for this mirror must cancel a substantial amount of higher-order spherical aberration.

There are many possible null-test geometries but, to solve our problem effectively, we need an arrangement with the following characteristics:-

1) The ability to null the wavefront to .1 wave precision
2) Compatibility with a 4 inch aperture Zygo interferometer
3) The ability to produce a traceable, calibrated measurement.

With these requirements in place, however, most of the null test geometries look less attractive. In particular item 3, traceability and calibration, is specially hard to satisfy.

In principle, we can design a multi-element, transmitting spherical lens to perform the null-lens function. Our initial efforts, however, showed we would need a lens of considerable complexity to satisfy the wavefront requirements of item 1. Unfortunately, this complexity violates the traceability requirements of item 3.

Each element in a transmitting null-lens introduces two curvature tolerances, two form-error tolerances, a thickness tolerance, a separation tolerance, a refractive index tolerance, a homogeneity tolerance and numerous centration tolerances. A single-element null lens, therefore, will provide a significant challenge. A multi-element lens will be very difficult or impossible.

There are several simple null-test geometries which use a reflecting asphere. In general, however, geometries which use a small diameter asphere require a large aperture interferometer. Geometries which work with a small aperture interferometer require a large diameter asphere.

We can measure small diameter aspheres by contact profilometry, but nothing as big as our test mirror. To calibrate a large aspheric null-lens, we must solve independently a problem equivalent to our initial test problem.

We propose, therefore, to use the diffractive arrangement shown in figure 3. The null lens is a diffractive mirror, diamond-machined in aluminum-alloy. Figure 4, which shows the wavefront aberration of the combination, demonstrates the null lens satisfies item 1. The optical interface with the interferometer is a well-corrected intermediate image and a transmission sphere, which is compatible with item 2.

Item 3, however, was the major issue which made us choose this arrangement. It has the following merits which aid traceability:-

- Provided the substrate is adequately flat, the wavefront from the null lens is uniquely defined by the grating spacings. Errors in the groove profile will effect the diffraction efficiency, but not the wavefront shape.
- The diamond-machined diffractive mirror has a good mechanical mounting datum, machined at the same setting as the grating.
- An all-reflecting geometry removes problems from material homogeneity and refractive index tolerances.
- The grating tolerances are easily calculated, since there is a simple relation between the wavefront slope and the grating spacings.

We can calibrate the null-lens using the following procedure:-

- Machine a flat surface on the grating substrate.
- Measure flatness with a reference flat.
- Machine grating profile on substrate.
- Measure groove diameters and compare with nominal and tolerance data.

If all these items are satisfied within tolerance, the null-lens will generate the correct wavefront.

So far, the design for the null-lens is complete. It has 138 grooves, and the smallest spacing is .006 inch. We also have theoretical projections of the light-loss caused because diamond-turning does not faithfully reproduce sharp corners in the groove-pattern. We will present this data in the paper.

The programming for the diamond-turning lathe is complete and we will machine the null-lens in March 1992. We intend to show interferograms of the combination and other results in the paper.

1.00 IN

CEE 11-Feb-92

FULL SCALE

Figure 1

TANGENTIAL   0.00 RELATIVE   SAGITTAL

FIELD HEIGHT

(0.000°)

25.00   25.00

−25.00   −25.00
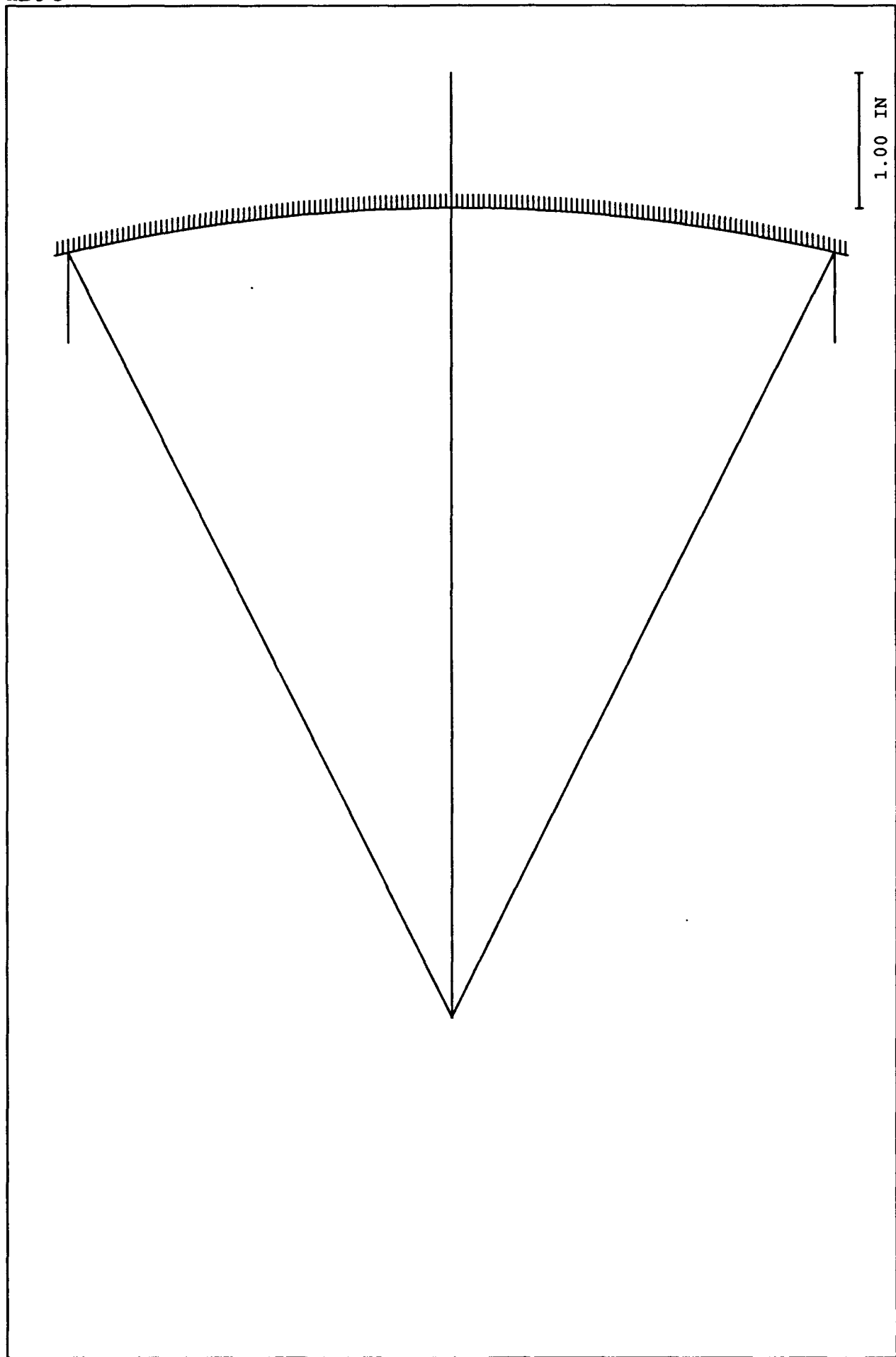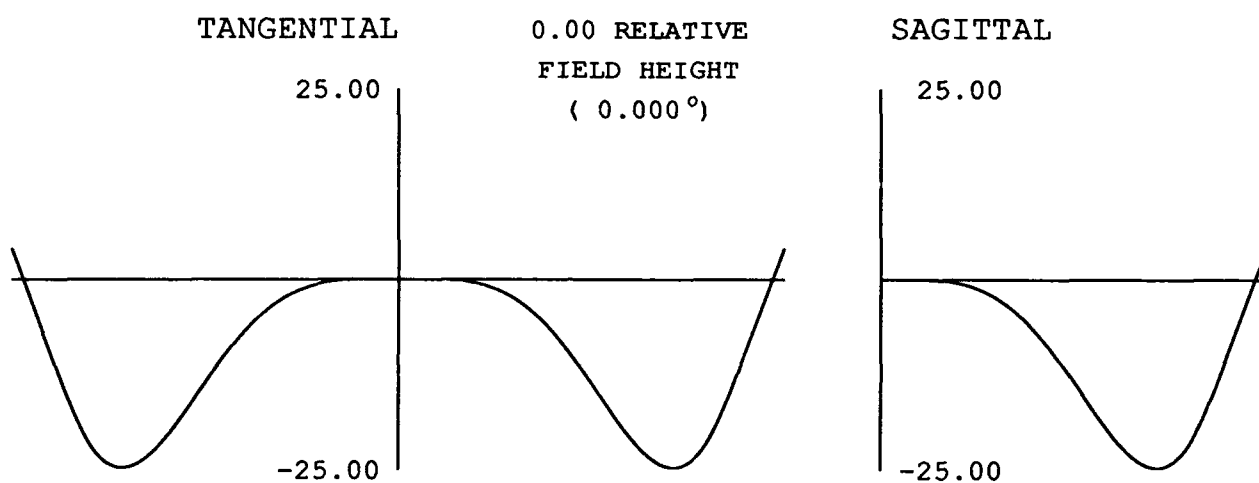
Figure 2

OPTICAL PATH DIFFERENCE (WAVES)

CEE   11−Feb−92

633.0 NM

1.00 IN

FULL SCALE

Figure 3

Y-FAN   0.00 RELATIVE   X-FAN
                FIELD HEIGHT
   0.10   (0.000°)   0.10

-0.10   -0.10

Figure 4

OPTICAL PATH DIFFERENCE (WAVES)

CEE   11-Feb-92

——————————— 633.0 NM

Design of Dynamic Imaging Systems using SLM based Kinoform Lenses

Eddy C. Tam
Department of Physics
University of North Carolina at Charlotte, Charlotte, NC 28223
Tel: (704) 547 2816

Qiwang Song
Department of Electrical and Computer Engineering
Syracuse University, Syracuse, NY 13244
Tel: (315) 443 1516

The subject of diffractive optics has been studied for many years. Some of the applications in this area are the use of Fresnel zone plates in x-ray or gamma ray imaging, modulation zone plates in laser machinery, computer generated holograms in optical interconnects and optical computing, and microlenses in laser beam and LEDs focusing. However, there is not much attention in spatial light modulator (SLM) based dynamic diffractive optical elements. In this paper, we would like to study the design of SLM based kinoform lenses in dynamic electro-optical imaging systems. The phase relief profile of a spherical lens, usually called a kinoform lens, is implemented onto a continuous phase SLM. The focal length of the kinoform lens can then be changed at the frame rate of the SLM. This dynamic lens will be incorporated with other refractive lenses to give an electro-optical imaging system which does not require any movable mechanical parts for focusing and/or zooming. More importantly, focusing/zooming can be accomplished at the frame rate of the SLM, typically in the order of 30 to 40 ms per frame for a commercially available nematic liquid crystal light modulator. This speed represents at least an order of magnitude faster than that required in a conventional focusing or zooming system based on mechanical motion of lenses.

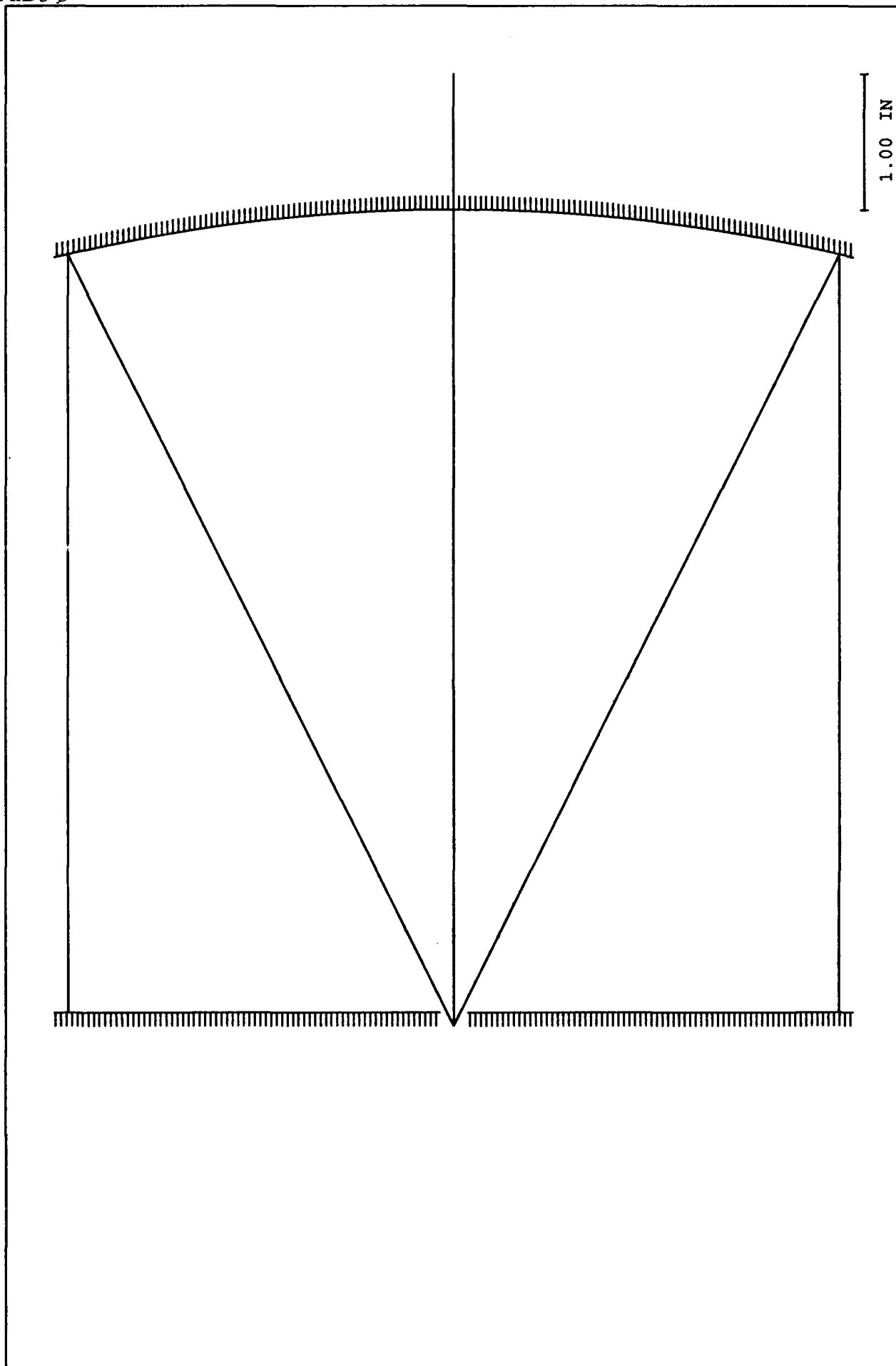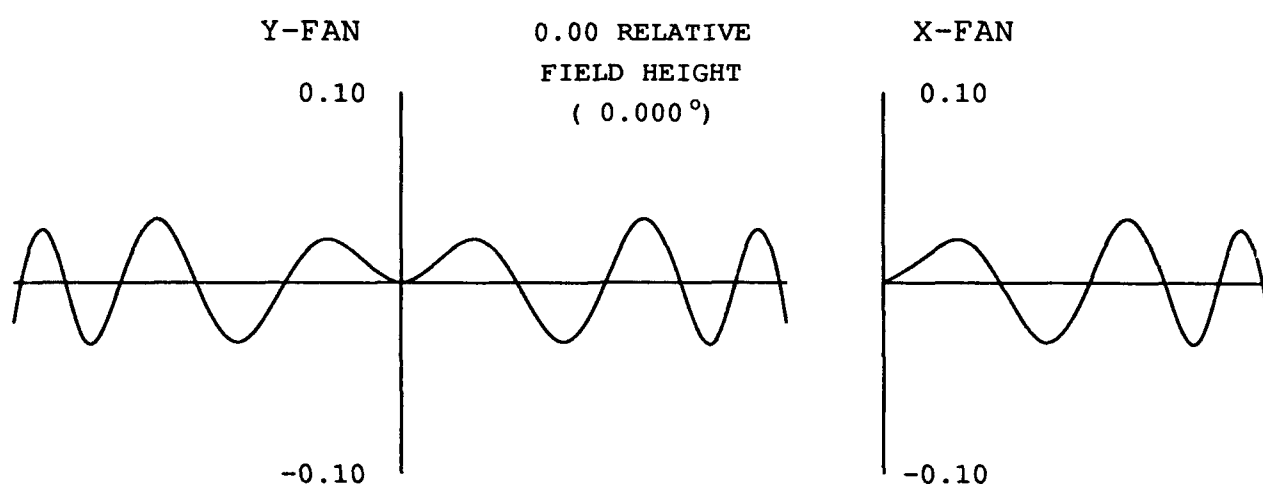The key elements of this system are the electrically addressable continuous phase SLMs. Currently, we are investigating the twisted nematic liquid crystal SLMs. Usually, these kind of modulators are made up with grid structure patterns, the crossing of which forms a picture element (pixel). The phase modulation properties is due to the birefringence of the liquid crystal as a function of the applied voltage across the pixel. In order for the modulator to implement a lens, we recall that the phase distribution provided by a lens is given by

$$\phi(x) = -(x^2 k) / (2f),\qquad\qquad 1$$

where x is the coordinate along the active direction of the lens, k is the angular wave number, and f is the focal length. To implement this lens onto the SLM, the phase function is first sampled by the pixel structure. The 2π modulus of the sampled function is then written onto the modulator. We shall call this the sampled kinoform lens. Due to the grid structure of the pixels, the pattern at the focal plane of this sampled kinoform lens is not a single focal peak, but can be approximated by an array of focal peaks given by the expression:

$$F(u) = \exp\left[jk(f + \frac{u^2}{2f})\right] \sum_{n=-N/2}^{N/2} \delta(u - n\frac{f\lambda}{d}) \operatorname{sinc}\left[(au)/(f\lambda)\right]\qquad\qquad 2$$

where d is the pitch of the pixel and a is the width of the pixel. In here we only consider the 1-D case for simplicity, and the results can easily be generalized into 2-D case. These multiple orders generate "ghost" images besides the zero-order image. However, the intensity ratio of the n-th order focal peak to the zero order focal peak is given by

$$\zeta_n = \operatorname{sinc}^2\left[n\frac{a}{d}\right].\qquad\qquad 3$$

If $d{:}a = 10{:}9$ (for example, from an SLM made by DisplayTech Company), then $\zeta_1 = 0.012$, $\zeta_2 = 0.010$, and $\zeta_3 = 0.009$. Hence, the noise due to the higher order images are acceptable in many applications.

Since $\phi(x)$ varies as x^2, the diameter of the sampled kinoform lens is limited by the dimension of the pixel. If it is required that every light element within the outermost pixel of the kinoform lens are all in phase with each other

at the focal spot, then the maximum usable diameter D of the sampled kinoform lens is given by

$$f = (aD)/\lambda \qquad\qquad 4$$

This equation limits the minimum modulus of the focal length f_{SLMmin} of a sampled kinoform lens for a given lens diameter. For any realistic values of a, Eq.4 represents a lens of very slow speed indeed.

To increase the speed, we can cascade a higher power imaging lens of focal length f_L with the kinoform lens. The combined effective focal length becomes $f = (1/f_L + 1/f_{SLM})^{-1}$. These two elements are placed in contact to maximize the change in f as a function of f_{SLM}. Since f_{SLM} can be adjusted at the frame rate of the SLM, the hybrid lens unit becomes a dynamic lens with adjustable focal length. When using this hybrid lens in an imaging system, the separation between the hybrid lens and the detector can be set at a fixed distance, independent of the location of the object to be focused on. Instead of moving the imaging lens back and forth for different object positions, the focal length of the hybrid lens can be modified. For example, if the detector is set to be at f_L behind the hybrid lens, then objects located at infinity can be focused onto the detector by implementing an infinity focal length kinoform lens onto the SLM. When f_{SLMmin} is implemented onto the SLM, the hybrid lens attends its highest power and can focus on an object located at f_{SLMmin} in front of the lens. This imaging system is analogy to that of a human eye: The dynamic hybrid lens changes its focal length by electro-optical birefringence effect, whereas the eye lens changes its focal length by contraction or relaxation of the ciliary muscle; the fixed separation between the hybrid lens and the detector is analogy to the fixed separation between the eye lens and the retina; and both systems have a "near point".

An experiment was carried out to demonstrate the dynamic focusing ability of the hybrid system. We used a 10 cm focal length convex lens as the refractive lens, and a CCD camera as the detector. Figure 1a shows the image captured by the hybrid system when a 140cm focal length kinoform lens was implemented onto the SLM. Figure 1b shows the image captured by the same system when the SLM was turned off. The light source used in this experiment was from a regular household light bulb, and the f-number of the system is f/9.3.

(a)   (b)
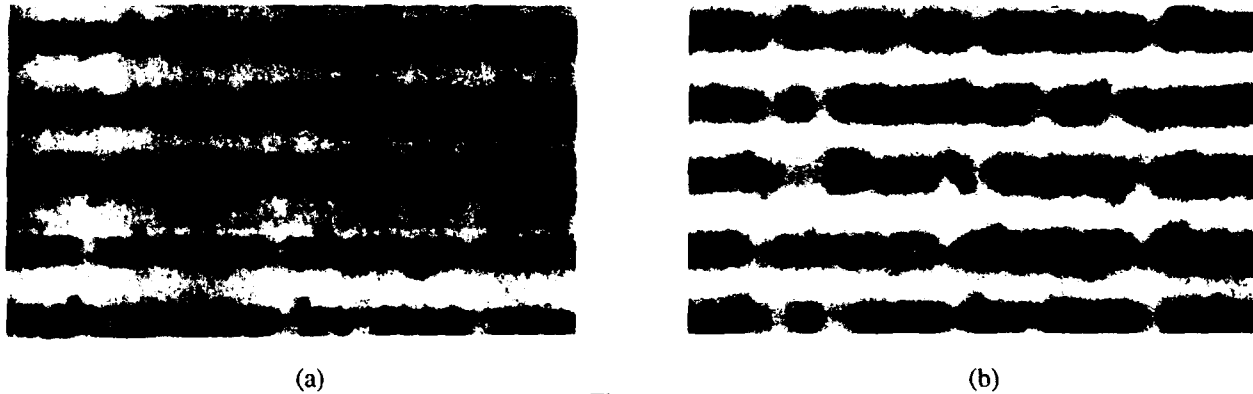
Figure 1

The cascade refractive/diffractive lens configuration not only increases the power of the kinoform lens, it also serves as partial correction for chromatic aberration of the kinoform lens. It is known that diffractive lenses suffer severely from the chromatic aberration according to the equation $f_{SLM}(\lambda) = f_o(\lambda_o/\lambda)$, where f_o is the designed focal length for wavelength λ_o. However, most optical materials exhibit refractive indices which decrease with increasing wavelength. Therefore, a hybrid refractive/diffractive doublet can be designed to achieve partial chromatic compensation. For example, we have calculated the dispersion of a 10cm focal length convex lens made with BK7 glass cascaded with a SLM based kinoform lens. Figures 2a through c plot the focal lengths of the hybrid lenses vs. wavelength when kinoform lenses of focal lengths 1000cm, 170cm and 80cm are implemented onto the SLM accordingly. The dotted lines in these graphs are the dispersion due to a single BK7 glass convex lens at the corresponding effected focal lengths, and the horizontal lines show the desire focal lengths. It can be seen in Fig. 2b that the hybrid lens is almost achromatized, and dispersion at f_{SLMmin} = 80cm is similar to that due to a single BK7 refractive lens.

(a)   (b)   (c)

Figure 2

The simple architecture discussed previously can perform electro-optical focusing at high speed. However, it does not have zooming ability because once the object is focused, the system does not permit a further change in focal length without defocusing the image. With the use of two dynamic hybrid lenses, electro-optical zooming and focusing can be accomplished s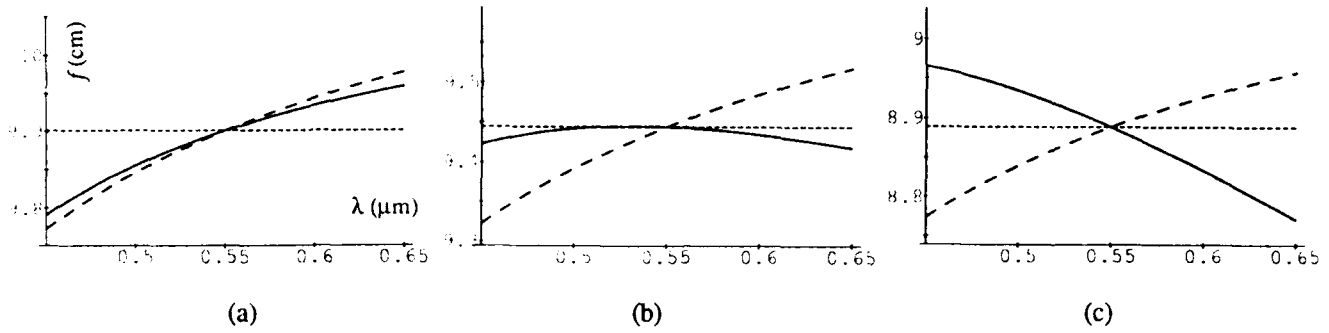imultaneously. Consider Fig. 3, with the focal lengths and distances as shown. Note that the subscripts 1 and 2 refer to the lenses in the front and back units accordingly, and the value d denotes the separation between the two units. The effective focal length of the system as a whole is given by

$$1/f_e = 1/f_1 + 1/f_2 - d/ (f_1 f_2) .$$ 5

From geometric optics, it can be derived that the object distance s_o and image distance s_i must satisfy the equation

$$s_i = \frac{f_2 d - [(f_1 f_2 s_o) / (s_o - f_1)]}{d - f_2 - [(f_1 s_o) / (s_o - f_1)]} .$$ 6

Since this system does not have any moving parts, the value of s_i and d is fixed. However, since f_1 and f_2 can be electro-optically modulated, there exists different values of f_1 and f_2 such that Eq. 6 is satisfied for different object distances s_o. This property accounts for the electro-optical focusing capability of the system. Moreover, for different values of s_o, the values of f_1 and f_2 can be evaluated to satisfy both Eqs. 5 and 6 simultaneously for different user-selected effective focal lengths f_e. This is in parallel to the zooming property of a conventional zoom lens for which the image plane is held fixed while the effective focal length of the lens is changed by mechanically driving up-and-down several lenses within the system.

$$f_1 = (1/f_{1L} + 1/f_{1SLM})^{-1}$$

$$f_2 = (1/f_{2L} + 1/f_{2SLM})^{-1}$$
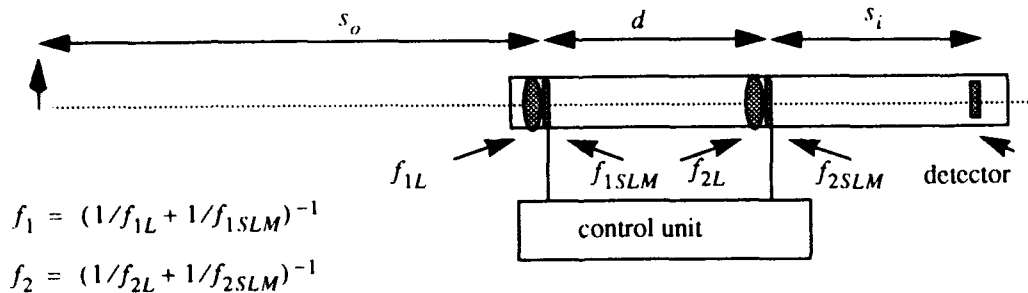
Figure 3

In summary, we have discussed the design of dynamic imaging systems using SLM based kinoform lenses. These systems can perform focusing/zooming at much higher speeds than its mechanical counterpart. The use of refractive lenses in this hybrid lenses increases the speed of the lenses and partially compensates for the chromatic aberration due to the diffractive lenses. These dynamic imaging/zooming systems will find applications in which high speed target acquisition is a major concern and the quality requirement of the images is not crucial. Robotic vision and automated navigation of land vehicles are potential candidates in these categories.

Diffractive properties of gelatin as an aerogel

Richard D. Rallison, Stephen E. Bialkowski
Ralcon Corp and Utah State University
8501 S 400 W, Box 142
Paradise Utah, 84328-0142
Ph-801 245 4623, fax-801 245 6672

Summary

Shankoff had discovered that dichromated gelatin could have an index modulation as high as .26 as far back as 1968[1] and Meyerhofer showed that this implied a reduction of effective index of refraction (n) from 1.54 to 1.27 as well as explaining the increase in thickness (T) of a developed hologram of from 1.3 to 1.4 times the original thickness before exposure.[2] The results or effects of the expansion are touched on but the implications of the change in bulk index are not discussed at all. Figure 1 shows the usual result of making a transmission grating with slanted planes, the developed hologram will playback at an angle that indicates that the planes have changed to a smaller angle due simply to the expansion of the film. This is also the special case where the light makes a 90 degree turn in the grating and no P polarized light can be diffracted. If only the planes were tipped then the internal angle of 90 degrees would be approximately maintained in spite of a changed external angle but in fact the angle changes to an angle less than 90 degrees because as the bulk index went down the effective spatial frequency went up and P light is still diffracted at lambda 1. 45 degree slants are difficult.

The relative magnitudes of the effects can be seen in figure 2 where we wish to make a grating that has an input of 0 degrees and an output of 80 degrees for 633 nm light. Without change in T and n it could be made at 488nm using 7 and 62 degree construction waves. The tilt from a change in T causes reconstruction at -7 and 62 degrees but we observe that it actually reconstructs at -12 and 55 degrees. When we account for the change in n we see that we must expose at 14 and 86 degrees to end up with an internal tilt of 25 degrees instead of 20 and the diffraction angle will be 51 degrees, not the originally assumed 40 degrees to produce an 80 degree output beam. An experimental proof that the index really is 1.27 comes from making a grating as shown in figure 3, where at 64 degrees the internal angle is 90 degrees and P is zero for any modulation while S goes through 2 maxima. Figures 4 through 9 are all derived from Kogelnik[3] and plot effeciency for S and P vs. index modulation (delta n), in plane gratings.

Prior to discovering the importance of the index change we tried to make a grating that diffracted all S and no P at 39 degrees as shown in figure 5. It did not work because it depended on the internal angle being 24 degrees but by experimenting we succeeded in 15 micron thick films at 34 degrees which could only work if we had a bulk index of 1.35. We also tried to make a grating at 50 degrees external and 30 degrees internal, (assuming n stayed at 1.54), which should have diffracted all P and no S, (fig. 7). Experimenting at angles from 36 to 53 degrees led us to a perfect fit at 38 degrees implying an n of 1.24 in a 5 micron film and a deta n of .135, (fig. 8). The fit was verified by finding equal crossing points before and after the peaks. Another accidental proof occurred during experimenting at 48 degrees where we were able to get both S and P equal to nearly 100 % as shown in figure 9 for a delta n of .19 in 5 micron film.

The model for conformal reflection structures, figure 10, also shows proof of the low effective n in reflection holograms. The reflector reconstructs at exactly the same wavelength that it was made at, at normal incidence, leading us to suppose that there has been no expansion. As we go off axis we get the dispersion curve of a material that matches the lower curve in figure 11. A simple test reveals that P light is completely transmitted at 64 degrees off the normal for a range of wavelengths around 459 nm. Figure twelve is the dispersion curves for each n and shows almost 100 nm difference in bandwidth between the two cases. Since delta n and spatial frequency are not crucial to this effect, very broadband and high contrast polarizing filters may be made on flat plates as shown in figure 12 where a chirp and high delta n are used. These effects preclude the making of precision optics without first considering the steps needed to correct for or minimize the changes in n and T. Perhaps equally as important the variable low index allows the construction of several novel polarization sensitive or insensitive devices.

References

1. T. A. Shankoff: Appl. Opt. 7, p2101 (1968)
2. D. Meyerhofer: Springer-Verlag, Holograpic Recording Materials vol 20, chapt.3 p84(1977)
3. H. Kogelnik: Bell Syst Tech J. vol 48, p2909 (1969)
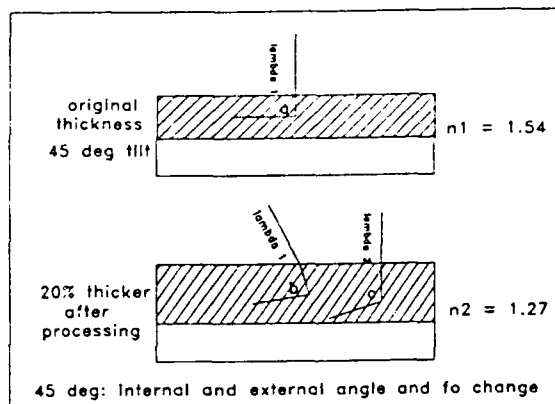
figure 1- 45 degree slant of planes
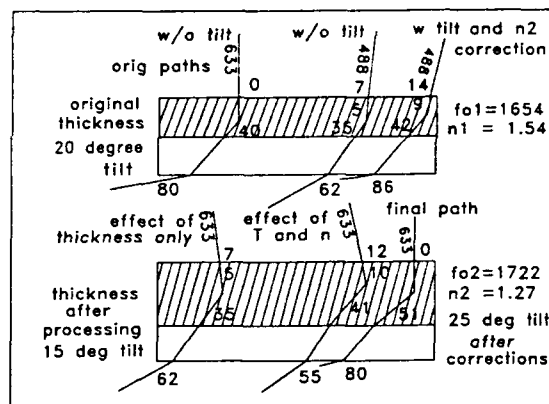
figure 2- compensating for change in n and T
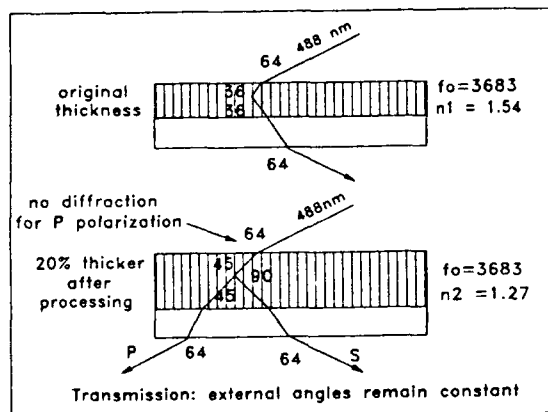
figure 3- grating that will prove low n
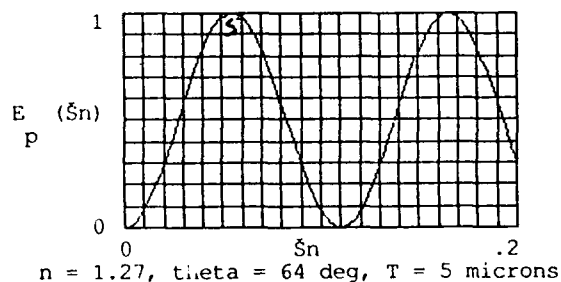
figure 4- effeciency of S in fig 3 grating

E_p(Šn)

0   Šn   .10
n = 1.54, theta = 39 deg, T = 15 microns
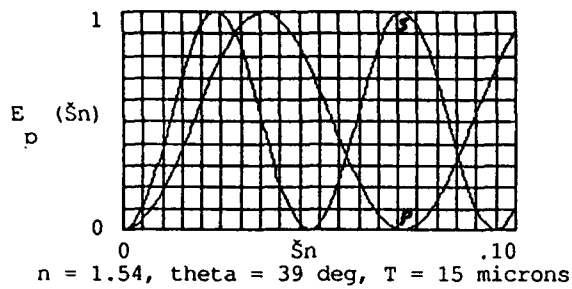
figure 5- conditions for 100% S, 0% P

E_p(Šn)

0   Šn   .10
n = 1.35, theta = 34 deg, T = 15 microns
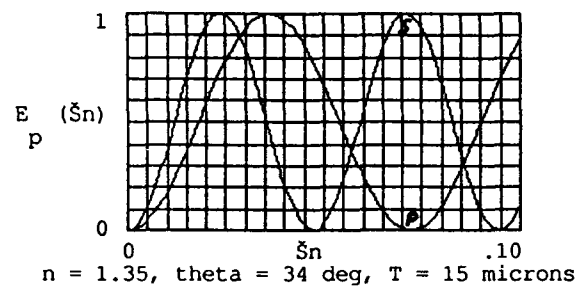
figure 6- experimentally determined best fit for 0 P

E_p(Šn)

0   Šn   .2
n = 1.54, theta = 50 deg, T = 5 microns
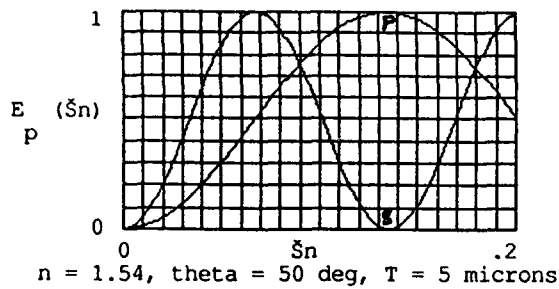
figure 7- conditions for 100% P, 0%S

E_p(Šn)

0   Šn   .20
n = 1.24, theta = 38 deg, T = 5 microns
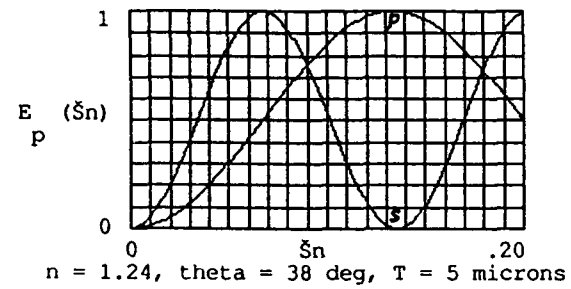
figure 8- experimentally determined best fit for 0 S

E_p(Šn)

0   Šn   .2
n = 1.27, theta = 48 deg, T = 5 microns
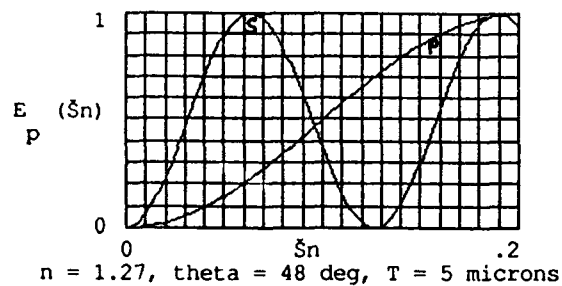
figure 9- best fit found for max S and P
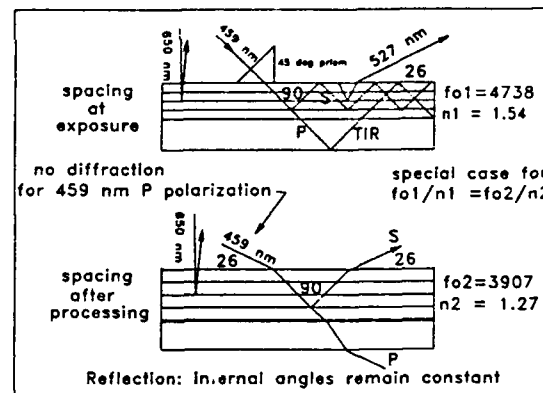
figure 10- conformal reflection grating model

λ2(b), λ3(b)

Reflector external angle and λ dependence on n

figure 11- dispersion curve for reflectors
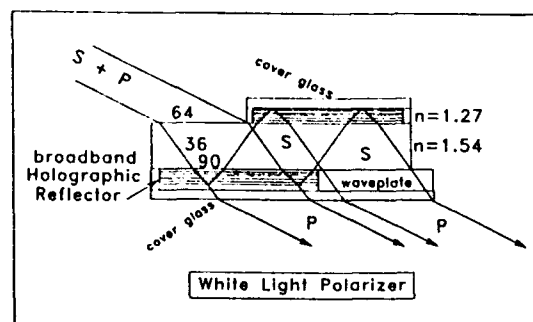
figure 12- practical new polarizer design

Binary Mask Generation For Diffractive Optical Elements Using Microcomputers

Donald C. O'Shea, James W. Beletic and Menelaos Poutous
Center for Optical Science and Engineering
Georgia Institute of Technology, Atlanta, GA 30332
(D.C. O'Shea and M. Poutous are with the School of Physics 404-894-3992 and J.W. Beletic is with Georgia Tech Research Institute 404-894-3646)

A new technique for generation of binary masks for the fabrication of diffractive optical elements is presented. This technique, which uses ordinary desktop publishing software and hardware in conjunction with a standard photoreduction camera, is much faster and less expensive than the conventional methods. The short turnaround time and low cost should give researchers a much greater degree of flexibility in the field of binary optics and enable wider application of diffractive optics technology. The paper includes examples of optical elements made by the new technique.

I. Introduction

The design and fabrication of diffractive optical elements, often called *binary optics*, can be divided into two main steps. The first step involves the design and generation of binary masks which define the desired optical surface. The second step involves the transfer of the binary mask pattern to photoresist and subsequent transfer of the photoresist surface relief to the substrate by ion beam etching. The photoresist and ion etching processes have been highly refined by the microelectronics industry. Given a high quality binary mask, sta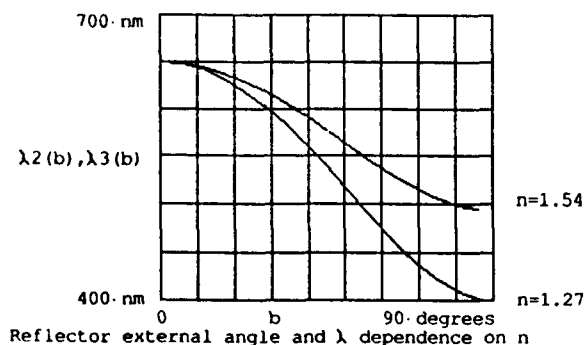ndard clean room equipment can readily attain 1 μm feature size and etch accuracies of 100Å (equivalent to $\sim 1/100$ wave optical accuracy) — this precision is more than adequate for most binary optics applications. The photoresist and ion etching processes are routine procedures; the combined turnaround time is approximately one day. However, the design and generation of binary masks is typically a very complicated and expensive process with a substantial time period (up to months) between initial concept and finished mask. The difficulties and expense of binary mask generation have been major impediments to the widespread incorporation of binary optics technology into modern optical engineering.

We have developed techniques that enable researchers to produce high quality binary masks quickly and inexpensively. This methodology should permit researchers in diffractive optics a greater degree of flexibility in designing and fabricating binary masks. The low cost should also enable wider access to binary optics technology.

II. Conventional Mask Generation

Binary masks are generated by exposing and developing the photoresist (or photoemulsion) on a mask plate. Two standard methods of exposure have been developed for the fabrication of microelectronics: (i) optical exposure by a *pattern generator*, and (ii) exposure by an electron beam in an e-beam machine. The e-beam approach can generate the finest features, however due to the small scale of the electron beam it is extremely time consuming to expose a pattern of large extent.

The pattern generator is a machine which constructs a mask pattern via a series of flash exposures of a rectangular or trapezoidal aperture. The design input to most pattern generators is compiled as a series of commands that control the translation, rotation, and size of the rectangular aperture. The more elaborate the design, the more time consuming and expensive will be the generation of the mask. This represents a serious disadvantage when it comes to all but the simplest of binary masks for diffractive optics, since many elements require curved lines. These curved lines can only be generated by approximating them with smaller apertures, thereby increasing the number of flashes, the time to complete the pattern, and the cost.

In general, binary mask generation is a time consuming, laborious and expensive process. The optical design, which may be originally specified as an analytical equation, must be fractured into a primitive exposure set, which may to some degree compromise the original calculation. The series of commands in the exposure set must then be encoded into specialized formats and transmitted to the mask generation facility. Since the mask generation is typically at a remote site, a month or longer delivery time is not uncommon. These masks are usually very expensive, especially in the case of complicated designs (as much as $3000 apiece).

III. Desktop Publishing Resources

In contrast to the computer-aided design stations and the mask generators used in semi-conductor fabrication, there is another technology that is capable of elaborate pattern generation, but is considerably more accessible to most researchers. This is the desktop publishing field that has grown up in the past five years as inexpensive graphics-oriented microcomputers and laser printers have become readily available.

The first benefit of this new technology is that the problem of filling regions of any arbitrary shape is solved by an elaborate page description language, called *PostScript* (developed by Adobe Systems, Inc.). This language is the most widely used method of transferring complex graphics to a wide range of output devices that render the graphics with a high degree of accuracy. The language has been developed so that resolution limitations are defined by the printing device and not by the language.

The PostScript language specifies a format for describing graphics that permits different software programs to exchange the graphical information. This format, Encapsulated PostScript Format (EPSF), enables one to generate an illustration in a drawing program, import it into a word processing program, modify it as desired and print it out in a high resolution format on a laser printer.

We have tested a number of commercially available software programs and have found that an illustration program from Aldus Corporation, Aldus Freehand, provides the control over placement and size of details necessary for generating the binary patterns we require. We also have found the computation program Mathematica to be very useful. It enables a researcher to easily undertake complex functional programming using ready made mathematical functions and produce Postscript output.

The aim of our efforts was the generation of binary masks on a high resolution device. One question that arose in the course of this research was the "resolution" of the device we were using. As a rule of thumb, we have found that the number of line pairs that can

be produced by a printer is about one eighth of the number of dots per inch. For example, a high resolution, 2540 dpi printer has a line pair has a width of about 80 microns with a minimum feature size of 40 microns.

In the course of our research we have used the Linotronic 300 printer (2540 dpi), manufactured by Linotronic AG, Germany. At the level of 40 micron feature size, the binary masks that could be produced would be useful as little more than a demonstration of technique. We can obtain the required detail by standard photomask reduction techniques used in the semiconductor industry. The photoreduction camera we use is capable of reductions of 10 and 50 times; the minimum feature size that we can reliably produce at the present time is 5 microns.

IV. Experiments

We are in the process of fabricating the following optical elements:

- A random phase array for use in a holographic recording system. This piece consists of a 16 by 16 square array of small squares, 50 microns on a side and spaced 100 microns apart. The phase of each square is randomized so as to suppress a strong zero order in the resulting diffraction pattern and minimize crosstalk between adjacent bits.

- A Dammann grating which is a diffractive optical element consisting of one or two dimensional linear patterns of regions that produce either no phase change or a 180° phase change. These gratings can be produced with a single mask and a single etch cycle. The purpose of a Dammann grating is to generate a series of grating orders of equal intensity; in the fields of diode laser arrays and multiple detector arrays there are applications as beamsplitters and combiners.

- A microlens array for a wavefront sensor camera. This optic consists of a 100 x 100 array of square lenses, each 128 microns diameter with focal distance of 6 mm. Due to the low power and small lens diameter, this lenslet array is a white light element.

- A random phase plate for simulation of atmospheric phase distortions. This large diameter (100 mm) optic, being made in collaboration with the Max Planck Institute (Germany), must be a white light element with several microns of phase variation across the surface. We will be using the same fabrication techniques but will extend them to deep etches and many levels (8 masks for 256 levels).

Georgia Tech has a microelectronics clean room facility on campus that includes all of the equipment required for binary optics fabrication. Combined with our methodology for mask generation, we can quickly and inexpensive produce binary optics components for a variety of applications.

V. Conclusions

We have described a number of tools and techniques that can provide easy availability of binary mask generation to students and researchers. By taking advantage of the widely available illustration programs that use PostScript to generate the documents for the binary optics designs and to place mathematically generated patterns within these documents, anyone with a graphically oriented microcomputer can generate binary mask patterns. This takes the field of diffractive optics design out of the realm of the specialist and enables interested researchers to grapple with the problems in constructing a design.

METHODS FOR DIFFRACTIVE ELEMENTS SURFACE PROFILE FABRICATION

A.G. Poleshchuk

Institute of Automation and Electrometry, Russian Academy of Sciences, Siberian Branch,

630090 Novosibirsk, Russia

INTRODUCTION

The progress in optics is related to wide application of computer-synthesized diffractive optical elements (DOE). The lithography technology allows one to fabricate easily a DOE with binary profile. Using a set of $N = 3$-4 masks one can fabricate multilevel DOE with the diffraction efficiency (DE) over 90% [1]. Another way to form a DOE profile is based on incoherent spatial filtering of a periodic mask spectrum and bleaching of the exposed film [2]. This method simplifies substantially the process of DOE fabrication because it does not involve fabrication and aligning of a set of masks. However, this method allows to fabricate only periodic DOE.

The paper presents the investigation results of a new method [3] for fabrication of high-efficiency DOE based on the technique of halftoning and incoherent spatial filtering combined with the ordinary lithography process. The comparison is carried out of characteristics of the method proposed with known ones – continuous-tone and multilevel.

PRINCIPLE OF DOE FABRICATION

The fabrication problem of a phase-only DOE (kinoform) with the transmission function $T(x) = \exp[if(x)]$, is solved by forming a relief $h(x) = f(x)/k(n - 1)$ in the substrate, where $k = 2\pi/\lambda$, λ–the wavelength, n – the refractive index. Such a relief $- h(x) = D - cI(x)$, where c is a coefficient, can be produced by exposing of a resist layer with the thickness D by radiation of intensity $I(x)$. If $I(x)$ is proportional to the phase function $f(x)$, a DOE with the transmission function $T(x)$ is formed in the resist layer. In other words, for this purpose a continuous-tone mask with the transmission function $U(x) \sim f(x)$ is neces-

sary. If is rather difficult to fabricate such a mask, thus it is proposed to substitute a raster mask with binary transmission for continuous-tone one, using one of known algorithms for image binarization. The projection system of a lithography setup filters the spatial frequencies of the rastered mask transmission function. Fig. 1a depicts the schemes of the setup for performing the method. Raster mask 2 is illuminated with incoherent light flux 1. Projecting system 3 forms the intensity distribution close to function $f(x)$ in the resist plane. The relation between the cutoff frequency F_c of the optical transmission function (OTF) of lens 3 and frequency spectrum fx are shown on Fig.1b. According to the sampling theorem, the relation $f_x < F_c < F_d$ must take place.

Fig. 1.

METHODS OF RASTERING

Two methods were studies for forming continuous phase DOE profile – with the algorithms of pulse-density and pulse-width modulation (PDM and PWM). Fig 2 a,b correspondingly, show the transmission function of a PDM-rastering mask and its intensity spectrum $G(f_x)$. One can see that in the lower frequency range it also contains
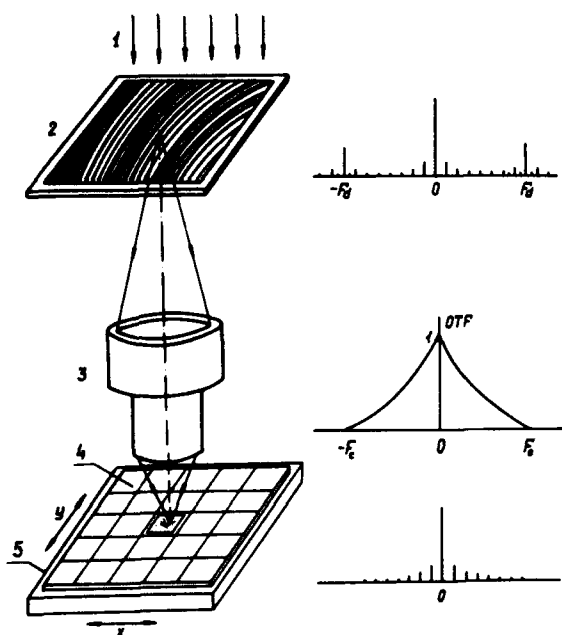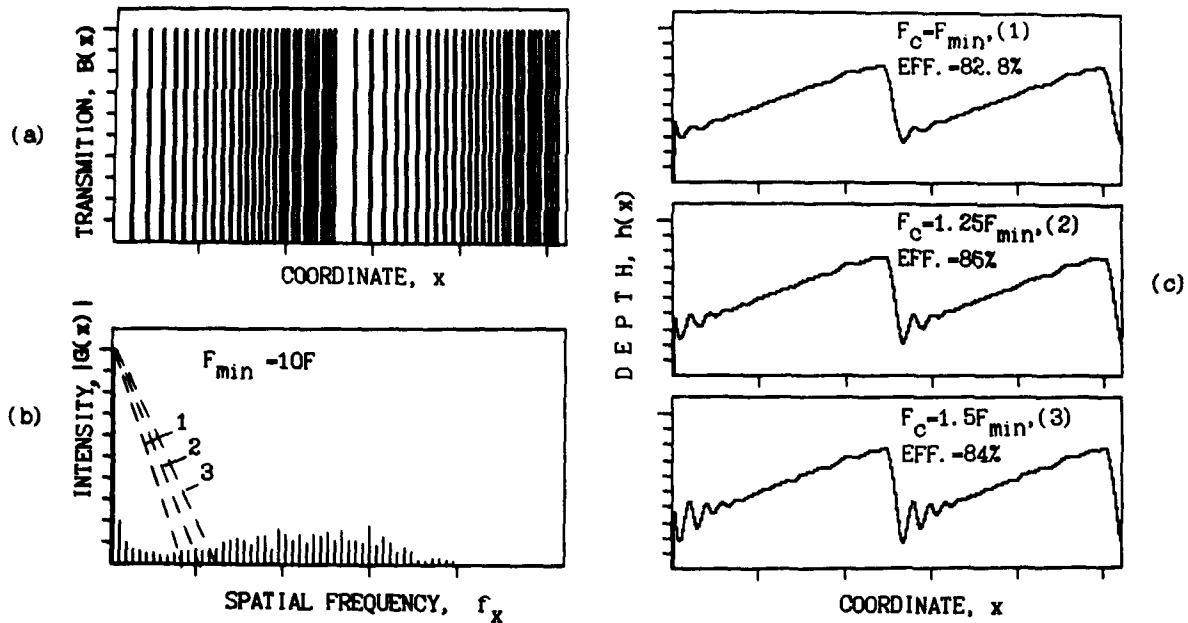
Fig. 2.
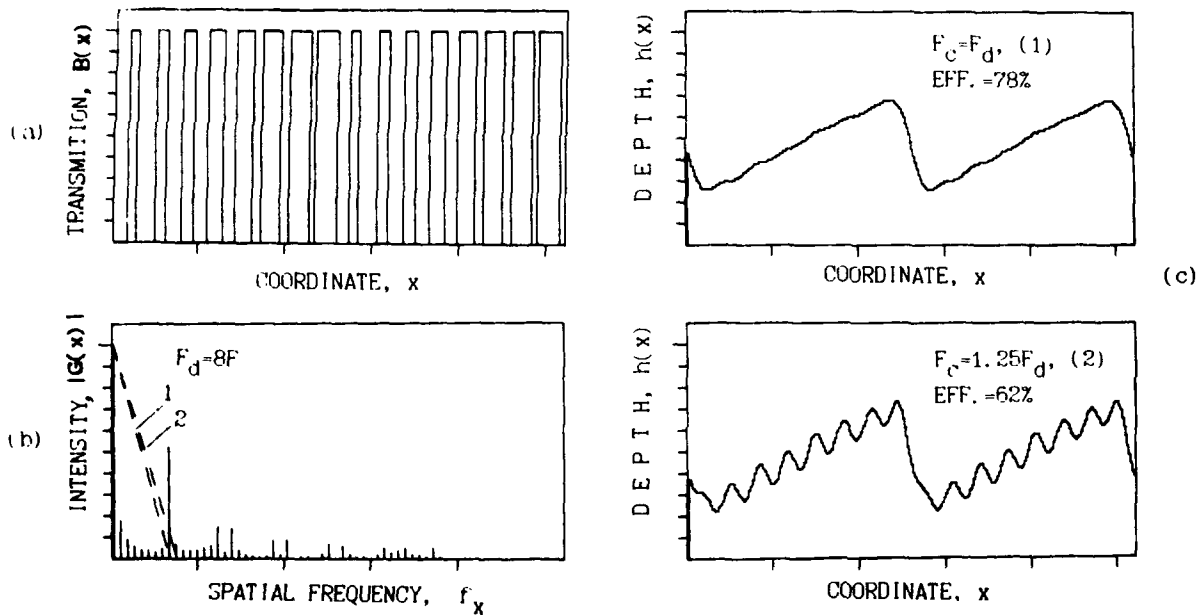
Fig. 3.

combinative components. The relief depth in resist depends on the value of the cutoff frequency of the OTF (dotted lines on Fig 2,b). Fig 2c shows the relief shape for three values of F_c/F_{min} (F_{min} is minimum discretization frequency) under constant spatial frequency $F = 1/T$ of the saw-tooth function. As F_c grows, the relief shape h(x) approaches saw-tooth shape. The binarization of initial function $U(x)$ causes distortions that can be well observed when $F_c > F_{min}$.

Under PDM the spatial frequency of the raster strips is constant, their width being proportional to the value of function $f(x)$) being coded in the points of discretization. Fig 3 a,b show, correspondingly, the transmission function of a PWM- rastered mask and the modulus of its spatial spectrum. The mask spectrum at Fd frequency has a component caused by the discretization. Fig. 4 presents the dependence of a DE saw-tooth grating as a
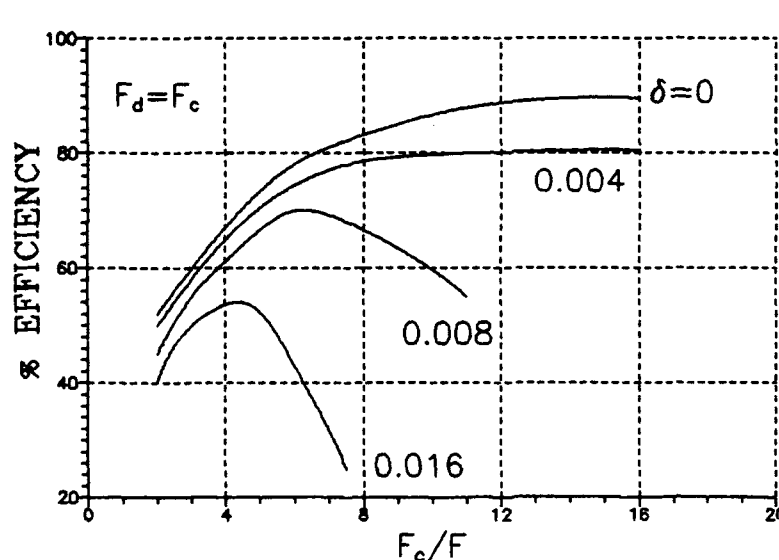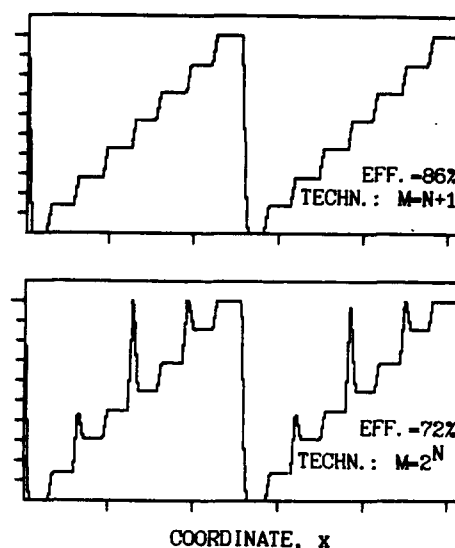
Fig. 4.   Fig. 5.

function of the number m of harmonics forming the image in the resist plane under different values of relative mean square error $\delta = \sigma/T$ in the raster lines location. As the errors grow, DE decreases rapidly.

MULTILEVEL TECHNOLOGIES

Photolithography multilevel method for DOE fabrication comprises the preparation of a set of masks and, consequently, their topology transfer into the substrate relief. Two varieties of this method are known. Fig 5 a,b show the examples of relief forming with both variants of multilevel method in the presence of fabrication errors. One can see that real DE is much lower than ideal one (95%). The DOE characteristics are mostly affected by the mask fabrication errors. The comparison of multilevel and raster technologies demonstrated that the technology proposed has advantages mostly when fabricating DOE with the size of zones less than 5–10 μm.

EXPERIMENTAL RESULTS

For discretization of the continuous-tone function the PWM algorithm was chosen. The raster mask was fabricated on a circular laser image generator [4]. The DOE microrelief was formed in a layer of resist FP-051 about 2 μm thick, and next, by means of ion etching it was transferred into the substrate. The relief depth in the resist was controlled by the value of exposure. Lenslet arrays (N.A. = 0.1) and aberration correctors were fabricated. DE over 80% was achieved under the size of saw-tooth zones 4-5 μm.

REFERENCES

1. G.J. Swanson, W.B. Veldkamp, "Diffractive optical elements for use in infrared system", Optical Engineering. 28, p. 605–608, (1989).

2. O. Bryndahl, "Formation of blased grating", J. Opt. Soc. Am., 60, p. 140–141, (1979).

3. A.G. Poleshchuk, Fabrication of High Efficient Elements for Diffractive and Integrated Optics by Photorastered Technology, The 5-th National Conference on Optics and laser engeneering, May 18-20, 1989, Varna, Bulgaria. p. 7-8.

4. V.P.Koronkevich, A.G.Poleshchuk et al., Fabrication of kinoform optical elements, Optik, 67, p. 259-266 (1984).

MacBEEP: A Desktop System for Binary Optics*

Philip S. Levin and Lawrence H. Domash
Foster-Miller, Inc., 350 Second Ave., Waltham, MA 02154
tel. 617-290-0992

1. The Need for Low Cost Binary Optics Methods

Binary optics is widely recognized as an important advance, but the full development of applications has been inhibited by the limited availability of the necessary software and hardware tools to experiment with binary elements. Special purpose scientific binary optic design software and e-beam fabrication facilities are found in only a few laboratories, to which most university or government researchers or industrial designers have little access.

We report some results of an ongoing project named MacBEEP (Macintosh-based, Binary Elements Encoded in Phase) whose purpose is to develop low cost methods for creating binary elements of various resolution levels easily and quickly using more widely available equipment. Initial goals were to optimize the use of personal computers and PostScript compatible laser typesetters which are widely available in most cities on a rental basis as part of the desktop publishing service industry, develop appropriate software to work in combination with commercially available programs, and evaluate various simple processing methods to convert binary amplitude film to binary phase objects, leading to an integrated software, hardware and processing approach to make the best binary elements possible within two self imposed limitations--ease of use and low cost. Laser typesetters offer 10 μm resolution on film, which may be used directly or as masks for photoreduction. A second stage of the program extended the MacBEEP system to include a high resolution output device, a scanning electron microscope, with feature sizes as small as 0.05 μm. In previous reports (1), we showed that PostScript (2), the industry standard page description computer language for desktop publishing, could be used to conveniently encode holographic patterns. PostScript describes patterns in a universal file format which can be proofed on paper at 80 μm resolution using PostScript-compatible office laser printers and then used to produce film output at 10 μm resolution using industrial laser typesetters (3).

2. MacBEEP System

A Macintosh IIx computer with numerical accelerator, frame grabbing board and CCD camera was the host computer. While IBM family PCs may also be used, the Mac is well adapted for image/graphics applications and supports the easy interchange of graphical data among programs. Our approach was to combine the capabilities of a suite of available commercial CAD, graphics or mathematical computation programs to compute a binary element in stages, passing the data from program to program. We modified a public domain image processor (5) by adding the capability for 512 X 512, 32 bit forward and inverse fast Fourier transforms, facilities for exchanging large 32 bit files with Mathematica (4), and precise software control of PostScript-based imagesetters, particularly with regard to scaling, pixel boundaries, page placement and tiling of patterns (Figure 1). Two output devices have been used to date. The Linotronic 300 Imagesetter, a 2540 pixel per inch HeNe laser-based laser film recorder, produces up to 25,000 X 25,000 10 μm pixels. Scanning electron microscopes produce 0.05 μm spot size. Although our research included some efforts to optimize the Linotronic hardware, adjust it to expose special films and other techniques which require access to a dedicated machine, many of our results can be duplicated simply by outputting PostScript files to any standard service-bureau imagesetter, available in most U.S. cities for charges on the order of $4-10 per film page.

3. Processing Alternatives for Laser Imagesetters

In addition to software development and system integration, we investigated various alternative methods of converting binary amplitude films produced by the Linotronic to binary phase elements. Based on the overall system goal of easy use, low cost, and fast turnaround, we were primarily concerned with identifying techniques accessible to the average laboratory. The methods we tried included bleached holographic film (Figure 2), contact printing to photoresist, contact printing to a photopolymer, etched glass, and 5X photoreduction. To compare the results, we used a single Dammann grating pattern test file for each of the processing alternatives.

4. SEM Pattern Generators

SEMs cost approximately 5% as much as microelectronics e-beam facilities and represent an attractive output device if used in microlithography mode. We have demonstrated the feasibility of using scanning electron microscopes in a direct-write mode to produce binary holographic optical elements with sub-micron resolution. We generated optical pattern descriptions in both analytic and digital formats, i.e. in vector format and in bitmap format, and used commercial SEM drivers (6,7) to control the positioning coils of a scanning electron microscope to write the pattern in e-beam resist; an example is in Figure 4.

5. Results and Summary

For the purposes of comparing diffractive performance, an outside vendor fabricated a submicron resolution Dammann grating by traditional means of e-beam lithography at a cost of approximately $3000. Figure 3 shows the optical reconstruction of an element generated by MacBEEP at a cost of less than $20.

MacBEEP is an integrated software, hardware and processing system based on equipment readily available to many optical researchers and designers. Laser film recorders, with 10 μm pixels, may be used on a dedicated basis or else are widely available through local service providers. An SEM may be driven from the same system. The system may be used to produce useful binary optics for a variety of experimental, developmental, educational and proof-of-concept applications.

6. References

1. L. Domash and P. Levin, Computer Holographic Elements Using PostScript Laser Printers, Topical Meeting on Optical Computing, Technical Digest Vol 9, Optical Society of America, Salt Lake City, 1989.
2. PostScript is a product of Adobe Systems, Inc.
3. Linotype-Hell GmbH., Germany.
4. Wolfram Research Corp.
5. "Image," a program created by Wayne Rasband of the National Institutes of Health. The cooperation of Mr. Rasband is gratefully acknowledged.
6. JC Nabity Lithography Systems, Nanometer Pattern Generation System, Bozeman, MT.
7. Raith Inc., ELPHY System, Farmingdale, NY.
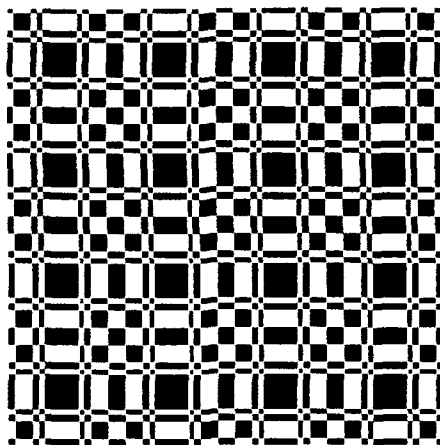
Figure 1. Dammann grating PostScript file pattern created in MacBEEP. This pattern was used to evaluate a variety of processing approaches.
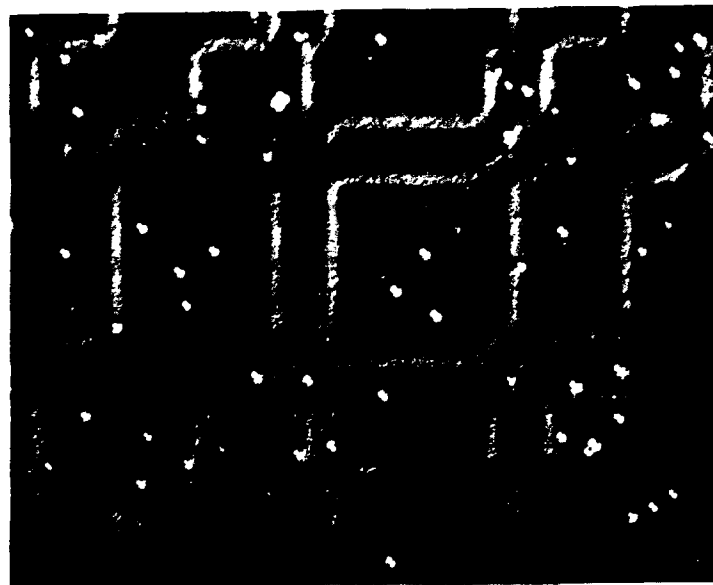
Figure 2. 100X photomicrograph of bleached Agfa 10E75 film with pattern of Figure 1. The film was exposed by direct-write with a laser printer.
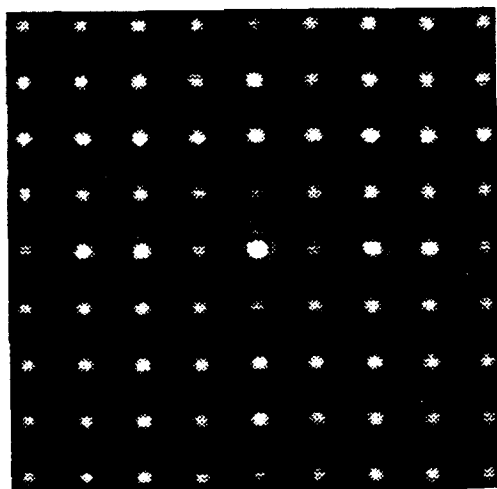
Figure 3. Optical reconstruction for the bleached sample of Figure 2. The ideal reconstruction would have a 9 x 9 pattern of equal intensity beamlets. Cost to produce this sample was less than $20.
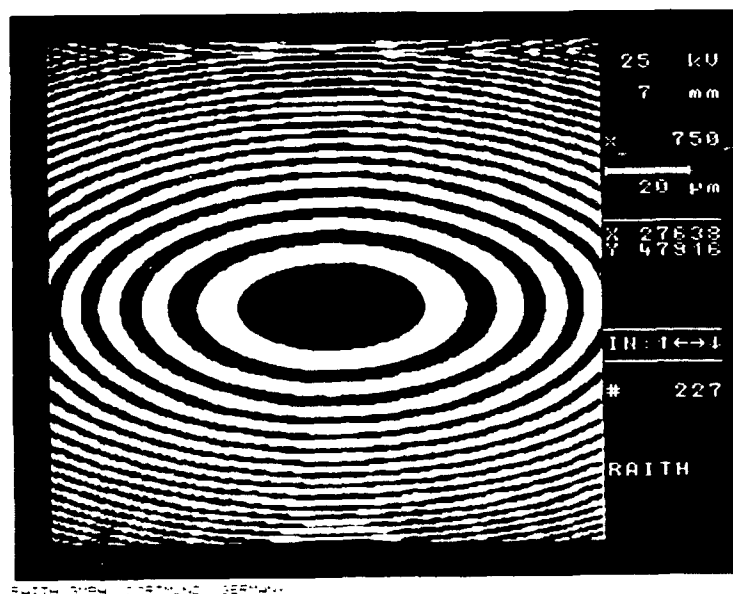
Figure 4. 750X SEM micrograph of section of a SEM raster-written 4 x 8 zoneplate array exposed in PMMA resist.

Holographic Optical Elements for Incoherent Spatial Filtering with Longitudinal Periodicity

S. Grüner Hanson, Risø National Laboratory, DK-4000 Roskilde, Denmark

1. Introduction

Self-imaging without conventional optical elements has been studied extensively. A good overview of the field has recently been published[1]. Diffraction by white light by two equal periodic structures is usually referred to as the Lau effect, and will form the basis for the structures which are considered in this investigation.

Optical transfer functions giving rise to longitudinal periodicity have applications in various fields including interferometry[2], spatial filtering[3], and acoustooptics[4].

Linear gratings have the property of being translationally invariant. Observing a linear periodic grating which is cyclically shifted perpendicularly to the grating lines will give rise to no change in the perceived image if the shift is an integer multiple of the grating period. Shifting of the grating along the optical axis, or rotated around any axis, either the optical axis or an axis perpendicular to this axis, results in a change in the structure of the image. It is the purpose of this contribution to investigate the basic "grating" structures which have cyclic invariance for the various translations and rotations. The filter which provides an invariance for translations along the optical axis will be described in detail and the application of these filters for facilitating longitudinal periodicity for white light illumination will be analyzed and experiments presented.

2. Theory for on-axis shift invariant holographic filters

Consider a rotationally symmetric amplitude filter with a periodic transmission function which can be written

$$T(\rho)=1/2[1+Cos[\varphi(\rho)]], \qquad (1)$$

where $T(\rho)$ is the radial transmission function, and $\omega(\rho)$ is the radially dependent cyclic frequency. Two observers situated at the distances $\mathscr{L}$ and $\mathscr{L}+\Delta\mathscr{L}$ from the amplitude filter will - apart from boundary effects - observe identical patterns if

$$\partial\varphi/\partial\rho\equiv\omega(\rho)=2\pi\ \mathscr{L}/(\Delta\mathscr{L}\ \rho). \qquad (2)$$

The filter function can therefore be written;

$$T(\rho)=1/2[1+Cos[\omega_0\ Log[\rho/\rho_1]]] \text{ for } \rho\ \ \rho_1. \qquad (3)$$

This filter has a radially decreasing fringe spacing in contrast to the Fresnel plate. As the radius decreases, the cyclic frequency will increase ad infinitum. Consequently an inner radius ρ_1 has to be introduced in order to realize the filter. If the outer radius is ρ_2, we will have the following three figures pertaining to the filter, namely the maximum fringe spacing Λ_{max}, the minimum fringe spacing Λ_{min}, and the total number of cycles N:

$$\Lambda_{min}=2\pi\ \rho_1/\omega_0;\ \Lambda_{max}=2\pi\ \rho_2/\omega_0;\ N=(\omega_0/2\pi)\ Log[\rho_2/\rho_1].$$

The filter thus introduces a phase shift for a scaling in the radial ρ-direction.

1

If two identical logarithmic gratings are placed at a mutual distance of ΔL preceding an incoherent source, the on-axis intensity at a distance L will be given by:

$$I(L) \propto \frac{2\pi}{(L+\Delta L)^2} \int_{\rho_2/\beta}^{\rho_2} d\rho \; \rho \; T(\rho) \; T(\beta \; \rho), \tag{4}$$

where $\beta = L/(L+\Delta L)$ is the scaling factor. If spatially high frequency contributions are discarded, the on-axis intensity can be shown to be proportional to:

$$I(L) \propto [1 + \text{Cos}[\omega_0 \; \text{Log}[\beta]]]. \tag{5}$$

An oscillation in the axial intensity distribution, which is to first order independent of the lack of temporal and spatial coherence, is observed. The fringes are not equidistant, but the fringe spacing Λ_L is given by:

$$\Lambda_L = \frac{2\pi \; L \; (L+\Delta L)}{\omega_0 \; \Delta L} \tag{6}$$

The theoretical modulation depth of the on-axis intensity variation is 50% for an amplitude filter. A thin diffraction grating could provide a higher modulation.

3. General filters with shift- and rotational invariance

Considerations identical to the ones above will lead to the following basic filters with the invariance properties:

Invariance	Expression	Type
rotation about axis $\perp$ optical axis	$1/2(1 + \text{Cos}[\omega \; \text{Log}[x/x_0]])$	Linear log grating
rotation about optical axis	$1/2(1 + \text{Cos}[N \; \text{ArcTan}[y/x]])$	Spoke target
shift perpendicular to the optical axis	$1/2(1 + \text{Cos}[\omega \; x])$	Linear grating
shift along optical axis	$1/2(1 + \text{Cos}[\omega \; \text{Log}[\rho/\rho_0]])$	Rotational symmetric logarithmic filter

Like the rotational symmetric filter these filters will have imaging properties with incoherent light if placed a distance behind each other.

2

4. Experimental results with circular symmetric logarithmic filter

Two binary holographic transmission filters with a transmission function equal to the rounded value of expression (3) were manufactured by E-beam lithography. The parameters were: $\omega_0 = 200$; $\rho_1 = 96$ μm; $\rho_2 = 12.5$ mm which gives the following derived parameters $\Lambda_{min} = 3$ μm, $\Lambda_{max} = 393$ μm, and a total of N = 155 cycles. The following figures depicts the intensity distribution on the axis as a function of the distance to the exit filter for a mutual distance of 65 mm between the two filters.
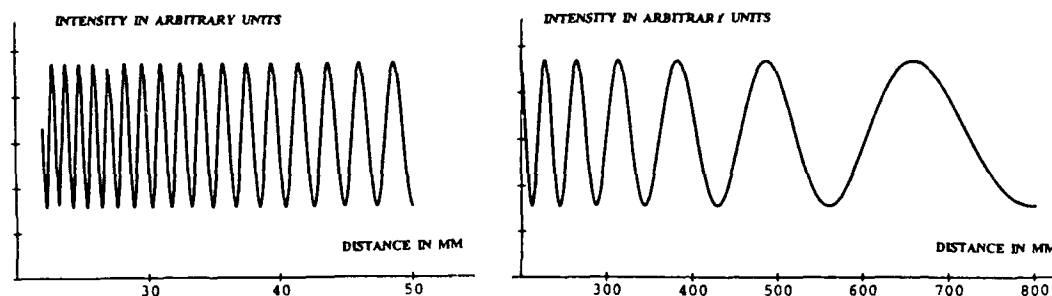
Fig. 1. On axis intensity for incoherent illumination of two logarithmic filters with a mutual distance of 65 mm.
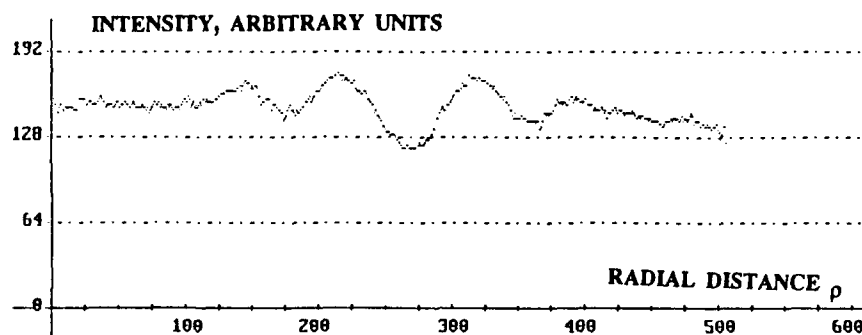
Fig. 2. Intensity distribution perpendicular to the optical axis for imaging of the experimental filter.

References:

1 K. Patorski, *The self-imaging phenomenon and its applications*, Progress in Optics, Vol. XXVII, Elsevier Science Publishers, 1989.

2 S. Jutamulia, T.W. Lin, and F.T.S. Yu, "Real-Time Color Coding of Depth Using a White-Light Talbot Interferometer", Opt. Commun. 58, 78-82 (1986).

3 C. Colautti, E.E. Sicre, and M. Garavaglia, "Incoherent Optical Spatial Filtering Based on the Lau Effect," Opt. Commun. 57, 16-20, 1986.

4 N. Saiga and Y. Ichioka, "Visualization of the Strain Wave Front of a Progressive Acoustic Wave Based on the Talbot Effect," Appl. Opt. 24, 1459-1465 (1985).

3

Achromatic Fraunhofer and Fresnel diffraction patterns: theory and experiment

P. Andrés, J. Lancis, W.D. Furlan*, and V. Climent

Universitat Jaume I, Departamento de Ciencias Experimentales, 12080 Castellón, Spain.
Telephone: 34-64-345700, Fax: 34-64-345715
*Universitat de Valencia, Departamento de Optica, 46100 Burjassot, Spain.

1. Introduction

The optical Fourier transform provided by an ideal achromatic Fourier transformer is located in a single Fraunhofer plane, but with the same magnification for each wavelength [1]. Similarly, an achromatic Fresnel diffraction pattern results from the in-plane superposition, with the same scale, of the incoherent monochromatic versions of a specific Fresnel pattern generated by the spectral components of the incident light.

The use of diffractive optical elements (DOEs) seems to be limited to quasimonochromatic optical systems due to their severe chromatic aberrations. However, some appropiate combinations of DOEs and refractive achromatic lenses allow to obtain both achromatic imaging setups [2] and achromatic Fourier transformers [3-5]. In all cases, the minimum number of optical components is three, and at least two of them are diffractive elements.

In this contribution we present an all-diffractive achromatic Fourier transform system working with white-light converging spherical wave illumination. Our optical device simply consists of two on-axis blazed zone plates. Here, the wavelength compensation is again performed taking advantage of the chromatic aberrations of DOEs. The above system allows to obtain the achromatic Fourier transform (AFT) at a finite distance with very low chromatic aberrations over the entire visible spectrum.

Our proposed device uses two DOEs and does not require any dispersive or achromatic conventional objective, resulting in a very compact and easy-implemented setup. Moreover, our proposal has also the following remarkable feature, the scale factor of the Fourier transform can be varied by simply moving the input signal along the optical axis of the system, but the achromatism remains unchanged. Consequently, a novel and flexible achromatic scale-tunable Fourier transformer is obtained.

We also point out that our approach can be used in a very simple way for achromatizing Fresnel diffraction patterns. In this way, it is possible to obtain an achromatized version of a selected Fresnel pattern of any pupil, using a single zone plate. Here, the position of the input transparency along the optical axis permits to select the Fresnel diffraction pattern to be achromatized. Some works in the direction of achromatic Fresnel holograms [6] and achromatic Fresnel diffraction patterns for the case of polychromatic self-images [7] were previously done.

The above results allow the extension of some of the conventional monochromatic information processing techniques to polychromatic signal processing, and consequently colour signals could be employed as input objects.

2. All-diffractive achromatic Fourier transformer

Our suggested setup is depicted in Fig.1. The input transparency is illuminated with a polychromatic spherical wavefront beam, with end wave numbers σ_1 and σ_2, converging towards the point source S placed at a normal distance z beyond the aperture. The first zone plate, ZP_1, provides the Fourier transform of the input object at a different plane and with a different scale for each wavelength. A second zone plate, ZP_2, inserted at the virtual source plane, is able to recombine all of them, in a first-order approximation, in a single picture, if the following constraint is fulfilled

$$Z_o' = \frac{-d^2}{Z_o} \quad . \tag{1}$$

The constants Z_o and Z_o' represent the focal distance of ZP_1 and ZP_2, for a wave number σ_o, respectively, and d denotes the separation between the zone plates. In this way, the first-order AFT of the input is obtained at a distance d' such that

$$d' = \frac{-d^2}{d+2Z_o} \quad . \tag{2}$$

If we want to obtain a real AFT, i.e. $d'>0$, from Eqs.(1) and (2) we infer that ZP_1 and ZP_2 should be a diverging and converging zone plate, respectively, and the value of the dimensionless parameter α, defined as $\alpha = |Z_o'/Z_o|$, must be $0<\alpha<4$. It is also convenient, for experimental reasons, to express the distances d and d' in terms of the focal length of both zone plates. From Eqs.(1) and (2) we have that

$$d = -\sqrt{\alpha}\, Z_o \quad , \text{and} \quad d' = \frac{\alpha}{\sqrt{\alpha}-2} Z_o \quad . \tag{3}$$

3. Residual chromatic aberration

Since we develop a first-order theory, the proposed setup suffers from residual chromatic aberration. In order to evaluate it, the amplitude object distribution is propagated throughout the optical system, using Fresnel diffraction theory. The result is that for each wave number the Fraunhofer pattern is achieved at a distance R' from ZP_2 given by

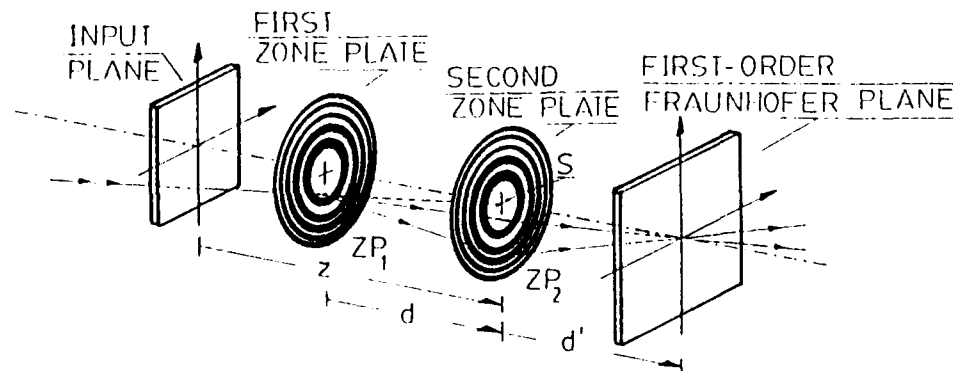$$R'(\sigma) = \frac{d'}{1 + \frac{1}{2-\sqrt{\alpha}}\frac{(\sigma-\sigma_o)^2}{\sigma\sigma_o}} \quad , \tag{4}$$

Figure 1.

and the scaling of the Fourier transform is

$$x = \frac{zu/\sigma}{\left(2 - \sqrt{\alpha}\right) + \dfrac{(\sigma - \sigma_o)^2}{\sigma\sigma_o}} \quad , \quad y = \frac{zv/\sigma}{\left(2 - \sqrt{\alpha}\right) + \dfrac{(\sigma - \sigma_o)^2}{\sigma\sigma_o}} \tag{5}$$

where x and y are Cartesian coordinates and u and v spatial frequencies, and z is illustrated in Fig.1. In this way, it is possible to show that the greatest value of the relative chromatic aberration (both, axial and lateral), CA_M, expressed as a percentage, is given by

$$CA_M = \frac{100}{1 + 2\beta\left(2 - \sqrt{\alpha}\right)} \quad , \tag{6}$$

where $\beta = \sqrt{\sigma_1\sigma_2} / (\sqrt{\sigma_1} - \sqrt{\sigma_2})^2$. We would like to emphasize that the scale factor, see Eq.(5), varies with z, and consequently it is a function of the longitudinal position of the input, but the maximum chromatic aberration only depends on the value of α for a determined spectral content of the incident light. It appears that $\alpha < 1$ is enough to achieve the chromatic error less than 4% even when the temporal spectrum of the incoming radiation spreads over the total visible region.

Results of laboratory experiments will be reported to demonstrate experimentally both the achromatic and the scale-tunable Fourier transforming properties of the optical configuration in Fig.1 constructed following the prescriptions of Eq.(3).

4. Achromatic Fresnel diffraction patterns

It is very interesting to recognize that the results of the two preceding sections can be applied to achromatize not only the Fraunhofer pattern but also an arbitrary Fresnel diffraction pattern of the input object.

To this end, let an input transparency be illuminated by a polychromatic converging spherical light beam. The optical device is a single zone plate, ZP, of focal length Z_o' , inserted at the virtual source plane. The output plane - or first-order achromatic Fresnel plane - is placed at a distance d' from ZP. We identify the pattern to be achromatized by the distance R_o at which it appears, when the input object is illuminated by a monochromatic parallel beam of wave number σ_o. It is possible to show that all the above equations hold for the present case, replacing Z_o by R_o and noting that d is now the distance to ZP from the input plane.

We will also report some experimental verifications of this procedure.

5. References

[1] J.L. Horner, *Optical Signal Processing* (Academic, New York, 1987), Ch. 2.

[2] D. Faklis and G.M. Morris, Opt. Eng. **28**, 592 (1989).

[3] R.H. Katyl, Appl. Opt. **11**, 1255 (1972).

[4] R. Ferriere and J.P. Goedgebuer, Appl. Opt. **22**, 1540 (1983).

[5] S. Leon and E.N. Leith, Appl. Opt. **24**, 3638 (1985).

[6] R.H. Katyl, Appl. Opt. **11**, 1248 (1972).

[7] B. Packross, R. Eschbach, and O. Bryngdahl, Opt. Commun. **50**, 205 (1984).

Ultra Lightweight Diffractive Eyepiece
Robert E. Aldrich

Many have suggested the use of diffractive optics as color correctors in the IR, some have never built such devices. Plastic aspheric eyepieces are lighter weight than conventional glass spherical optics due to plastics smaller specific gravity and the superior correction of aspheres, which allows for fewer elements.

Combining the precision of OPT plastics and diffractive optics allows for Ultra light weight eyepiece design.

A Holographic-Element-Array-Based Laser Directional and Wavelength Discrimination Device

Jenkins Chen and Freddie Lin

Physical Optics Corporation

Research and Development Division

20600 Gramercy Place, Suite 103

Torrance, California 90501.

(310) 320-3088

William Liu

Multispace

2746 North Durfee Avenue, Suite M

El Monte, California 91732.

(818) 444-8863

Laser directional and wavelength sensing devices which can be mounted on a variety of military platforms are needed for possible future optical countermeasure systems. Presently, extremely sensitive and rugged photodetectors operating from NUV to FIR are commercially available. However, determining the direction and wavelength of the illumination is more difficult than merely detecting its presence. What is required is a compact low-power device that quickly gives an unambiguous directional and wavelength indication of laser illumination and makes good estimates of the laser energy's temporal characteristics (pulse frequency and type of modulation), preferably for several wavelengths.

We have investigated the possibility of using grating array with various spatial frequencies and orientations situated on a transparent optical substrate as a laser directional and wavelength sensor. The gratings can be made either to couple the incoming laser light into an optical waveguide, or only to deflect the incoming laser light to a specific angle. The angular and wavelength resolution of our laser warning sensor (based on phase gratings in a volume hologram) ranges from 0.1° to 3°, and from 0.5nm to 20nm, respectively, depending on the design and structure of the grating/optical substrate combination. The sensor requires no lens or other optical adjuncts, therefore, the conventional optics' minimum distance associated with the f number is not required for the sensor to function. This ability would make installing the sensor extremely easy; the detectors could be installed in a manner similar to putting on a tile.

Two approaches have been studied in our experimental work. The first is the waveguide grating coupler approach (see Figure 1). It is based on a holographic element array in a single mode optical waveguide, with high angular resolution of <0.1° and high wavelength discrimination ability of <1nm. Light is coupled into the optical waveguide through mode coupling at the holographic grating and the waveguide interface. Only light of the desired wavelength arriving from one small solid angle will enter the waveguide and propagate to the detector, constrained by both the waveguide mode propagation angle and the Bragg condition. Furthermore a multiplexed hologram, i.e., a hologram with several gratings, can feed multiple detectors such that several combinations of wavelength and direction could be realized by a single holographic element. A number of experiments with multiplexed and non-multiplexed holographic element arrays in single-mode optical substrates have been conducted. The results of these experiments will be presented in the conference. The resolutions of directional and wavelength discrimination are dependent on the number of modes and the mode confinement quality of the waveguide.
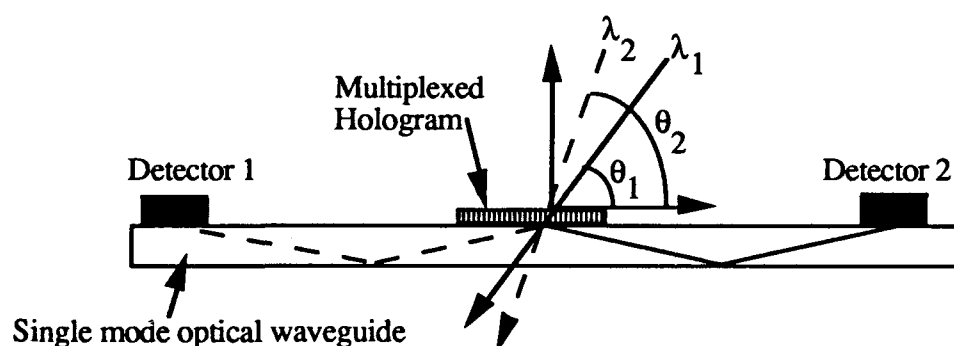
Figure 1.   A multiplexed hologram will couple a different wavelength coming from a different direction to a specific detector.

The second approach is based on a free-space grating deflector approach (see Figure 2). It is very easy to cover a large field of view with relatively few grating deflectors, but the angular and wavelength resolving power is only ~3° and ~20nm, respectively. The wavelengths of the incoming laser threats can be resolved by using multiple gratings, as in multiplexed holograms, where each grating is sensitive to one particular wavelength. This approach will yield a functional device with much simpler detector configuration and fabrication process. In order to demonstrate the feasibility of using free space holographic gratings to construct a laser warning device, a 5 X 5 grating array was constructed. Each grating was sensitive to directions within +1.5° and -1.5° of the designed incident angle.

Incoming laser threat

Diffracted beam

Phase hologram

Transmitted beam

Optical
Substrate

Ring of Detector Array
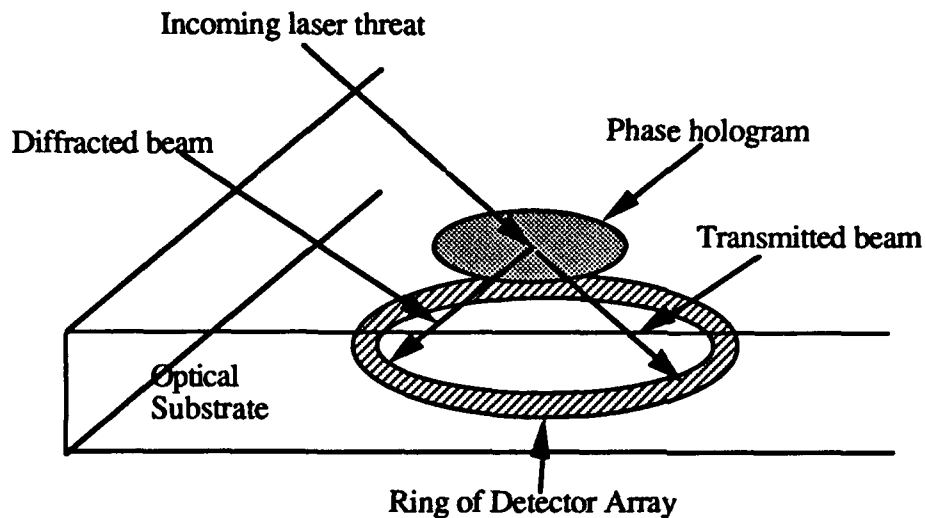
Figure 2.   Phase holograms and detectors are placed on the top and bottom of an optical
substrate, respectively.

In summary, both approaches operate on the Bragg scattering principle to reflect only light of a
specific wavelength band coming from a specific range of incident angles, with the first approach
having the waveguide mode propagation angle as an additional constraint. The overall
angular/wavelength acceptance range will depend on both the holograms and the configuration of
the optical substrate used. In such a way, both components can be used to adjust the resolution of
the angular/wavelength detection scheme.

Lamellar Gratings as Polarizing Elements
for Specularly Reflected Beams

Charles W. Haggans and Lifeng Li
Optical Sciences Center
University of Arizona, Tucson, AZ 85721
(602)-621-2031

Raymond K. Kostuk
Electrical and Computer Engineering Department
and Optical Sciences Center
University of Arizona, Tucson, AZ 85721

I. INTRODUCTION

Reflection of light from a high spatial frequency lamellar grating at a glass-air ($\Theta > \Theta_c$) or glass-metal interface introduces a phase shift between the orthogonal polarization components. If a conventional incidence geometry is used (grating vector parallel to the plane of incidence), no polarization conversion occurs. Thus, gratings of this type can be used as phase compensation and retardation elements operating on a specularly reflected beam.

If light is conically incident on this type of grating (grating vector not in the plane of incidence), polarization conversion between the orthogonal polarization components occurs upon reflection (the ratio of the orthogonal polarization component amplitudes is modified). In general, a phase difference between the two components is also introduced in this reflection. Thus, if a phase compensation element is cascaded with a conically mounted high spatial frequency grating, a linear polarization rotator can be obtained.

In this paper, we will give examples of grating profiles and incidence geometries that enable lamellar profile gratings to function in reflection as arbitrary phase compensators, quarter-wave and half-wave retarders, and arbitrary angle polarization rotators.

II. THEORY

Two rigorous models were used to analyze the polarization properties of high spatial frequency lamellar gratings. A coupled-wave method[1] was used to analyze dielectric gratings with depths ≤ 1.0 µm. A modal method[2] was used for dielectric gratings with depths > 1.0 µm and for metallic gratings. The incidence and grating geometry used for both models is shown in Figure 1. In this figure, arbitrarily polarized light is incident on a grating at the interface between two media. The polar angle of incidence exceeds the critical angle for dielectric gratings, and the grating period is short enough to ensure that only the zeroth reflected order propagates. We use the convention and notation of Born and Wolf[3] to describe the states of polarization. In this notation, α is the arctangent of the ratio of the field component amplitudes ($\alpha = \mathrm{atan}(A_s/A_p)$) and δ is the phase difference between the components ($\delta = \phi_s - \phi_p$).

III. RESULTS

a. Gratings for Phase Retardation

Figures 2 and 3 demonstrate that a lamellar dielectric grating in a non-conical mount ($\Phi=0°$) can be used to introduce any unique phase difference δ_r ($\delta_r=\phi_{rs}-\phi_{rp}$) between the orthogonal polarization components of light reflected from the grating. Figure 2 is a plot of δ_r as a function of grating depth (d) for a grating at a glass-air interface ($\Theta=45°$, $\Phi=0°$, $\Lambda=0.3$ µm, dc=0.5, $n_1=1.51$, $n_2=1.0$, $\alpha_i=45°$, and $\delta_i=0°$). Figure 3 is a similar plot with $\Phi=90°$ and dc=0.7. Data for these curves was generated using the coupled-wave model. These plots show that the depth of the grating can be varied to introduce any phase difference from -180° to 180° to an incident linearly polarized beam. For both of these figures, $\alpha_r=45°$ because there is no polarization rotation, and the zeroth reflected order diffraction efficiency is 1.0 because there is no transmission or absorption.

When $\delta_r=\pm90°$ and $\alpha_r=45°$, the reflected light is circularly polarized. If light is incident with $\alpha_i=45°$ and $\delta_i=0°$ and the reflected light is circularly polarized, the grating acts as a quarter-wave retarder. In Figure 2, $\delta_r=-90°$ at a depth of approximately 0.55 µm. Thus, reflection of light from a grating with this depth converts a linearly polarized incident beam into a left circularly polarized beam. Similarly, a grating depth can be selected from Figure 3 which would give right circularly polarized light on reflection (d≈0.42 µm).

A design point for a half-wave retarder is given in Figure 3. At d≈0.6 µm in this figure, $\delta_r=180°$ is obtained. The output polarization vector for a linearly polarized beam reflected from this grating is rotated by an angle of $2\alpha_i$ with respect to the incident polarization vector, giving $\alpha_r=-\alpha_i$.

b. Gratings for Polarization Conversion

Reflection of conically incident light with polarization angle α_i from a high spatial frequency lamellar grating can give an arbitrary output polarization angle α_r. This occurs because varying degrees of polarization conversion occur as the grating depth and azimuthal angle of incidence are varied. Deep dielectric gratings are required to obtain significant polarization conversion. However, relatively shallow metallic gratings can perform the same function.

Figure 4 is a contour plot of α_r versus d and Φ for a linearly polarized beam incident on a grating at a glass-metal interface with $n_2=0.175-i4.91$, $\alpha_i=45°$, $\delta_i=0°$, and the other parameters as in Figure 2. The modal model was used to generate this data. Note that values of α_r from <5° to >85° can be obtained for d<0.2 µm. Near $\Phi=75°$ and d=0.1 µm, the reflected beam is nearly p polarized ($\alpha_r\approx0°$). Similarly, near $\Phi=27°$ and d=0.05 µm, the output beam is nearly s polarized ($\alpha_r\approx90°$). By varying the azimuthal angle of incidence and the depth, gratings with intermediate values of α_r can be selected. A linear polarization rotator can be formed by cascading a phase compensation grating with the polarization conversion grating to correct the phase difference introduced by the conversion grating.

IV. CONCLUSION

Rigorous electromagnetic grating theory indicates that high spatial frequency lamellar gratings at glass-air and glass-metal interfaces can be used as phase compensation, retardation, and linear polarization rotation elements for specularly reflected beams.

V. REFERENCES

1. Model is based on the work of M.G. Moharam and T.K. Gaylord, JOSA 73, 1105 (1983) and JOSA 72, 1385 (1982).
2. L. Li, paper ThBB4, in OSA Annual Meeting Technical Digest,1991, Vol. 17, 168.
3. M. Born and E. Wolf, Principles of Optics, (6th ed) pp. 24-30.
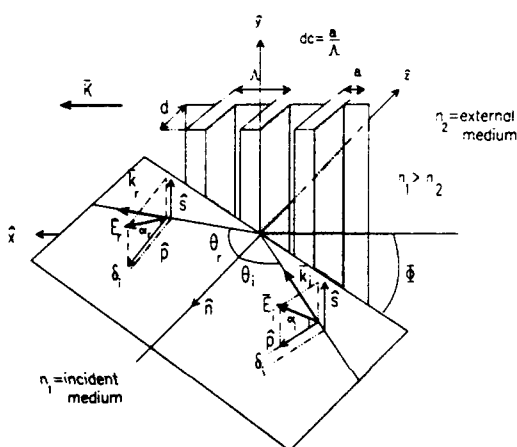
Fig. 1.   Diffraction geometry.
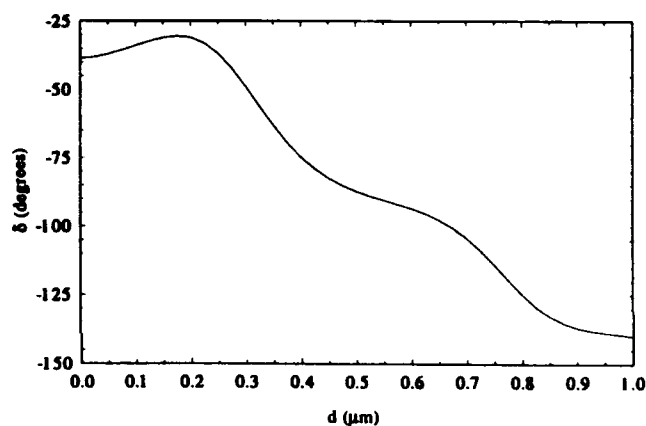
Fig. 2.   s-p phase difference versus grating depth for the zeroth reflected order. $\Theta=45°$, $\Phi=0°$, $\Lambda=0.3$ µm, dc=0.5, $n_1=1.51$, $n_2=1.0$, $\alpha_i=45°$, and $\delta_i=0°$.
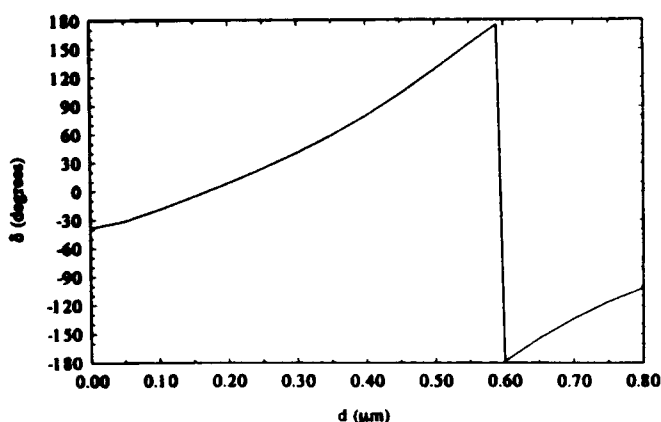
Fig. 3.   Same as Fig. 2 with $\Phi=90°$ and dc=0.7.
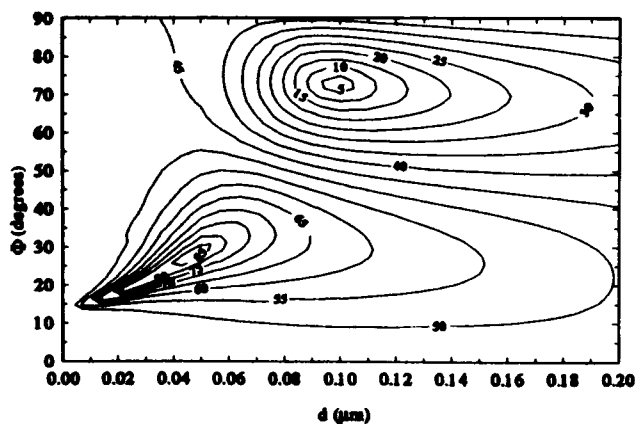
Fig. 4.   Contour plot of polarization angle versus azimuthal angle of incidence and depth for the zeroth reflected order. Parameters as in Fig. 2 with $n_1=0.175$-i4.91.

Fabrication Technologies 3

WA 8:30am–10:00am
Cabildo Room

Peter P. Clark, *Presider*
Polaroid Corp.

Blazed Diffracting Optical Components

M.C. Hutley
National Physical Laboratory
Queens Road, Teddington, Middlesex
United Kingdom TW11 0LW

1. The blazed profile effectively "unwraps the cann spiral," i.e., it provides just the right amount of phase lag to compensate for the change in path difference as one goes from one side of a groove to the other. This description is helpful in understanding the performance of various approximations to a triangular profile (e.g., discrete steps and rounded edges).

2. Grooves may be manufactured in three ways:
   a. Mechanically (ruling engine or lathe)
   b. Generating artwork: drawing a photoreducing; direct writing with laser or E beam
   c. Recording interference fringes

3. Mechanical methods have the advantage of good control over groove profile but are slow and effectively limited to gratings and zone plates.

4. Artwork is usually generated on some form of computer plotter. The quality of the final product depends upon the mechanical accuracy of the plotter and the performance of the camera. Systematic errors can, in principle, be compensated for in the software. A blazed groove profile may be generated by varying the density (grey level) across the groove. This is ultimately copied into photoresist as a corresponding variation in depth. The number of grooves that may be made in this way is rather limited but the technique is useful for infrared components.

5. In principle it is possible to produce a blazed profile by controlling the exposure across the groove when writing directly into photoresist using a laser or an E beam plotter. A more practical approach has been to superimpose a series of binary masks and build up a digital approximation to a triangular profile. For coarse structures the efficiency is quite high with relatively few steps but the numerical aperture that can be achieved is limited by the accuracy of mask alignment and the resolution of the copying process.

6. A good approximation to a triangular profile may be achieved by recording oblique standing waves in photoresist. This is a very simple method for making gratings and zone plates blazed for use in reflection in the ultraviolet. Longer blaze wavelengths can be achieved by ion etching the profile into the substrate so as to increase the depth.

7. Normal two-beam interferometry will produce a quasi sinusoidal profile and in principle it is possible to combine a series of exposures and build up any profile by Fourier synthesis. In practice it is very difficult with more than two components and then only for plane gratings. Coarse blazed structures can be produced by spatial filtering but this is of limited practical value.

8. Multiple beam fringes of high finesse may be scanned across one fringe period under computer control so that an appropriate exposure is given at each point. In principle it is possible to generate any desired profile in this way and the use of Febry Perot transmission fringes has been successfully applied to the manufacture of blazed zone plates.

9. It is possible to arrange the relative amplitudes and phases in a multiple beam interferometer to generate an asymmetrical intensity distribution. Reflection fringes from a Faby Perot interferometer have also been used to make blazed zone plates.

Implementation of a Packed Data Format for Production of Computer Generated Holograms by E-beam Lithography

Daniel M. Newman
Purdue University
Electrical Engineering
253 Sheetz, Apt. 16
W. Lafayette, IN 47906
(317) 743-6022

Robert W. Hawley
Purdue University
Electrical Engineering
EE Box 204
W. Lafayette, IN 47907
(317) 463-0324

Neal C. Gallagher
Purdue University
Electrical Engineering
MSEE Room 326
W. Lafayette, IN 47907
(317) 494-3518

I. Introduction

Electron beam lithography has become the method of choice for producing computer generated holograms. The demand for these high quality diffractive optics has made their fabrication much more than a research interest. Unfortunately, the electron beam machines themselves have not kept pace with the demand for this new application. The pattern data formats used with these machines were developed with the VLSI industry in mind. As a result they are not well suited for exposing the arbitrary fringe patterns found in many computer generated holograms.

Ideally, one would like to take an arbitrary phase equation and compute and expose the appropriate fringe pattern at the same time with a single machine; however, the computers that actually control the e-beam machines are too slow to accomplish this task in a reasonable period of time. As an example the Cambridge e-beam machine at Purdue University is driven by a PDP-11 computer running the RSX-11 operation system. Although the PDP-11 is powerful enough to handle the computation involved in exposing a typical VLSI pattern, it would hardly be adequate for the task of computing fringe patterns for a hologram. It seems very unlikely that a system powerful enough to achieve this ideal goal will be available in the near future.

After putting aside the idea of controlling the electron beam directly during computation of the hologram, we are left with a serious problem; enormous amounts of pattern data are required to specify the hologram. Hundreds of megabytes of storage are needed to specify even a small hologram of a few square centimeters. Previously, a pattern data format has been described by Hawley and Gallagher [1] that requires significantly less storage space than the current pattern data formats. This method uses a combination of run-length coding and Lempel-Ziv-Welch (LZW) coding [2] to achieve compression ratios of up to two orders of magnitude. The adaptive nature of the LZW coding algorithm makes it suitable for

arbitrary fringe patterns as well as patterns found in VLSI designs. No implementation of this method had been completed at the time of its first publication. Using the format requires that changes be made to the software that drives the electron beam machine which involved overcoming several obstacles. This paper offers details to implementation and a few slight modification to the method described in [1].

II. Image Calculation and Compression

The calculation and compression of the image is done by a single program. The fringe pattern is calculated in patches which are 1024 by 1024 exposure elements (exels) in size. Such a patch is refered to as a ten bit field because 10 bits are needed to specify the X and Y coordinates of any particular exel. This size was chosen due to a physical constraint imposed by the Cambridge e-beam machine. To avoid distortion one must avoid exposing a rectangle that crosses a 10 bit field boundary.

Compression of data consists of taking blocks of run length codes and assigning a single LZW code to each block. Hawley and Gallagher had suggested a particular hashing technique for assigning compression codes. They have since improved the speed of the compression algorithm by using a double hashing technique.

The time require to compute the fringe pattern and compress its pattern data can still be a problem. On a sun 4 server it can take several hours to compute and compress a 15-bit field. To accomplish the calculation time in minutes instead of hours, a group of undergraduates at Purdue is programming the algorithm on a parallel supercomputer architecture (MasPar). Early results show that one might expect up to two orders of magnitude improvement in computation time.

III. Decompression and Exposure

The decompression code was developed in C language and tested on a Sun 4 before being ported to the PDP-11. The code was developed from the pseudo code in [1] which needed a slight correction and some modifications to be better suited for the C language implementation. The PDP-11 is limited to a virtual address space of 64 kilobytes. As a result, some additional memory management code had to be written for the PDP-11 to handle access of the 128K table required for the LZW codes. Several low level operating systems calls were needed to accomplish this. The next step was to integrate this code into the e-beam driver software (QSYS). This was the most difficult and frustrating step. QSYS is very large and does not leave much space for the addition of code in memory. A significant effort was required to shuffle the code segments so that the

decompression software could fit. An almost intimate understanding of QSYS was required in order to accomplish this.

IV. Results

With the improvements made on the hashing, the number of unsuccessful hash searches was reduced by two orders of magnitude. This improved performance but most of the computation is still in the floating point operations of the phase equation. The net result was an increase in speed of compression of roughly 15%. A Sun 4/60 took approximately 12 hours to compute and compress an entire 15-bit field. This is roughly 45 seconds per 10 bit field. A 10 bit field took only 0.7 seconds to decompress. Unfortunately, the PDP-11 is incapable of these speeds. The PDP-11, took 30 seconds to decompress a 10 bit field. This means to expose a full 15 bit field will take at least 9 hours.

V. Conclusion

The algorithm clearly adds much needed ability to expose large and detailed computer generated holograms. The time to calculate such an image is lengthy but the exposure time is more disturbing. It takes 9 hours to do a single 15 bit field which is still a small hologram. Exposing a hologram of only a few square centimeters using a .1 micron resolution would take weeks. This is clearly impractical.

There are two solutions to the exposure problem. The LZW decompression algorithm is relatively simple and could be implemented in hardware. With some simple dedicated hardware, the decompression could done very fast. The other route, which would require more investment, is to leave the PDP-11 behind and use a machine with newer technology. This way all future work could be developed in a high level language, like C, and there would be no extra time spent working around the inadequacies of the PDP-11. More enhancements would be cheaper to develop because one would not be using machine dependent code. Unfortunately, the later alternative is very unlikely at this time.

References

1. R.W. Hawley and Neal C. Gallagher, "Efficient electron beam pattern data format for the production of binary computer generated holograms," Applied Optics **29**, 2 (1990).

2. T. A. Welch, "A technique for high-performance data compression," IEEE Computer **17**, 8 (1984).

Processing Error Limitations on Performance
of Diffractive Optical Elements

J. Allen Cox

Honeywell Systems & Research Center
10701 Lyndale Avenue S.
Bloomington, MN 55420
612/887-4369

1. INTRODUCTION

The use of lithographic and etching techniques to fabricate phase-only diffractive elements was first demonstrated by d'Auria et al[1] and has now become popular following the improvements in the technology driven by the microelectronics industry. In the usual approach, a staircase approximation to the ideal continuous phase profile is implemented in the substrate using a binary mask-and-etch sequence in which the number of phase levels generated is a power of two. Performance is usually discussed in terms of diffraction efficiency and image quality. Dammann[2] first showed how to calculate diffraction efficiency for the staircase structures using the Fourier theory. Image quality, for those diffractive elements which form images, has been modeled either using raytrace codes with an infinite index approximation or using brute-force integration of the scalar Kirchhoff equation[3].

Mostly, performance has been calculated only for geometrically perfect profiles without considering the unavoidable effects of processing errors. Such predictions thus represent an upper limit on performance expected for real elements. The effects of processing errors on diffraction efficiency have been investigated both theoretically and experimentally by the author[4], and an independent theoretical treatment has been given at the same time by Farn and Goodman[5]. The diffractive elements in both cases were the staircase type. Cox et al.[4] showed conclusively that processing errors resulting from mask alignment and from photoresist linewidth at a mask alignment interface were the most significant in degrading diffraction efficiency and gave guidelines for the upper limits on alignment accuracy needed to achieve acceptable performance.

Here, the previous results are extended to include image quality as measured by the modulation transfer function (MTF) and location of characteristic features around focus. Specifically, I report the results of an experimental study to determine the sensitivity of image quality and diffraction efficiency of Fresnel phase lenses to processing errors. Some of these results have been reported recently[6,7] in more detail.

2. DESCRIPTION OF EXPERIMENTS

Test Elements and Measurements

The test element for all experiments is a Fresnel phase lens (2.54 cm diameter) fabricated in fused silica. It is designed to be f/10 at 632.8 nm. This element has proved to be particularly convenient for measuring sensitivities to processing errors for both diffraction efficiency and image quality. In terms of image quality, it is well known that this element converts a monochromatic, collimated, normally-incident wavefront into a purely spherical converging wavefront and thus to focus light with absolutely no spherical aberration. This property makes this element particularly easy to test. In terms of diffraction efficiency, we use a variable iris to divide the element into ten annular zones of equal area, each having a different average fringe width. This permits us to measure efficiency as a function of the error-to-fringe-width ratio. Finally, the Fourier theory is valid for f/10 elements, and we thus have a simple mathematical approach to implement error models and compare model predictions with the experimental data.

Three two-level, six four-level, and four eight-level test elements were fabricated by means of contact printing lithography and reactive ion etching. The four-level elements require two masks and two etchings. There are thus two etch-depth errors and one mask alignment error. Line-width errors at the mask interface of the four-level elements were determined by electron microscopy to be quite small compared to the mask alignment errors. The four-level elements were fabricated in two groups having "small" mask alignment error and intentionally "large" mask alignment error. In the latter group, the etch-depth errors were made quite small. All eight-level elements were fabricated in the same fashion as the "small-error" four-level elements.

Measurements

Diffraction efficiency in each annular zone was measured on every element as described in reference 4. Image quality was measured primarily in terms of the modulation transfer function (MTF) calculated from knife-edge response data. At least eight scans were recorded for each element. MTF curves for the eight scans were averaged and plotted. Measurements were made at two different HeNe laser wavelengths (632.8 nm and 543.5 nm). After spatially filtering with a pinhole and beam expanding, the beam intensity across the test element typically was uniform to within eight percent. Image quality was also checked qualitatively by examining the blur spot under a microscope.

Experimental Results

The measured diffraction efficiency data as a function of zone number were shown for the two-level and four-level elements in references 6 and 7. In summary, the data indicate that diffraction efficiency is insensitive to both etch-depth and linewidth errors routinely achieved in the fabrication process. However, mask alignment error is a significant error source. Even mask alignment errors on the order of 0.25 μm decrease the efficiency by three to eight percent per mask alignment. It was shown in reference 4 that mask alignment must be done to within 0.1 μm in order to achieve acceptable performance for this f/10 element. For the eight-level elements, the difference between the theoretical (95%) and measured efficiencies was approximately double the difference in the "small-error" four-level elements. The efficiency varied from 88 - 90 percent in the inner zone to about 80 percent in the outer zones.

Image quality

MTF curves for the two-level elements, the "small-error" four-level elements, and the eight-level elements all showed diffraction-limited behavior over a range of frequencies from 0 to 140 cy/mm. Cutoff occurs at 158 cy/mm, and between 140 and 158 cy/mm the MTF values were dominated by noise. Diffraction-limited MTF data were observed at both 632.8 nm and 543.5 nm. This conclusion is supported by visual examination of the blur spot with a microscope. In each of the "small-error" elements, the blur spot appeared quite circular, and, more importantly, exhibited very symmetrical behavior on either side of focus. This point can be illustrated quantitatively by measuring the location of the central dark spot, corresponding to one wave of defocus, occurring on either side of the focal spot. For example, the central dark spot in element Q5 lay at -538 μm and +523 μm compared with the predicted value[8] of +/- 532 μm. Similar results were found for all of the "small-error" elements. Thus, there is indeed very little spherical aberration present in these elements. As a further benchmark for comparison, the same measurement was made on a Nikon Micro-Nikkor camera lens, stopped to f/10, and the central dark spots were found to lie at -643 μm and +567 μm.

Mask alignment error gives rise to an asymmetry in the aperture of the element, and one should expect astigmatism or coma to be associated with this error. The presence of these aberrations was tested by performing knife-edge scans in orthogonal directions on the four-level elements.

The resulting MTF curves for the "small-error" elements exhibited very small differences between the two scan directions, and in fact in every case the difference lay within the repeatability limits of the measurement. The "large-error" elements, on the other hand, showed a very dramatic effect of aberration in the two MTF curves. Based on analysis with a ray tracing program, we found that the difference could be attributed to approximately one wave of aberration. Once again, the quantitative data are supported by visual examination of the blur spots: the "small-error" elements had circular blur spots, while the "large-error" elements exhibited noticeably oblong blur spots. The degradation in both diffraction efficiency and MTF correlated quite well with the magnitude of the mask alignment error in each of the "large-error" elements.

3. SUMMARY

On the basis of these experiments, we can conclude that all three error sources, with magnitudes routinely achievable with existing technology, have only a minor impact on a kinoform's image quality. With regard to diffraction efficiency, only mask alignment error is significant, and an error of only 0.25 μm can degrade performance in kinoforms having fringe widths comparable to our f/10 elements. It should be pointed out, however, that a large loss in diffraction efficiency does NOT affect image quality as long as the loss is reasonably uniform across the aperture. This can be easily seen from the MTF curves for the two-level elements which have only 40.4 percent efficiency in first order. The remaining 60 percent of the light intensity is distributed in the negative and higher positive orders and appears as very diffuse, very low-intensity background at the first-order focal point. This background is too small to significantly affect the contrast in the image. Similarly, any near-angle scatter arising from processing errors is evidently not significant.

Moreover, on the basis of our measurements, we can draw some more general conclusions on the relative importance of the various error sources to diffraction efficiency and image quality. First, our data supports the conclusion that image quality is determined primarily by the accuracy with which the Fresnel zones are defined, and thus image quality is mostly a function of errors in the first-level mask. This conclusion should not be surprising since the first-level mask is nothing more than a very low efficiency (5 - 10 percent) computer-generated hologram (CGH). CGHs have been used for years in interferometers to test aspheric optics. Second, the subsequent masks used in the "binary optics" process serve only to define the phase profile within each Fresnel zone, and it is this profile which primarily determines diffraction efficiency. Thus, process errors affecting the phase profile play a predominant role in determining diffraction efficiency.

4. REFERENCES

1. L. d'Auria, J.P. Huignard, A.M. Roy, and E. Spitz, "Photolithographic Fabrication of Thin Film Lenses," Opt. Commun. Vol 5, 232 (1972).
2. H. Dammann, "Blazed Synthetic Phase-Only Holograms," Optik, Vol. 31, pp. 95-104, 1970.
3. D.A. Buralli, G.M. Morris, J.R. Rogers, "Optical performance of holographic kinoforms," Appl.Opt., Vol.28(5), pp.976-83, 1989.
4. J. A. Cox et al., "Diffraction efficiency of binary optical elements," Proc. SPIE, Vol. 1211, pp.116-24, 1990.
5. M.W. Farn and J.W. Goodman, "Effect of VLSI fabrication errors on kinoform efficiency," Proc. SPIE, Vol. 1211, pp.125-36, 1990.
6. J.A. Cox, B. Fritz, T. Werner, "Process-dependent kinoform performance," Proc. SPIE, Vol. 1507, pp. 100-9 (1991).
7. J.A. Cox, B. Fritz, T. Werner, "Process error limitations on binary optics performance," Proc. SPIE, Vol. 1555 (1991).
8. M. Born and E. Wolf, **Principles of Optics**, (Permagon, Oxford, 1980), p 441.

Performance of Diffractive Optics

Lewis F. DeSandre, Van A. Hodgkin, and J. Merle Elson
Physics Division, Research Department
Naval Air Warfare Center—Weapons Division
China Lake, CA 93555-6001

Tianji Zhao and Angus Macleod
The University of Arizona
Optical Sciences Center
Tucson, AZ 87521

Carl Buzcek
Laser Systems and Research
Escondido, CA 92029

Combination diffractive and refractive optical systems offer numerous and exciting possibilities as alternatives to all refractive systems. Combinations of refractive and diffractive elements can work very well together for certain applications. Also, diffractive elements can be used solo in more restricted cases such as monochromatic and narrow-field-of-view applications. Diffractive elements can be computer designed, lightweight, used to control aberrations, and used to shape the wavefront. While diffractive elements definitely have much potential for the right applications, there are some possible drawbacks. These include questions of diffraction efficiency and light scattering due to random imperfections. In this work, we propose to address some of these issues.

A coaxial pair of independently rotatable transmissive wedges can be used to steer a beam throughout a large field of regard. A refractive wedge can be emulated by a transmission grating. In this work, we use such transmission gratings as diffractive elements of study. Thin silicon wafers approximately 20-mils thick have been fabricated by ion-beam milling into two- and four-phase level gratings designed to emulate a wedge for use at 10.6-μm wavelength. Numerous samples are measured for bidirectional transmission diffuse scattering (BTDF) at 10.6 μm including diffraction peaks as well as the diffuse scattering between orders. The incident beam is polarized both perpendicular and parallel to the direction of the grooves. Also measured is a virgin silicon wafer without grooves as a reference. After these measurements, the samples are coated with a thin dielectric antireflection coating and the BTDF measurements repeated. Before and after the coating process, selected samples are subjected to profilometric measurements.

The BTDF measurement results are compared with theory. A rigorous coupled wave diffraction theory is used to predict the diffraction intensity both before and after coating. Also, scalar Fourier diffraction analysis is used and includes diffuse scattering due to random imperfections.

Design Techniques for Diffractive Optics

WB 10:30am–12:00m
Cabildo Room

Dale A. Buralli, *Presider*
Sinclair Optics Inc.

Signal Synthesis and Coding in Diffractive Optics

Frank Wyrowski
University of Essen, Germany
Physics Department

1.Introduction

Diffractive elements (DE) allow the manipulation of an electromagnetic wave by diffraction. Dependent on the choice of the diffraction theory employed to calculate the DE, different parts of diffractive optics can be defined. Digital holography is the part that is based on the use of scalar diffraction theory.[1] The transmittance or reflectance of the DE is calculated by geometrical optics and the wave propagation by paraxial wave optics. Of particular importance are the Fresnel- and the Fourier transform.

Denoting the transmittance or reflectance of the DE by $G(x')$, the illumination of the DE with a plane wave leads to the diffraction pattern $g(x) = \mathcal{P}G(x')$. The operator $\mathcal{P}$ indicates the wave propagation, e.g. the Fresnel- or Fourier transform. Due to the fabrication and the application of the DE the set of values of $G(x')$ is in general restricted. First, there are DEs that only influence the phase of the illumination wave. They are called diffractive phase elements (DPE). $G(x')$ is the transmittance or reflectance of a DPE when it is in the set

$$I\!H(\text{DPE}) = \left\{ G(x') \middle| |G(x')| = 1 \right\}. \tag{1}$$

Second, there are the diffractive amplitude elements (DAE) with the set

$$I\!H(\text{DAE}) = \left\{ G(x') \middle| 0 \leq G(x') \leq 1 \right\}. \tag{2}$$

Furthermore, the fabrication of a DE is drastically simplified by a quantization of the phase or amplitude of $G(x')$ into Z levels, which leads to the sets $I\!H(\text{DAE};Z)$ and $I\!H(\text{DPE};Z)$.

The optical function of a DE is the generation of a specified signal wave $f(x)$ as part of the diffraction pattern $g(x)$, i.e.

$$g(x) = \mathcal{P}G(x') = \alpha f(x - x_\circ), \qquad x \in I\!F. \tag{3}$$

The signal window $I\!F$ indicates an area in which the diffraction pattern is proportional to the signal wave $f(x)$. In contrast to the signal wave $f(x)$, $g(x)$ is not zero outside of $I\!F$. An offset x_0 of the signal window is possible. α is a scale factor. Examples of the signal wave $f(x)$ are: a desired impulse response in an optical filter system, or an

array of light spots for array illumination. In the second case only the intensity $|g(x)|^2$ is of concern. Thus, the phase of $f(x)$ can be used as a free parameter. In the following we refer to complex signals when the phase is not free, e.g. signals for coherent filter systems, and to positive signals in the other case, e.g. signals for array illumination. In order to avoid speckles the phase freedom is restricted when the signal wave does not consist of light spots but of a continuous distribution.[2,3]

A basic feature of a DE is its diffraction efficiency η. Informations about η are of importance to be able to judge the possibilities and limits of diffractive optics in an actual application.

2. Diffraction efficiency of diffractive elements

The diffraction efficiency of a DE is defined by

$$\eta = \|g(x)\|_{I\!\!F} = \alpha^2 \|f(x - x_0)\|, \tag{4}$$

with $\| \ldots \| = \langle | \ldots |^2 \rangle = \int | \ldots |^2$. A normalized energy of the illumination wave is assumed without restriction of generality. Then, η is the energy of the diffracted wave within $I\!\!F$. Furthermore, $|F_v(x')| = |\mathcal{P}^{-1} f(x - x_0)| \leq 1$ is assumed to fix the energy of the signal wave within $I\!\!F$, i.e., $\|f(x - x_0)\|$ is specified by the desired optical function of the DE. Therefore, α determines the resulting diffraction efficiency. The question for an upper bound η_ℓ of the efficiency η is of great importance for applications of diffractive optics.

For the special case of the 'point signal' $f(x - x_0) = \delta(x - x_0)$ table 1 summarizes in the second column the well-known upper bounds of the diffraction efficiency of different types of DEs. Blazed gratings and Fresnel lenses reach these bounds, i.e. $\eta = \eta_\ell$ or $\eta(Z) = \eta_\ell(Z)$.[4]

A main issue of the coding theory in digital holography deals with the derivation of upper bounds of the diffraction efficiency for signal waves $f(x)$ of general shape, e.g. an impulse reponse or an array of light spots.[1]

3. Upper bound of the diffraction efficiency of diffractive elements

The coding theory treats the analysis of the coding equation $C F_v(x') = G(x')$. C indicates the coding methods. Independent of C it is possible to describe the upper bounds of η for all types of DEs with the help of [1,5]

$$\beta = \frac{\langle |F_v(x')| \rangle^2}{\|F_v(x')\|} < 1. \tag{5}$$

$\beta = 1$ is valid for the 'point signal'.[6] In case of complex signals β is a signal dependent factor. The signal phase can be used to optimize β for positive signals. A typical optimization result is $\beta \approx 0.9$. Table 1 summarizes the use of β to formulate η_ℓ for different types of signals.[1]

Table 1: Upper bounds η_ℓ of the diffraction efficiency of different types of signals and DEs

DE	'point signal'	complex signal	positive signal
analog DPE	1	$\beta < 1$	≈ 0.9
quantized DPE	$\text{sinc}^2[1/Z]$	$\text{sinc}^2[1/Z]\beta$	$\approx \text{sinc}^2[1/Z]0.9$
binary DPE (sym. signal)	0.405 0.81	$4/\pi^2\beta$ $8/\pi^2\beta$	$\approx 4/\pi^2 0.9 = 0.365$ $\approx 8/\pi^2 0.9 = 0.729$
DAE	0.101	$1/\pi^2\beta$	$\approx 1/\pi^2 = 0.091$

For signals of general shape the achieveable diffraction efficiency η is always smaller than the upper bound η_ℓ in order to obtain high signal–to–noise ratios (SNR) in the signal window $I\!\!F$.[1] Thus, $\eta = \eta_\ell - \Delta\eta$ with the deviation $\Delta\eta > 0$ results. The coding theory permits the conclusion, that $\Delta\eta$ can be minimized by coding methods C which only deviate as much from the corresonding projection operators $C_p : F_v(x') \longrightarrow I\!\!H(\text{DAE};2)\vee I\!\!H(\text{DPE}) \vee I\!\!H(\text{DPE};Z)$ as it is required to achieve an acceptable SNR.[1] These C can be formulated on the basis of iterative Fourier or Fresnel transform algorithms.

The coding theory of digital holography allows the formulation of upper bounds of the diffraction efficiency of diffractive elements and a characterisation of coding methods that optimize η. Both results are of importance for the design and application of diffractive elements.

References

1. F. Wyrowski and O. Bryngdahl,"Digital holography as part of diffractive optics," Rep. Progr. Phys., in press (1992).
2. F. Wyrowski and O. Bryngdahl, J. Opt. Soc. Am. **A5**, 1058 (1988).
3. R. Bräuer, F. Wyrowski and O.Bryngdahl, J. Opt. Soc. Am. **A8**, 572 (1991).
4. H. Dammann, Optik **31**, 95 (1970).
5. F. Wyrowski,"Upper bound of the diffraction efficiency of diffractive phase elements," Opt. Lett., in press (1991).
6. F. Wyrowski, Opt. Commun. **81**, 353 (1991).

Phase Optimization Of Kinoforms By Simulated Annealing

N.Yoshikawa and T.Yatagai
Institute of Applied Physics, University of Tukuba
Tukuba , Ibaraki 305 , Japan

The kinoform[1] is a phase-only computer-generated hologram which has some advantages because of its high efficiency. Some studies on the optimization of the phase distribution in the kinoform has already been reported by several authors to the present[2,3]. In most of studies, the iterative method were chiefly adopted to optimize the phase distribution in the kinoform. However, in the iterative method, a system to be optimized may be trapped the local minimum , so that the global minimum is not always found. The optimization of a simple kinoform by the simulated annealing(SA) algorithm[4] has already been studied by Turunen et al.[5]. The SA algorithm is a method of finding the global minimum in a system to be optimized.

In the present paper, we discuss the SA algorithm for the optimization of the phase distribution in the kinoform in order to reconstruct the desired image, and some experimental results. In reconstruction experiments, we use the phase modulation made of liquid crystal spatial light modulator (LCSLM)[6]. We consider a Fourier transfer kinoform. Let the complex amplitude to be reconstructed $u(x,y) = a(x,y)\exp[i\varphi(x,y)]$, where $a(x,y)$ and $\varphi(x,y)$ denoted the amplitude and the phase. Then its Fourier transform is given by

$$U(v,\mu) = A(v,\mu)\exp[i\theta(v,\mu)] = \iint u(x,y)\exp[-2\pi i/\lambda f(vx+\mu y)]dxdy ,\qquad(1)$$

where λ is the wavelength and f is the focal length. In kinoform approximation, the amplitude is a constant; $A(v,\mu) = A$ for $v, \mu \in S, 0$ otherwise, S represents a spatial bandwidth constraint of the kinoform. The phase $\theta(v, \mu)$ of the kinoform is designed such as $0 < \theta(v, \mu) \leq 2\pi$. However, we use the quantized phase, which are described by the staircase function $\theta(v,\mu) = (2n+1)\pi/L$, n = 0,1,..,L-1,where L is the number of the quantization levels[7]. Then the kinoform is represented by the nonlinear phase distribution in which each pixel has each quantized phase. The system to be optimized by the SA algorithm is characterized by a cost function of the system. When the SA algorithm is applied to the optimization of the phase distribution in the kinoform, the phase distribution $\theta(v,\mu)$ is a variable to be optimized. The reconstructed image can be obtained from ,

$$I(x,y) = |u(x,y)|^2 = |\iint U(v,\mu)\exp[2\pi i(vx+\mu y)]dvd\mu|^2.\qquad(2)$$

The total power of the reconstructed image is defined as $P_{all} = \iint I(x,y)dxdy$ and the total power of the desired image is defined as $P_{ideal} = \iint I_{ideal}(x,y)dxdy$. Then the cost function in the optimization of the phase distribution in the kinoform is defined as

$$f = \Sigma\Sigma|P_{all}(x,y) - P_{ideal}(x,y)|^2.\qquad(3)$$

By the phase at only one point is changed without other points, we get $\Delta f = f^{new} - f^{old}$. If $\Delta f < 0$, then the new phase distribution is accepted, if $\Delta f > 0$, then it is determined whether it is accepted or rejected by the probability, $P(\Delta f) = \exp[-\Delta f/T]$. This procedure is repeated. If Δf change no longer under 0.05 than any iteration then the system to be optimized is stable. The temperature should decrease slowly for the system

enough not to get trapped in the local minimum. We adopt the temperature schedule, $T = T_0/(1+t)$, where T_0 is initial temperature and t is the iteration number[8]. The temperature is, then, decreased according to the schedule. Above procedure is repeated again.

In computer simulation, we consider the desired image as the letter 'E' with a size of 64*64. We calculate with quantized phases of the kinoform and the maximum iteration number 300. For finding the difference from the different quantizing level, we show the change of each cost function in Fig.1. The cost function of 8 level has the error within about 10%, and 16 levels about 5%. The sufficient quantizing level is 8 in this computer simulation. It may be considered that the increase of the quantizing level causes the increase of the search region; therefore, the enough search can not be performed by the SA algorithm, which rely on the computational times. Consequently, it is noted that the 8 quantizing level of the phase is enough for a size of 64*64 kinoform in the SA algorithm. On the effect from the number of the pixel in the kinoform, if under the size of 64*64 then the enough quantizing level is 8, if over the size of 64*64 then the level increases over 8 with the size, however, 8 level is also enough.

The experiments are performed to verify the results of the phase distribution in the kinoform derived by the SA algorithm. We use a LCSLM instead of the conventional device such as photographic film. The phase is modulated by using bifingence effect of a liquid-crystal. The modulation property of a LCSLM is shown in Fig.2. The phase modulation is controlled by a computer. It may be recognized that a LCSLM is sufficiently satisfied. Compared with the conventional method, the kinoform can be made in shorter time and more easily modified. A experimental configuration with a LCSLM for reconstructing the kinoform is shown in Fig.3. The kinoform is estimated by the reconstructed image detected by a CCD camera. The reconstructed image is shown in Fig.4. The reconstructed image agrees well with the ideal image.

In conclusion, we have shown that the optimization of the phase distribution in the kinoform is performed by the SA algorithm and the optimized kinoform is reconstructed by a LCSLM which can modulate the phase of the kinoform. In the optimization of the kinoform, using the SA algorithm is better over 50% than not using it. According to the result that the optimized kinoform is reconstructed with a LCSLM, the reconstruction image is agree well with the desired image. We have also considered about the quantizing phase of the kinoform. The quantizing level for the kinoform of the size 64*64 is sufficiently 8 levels.

References

1. L.P.Lesem,P.M.Hirsch and J.A.Jordan,Jr.,IBM j.Res.Dev.13,150 (1969).

2. M.C.Gallagher and B.Lui,Appl.Opt.12,2328 (1973).

3. J.R.Fienup,Opt.Eng.19,297 (1980).

4. S.Kirkpatrick,C.D.Gellatt and M.P.Vecchi,Science 220,671 (1983).

5 J.Turunen,A.Vasara and J.Westerholm,Opt.Eng.28,1162 (1989).

6. J.Amako and T.Sonehara,OYOUBUTURI in Japan (1990).

7. T.Yatagai and M.Takeda,Optik.43,337 (1975).
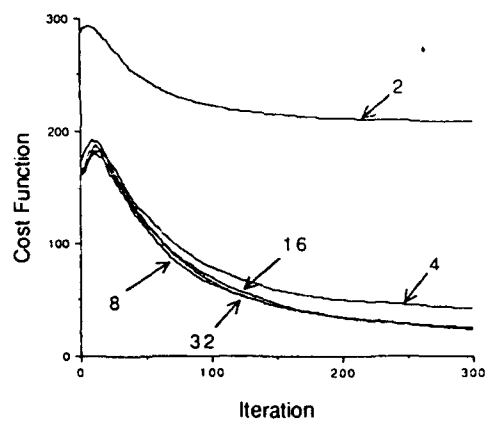
8. H.Szu and R.Hartley,Phys.Lett.122,157 (1987).

Fig.1. Change of the cost function resulting
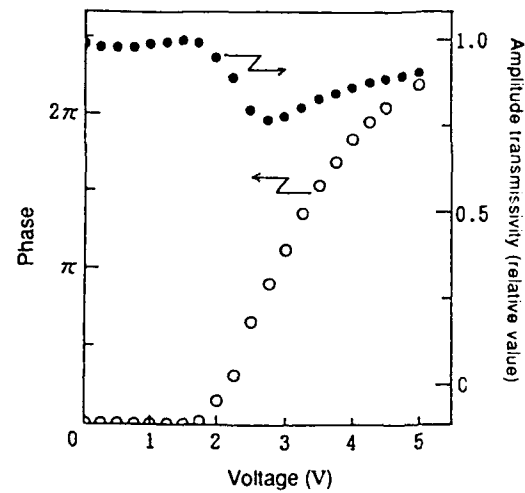from the different quantized level.
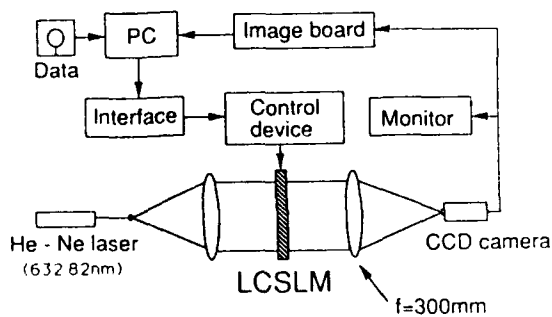

Fig.2. Light modulation character of LCSLM.

Fig.3. Experimental configuration for
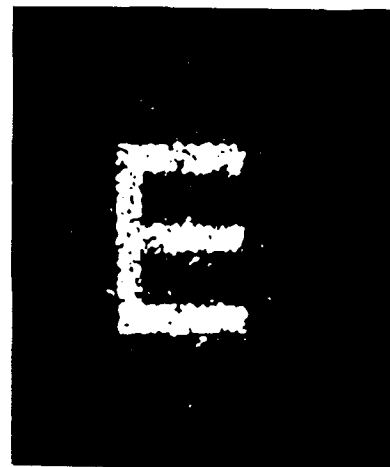reconstructing kinoforms.

Fig.4. A reconstructed image of optimized kinoform.

Annealing Binary Fresnel Holograms for Shaped Beam Generation

Clark C. Guest*
c/o Commander
U. S. Army Missile Command
AMSMI-RD-WS-PO(Dr. Guest)
RSA, AL 35898-5248
(205) 876-8247

Many applications arise in optics and other regimes of electromagnetic waves that require the generation of a beam with a specified two dimensional profile. Optical power is provided in the form of a plane or spherical wave having a known amplitude profile. An optical system must then be designed to transform this input into a beam that produces the desired intensity distribution at a plane a known distance away. This distance often falls within the Fresnel diffraction regime of the optical system.

Computer generated holograms (CGH) provide a flexible, conceptually simple means of beam profile transformation. If the hologram can be recorded with complete control of the amplitude and phase transmittance of each pixel, then design is straightforward. However, common implementations of CGH require that these quantities be discretized. For high optical efficiency, the amplitude transmittance is often set to unity for all pixels, giving a phase-only hologram. Phase only holograms can be implemented lithographically as etched surface relief patterns for fixed holograms, or on phase modulating spatial light modulators for dynamically programmable holograms. Both methods of implementation favor binary quantization of the hologram phase. Lithographic fabrication of binary phase holograms requires only a single masking step. Time consuming and error prone alignment of multiple mask levels is required if finer discretization is used. With the current state of the art in spatial light modulators, those with binary valued pixels, such as ferroelectric liquid crystal or magnetooptic based devices, provide the best combinations of speed, space bandwidth, and availability. There are fundamental reasons to believe that for any level of technological advancement, binary devices will have performance superior to analog devices. The principal factor weighing against the use of binary discretization of phase is the limitation of the optical efficiency of such elements to 40%. However, for many applications, simplicity of implementation outweigh optical efficiency considerations.

Design of binary phase only holograms is not as straightforward as that of continuous valued holograms. The naive approach of designing a continuous valued hologram for the given application and then creating a binary phase only hologram by applying a threshold yields poor results. The optimum binary phase state of each pixel of the hologram must be determined. A general purpose optimization technique known as simulated annealing can be applied. This technique has previously been applied for designing phase only holograms for spot array generation[1], pattern recognition[2], and optical interconnects[3].

Simulated annealing is a computational technique analogous to thermal annealing of metals. A metal object can be strengthened by slowly cooling it from a high temperature. As metal atoms are jostled by the thermal energy they find their lowest energy position in the crystal. The lowest energy state is the most tightly bound and therefore the strongest. In simulated annealing the system to be optimized is described by its state variables. A system energy is defined as a function of these state variables so that a minimum energy corresponds to optimal system performance. State variables are initially set to random values. Then they are perturbed by a small amount. If the perturbed state has lower energy than the original state, the perturbation is retained. If the perturbation raises the system energy, the perturbation will be retained or rejected according to a calculated probability. The probability depends on a system temperature parameter. The system temperature is started at a high value, which corresponds to a high probability of keeping energy increasing perturbations. Through many iterations of perturbation the temperature is gradually

---

*on sabbatical from the University of California San Diego

lowered which leads to less chance of retaining such perturbations. Exploration of higher energy configurations during the early phases of annealing ensures that the system does not lock into configurations that are locally optimal but inconsistent with a global optimum.

Application of simulated annealing to the design of binary phase only holograms takes the binary values of the hologram pixels as state variables. The system energy function incorporates terms measuring similarity of the diffracted pattern to that specified and overall optical efficiency. A high degree of similarity and high efficiency give low system energy. The precise form of the energy function is not critical so long as it captures these characteristics.

Simulated annealing is notoriously computationally intensive. Yet, with existing computers it is tractable for many useful problems. Care should be taken to minimize the requirements on the problem solution. In particular, this means limiting the number of hologram pixels and the number of pixels monitored in the output plane to their minimum useful values. Computation time per iteration is linear in both the number of hologram pixels and the number of output pixels. The number of iterations is not directly related to either quantity, but has been observed to increase with either number, particularly the number of hologram pixels.

A design typically begins with a specification for the size and shape of the desired output distribution. A dark border should be maintained outside the illuminated shape to ensure that the transition to zero intensity is appropriately abrupt. In general, monitoring a large portion of the output plane to eliminate spurious peaks is unnecessary. Terms in the energy function that maximize the optical efficiency of the output shape draw power away from other regions. Of course, one should bear in mind that any off-axis pattern diffracted from a binary structure will have a Hermitian twin mirrored about the optical axis. Now, suppose the shape and its border are embedded in a circumscribing square. The spatial extent of the square determines the maximum size of the hologram pixel that may be used,

$$\Delta x_h = \lambda z / L_o$$

where Δx_h is the side length of the hologram pixel, λ is the optical wavelength, z is the distance from the hologram plane to the output plane, and L_o is the side length of the circumscribing square. To minimize computation, this maximum pixel size is the size that should be used. Note that this assumes an on axis output pattern. If the pattern is off axis, then L_o is the side length of a square centered on the optical axis and enclosing the output figure. Next, a tolerance should be placed on how closely the shape of the output figure must be approximated. This should be set to as coarse a value as acceptable. Representing the shape with discrete pixels will always be accurate to within half a pixel, so the side length of an output pixel may be set to twice the tolerance value. With the size of an output plane pixel fixed, the extent of the required hologram may be determined. The minimum side length of a square hologram is,

$$L_h = \lambda z / \Delta x_o$$

where Δx_o is the side length of an output plane pixel.

The values that have been calculated are the optimum values that will minimize the calculation required for annealing. However, often these values a incompatible with other system constraints. For example, the hologram may have to be larger to match the size of the input beam. If the beam size is fixed, perhaps z can be altered to match the size of the hologram. In any case, the number of pixels in the hologram may be increased, but with the anticipation of a corresponding increase in computational design effort.

For the presentation, examples of annealed binary Fresnel holograms and their diffracted patterns will be presented. Results of a study of computational load as a function of the number of hologram pixels and output pixels will be included.

1. M. R. Feldman and Clark C. Guest, "Iterative Encoding of High-Efficiency Holograms for Generation of Spot Arrays," *Opt. Lett.* **1 4**: 479-481, May 15, 1989.

2. M. S. Kim and Clark C. Guest, "Experimental Results with Annealed Binary Phase Only Filters Fabricated with E-beam Lithography," *Appl. Opt.* **29**: 3380-3386, Aug 10, 1990.

3. M. S. Kim and Clark C. Guest, "Experiments with Block Quantized Binary Phase Holograms for Optical Interconnection," *in submission*.

Diffraction efficiency of multi-level binary optics lenses

William H. Southwell
Rockwell International Science Center
1049 Camino dos Rios
Thousand Oaks, California 91360
(805) 373-4485

A kinoform surface designed to perfectly focus incident plane waves can be expressed[1] by a surface sag s given by

$$s - g_m = \frac{c_m y^2}{1+\sqrt{[1-(1+\kappa)c_m^2 y^2]}},$$ (1)

where $m = 0,1,2...$ is the zone number, $g_m = \lambda m/(n_1-n_2)$ is the offset of the projected vertex plane of the mth zone from the $m=0$ zone, n_1 is the incident refractive index, n_2 is the refractive index of image space, $\kappa = -(n_1/n_2)^2$ is the conic coefficient, and the curvature in the mth zone is given by

$$c_m = \frac{n_2}{f(n_2-n_1)+\lambda m},$$ (2)

where f is the lens focal length. Applying the condition that the path length between adjacent zones differ by one wavelength, the radial height of the zone edges or surface discontinuities is given by

$$y_m = \sqrt{[2f\lambda/n_2 + (\lambda m/n_2)^2]}.$$ (3)

The longitudinal surface discontinuity e_m at top of the mth zone is found by equating $e_m = s$ in Eq.(1) at the height y_{m+1} given by Eq.(3),

$$e_m = \frac{c_m y_{m+1}^2}{1+\sqrt{[1-(1+\kappa)c_m^2 y_{m+1}^2]}} + g_m.$$ (4)

Although an approximation to Eq.(4) is given by $e_m \approx \lambda/(n_2-n_1)$, the magnitude of e_m tends to decrease with increasing zone number m. This may be seen by observing the depths of the jumps of the smooth surface in Fig. 1.

The ring radii is determined by solving Eq.(1) for y when $s = s_{mj} = e_m(j-1)/2^J$, where $j = 1,2,3...2^J$ in each of zone m. The result is

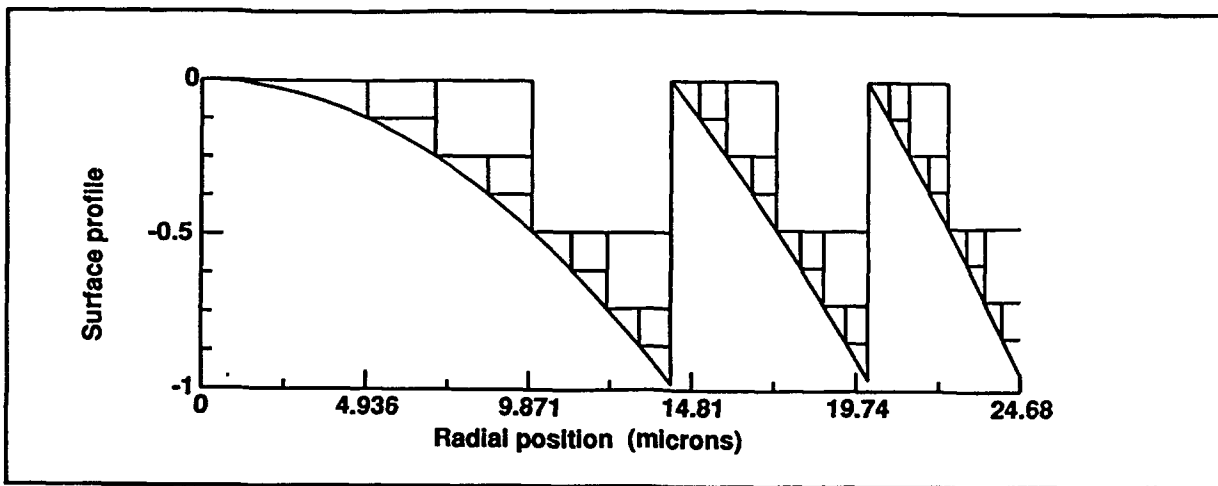$$y_{mj} = \sqrt{[(s_{mj}-g_m)\{2/c_m - (1+\kappa)(s_{mj}-g_m)\}]}.$$ (5)

Fig. 1. Kinoform lens (curved figure) and the 2,4, and 8 level approximation.

For surface relief processing[2] all comparable etch depths are the same. This is accomplished by using a constant e_m in Eq.(5). Three masks are shown in Fig. 1.

The diffraction efficiency is determined from the on-axis irradiance in the focal plane. The diffraction integral determines the electric field strength at that point. For a circularly symmetric system and an on-axis field point, the field at focus is

$$u(0,f) = \frac{1}{2\pi}\int \frac{u(\rho,0)\exp(-ikr)f(ik+1/r)}{r^2} \, dA , \qquad (6)$$

where in this equation $k=2\pi/\lambda$, $r=\sqrt{[f^2+\rho^2]}$, and $dA=2\pi\rho d\rho$. ρ is the aperture radial coordinate, which varies from 0 to a, the beam semidiameter. The integration is over a plane where the incident field is uniform in amplitude and where the phase in each sub-zone is $\phi_{mj}=2\pi s_{mj}(n_2-n_1)/\lambda$. Thus the diffraction integral may be written as a sum over all zones of an integral over that zone,

$$u(0,f) = ikf \sum_n^N \exp(i\phi_{mj}) \int \frac{\exp(-ix) \, dx}{x} , \qquad (7)$$

where a change of integration variable was made from ρ to $x=kr$. The limits on the x-integral are from x_{n-1} to x_n where n counts all sub-zones in order from the center out. That is, start with m=0 and let j=1,2...2^J, then m=1 and repeat j=1,2...2^J, etc. The integration limits are

$$x_n = 2\pi\sqrt{[f^2+y_{mj}^2]}, \qquad (8)$$

where $x_0=2\pi f$ and the upper limit on the last zone is $x_N=2\pi\sqrt{[f^2+a^2]}$, which means the beam diameter rather than the lens diameter determines the aperture limits for the diffraction integral (as long as the lens is larger than the beam).

The diffraction efficiency (with Fraunhofer normalization[3]) as a function of beam f/number is shown in Fig. 2. The kino lens approaches unity diffraction efficiency for large f/numbers. Also note the oscillations with beam f/number for the binary approximations. The edge of the beam, which may not occur at a zone edge, acts like a diffraction edge; a factor not accounted for in the sinc function estimation of diffraction efficiency.

Shown in Fig. 3 are the positions of the beam edge at the maximums and minimums in the diffraction efficiency for two-level lens. It is seen that the maximums are not at the zone edges.

Figure 4 shows the two-level configuration for an f/3.385 beam, which has a diffraction efficiency of 0.36 (a minimum in Fig. 2). The ring radii were then numerically adjusted to maximize the diffraction efficiency at that f/number. The diffraction efficiency was increased to 0.43. The new ring structure is also shown in Fig. 4.
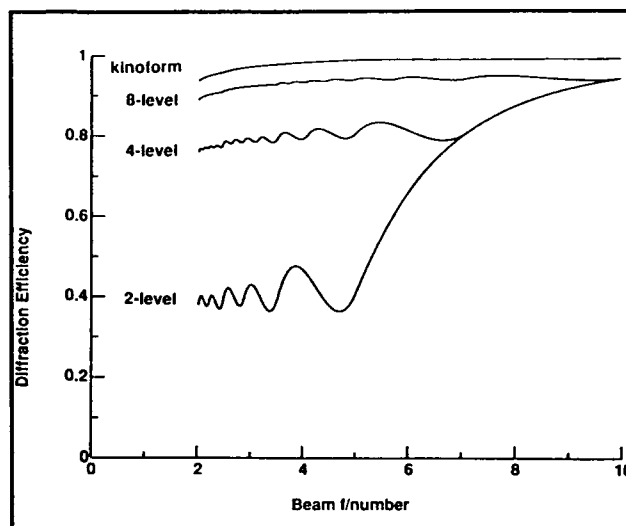
Fig. 2. Diffraction efficiency for 2,4, and 8 level binary optics lenses.
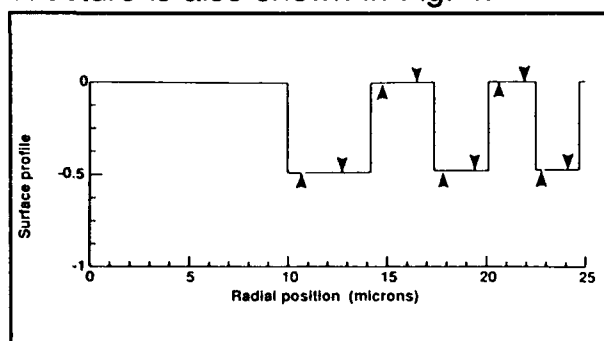
Fig. 3. Beam width for maximum ▼ and minimum ▲ diffraction efficiency.
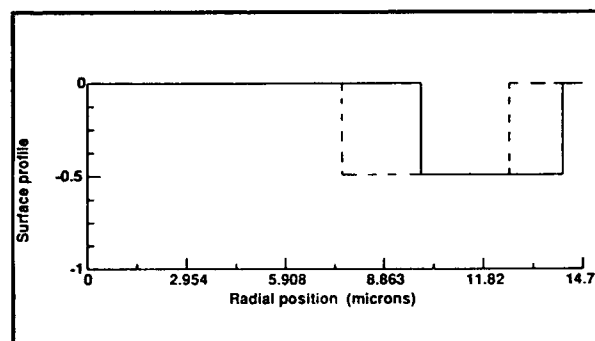
Fig. 4. Conventional (solid lines) and optimized (dashed lines) ring positions.

References
1. W. H. Southwell, "Ray tracing kinoform lens surfaces," Appl. Opts. (accecpted for publication) 1992.
2. G. J. Swanson, "Binary Optics Technology: The Theory and Design of Multilevel Diffractive Optical Elements," Technical Report 854, MIT Lincoln Laboratory, 14 August 1989.
3. M. Born and E. Wolf, *Principles of Optics*, 4th ed. (Pergamon, Oxford, 1970), p.386.

Optical Interconnects for Computing 2

WC 2:00pm–3:30pm
Cabildo Room

Jurgen Jahns, *Presider*
AT&T Bell Laboratories

Diffractive optical elements for optoelectronics

Norbert Streibl
Physikalisches Institut der Universität
Staudtstr. 7, D-8520 Erlangen, Germany
phone: (+49) 9131 - 858395

Introduction

Diffractive optical elements (DOEs) rely on the deflection of light waves by diffraction on microstructures rather than on refraction by smooth surfaces. They are well-suited for applications involving monochromatic light and lasers: They are *flexible* in design (synthetic holograms are designed by CAD), it is possible to fabricate *array-optics* (several elements precisely positioned side by side on one single substrate). DOEs may perform several functions at the same time (for example focusing, deflecting and beam splitting can be *integrated* into one component), they are often fabricated by *planar* technologies well known from microelectronics and they can be *replicated*, once one master has been made. Often DOEs are smaller and lighter in weight than conventional optical elements. Typical problems with DOEs are their *wavelength dependence* and the achievement of high *diffraction efficiencies* and low levels of *straylight*. Since DOEs usually have only very few optical surfaces (often just one) for diffractive lens systems the correction for *aberrations*, the field of view or tolerances against wavelength detuning are in many cases insufficient.

Integrated optoelectronic or photonic devices, such as detector arrays or laser arrays, very often call for geometrically similar arrays of optical components, that may be realized as DOEs. Applications are for example parallel optoelectronic interconnections (especially over short distances within data processing systems, where multiplexing of parallel channels does not pay). A second important field are optical sensors, where miniaturization and the combination of the optics with diode lasers and photodetectors into microsystems is important. In this review paper some DOEs together with examples for applications in optoelectronics are presented.

Deflection elements for parallel point-to-point interconnections

Optical interconnections within high-speed data processing systems have been proposed because they offer high bandwidth, alleviate problems with impedance matching, eliminate ground loops and ultimately allow for higher packing densities than electronic interconnections. Parallel optical interconnections may use fiber

bundles for guiding the light or imaging systems, that may employ DOEs. Fig. 1 shows a demonstration experiment [1] for an optoelectronic backplane, that has been performed with a light guiding glass plate and holographic coupling elements. In order to obtain maximum diffraction efficiency with large deflection angles volume holograms in dichromated gelatine (DCG) are employed. Wavelength detuning from the blue recording wavelength to the near infrared had to be investigated. Data rates in the 500 MBit/s range per channel have been demonstrated. The straylight of the deflection elements and its angular dependence was determined for DCG since this is critical for an acceptable signal to noise ratio. Facetted holograms consisting of arrays of deflection elements with different deflection angles were recorded for rearranging the order of parallel data channels between two planes. One- and twodimensional arrangements of such permutation elements are shown.

Beam splitters for multipoint interconnections and bus systems

If beam splitting devices are employed, one single signal can be directed to several receivers simultaneously. Obviously such multiple beam splitters are required for the broadcasting of signals, such as clock-distribution in a data processing system or in an interconnection system with bus topology [2] (many talkers and many listeners simultaneously on one single line). Multiple beamsplitters, that generate an array of beams out of one input beam, have found also many more applications, such as the illumination of optical modulator arrays, coherent coupling of laser arrays etc. Often they are realized [3] as synthetic holograms, kinoforms or special phase gratings, such as the Dammann-grating. Fig. 2 shows schematically a multipoint interconnection consisting of an imaging system with a phase grating for fanout.

Acknowledgement

References

[1] Haumann, H.-J. et. al.: "Optoelectronic interconnection based on a light guiding plate with holographic coupling elements", Opt. Engin. 30, 1620 (1991).

[2] Krackhardt, U. et. al.: "Concept for an optical bus-type interconnection network", Appl. Opt. accepted (1991).

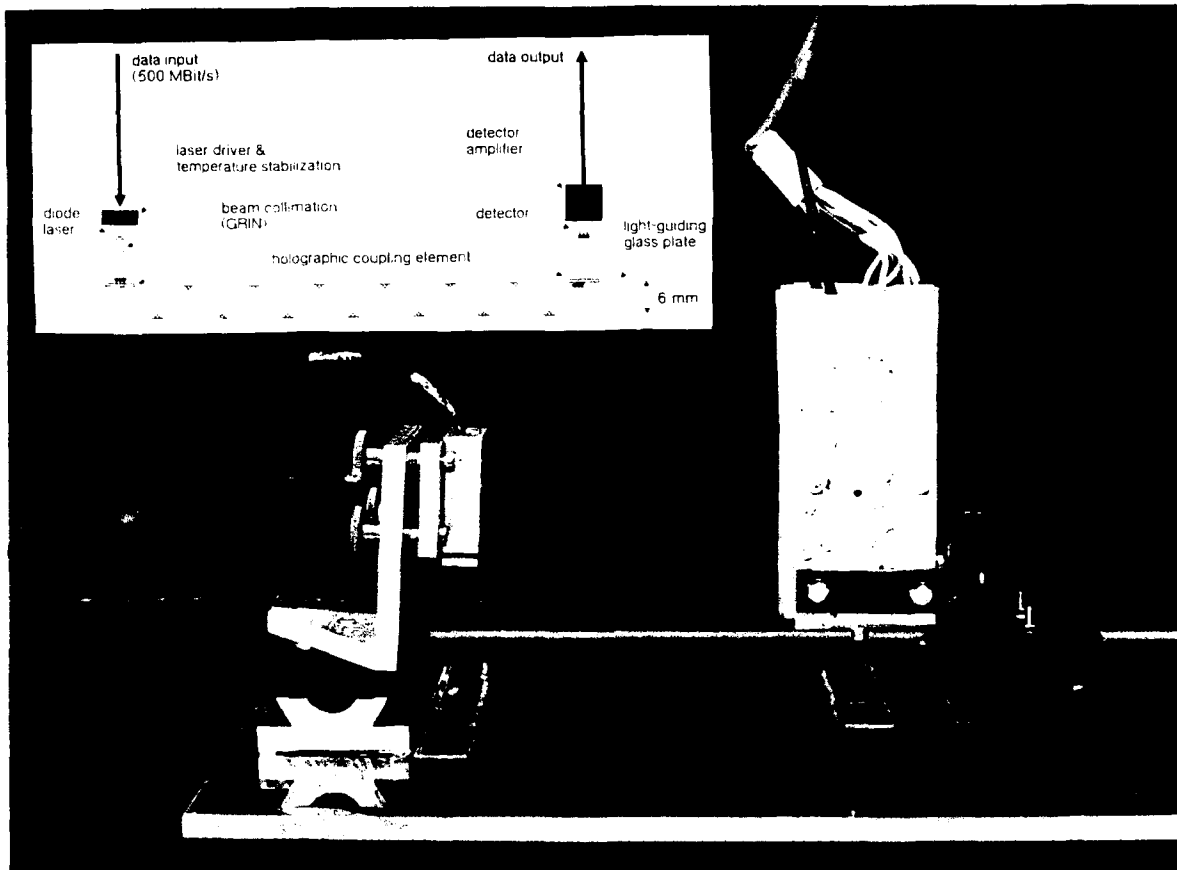[3] Streibl, N.: "Beam shaping with optical array generators", J. Mod. Opt. 36, 1559 (1989).

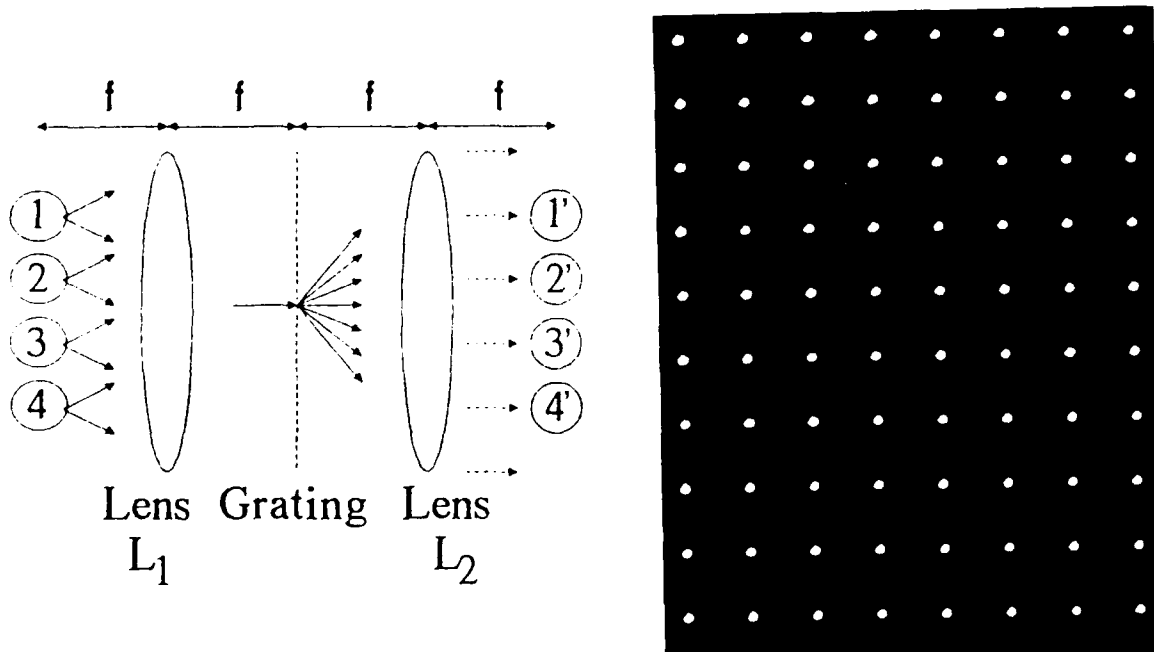Fig. 1: Demonstration setup for an optoelectronic backplane (inset: one channel).

Fig. 2: Setup of a multipoint interconnection with grating as multiple beamsplitter and part of the output pattern of a multiple beam splitter

Analysis of Weighted Fan-out/Fan-in Volume Holographic Interconnections

Gregory P. Nordin

University of Southern California
University Park MC-0483
Los Angeles, CA 90089-0483

Praveen Asthana

IBM Corporation
9000 S. Rita Rd.
Tucson, AZ 85715

Armand R. Tanguay, Jr. and B. Keith Jenkins
University of Southern California
University Park MC-0483
Los Angeles, CA 90089-0483

Summary

Volume holography has often been proposed as an interconnection technology for photonic neural network implementations [1] because it appears to potentially meet the critical requirements of providing both large numbers of interconnections *and* a weighted fan-out/fan-in topology. The feasibility of using volume holograms for large-scale weighted fan-out/fan-in interconnection applications depends in part on the *fidelity* with which the interconnection weights can be implemented, and on the *throughput* that can be achieved in the volume holographic interconnection system. In addition, an important implementation issue is the *number of exposures* required to record a particular interconnection configuration because this can impact the total writing time and required exposure schedule.

In many neural network algorithms, the interconnections between any two layers can be represented as $\rho = Wx$ in which each component of the vector x represents the output of a neuron unit in the input layer, W is the interconnection matrix, and each component of the vector ρ is the input to a neuron unit in the output layer. A typically proposed volume holographic interconnection architecture that performs this interconnection function [1] (hereafter referred to as a "conventional" architecture) is shown in Fig. 1. Each interconnection between a pixel in the input plane and a pixel in the output plane (not shown) is implemented as a single diffraction grating in the holographic recording medium. The weight of the interconnection is related to the relative diffraction efficiency of its associated grating.

For adaptive neural networks in which a learning algorithm is implemented, the weight matrix is typically formed by successively presenting training patterns (consisting of an input image at the input plane and its associated training image at the training plane) to the system until the appropriate error criterion is minimized. In a conventional architecture, there are three methods to record the desired interconnection gratings during the presentation of a single training pattern to the system. In the first method, all of the pixels in the input and training planes are turned on simultaneously. Since the light from each pixel is mutually coherent, the desired interconnection gratings are formed. In addition, undesired gratings are created that form *intraplanar* connections amongst the pixels of both the input plane and the training plane. As is generally recognized, these additional coupling paths introduce a serious source of crosstalk into the interconnection system. By recording the desired gratings in a page-wise sequential (*i.e.*, a single pixel in the input plane simultaneously with all of the training plane pixels) or fully sequential (*i.e.*, a single input pixel with a single training pixel) manner, some or all of these coherent crosstalk gratings may be avoided. The cost, however, is to require additional exposures compared to the simultaneous recording method. For an interconnection system connecting N input nodes to N output nodes (an "N-N" interconnection), the simultaneous recording method requires one exposure per training pattern whereas the page-wise sequential and fully sequential methods require N and N^2 exposures, respectively. For large numbers of interconnections (the situation for which holographic interconnections are presumably attractive), this could result in impractically long training sessions.

We quantitatively examined the reconstruction fidelity and throughput of the conventional architecture by numerically modeling a 10-10 interconnection system using the optical beam propagation method. A linear holographic recording medium was assumed with unlimited modulation range. Ten training patterns of random intensities were used to generate the (nearly independent) weight matrix recorded in the holographic medium. For this choice of weights, the RMS error of the diffracted outputs [2] for a conventional architecture is shown in Fig. 2a for simultaneous (with R=1, in which R is the beamsplitter ratio in Fig. 1), page-wise sequential (R=100), and fully sequential recording (R=1). The horizontal axis represents the grating strength (in radians) of the largest interconnection grating recorded in the medium. The interconnection is readout with a set of mutually coherent random intensity beams. The optical throughput is shown in Fig. 2b. As expected, the RMS error of the reconstructed outputs is large for simultaneous recording. There is little improvement in the error in going to page-wise sequential recording using a beamsplitter ratio of 100. This can be understood as follows. During the recording of a single training pattern, the crosstalk gratings connecting the pixels within the training plane are exposed N times. The desired gratings, however, each receive only a single exposure. When the undesired crosstalk gratings are eliminated using fully sequential recording, the RMS error drops dramatically such that it is still relatively low at a peak throughput of over 85%.

An alternative volume holographic interconnection architecture has recently been proposed [3] that requires only one exposure per training pattern and yet minimizes undesired crosstalk gratings. This architecture includes an optical source array in which each source is individually coherent, but mutually incoherent with all other sources. In Fig. 3 we show a modification of this architecture that for implementation in certain photorefractive materials does not suffer from an inherent throughput loss due to multiple beam superposition. Using lenses L_1 and L_2 (see Fig. 3) a set of subholograms (which may partially overlap) are recorded in the holographic medium. Each subhologram consists of a 1-N fan-out connecting a single input pixel to every output pixel (with the aid of an imaging lens following the holographic medium [not shown]).

Numerical modeling results for this multiple source incoherent/coherent architecture (for R = 100) are shown in Fig. 4 (in which non-overlapping subholograms are assumed). The weight matrix and random inputs are the same as used above for the conventional architecture. The RMS error of the diffracted outputs is comparable to the results obtained for fully sequential recording in a conventional architecture, and yet the multiple source incoherent/coherent architecture requires only a single recording per training pair.

In addition to requiring fewer exposures to achieve the same level of fidelity and throughput as obtained for fully sequential recording in a conventional architecture, the multiple source incoherent/coherent architecture offers several further advantages. First, the weighted interconnections stored in the volume holographic medium can be copied to another volume holographic medium in a one-step process (which is useful, for example, for transferring a set of learned weights from a dynamic to a permanent holographic medium) [4]. Second, since the source array shown in Fig. 3 consists of optical sources that are individually coherent but mutually incoherent, the summation at the output nodes is performed by the fan-in of mutually incoherent beams. This eliminates the requirement for strict positional stability of the optical components during readout (which is required in a conventional architecture for readout with mutually coherent beams). No degradation in throughput (see Fig. 4b) is suffered with the use of mutually incoherent beams because an angular fan-in is used at each output node.

[1] D. Psaltis, D. J. Brady, and K. Wagner, "Adaptive Optical Networks Using Photorefractive Crystals," Appl. Opt. 27, p. 1752-1758.

[2] C. Slinger, "Analysis of N-to-N Volume-Holographic Neural Interconnect," J. Opt. Soc. Am. A 8, p. 1074-1081.

[3] B. K. Jenkins, G. C. Petrisor, S. Piazzolla, P. Asthana, and A. R. Tanguay Jr., "Photonic Architecture for Neural Nets Using Incoherent/Coherent Holographic Interconnections," Proceedings of OC'90, Kobe, Japan (1990).

[4] S. Piazzolla, B. K. Jenkins, and A. R. Tanguay, Jr., "Single Step Copying Process For Multiplexed Volume Holograms," submitted to Optics Letters.
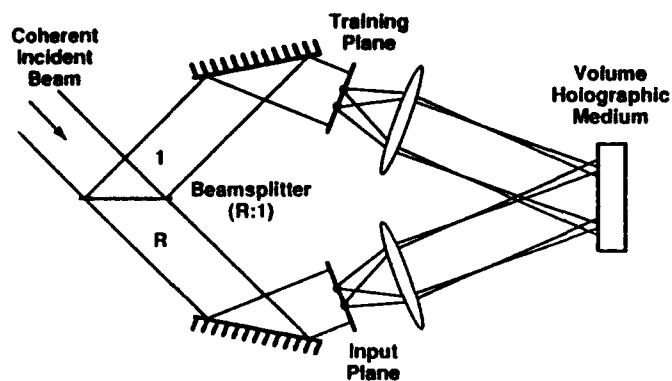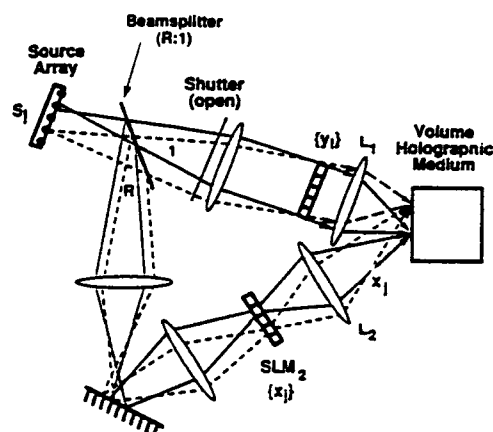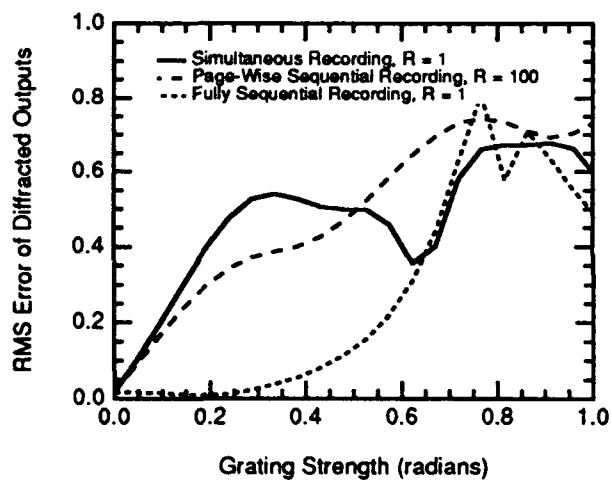
Figure 1
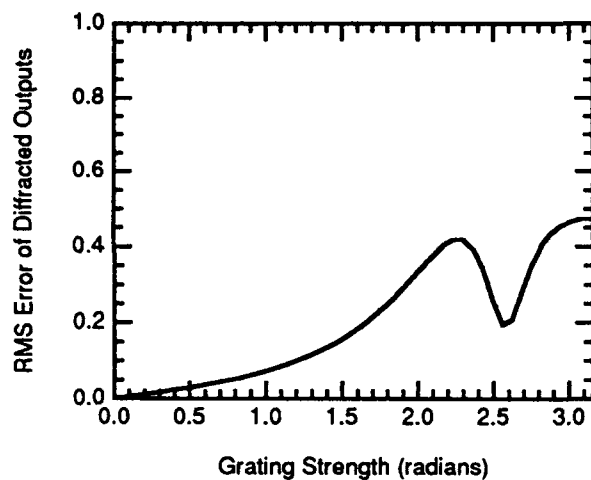

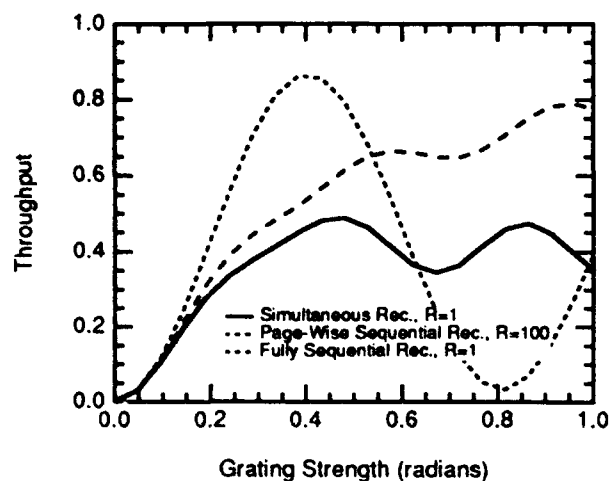**Figure 3**

Figure 2a

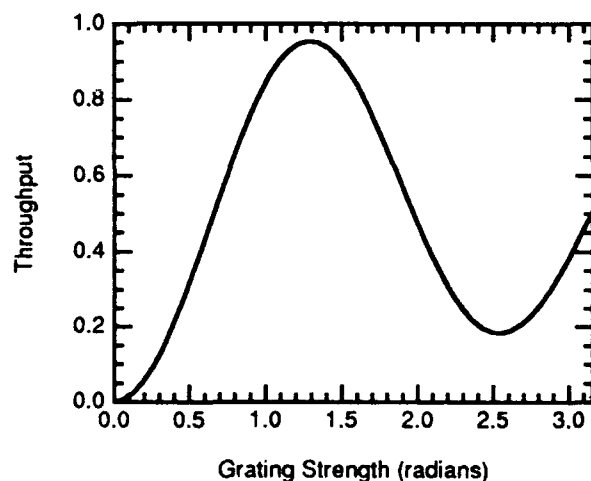**Figure 4a**

Figure 2b

Figure 4b

Acoustooptic Programmable Spot Array Generator

Joseph N. Mait and Dennis W. Prather
Harry Diamond Laboratories
SLCHD-ST-OP
2800 Powder Mill Road
Adelphi, Maryland 20783

Ravindra A. Athale
Electrical and Computer Engineering
George Mason University
Fairfax, Virginia 22030

In some optical computing architectures [1] array generators are used to establish an array of fixed, regular interconnects between two planes. Because system programmability is achieved elsewhere, the ability to reconfigure the array is not a requirement and the array generator can be fabricated as a fixed phase filter. In contrast, for optical processing applications such as optical morphology [2] reconfigurability and programmability of the spot array are essential, for which purpose magneto-optic spatial light modulators [3] and acoustooptic (AO) modulators [4] have been employed.

However, due to the binary nature of the array generating functions, the spot arrays in Refs. 3 and 4 were generated with low diffraction efficiency. To generate reconfigurable two-dimensional spot arrays with high diffraction efficiency, the system represented in Fig. 1 has been constructed. The system consists of two AO cells oriented orthogonally to each other and driven by two arbitrary waveform generators. As a result of using this architecture, at any instant in time, only separable spot arrays $q_s(x, y)$ can be generated:

$$q_s(x, y) = r(x)\, s(y).$$

Since the generation of each component spot array is similar, the generation of only a single component, the x-axis spot array $r(x)$, is considered:

$$r(x) = \sum_{n=N_1}^{N_2} a_n\ \exp(j\theta_n)\ \delta(x - nd_x),$$

where the magnitude a_n and phase θ_n specify the nth spot of the spot array and d_x is the x-axis spacing between spots in the image plane. The corresponding spatial frequency function is given by

$$R(u) = \sum_{n=N_1}^{N_2} a_n\ \exp(j\theta_n)\ \exp(-j2\pi nu d_x).$$

The function $R(u)$ represents the form of the array generator necessary to generate the spot array $r(x)$ and is independent of the means for its realization.

For an AO realization, the modulator drive signal necessary to generate $r(x)$ is given by

$$v_x(t) = |R(\frac{Vt}{\lambda f})|\ \cos[2\pi\nu_{AOx}t + \arg\{R(\frac{Vt}{\lambda f})\}].$$

The argument $Vt/\lambda f$ relates the spatial frequency variable u to the spatial dimensions of the Fourier plane through the scale factor λf, where λ is the wavelength of the illumination and f is the focal length of the transform lens in Fig. 1. Via the cell sound velocity, V, the argument also relates spatial dimensions within the cell to temporal dimensions. The effect of the drive signal $v_x(t)$ is to launch a moving, modulated grating onto the AO cell.

In the (1,1)-diffracted order of the system, the drive signals $v_x(t)$ and $v_y(t)$ generate the spatio-temporal response $p_s(x, y; t)$:

$$p_s(x, y; t) = \sum_{n=N_1}^{N_2} \sum_{m=M_1}^{M_2} a_n \, a_m \exp\{j[2\pi(\nu_{AOx} + \nu_{AOy} + n\nu_x + m\nu_y)t + \theta_n + \theta_m]\} \, \delta(x - nd_x, y - md_y).$$

The temporal component contains only the Doppler shift produced by the moving grating in the Fourier plane and not the frequency of the illumination. If $p_s(x, y; t)$ is detected in a time integrating fashion, the system response, $z_s(x, y)$, is

$$z_s(x, y) = \sum_{n=N_1}^{N_2} \sum_{m=M_1}^{M_2} |a_n a_m|^2 \, \delta(x - nd_x, y - md_y).$$

The actual spot array generated therefore corresponds to the intensity of the desired array, which is not considered a serious disadvantage. In fact, the ability to arbitrarily specify array phase can be used to design high diffraction efficiency arrays. If the drive signals are modified during successive time intervals, time integration also allows nonseparable arrays to be synthesized from separable arrays:

$$z(x, y) = \sum_{k=0}^{K} z_{s,k}(x, y).$$

The separable spot arrays represent the outer product decomposition of the desired nonseparable array [5].

To design efficient one-dimensional array generators, for fixed a_n, a phase-only constraint can be assumed, i.e., $|R(u)| = 1$, and the phase values θ_n can be determined such that a high diffraction efficiency is obtained [6,7]. However, because the amplitude transmission of the AO devices is unconstrainted, the phase-only constraint is not a requirement and small variations in the magnitude can be used to produce uniform, as well as efficient, spot arrays.

A 9 × 9 separable spot array generated by the AO system is shown in Fig. 2(a). The approximate phase-only characteristic of the array generator is represented in Fig. 2(b) by a single period of the magnitude $|R(u)|$ used to drive the AO cells. The uniformity of the spot array is indicated in the cross-sectional views of Figs. 2(c) and 2(d). Figures 3(a) and 3(b) are two nonseparable arrays generated by the system. Three outer product terms were used to generate the cross in Fig. 3(a), whereas only two were used to generate the plus sign in Fig. 3(b). The AO devices used to generate the spot arrays were Isomet TeO_2 cells having a 100 MHz center frequency and a 50 MHz bandwidth. The sound velocity, V, in a single cell is 617 m/s and the active aperture of the system is 4 mm × 4 mm, which corresponds to a 6.5 μs time aperture. The amplified outputs from two Analogic polynomial waveform generators model 2040 were used to drive the AO cells. The focal length, f, of the transform lens was 200 mm and the illumination wavelength, λ, was 632.8 nm. The arrays were generated with $\nu_x = \nu_y = 1$ MHz or, equivalently, $d_x = d_y = 0.2$ mm.

An AO system has been demonstrated that is capable of generating reconfigurable two-dimensional nonseparable spot arrays. The analog nature of the AO devices provides considerable degrees of both magnitude and phase design freedom such that uniform and efficient arrays can be generated.

References
1. M. J. Murdocca, A. Huang, J. Jahns, and N. Streibl, Appl. Opt. **27**, 1651 (1988).
2. R. Athale, J. N. Mait, and D. W. Prather, Opt. Commun., to be published (1991).
3. J. A. Davis, S. W. Connely, G. W. Bach, R. A. Lilly, and D. M. Cottrell, Opt. Lett. **14**, 102 (1989).
4. E. Tervonen, A. Friberg, J. Westerholm, J. Turunen, and M. R. Taghizadeh, Opt. Lett. **16**, 1274 (1991).
5. R. A. Athale and J. N. Lee, Proc. IEEE **72**, 931 (1984).
6. H. P. Herzig, D. Prongué, and R. Dändliker, Japan. J. Appl. Phys. **29**, L1307 (1990).
7. U. Krackhardt, J. N. Mait, and N. Streibl, Appl. Opt., to be published (1991).
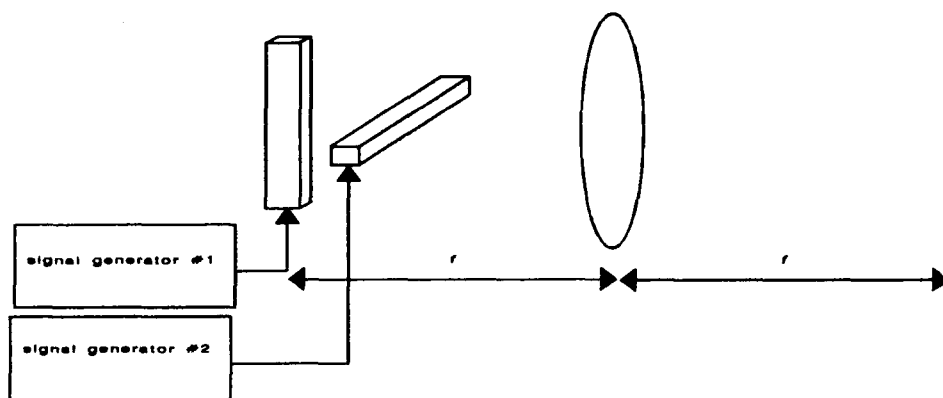
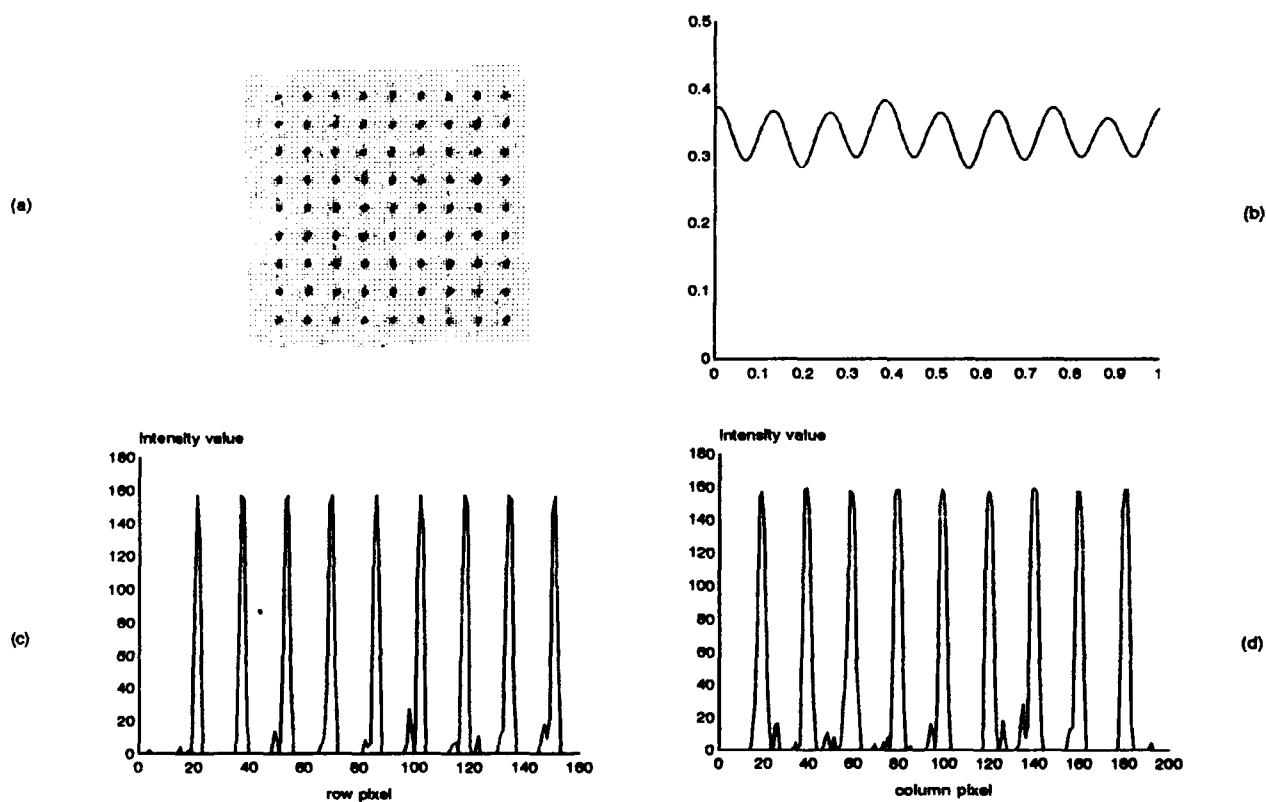Figure 1. Crossed Bragg cell system used to generate two-dimensional spot arrays.

Figure 2. (a) 9 × 9 separable spot array. (b) magnitude of single period of drive signal used for generation. (c) cross-sectional view of first row. (d) cross-sectional view of first column.
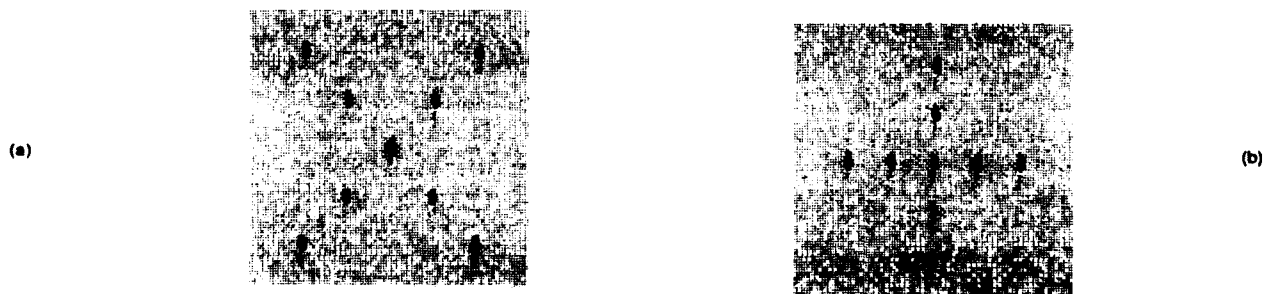

Figure 3. Nonseparable spot arrays generated using (a) 3 outer product terms and (b) 2 outer product terms.

MULTIPLE BEAM SPLITTER CHARACTERISTICS OF HOLOGRAPHIC SURFACE-RELIEF GRATINGS RECORDED NONLINEARLY

P. Langlois and R. Beaulieu, National Optics Institute
369 Franquet Street, Sainte-Foy (Quebec) G1P 4N8 Canada Tel.: (418) 657-7006

A. Beauregard, Lasiris Inc.
3549 Ashby, Saint-Laurent (Quebec) H4R 2K3 Canada Tel.: (514) 335-1005

1. INTRODUCTION

It has been recently reported that dielectric surface-relief gratings with conic cross-sectional shapes have high diffraction efficiency and produce several beams of similar intensities[1]. Although conic gratings give reasonably good characteristics, other surface-relief are worth considering.

A material frequently used for the preparation of phase relief gratings is photoresist. Typical exposure characteristics of photoresist materials are exhibited in Fig. 1 in the form of Δh - E curves where Δh represents the change in layer thickness caused by exposure E.

Experimentally, it was found that the thickness change is proportional to the exposure if the Shipley S1400-25 photoresist is developed in a 6:1 dilution of AZ-303A developer and that it varies as E^2 if the photoresist is developed in a 12:1 dilution. The material non linearity is represented approximatively by the following equation:

$$\Delta h = h_0 + aE^2 \tag{1}$$

where h_0 and a are constants.

When the photoresist is exposed to a holographic interference pattern and when the recording material acts linearly, surface-relief gratings with sinusoidal cross-sectional shapes are obtained. Unfortunately, sinusoidal gratings always produce at least one weak diffracted beam when they are used to divide a laser beam into several beams. If instead the photoresist is developed in a 12:1 dilution, the surface profile of the grating can be approximated by

$$Z(x) = h - h \sin^4 \left(\frac{\pi x}{p}\right) \tag{2}$$

where p represents the period of the interference pattern and h is the modulation amplitude.

2.0 DIFFRACTION PROPERTIES

To evaluate the diffraction properties of gratings whose cross-sectional shape is defined by eq. (2), a transmittance approach has been applied. Following the method of Magnusson and Shin[2], it is assumed that a normally incident plane monochromatic wave is diffracted by the grating into a number of plane waves. The transmittance of the grating structure may be expressed as the convolution:

$$T(x) = e^{-jk(n-1)Z(x)} * \sum_{m=-\infty}^{\infty} \delta(x - mp) \qquad (3)$$

where $j = \sqrt{-1}$, n is the refractive index of the grating material, $k = 2\pi/\lambda$ and λ is the free-space wavelength.

Since the grating involves a periodic structure, $T(x)$ may also be expressed as a complex Fourier series

$$T(x) = \sum_{m=-\infty}^{\infty} S_m e^{j2m\pi x/p} \qquad (4)$$

and the coefficients in the series are identified as the amplitudes of the diffracted waves. The diffraction efficiency of each diffracted wave is then given by

$$\eta_m = S_m^* S_m \qquad (5)$$

where the asterix denotes the complex conjugate and m is the diffraction order.

In Figs. 2 and 3 respectively, the ratio R of the maximum diffraction efficiency to that of the minimum diffraction efficiency and the total useful energy fraction E corresponding to the addition of the individual diffraction efficiencies for a seven-beam splitter are plotted as a function of the modulation amplitude h with $\lambda = 817$ nm and n = 1.635. Sinusoidal and parabolic profiles are shown for comparison. It is seen that the "nonlinear grating" offers the best performances with regards to the uniformity in intensity among the seven diffracted beams (lowest R value). Moreover, the nonlinear grating has a total efficiency 5 % higher than the parabolic grating thus providing 91 % of usefull energy (without taking into account Fresnel reflection losses).

Experimentally, surface-relief gratings with a period of 10 μm were generated by exposing samples coated with photoresist to the sinusoidal intensity distribution produced by the interference pattern of two He-Cd laser beams and by developing the samples in an AZ-303A developer 12:1 dilution. Fig. 3 shows a typical cross-sectional profile of a grating recorded nonlinearly as measured with a Dektak 3030 profilometer. Experimental data are indicated by the squares and eq. (2) has been used to trace the solid curve. A sinusoidal cross-sectional shape and a parabolic cross-sectional shape are also shown for comparison. Diffraction efficiencies including reflection losses have been measured at wavelength 817 nm using a collimated diode-laser beam and typical values are shown in fig. 5. These results are in good agreement with the calculation.

References

1. P. Langlois and R. Beaulieu, Appl. Opt. 29, 3434 (1990)
2. R. Magnusson and D.Shin, J. Opt. Soc. Am. A 6, 1249 (1989).
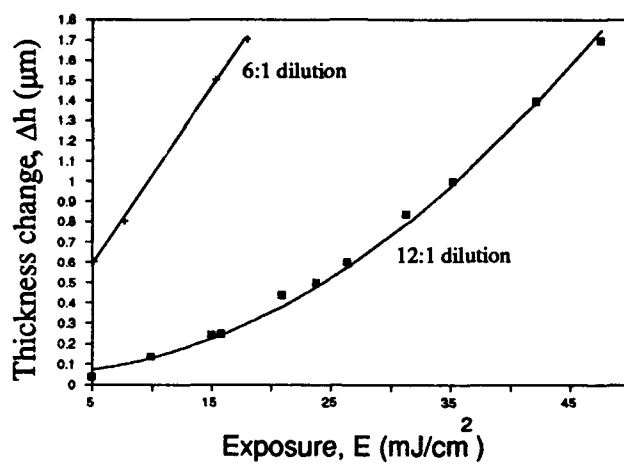
Figure 1

Figure 1

Figure 2
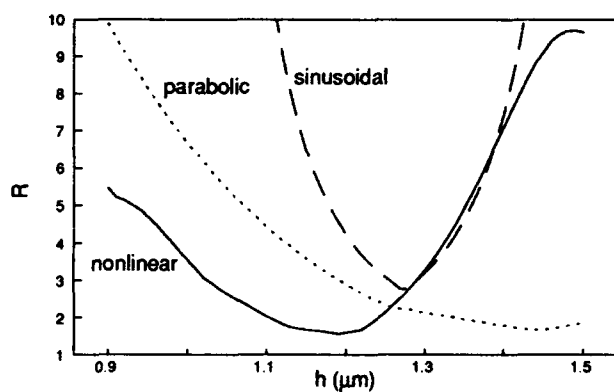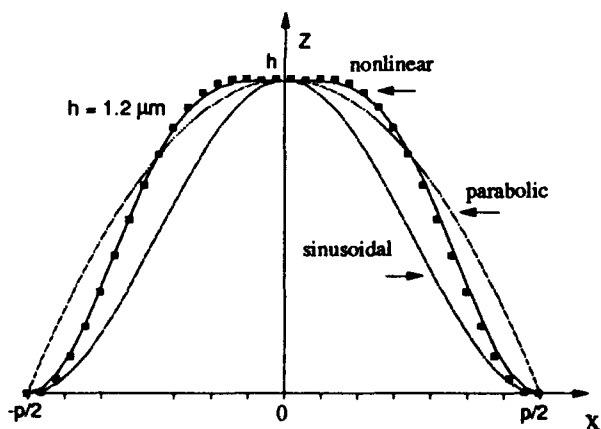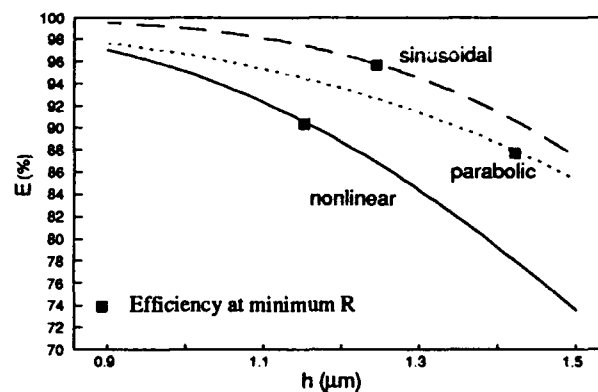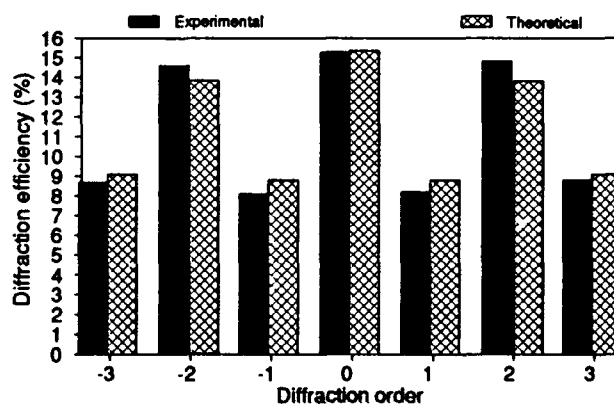

Figure 2

Figure 3

Figure 3

Figure 4

Figure 5

Ailawadi, N. K. — TuC2
Aldrich, Robert E. — TuD13
Andrés, P. — TuD12
Asthana, Praveen — WC2
Athale, Ravindra A. — WC3
Azzam, R. M. A. — TuB2, TuD1

Bare, Harold — MC3
Barsetti, S. — TuA3
Beaulieu, R. — WC4
Beauregard, A. — WC4
Behrmann, Gregory P. — MA4
Bélanger, M. P. — TuA3
Beletic, James W. — TuD8
Bialkowski, Stephen E. — TuD7
Black, T. D. — TuD4
Boiko, Yuri B. — MB4
Bojko, Richard — MC3
Bowen, John P. — MA4
Brubaker, J. L. — MC2
Buralli, Dale A. — WB
Buzcek, Carl — WA4

Calixto, Sergio — MB4
Chen, Jenkins — TuD14
Clark, Peter P. — MA1, MA3, WA
Climent, V. — TuD12
Cloonan, T. J. — MC2
Côté, M. — TuA3
Cox, J. Allen — MB, WA3
Craighead, Harold G. — MC3
Crisci, R. J. — MC2

Dändliker, R. — TuC3, TuD3
Delaney, W. F. — TuA2
DeSandre, Lewis F. — WA4
Domash, Lawrence H. — TuD10

Ehbets, P. — MB3, TuC3, TuD3
Elson, J. Merle — WA4
Evans, Clinton E. — TuD5

Feldblum, A. Y. — MC4
Fleming, Madeleine B. — MA2
Francis, Melvyn — TuD5
Fréchette, J. — TuA3
Furlan, W. D. — TuD12
Futhey, John A. — MA2

Galarneau, P. — TuA3
Gale, M. T. — MB3
Gallagher, Neal C. — MD, TuB1, WA2
Gaylord, Thomas K. — MD1
Giamona, Larry — TuA4
Giardina, K. A. — TuD1
Glytsis, Elias N. — MD1
Goltsos, W. C. — TuA2
Gremaux, Douglas A. — TuB1
Griswold, M. P. — TuA2
Gruhlke, Russell — TuA4
Guest, Clark C. — WB3

Haas, Franz — MC3
Haggans, Charles W. — TuB4, TuD15
Haidner, H. — MD2
Hanson, S. Grüner — TuD11
Hawley, Robert W. — WA2
Herzig, H. P. — TuC3, TuD3
Hinterlong, S. J. — MC2
Hinton, H. S. — MC2
Hodgkin, Van A. — WA4
Honey, David A. — MC3
Hutley, M. C. — WA1

Jahns, Jürgen — MC1, MC4, TuC2, WC
Jenkins, B. Keith — WC2

Kipfer, P. — MD2
Kjelberg, I. — TuD3
Kok, Yon-Lin — TuB3
Koronkevich, V. P. — TuC1
Kostuk, Raymond K. — TuD15
Kubalak, David — TuD2

Lancis, J. — TuD12
Langlois, P. — TuA3, WC4
Larson, D. A. — TuD4
Lee, Wai-Hon — TuA1
Leger, James R. — MC, TuA2, TuC, TuD
Lentine, A. L. — MC2
Levin, Philip S. — TuD10
Li, Lifeng — TuB4, TuD15
Lin, Freddie — TuD14
Liu, William — TuD14
Londoño, Carmiña — MA1, MA3

Macleod, Angus — WA4
Magnusson, R. — MD4
Mait, Joseph N. — WC3
Mansfield, W. K. — TuC2
McCormick, F. B. — MC2
Mikolas, David — MC3
Miller, J. Michael — TuC4
Moharam, M. G. — TuB
Morris, G. Michael — MA, MD3, TuD2
Morrison, Donald — TuD5
Morrison, R. L. — MC2
Mulgrew, P. P. — TuC2

Newman, Daniel M. — WA2
Nijander, C. — MC4
Nogues, Jean-Luc R. — MB2
Noponen, Eero — TuC4
Nordin, Gregory P. — WC2

O'Shea, Donald C. — TuD8

Pastalon, J. Z. — TuC2
Plummer, William T. — MA3
Poleshchuk, A. G. — TuD9
Poutous, Menelaos K. — TuD8
Prather, Dennis W. — WC3

DIFFRACTIVE OPTICS: DESIGN, FABRICATION, AND APPLICATIONS

ADDENDUM AND POSTDEADLINE PAPERS

APRIL 13–15, 1992
NEW ORLEANS, LOUISIANA

Diffractive Optics: Design, Fabrication and Applications
April 13-15, 1992
New Orleans, LA

Monday, April 13, 1992
11:20am

The diffractive optical element (DOE) provides unique and
improved chromatic aberration reduction for both visible
and IR optical systems and simplifies the optical design
form.

Wednesday, April 15, 1992
3:30pm

Optical Thyristors are promising devices for optical
switching and optical memory. They combine the functions
of detection, memory and emission in a single device with
low switching and holding powers. The three dimensional
integration of optical components is a promising approach
to achieving large interconnect densitites with simple
fabrication techniques. We have demonstrated that a 200
um diameter microlens fabricated by ion exchange in glass
is able to image one 4X4 photothyristor array onto a second
array with optical powers sufficient for cascading.

ADDENDUM

MA3
9:20am

TuD16
4:00pm (Addition)

Application of diffractive optical elements in visible and infrared optical systems

C. William Chen

Electro-Optical & Data Systems Group,
Hughes Aircraft Company, El Segundo, California 90245

ABSTRACT

The diffractive optical element (DOE) provides unique and improved chromatic aberration reduction for both visible and IR optical systems and simplifies the optical design form.

INTRODUCTION

The diffractive optical element (DOE) provides unique and improved chromatic aberration reduction for both visible and IR optical systems. Therefore, DOE simplifies the optical design form and improves the image quality of refractive optical systems. This paper formulates and analyzes the theory of chromatic aberration correction and compares DOE performance with that of a conventional optical element (COE). It presents several design examples with spectral bandwidth ranging from visible to long wavelength infrared to illustrate the advantages of optical systems using a DOE. DOE improves optical system performance while lowering the cost and weight by reducing the number of lens elements and desensitizing misalignment tolerances.

DOE has been applied to various imaging optical systems for more than 20 years. However, the applications so far are mainly limited to such systems as head-up and helmet-mounted displays, which have very narrow spectral bandwidths. H. Madjidi-Zolbanine and C. Froehly used a DOE to correct both axial chromatic and spherical aberrations of a single lens.[1] A. I. Tudorovskii put a Fresnel zone plate (FZP) in front of an f/16 achromatic doublet to reduce the axial secondary chromatic aberration.[2] Using DOE to correct the axial chromatic and spherical aberrations of a silicon lens was also proposed by G. J. Swanson and W. B. Veldkamp.[3] To obtain a very high diffraction efficiency for the DOE, Swanson and Veldkamp proposed a multistep-level kinoform-like FZP to replace the continuous kinoform FZP.[4] The authors call this new class of optical element binary optics because its fabrication method is similar to that of digital electronic parts.

I have proposed a new class of optical element consisting of an aspheric and a DOE to greatly simplify optical systems and improve image quality.[5] The aspheric surface and lens shape

factor of this new optical element eliminate spherical aberration and coma simultaneously. The diffractive optical surface corrects axial chromatic aberration and spherochromatism. This new class of optical element is particularly effective in simplifying a low f-number optical system.

Five design examples with spectral bandwidths in the visible, mid-wavelength infrared (MWIR), and long-wavelength infrared (LWIR) are given. For each design example, a conventional design and a DOE design are given. The geometric aberrations of each design are analyzed and compared. These examples are:

1. A dual-field-of-view (FOV) LWIR afocal telescope with 6.6X magnification for the narrow field and 2.2X magnification for the wide field

2. An f/1.4, 0.5-inch EFL, 18° FOV MWIR imager

3. A 10X MWIR afocal telescope

4. An f/3.2, 3-inch EFL, 10° FOV visible imager with 3 inches eye relief

5. A 33.5-mm EFL, 50° FOV eyepiece with 31.0 mm eye relief

Five design examples have shown analytically that DOE simplifies and improves optical systems with spectral bandwidth ranging from visible to LWIR. DOE is an excellent element to correct primary chromatic aberration of both MWIR and LWIR optical systems. For visible optical systems, DOEs are very effective in primary and secondary chromatic aberration reduction. DOE also significantly reduces the higher order aberrations as a result of its negative Abbe number and very dispersive nature.

REFERENCES

1. H. Madjidi-Zolbanine and C. Froehly, "Holographic correction of both chromatic and spherical aberrations of a single lens," Appl. Opt., vol. 18, no. 14, pp. 2385–2393, 1979.

2. A. I. Tudorovskii, "An Objective With a Phase Plate," Optics and Spectroscopy, vol. VI, no. 2, pp. 126–133, 1959.

3. G. J. Swanson and W. B. Veldkamp, "Infrared Applications of Diffractive Optical Elements," SPIE Proceedings, vol. 885, paper 22, 1988.

4. L. B. Lesem, P. M. Hirsch, and J. A. Jordan, Jr., "The Kinoform: A New Wavefront Reconstruction Device," IBM J. Res. Dev., vol. 13, pp. 150–155, 1969.

5. C. W. Chen, "Optical Element Employing Aspherical and Binary Grating Optical Surfaces," U.S. patent 5,044,706.

Cascading of two pnpn-Photothyristor arrays in a microoptical system: An experimental demonstration

K.-H. Brenner, W. Eckert, S. Kufner, J. Moisl, S. Sinzinger, G. Borghs[*], M. Kuijk[+], P. Heremans[*]

Angewandte Optik, Physikalisches Institut der Univ. Erlangen, 8520 Erlangen, Germany
[*]Interuniversity Micro Electronics Center (IMEC) vzw, Kapeldreef 75, Leuven, Belgium
[+]Vrije Universiteit Brussel, Dept. TONA, Pleinlaan 2, Brussels, Belgium

Abstract:

Optical Thyristors are promising devices for optical switching and optical memory. They combine the functions of detection, memory and emission in a single device with low switching and holding powers. The threedimensional integration of optical components is a promissing approach to achieving large interconnect densities with simple fabrication techniques. We have demonstrated that a 200 μm diameter microlens fabricated by ion exchange in glass is able to image one 4x4 photothyristor array onto a second array with optical powers sufficient for cascading.

Cascading of two pnpn-Photothyristor arrays in a microoptical system: An experimental demonstration

K.-H. Brenner, W. Eckert, S. Kufner, J. Moisl, S. Sinzinger, G. Borghs[*], M. Kuijk[+], P. Heremans[*]

Angewandte Optik, Physikalisches Institut der Univ. Erlangen, 8520 Erlangen, Germany
[*]Interuniversity Micro Electronics Center (IMEC) vzw, Kapeldreef 75, Leuven, Belgium
[+]Vrije Universiteit Brussel, Dept. TONA, Pleinlaan 2, Brussels, Belgium

1. Introduction

Optical Thyristors are promissing devices for optical switching and optical memory. Originally proposed as pnpn-switch /1/ this device structure is also known under the name VSTEP /2/ because of its vertical emission. Several improvements have been achieved such as differential swiching /3/ and extremely low switching energies /4/. Operating as photothyristors, they combine the functions of light detection, memory with holding powers down to 0.6 μW and light emission in a single device.

For the threedimensional integration of optical components we have recently proposed /5,6/ an approach which is purely based on reflective and refractive mechanisms of light deflection. These mechanisms, because of their insensitivity to wavelength changes, their large numerical aperture, the possibility of on-axis lens-operation and stacked assembly are considered the most likely candidates for microoptical systems. In this

Fig. 1 Layout for a stacked microoptical system /6/.

approach, as depicted in fig. 1 microlenses and microprisms allow a construction of conventional optical systems in the mm-size range. An important aspect for these microoptical systems is the surface quality of the micro-prisms, the imaging quality of the micro lenses and the achievable numerical aperture. In addition to the focal spot size the numerical aperture determines the amount of light that can be collected from a light source which radiates into a large solid angle.
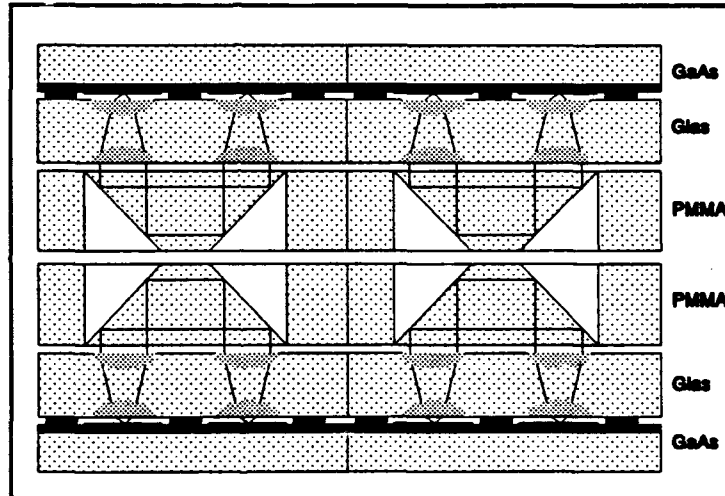
2. Optical Thyristor Array

The optical thyristor array /7, 8/ was grown by MBE on a p-type GaAs-wafer in layers of 500 nm p-doped GaAs, 300 nm n-doped GaAs, a 20 nm layer of $In_{0.1}Ga_{0.9}As$, 300 nm p-doped GaAs and 350 nm n-doped GaAs. Isolation is provided through a layer of silicon

nitride. Light emission occurs in the upper p-doped layer whereas the middle layer serves as the 'base'. In the 'on'-state the total emitted light power was measured as 30 μW, radiated in a 2π solid angle. All the cells within one array are electrically connected together through a top contact. Driven with a common load resistor this array operates as a winner-take-all network, since each cell inhibits the other cells. Thus only the cell with the largest photocurrent will switch to the on-state. This method of switching is advantageous because it is able to offer switching sensitivities of down to 0.1 nW as reported by Hara et al. /4/. Another advantage is that, due to the switching being introduced electrically, there is no critical-slowing-down phenomenon. Also, no critical biasing of the cells is required before switching. However electrical clocking is needed for the operation.

Optical Thyristor (OT) arrays have been fabrica.ed at IMEC in a cell-size range of 21x28 μm as the smallest cell size to 100x200 μm as the largest size. Fig. 2 shows a photograph of a OT-array with 21x28 μm cell size. The emitting area is approx. 20μm x 20μm with the remaining area occupied by the electrical contact. In the light emitting state the electrical power for maximum light output is approx. 10 mW whereas in the hold state 2 mW electrical power are sufficient to operate the device as a memory element.
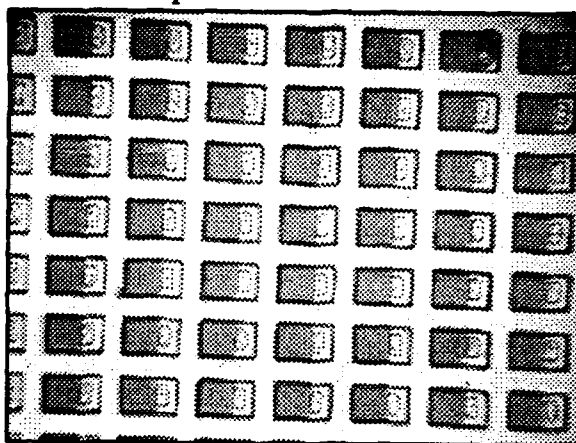

Fig. 2 Photograph of the 21μm x 28μm photothyristor array.

3. Fabrication of microlens arrays

The microlenses for these experiments were gradient index lenses which were fabricated by an ion-exchange process. The process we are using is the silver-sodium exchange as compared to the thallium-sodium ion exchange /9/. This process involves less toxic chemicals and is therefore easier to handle in a university environment. Nevertheless we achieved equally large phase shifts, which can be attributed largely to the used special glass type. This glass type was specially developed for waveguide

Fig. 3 Interferogram of the microlens.

applications by IOT. The masked substrate is exposed to a melt of silvernitrate, where the diffusion process takes place. For the mask metal we are presently using alumiminium. Fig. 3 shows an interferogram of a lens of the array used in the experiment. The diameter is 205 μm. For the process we are using, the resulting index change at the surface reaches a maximum value of approx. 0.10.
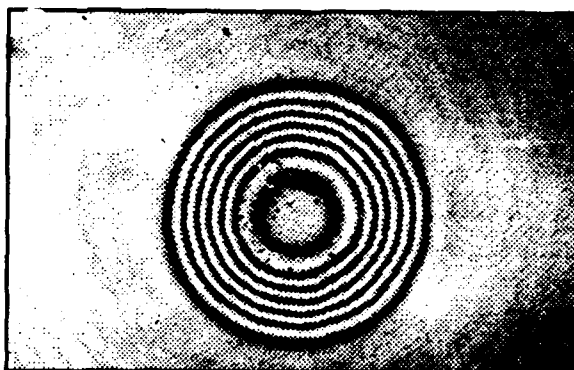
mask diameter (μm)	lens diameter (μm)	focal length (mm)	max. phase-shift (π)	numerical aperture
120	210	1.2	15.2	0.088
110	205	1.2	14.4	0.085
80	175	0.8	13.8	0.11
70	160	0.7	12.9	0.11
60	155	0.6	12.1	0.13
40	140	0.5	10.8	0.14

The diffusion coefficient for this glass type is strongly dependant on the local concentration. Thus the diffusion process is highly nonlinear and the index profile resulting from circular apertures provides good quality microlenses. According to measurements these lenses show a close to diffraction limited resolution. Tab.1 shows the spectrum of mask-diameters we have used together with the corresponding achieved optical parameters.

4. Experiments

The cascading experiment is illustrated in fig. 4. A microscope objective with a 10x magnification and a numeric aperture of 0.25 collects approx. 9 μW of the emitted 30 μW of light power.
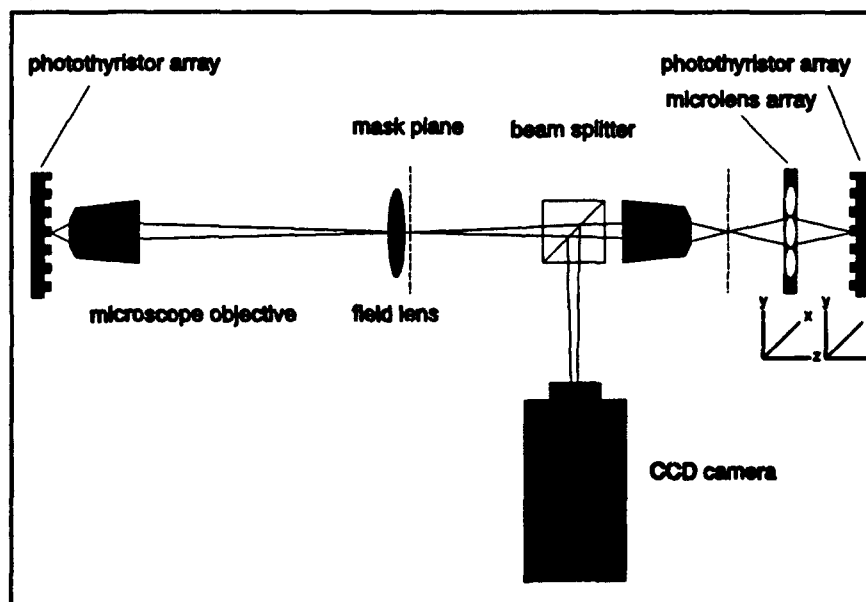

Fig. 4 Optical setup for the cascading experiment.

In combination with the field lens the second microscope objective with a 20x magnification and a numeric aperture of 0.5 generates a demagnified image of the input photothyristor array.

Within the microlens array only one lens is used in a 2f-2f-imaging configuration. Thus the intermediate image is imaged 1:1 onto the second photothyristor array. The CDD-camera observes an image of the second photothyristor array, which is formed by a 1:1 imaging step through the microlens and followed by a 20x magnification by the microscope objective. This way the image observed by the CCD-camera is roughly equal to the image of the first photothyristor array generated on the second array.

The first array was also mounted on a x-y-stage in order to be able to move the object plane. When only one pixel in the input array was turned on, switching could be observed as shown in fig. 5., which shows an image observed by the CCD-camera. By moving the input array, it was possible to switch different pixels in the output array, corresponding to the location of the lit pixel in the input array.
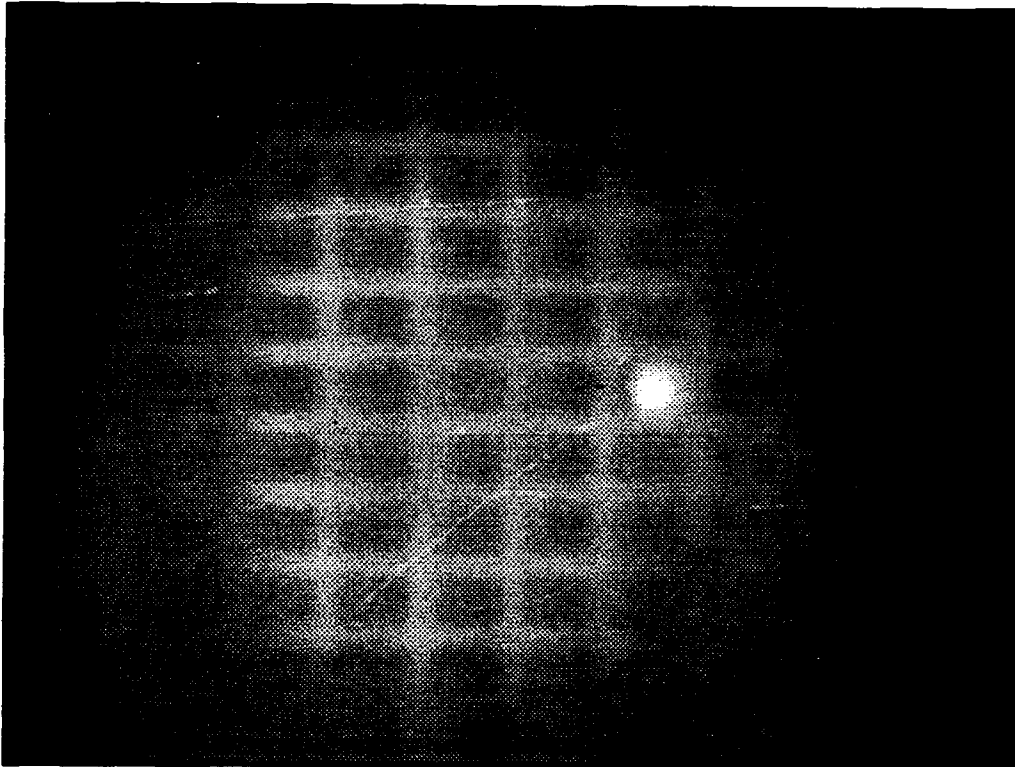

Fig. 5 Experimental result showing more than 4x4 cells which are imaged with one microlens. One cell is switched on optically by the previous array.

5. Conclusions

In conclusion we have demonstrated that a microlens fabricated by ion-exchange in glass with a diameter of 200 μm allows to image a region of the same diameter with sufficient imaging quality. Furthermore the sensitivity of the pnpn-switch as well the numeric aperture of the microlens is large enough to optically switch one array with another array. Thus the feasibilty of a combined microintegration of active and passive components is shown.

6. References

1.   J.I. Pankove et al., "A pnpn optical switch", SPIE Vol. 963, Optical Computing 1988, page 191

2.   K. Kasahara, Y. Tashiro, N. Hamao, M. Sugimoto, T. Yanase, "Double hetero-structure optoelectronic switch as a dynamic memory with low power consumption", Appl. Phys. Letter 52 (1988) 679-681.

3.   K. Hara, K. Kojima, K. Mitsunaga, K. Kyuma, "Differential optical switching at subnanowatt input power", IEEE Phot. Tech. Lett. Vol. 1 (1989) 370

4.   K. Hara, K. Kojima, K. Mitsunaga, K. Kyuma, "AlGaAs/GaAs pnpn differential optical switch operable with 400 fJ optical input energy", Appl. Phys. Lett. Vol. 57 (1990) 1075

5.   K.-H. Brenner, "3D-Integration of digital optical systems", in Optical Computing 1991 Technical Digest Series Vol. 6, Salt Lake City, p. 25-28

6.   K.-H. Brenner, "Techniques for integrating 3D-optical systems", in Proc. SPIE Vol. 1544 Miniature and Microoptics, p. 263-270

7.   P. Heremans, M. Kuijk, G. Borghs, "Array to array transcription of optical information by means of surface emitting thyristors", IEDM Tech. Digest 91, 433 (1991)

8.   M. Kuijk, P. Heremans, R. Vounckx, G. Borghs, "Maximum optical dose detection with a 16x16 monolithic thyristor array", IEEE Phot. Tech. Lett. April 1992.

9.   K. Iga, Y. Kokubun, M. Oikawa, "Fundamentals of Microoptics", Academic Press, Orlando 1984

Athermalization with Diffractive Optics

Carmiña Londoño, William T. Plummer, Peter P.Clark

Polaroid Optical Engineering

38 Henry Street

Cambridge, MA 02139

(617) 577-4115

Summary:

Often optical systems have to operate over a wide temperature range, resulting in changes of both first order properties and optical performance. These variations may be significant if the elements are made from plastics or infrared materials like Germanium, which have dn/dT's (change of index with temperature) which are at least 100 times larger than many of the visible optical glasses. If it is important to keep these changes to a minimum, then the system has to be athermalized.

Conventional athermalizing techniques can be subdivided into three major categories: mechanical, electronic and optically passive. The third consists of athermalizing a system by using the thermal properties of different optical materials. The use of a diffractive optical element to compensate for thermal variations is a new example of the third category. We will discuss the design procedures required to athermalize

optical elements by using kinoforms. We show that a one-piece lens can be constructed of a single material in such a way that its focal position and third order spherical aberration do not vary with temperature. Examples will be given for plastic, glass and Germanium. Other properties of these designs will also be noted.

The figure below illustrates an example of an athermalized plastic hybrid lens and a Germanium hybrid lens. In each case a kinoform is used on the second surface. The plastic lens is athermal to one part in 10^4 at 0.8 microns while the Germanium is athermal to one part in 10^8 at 10.6 microns, both from 0 to 40 degrees Celsius.

PMMA Athermat   Germanium Athermat
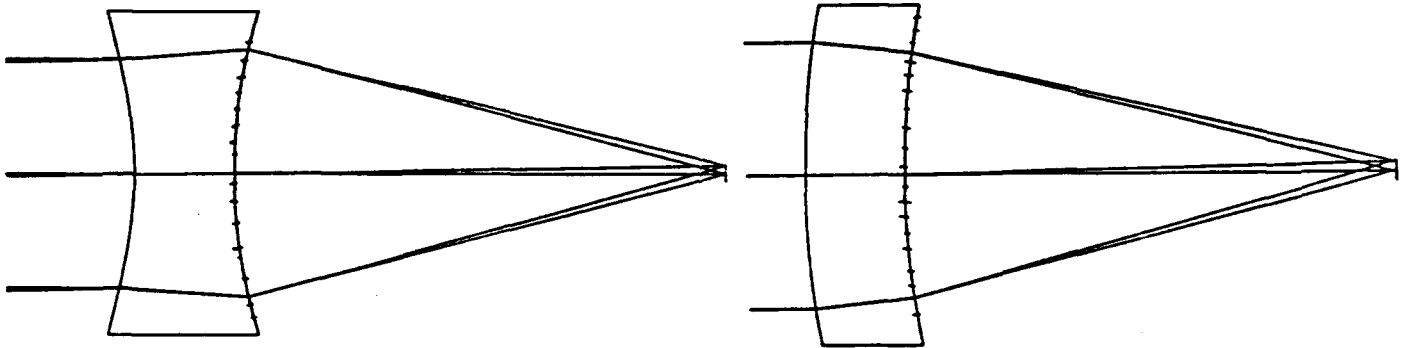
Beam Splitters Using Stratified Volume Holographic Grating.

Parameters of several beam splitters were obtained by optimizing the theory developed for calculating the diffraction amplitudes generated by a stratified volume holographic grating. A splitter in seven beams was then realised.

ANDRÉ GRANGER, LI SONG and R.A. LESSARD

Centre d'optique photonique et laser, Département de physique, Université Laval, Ste-Foy, Québec, Canada G1K 7P4
tel: (418) 656-2454

Beam Splitters Using Stratified Volume Holographic Gratings.

ANDRÉ GRANGER, LI SONG and R.A. LESSARD

Centre d'optique photonique et laser, Département de physique,
Université Laval, Ste-Foy, Québec, Canada G1K 7P4
tel: (418) 656-2454

In recent years, beams splitters have generated a lot of interest in the field of diffractive optics. Used primarily in robotic vision and optical interconnections, these devices are mostly realised using Dammann gratings and other less commonly used monolayer technics. We propose to acheive better results using a multilayer diffractive element, which can be seen as a volume hologram.

Our statified volume holographic grating consists of layers of sinusoidal phase gratings, separated by buffers of non-diffractive material. Using a convolution approach developed by Song and Lessard[1], the amplitudes of the diffracted beams from the device can be calculated. For a two layer stratified hologram, the amplitudes can be obtained by

$$\{\{\{A_{m,1}\} \cdot \{P_{m,1}\}\} \bullet \{A_{m,2}\}\},$$

where $A_{m,l}$ are the diffraction amplitudes generated by the lth layer, and $P_{m,l}$ are the propagators of each of the m diffraction amplitudes in the lth buffer. Because of the propagation in the buffer, one must realise that the amplitudes calculated are only valid for a predetermined incoming angle, which was chosen to be normal. The efficiencies of the diffraction orders are obtained by taking the square of the normalised amplitudes (normalised with respect to the incoming energy).

Being now able to calculate the diffraction amplitudes coming out of the device, an uniformity and concentration of the energy in the diffracted beams of interest must now be obtained to acheive a good beam splitter. To establish this goal, a function, chosen for being a good scale of these characteristics, was minimised with an algorithm of simulated annealing. The choice of this function was dependant on the number of fan-out beams, but all these functions which were subjected to optimisation bear similarities with the following

$$f(\varphi_1,...,\varphi_N,\Delta) = (\sum_{m=n \text{ orders}} \frac{(\eta - \eta_m)^2}{\eta_m})^2,$$

where the φ_i are the modulation amplitudes of the phase shift, and Δ is the period of each gratings. The global squaring is used to emphasize the variation of the function when a point of lower value is reached.

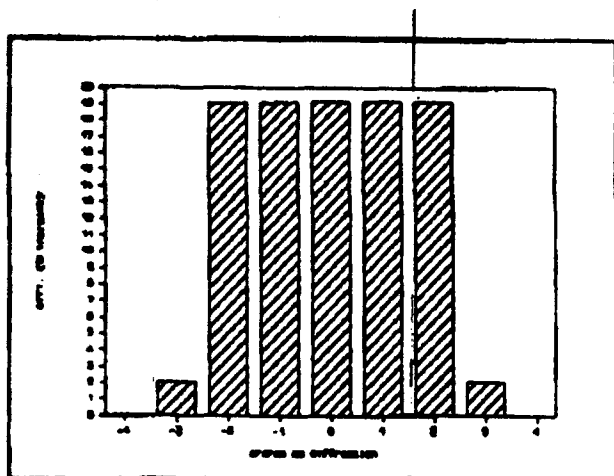Having run multiple simulations, interesting results were obtained for two, three,

Figure 1: Theoretical efficiencies of a
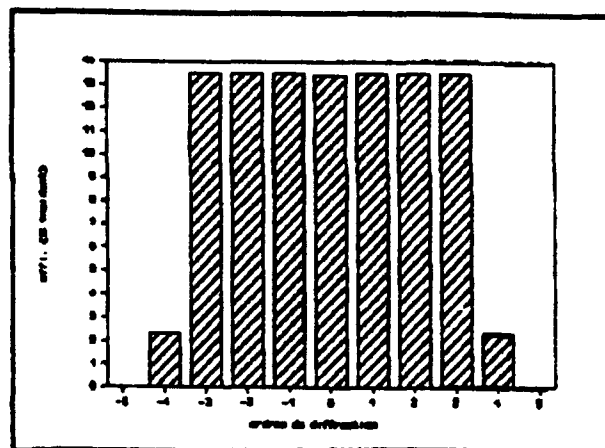five beams splitter.

Figure 2: Theoretical efficiencies of a
seven beams splitter.

five, seven and nine fan-out beams. Figure 1 presents the theoretical efficiencies of a beam splitter giving five beams, composed of two layers of diffractive material. The total efficiency obtained for the five beams was better than 95%, compared to an efficiency of 87% for a multilevel Dammann[2] and 80% for a classical Dammann grating[3]. It should be noted that a perfect uniformity of the five beams is acheived because, mathematically, our problem was to find a solution for the three unknowns (0, +1 and +2 orders, -1 and -2 orders being equal to their positive counterparts at normal incidence). In figure 2, the efficiencies of a seven beams fan-out are illustrated. The theoretical total efficiency of this two layers hologram is again of the order of 95%, compared to 77% for a conic profile[4] and 85% for a Dammann grating[3]. Because of the remarkable characteristics of this seven beam splitter, we chose to realise it experimentally to test our theoritical predictions.

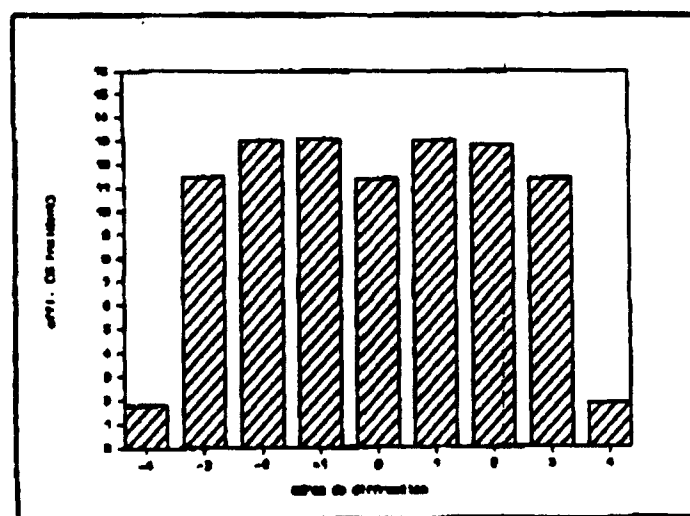First, we needed to find a technic of recording the desired sinusoidal paterns on

Figure 3: Experimental efficiencies of a
stratified 7 beams splitter

each side of the buffer. After a good characterisation of the material (in our case photoresist), a single exposure recording technic was developed. Using a Billet system as the recording set-up, a relatively good control of the parameters was possible, enabeling us to realise a seven beams splitter for which the characteristics are presented in Figure 3.

The total efficiency of this diffractive device is higher than 85%, which is better than 70% efficiency obtained with a conic grating profile[4]. The uniformity of the beams is found to be good, being less then 2 percentage points between the weakest and strongest beam. This characteristic is again much better than what was previously acheived with other technics. These remarkable results could be improved by using better standard fabrication technics. For example, the commercial glass plates that were used as buffer were not perfectly parallel and the characterisation of the photoresist was done under ordinary laboratory conditions.

In conclusion, the beam splitter which we realised using a stratified volume holographic grating showed good results and its performance justified our interest.

[1] Song L., Lessard R.A. (1990). "Theoretical and Experimental Study of Stratified Volume Holographic Gratings". Optics & Photonics News, 1, A124.

[2] Walker S.J., Jahns J. (1990). "Array generation with multilevel phase gratings". J. Opt. Soc. Am., 7, 1509-1513.

[3] Leger J.R., Swanson G.J. and Veldkamp W.B. (1987),"Coherent laser addition using binary phase gratings", Appl. Opt. 26, 4391-4399.

[4] Langlois P., Beaulieu R. (1990)."Phase relief gratings with conic section profile used in the production of multiple beams", Appl. Opt. 29, 3434-3439.

Borghs, G. - PD02
Brenner, Karl-Heinz - PD02

Chen, C. William - PD01
Clark, Peter - MA3

Eckert, W. - PD02

Heremans, P. - PD02

Kuijk, M. - PD02

Londono, Carmina - MA3

Moisl, J. - PD02

Plummer, William - MA3

Sinzinger, Setfan - PD02